Statistics and Scaling Laws of Turbulent Scalar Mixing at High Reynolds Numbers

Von der Fakultät für Maschinenwesen der Rheinisch-Westfälischen Technischen Hochschule Aachen zur Erlangung des akademischen Grades eines Doktors der Ingenieurwissenschaften genehmigte Dissertation

vorgelegt von

Michael Gauding

Berichter:

Univ.-Prof. Dr.-Ing. Dr.h.c. Dr.-Ing. E.h. Dr.sc.h.c. ETH Zürich Norbert Peters
Univ.-Prof. Dr.-Ing. Wolfgang Schröder

Tag der mündlichen Prüfung: 23. Mai 2014

Bibliografische Information der Deutschen Nationalbibliothek
Die Deutsche Nationalbibliothek verzeichnet diese Publikation in der Deutschen Nationalbibliografie; detaillierte bibliografische Daten sind im Internet über http://dnb.d-nb.de abrufbar.
1. Aufl. - Göttingen: Cuvillier, 2014
Zugl.: D 82 (Diss. RWTH Aachen University, 2014)

Nonnenstieg 8, 37075 Göttingen
Telefon: 0551-54724-0
Telefax: 0551-54724-21
www.cuvillier.de

1. Auflage, 2014
Gedruckt auf umweltfreundlichem, säurefreiem Papier aus nachhaltiger Forstwirtschaft.

ISBN 978-3-95404-744-4
eISBN 978-3-7369-4744-3

Vorwort

Die vorliegende Arbeit entstand während meiner Tätigkeit als wissenschaftlicher Mitarbeiter am Institut für Technische Verbrennung der RWTH Aachen University. Sie wurde im Rahmen des Exzellenzclusters “Maßgeschneiderte Kraftstoffe aus Biomasse” im Teilprojekt “Large-Eddy Simulations and Fine Scale Gas-Phase Mixing of Different Property Tailor-Made Fuels” durchgeführt.

Mein besonderer Dank gilt Herrn Prof. Norbert Peters für die Anregung und Förderung dieser Arbeit, seinen fachlichen Rat sowie seine vielfältige und engagierte Betreuung. Herrn Prof. Wolfgang Schröder danke ich für die Berichterstattung in der Prüfungskommission und die Begleitung des Promotionsverfahrens. Herrn Prof. Heinz Pitsch danke ich für die Übernahme des Vorsitzes der Prüfungskommission und Herrn Prof. Marek Behr danke ich für seine Tätigkeit als Beisitzer.

Von unschätzbarem Wert waren für mich die vielen Diskussionen in der Turbulenzgruppe mit Jens Henrik Göbbert, Fabian Hennig, Achim Wick, Philip Schäfer, Markus Gampert, Jonas Boschung und Peng Zeng. Insbesondere danke ich meinen Bürokollegen Jens Henrik Göbbert und Fabian Hennig für die kollegiale und hilfsbereite Zusammenarbeit sowie für die gemeinsame Zeit im Institut und darüber hinaus.

Weiterhin danke ich allen jetzigen und ehemaligen Mitarbeitern des Instituts für Technische Verbrennung, die ebenfalls zum Gelingen dieser Arbeit beigetragen haben. Insbesondere danke ich Bruno Kerschgens, Bernhard Jochim, Achim Wick, Joachim Beeckmann, Tobias Falkenstein, Christian Felsch, Olaf Röhl, Stefan Vogel, Jost Weber, Lipo Wang, Bernd Binninger, Günter Paczko und Sonja Engels.

Juan Pedro Mellado vom Max-Planck-Institut für Meteorologie hat mir in vielen Diskussionen wertvolle Ideen und Hinweise gegeben. Hierfür bedanke ich mich an dieser Stelle. Darüber hinaus bedanke ich mich bei Claudia Günther vom Aerodynamischen Institut und bei Bernd Hentschel von der Virtual Reality Group.

Ebenfalls danke ich allen Studenten, die mit mir zusammengearbeitet haben und mich durch ihre Studien- und Diplomarbeiten tatkräftig unterstützt haben.

Die numerischen Simulationen turbulenter Strömungen wurden auf den Supercomputern JUGENE und JUQUEEN am Forschungszentrum Jülich durchgeführt. Für

die Vergabe der Rechenzeit danke ich dem Jülich Supercomputing Center (JSC), dem Gauss Center for Supercomputing (GCS) und der Jülich Aachen Research Alliance (JARA).

Ein großer Dank gilt meinen Eltern, die immer an mich geglaubt und mich in meinem Werdegang vorbehaltlos unterstützt haben. Ihnen widme ich diese Arbeit.

Aachen, im Mai 2014

Michael Gauding

Abstract

In this thesis the turbulent mixing of a passive scalar and its Reynolds number dependence is studied by means of highly-resolved direct numerical simulation (DNS). The passive scalar is advected by statistically homogeneous isotropic turbulence and a uniform mean gradient is imposed on the scalar field which induces an anisotropy of scalar statistics. The Taylor microscale based Reynolds number is varied between 88 and 529.

It is customary to examine turbulent flows by means of two-point statistics, because they capture the dynamics of the non-local structure that is inherent to turbulence. First, an equation for the even moments of the scalar increment is derived from first principles that generalizes Yaglom's equation to statistically homogeneous but not isotropic scalar fields. This equation is interpreted as a scalar scale-by-scale energy budget equation that incorporates the energy flux through a sphere of radius r and is analyzed by means of DNS and in a filtered form in the context of large eddy simulations. Thereby, it is found that modeling the subgrid transport by an eddy-viscosity approach is suitable for statistically homogeneous turbulence to correctly predict the energy transport.

The generalized Yaglom equation serves as a starting point for further analysis of the Reynolds number dependence of the flatness of scalar increments. To this end, the evolution equation for the fourth order scalar increment is analyzed. It is shown that the non-universality of higher order moments originates from a coupling of dissipative effects to the inertial subrange. Based on this finding a normalization of the fourth order structure function is proposed that makes the curves of the normalized fourth order structure function collapse independently of Reynolds number.

The information about the local structure of turbulent flows is lost by taking ensemble averages over fixed separation distances in the sense of the Kolmogorov-Obhukov-Corrsin theory. This issue may be overcome by an approach that decomposes the turbulent field along a straight line into so-called turbulent line segments. The decomposition is based on the local extremal points of the scalar field so that within each individual line segment the scalar value varies monotonously. By this approach the linear separation distance between adjacent extreme points becomes an intrinsic stochastic quantity that is determined by the turbulent field itself. The decomposition is one-dimensional and can be easily related to conventional two-point statistics. The line segments are parameterized by their length ℓ and the scalar difference $\Delta\phi$ between the end points, and additionally, by the scalar mean gradient $g = \Delta\phi/\ell$. A statistical analysis of line segments based on these parameters is

conducted. The respective probability density functions (pdf) are computed and resulting conditional moments are compared with focusing on the Reynolds number dependence. The marginal length pdf becomes Reynolds number independent when normalized by the mean length ℓ_m. The mean length ℓ_m is shown to scale with the Kolmogorov length η and, additionally, this scaling law is derived theoretically. While the marginal pdf of the mean length obeys a quasi-universal distribution, this is not the case for the distribution functions of the scalar difference $\Delta\phi$ or the mean gradient g. Their tails are exponential or stretched-exponential and the non-Gaussianity becomes more pronounced toward small scales or for rising Reynolds numbers.

In a next step, the universality of small scales is examined by line segments and conventional statistics, where Kolmogorov's phenomenology is adapted to the method of line segments. The conditional moments of $\Delta\phi$ exhibit a clear inertial subrange scaling. Scaling exponents of the conditional moments are computed in order to analyze intermittency effects. Based on conditional statistics it is shown that an intermediate length scale has a major contribution to the mean gradients of line segments and that a scale similarity between the moments of mean gradients and the moments of the local gradients exists. Using this result, a presumed pdf is proposed to compute gradient statistics based on the principle of decomposition and reconstruction of line segments. Additionally, the method of line segments describes the local structure of turbulence. This understanding leads to a novel description of the physics behind cliff-ramp structures and provides a well-defined estimate for the length scale at which large cliff-like structures occur.

Zusammenfassung

Gegenstand dieser Arbeit ist die Untersuchung der Mischung passiver Skalare und deren Reynoldszahlabhängigkeit mittels hochaufgelösten direkten numerischen Simulationen (DNS) in statistisch homogener isotroper Turbulenz. Ein aufgeprägter mittlerer skalarer Gradient induziert eine Anisotropie skalarer Statistiken. Die mit der Taylorlänge gebildete Reynoldszahl liegt zwischen 88 und 529.

Turbulente Strömungen werden üblicherweise anhand von Zweipunktstatistiken untersucht, da diese die Dynamik nicht-lokaler Strukturen erfassen. Zunächst wird aus den Grundgleichungen eine Gleichung für die geraden Momente der skalaren Strukturfunktion hergeleitet. Diese Gleichung verallgemeinert die Yaglom-Gleichung für statistisch homogene aber nicht isotrope Felder. Sie wird als skalenabhängige Budget-Gleichung für die skalare Varianz interpretiert und mittels DNS sowie in gefilterter Form im Kontext der Large-Eddy-Simulation untersucht. Es wird gezeigt, dass eine Modellierung der Feinstrukturgrößen durch einen Wirbelviskositätsansatz geeignet ist um den Energietransport zwischen den Skalen in statistisch homogener Turbulenz zu beschreiben.

Basierend auf der verallgemeinerten Yaglom-Gleichung wird die Abhängigkeit der höheren Momente der skalaren Inkremente von der Reynoldszahl untersucht. Dazu wird eine Gleichung für das vierte Moment der skalaren Strukturfunktion herangezogen. Es wird gezeigt, dass die nicht-Universalität höherer Momente durch eine Kopplung von dissipativen Effekten in das Inertialgebiet entsteht. Mit dieser Erkenntnis wird eine Normierung des vierten Moments der skalaren Strukturfunktion vorgeschlagen, die zu einem universellen Verlauf der normierten Strukturfunktion führt.

Durch Ensemble-Mittelung von Strukturfunktionen über feste Separationsdistanzen gehen die Informationen über die lokale Struktur turbulenter Strömungen verloren. Im Rahmen dieser Arbeit wird daher eine Zerlegung des skalaren Feldes in sogenannte Liniensegmente durchgeführt die diese Einschränkung nicht aufweist. Diese Zerlegung basiert auf den lokalen Extremalpunkten des skalaren Feldes und ist so gewählt, dass innerhalb eines Liniensegments der Wert des Skalars monoton variiert. Durch diese Zerlegung wird die Länge der Segmente eine stochastische Variable die durch das turbulente Feld bestimmt ist. Diese Zerlegung ist eindimensional und kann direkt mit konventionellen Zweipunktstatistiken verknüpft werden. Die Liniensegmente werden mit ihrer Länge ℓ und der skalaren Differenz $\Delta\phi$ zwischen den Endpunkten parametrisiert. Als dritter abhängiger Parameter wird der mittlere Gradient $g = \Delta\phi/\ell$ eingeführt. Liniensegmente werden anhand dieser Parameter

statistisch untersucht. Die entsprechenden Wahrscheinlichkeitsdichtefunktionen und die sich daraus ergebenden Momente werden berechnet, wobei der Schwerpunkt auf Untersuchung der Reynoldszahlabhängigkeit liegt. Es wird gezeigt, dass durch eine Normierung mit der mittleren Segmentlänge ℓ_m die marginale Wahrscheinlichkeitsdichtefunktion der Segmentlänge unabhängig von der Reynoldszahl wird. Basierend auf DNS-Daten ergibt sich eine Skalierung der mittleren Segmentlänge ℓ_m mit der Kolmogorovlänge η. Diese Skalierung wird durch eine theoretische Analyse bestätigt. Ein quasi-universeller Verlauf findet sich hingegen nicht in den Verteilungsfunktionen der skalaren Inkremente oder des mittleren Gradienten g. Die Schwänze dieser Wahrscheinlichkeitsdichtefunktionen weisen einen exponentiellen oder gestreckt-exponentiellen Verlauf auf. Die Abweichungen der Verteilungsfunktionen von einer Gaussverteilung nehmen mit der Reynoldszahl zu.

Anschließend wird die Universalität der kleinen Skalen mittels Liniensegmenten und konventionellen Statistiken untersucht. Hierzu wird die Kolmogorov-Phänomenologie auf Liniensegmente übertragen. Konditionierte Momente zeigen eine deutliche Skalierung im Inertialgebiet. Zur Analyse der Intermittenz werden Skalierungsexponente berechnet. Darüber hinaus wird eine Skalenähnlichkeit zwischen den Momenten der mittleren Gradienten der Liniensegmente und der Momente der lokalen Gradienten nachgewiesen. Mit diesem Ergebnis wird ein Modell für die Wahrscheinlichkeitsdichtefunktion der Gradienten entwickelt. Die Methode der Liniensegmente ermöglicht die Untersuchung der lokalen Struktur der Turbulenz. Dies führt zu einem verbesserten Verständnis der Physik von sogenannten “Cliff-Ramp-Strukturen”, die in skalarer Turbulenz auftreten und ermöglicht eine wohldefinierte Bestimmung der Längenskala, auf der große lokale Gradienten auftreten.

Contents

1 Introduction

The turbulent motion of fluids and scalars is a highly complex problem. It is still one of the unsolved problems of classical physics, cf. Nelkin (1992) and Shraiman and Siggia (2000), and the description remains challenging. The understanding of turbulent flows and turbulent mixing is of great interests for many applications. Prominent examples are the turbulent combustion of chemical reactants and the dynamics of the atmosphere or the oceans. In those cases the evolution of the scalar affects the turbulent flow itself. Here, we focus on the case where the scalar is both conserved and passive and does not affect the flow field.

The main difficulties regarding the statistical description of turbulent flows originates from the non-locality and non-linearity of the governing equations. Turbulent flows are characterized by a very great number of degrees of freedom resulting in a wide range of interacting time and length scales. Therefore, a theory for turbulent flows must be a statistical one. Due to the non-locality it is customary to examine turbulent flows by means of two-point statistics. Most understanding of turbulence at high Reynolds numbers is based on the scaling theory developed first by Kolmogorov (1941a,b) and extended later to scalars by Obukhov (1949b) and Corrsin (1951). Based on dimensional arguments, this theory relates the statistics of velocity or scalar increments to the mean energy or scalar dissipation. By the Kolmogorov-Obhukov-Corrsin (KOC) theory the information about the local structure of the turbulent field is lost when taking ensemble averages over fixed separation distances. This issue was overcome by Wang and Peters (2006, 2008) by the theory of dissipation elements. Here, two-point statistics are calculated along gradient trajectories that connect local minimum and local maximum points in the scalar field. The spatial region formed by the ensemble of all gradient trajectories sharing the same extreme points is called dissipation element. They may be parameterized by the linear separation distance and the scalar difference between the extreme points. By this approach the linear separation distance itself becomes an intrinsic stochastic quantity that is determined by the turbulent field. In the present thesis we propose to decompose the signal of a passive scalar along a straight line into piece-wise monotonously increasing or decreasing line segments that start at a local minimum point and end at a local maximum point or vice versa. These line segments can be understood as one-dimensional dissipation elements. Thereby, we retain the property that the decomposition is determined intrinsically by the turbulent field, but because the decomposition is one-dimensional it can be easily related to conventional two-point statistics in the sense of the KOC theory.

At high Reynolds numbers, turbulent flows exhibit strong spatial and temporal fluctuations. The large structures of the flow at an integral length scale depend on the boundary conditions and cannot be considered as universal. On the other hand according to Kolmogorov's similarity hypotheses, cf. Kolmogorov (1941a,b), under the condition of sufficiently high Reynolds numbers, the small-scale structure of turbulent flows is assumed to become statistically isotropic and universal. In this case, it is expected to find generally valid statistics and scaling relations, as proposed by Kolmogorov's 2/3-law. However, small-scale statistics are affected by strong fluctuations of the dissipation; an effect that is called internal intermittency. Thereby, small-scale statistics, that may be described by the probability density function (pdf) of the velocity or scalar increments, depend on scale. At large separation distances this pdf is Gaussian but for separation distances in the inertial subrange it exhibits strong deviations from Gaussianity with progressively longer stretched-exponential tails. The non-Gaussianity becomes even more pronounced toward small scales where the scalar increment can be interpreted as a derivative. The similarity hypotheses propose an universal shape of the pdf of the scalar increment, where a normalization solely by standard deviation accounts for the dependence of the scale. However, the strong fluctuations of the dissipation destroy small-scale universality. This renders the similarity hypotheses invalid for moments larger than the second order. The deviations from the KOC prediction can be further observed by the anomalous scaling of the moments of the structure functions, or alternatively, by the Reynolds number dependence of the higher order non-dimensional moments.

In the course of this thesis we take the classical KOC theory as starting point to examine turbulent mixing of passive scalars. The results of this thesis strongly rely on Direct Numerical Simulations (DNS) that have been conducted for various Reynolds numbers with a Taylor based Reynolds number between 88 and 529. We solve for an incompressible, statistically homogeneous isotropic velocity field, and additionally, we solve for a statistically homogeneous passive scalar with imposed uniform mean gradient. In the course of the first chapter we introduce the governing equations, characteristic numbers and statistical tools. In the second chapter we describe the numerical algorithms, i.e. the pseudo-spectral method and the time stepping schema, of the newly developed highly-accurate flow solver. Then parallelization strategies, code design and code performance are presented. In the third chapter we present characteristic properties of the DNS simulations and conduct a comprehensive validation by means of theoretical results, experiments, and DNS results from other authors. In chapter 4 we derive a generalized evolution equation for the even moments of the scalar increment that accounts for large scale effects. This equation is interpreted as a scalar energy scale-by-scale budget equation. It is first evaluated by means of DNS and later applied in filtered form to *a-priori* and *a-posteriori* studies of Large Eddy Simulations. Additionally, this equation is the starting point to examine the Reynolds number dependence of scalar structure functions in chapter

6. In chapter 5 we introduce the method of turbulent line segments and conduct by means of DNS a statistical analysis of the parameters chosen to describe the line segments. The respective joint pdfs and marginal pdfs are computed and resulting conditional moments are compared with a focus on the Reynolds number dependence. Additionally, the method of turbulent line segments lead to a novel description of the physics behind cliff-ramp structures and provides an estimate for the length scale at which large gradients occur. In chapter 6 we examine the universality of small scales by line segments and conventional statistics, where Kolmogorov's phenomenology is adapted to the method of line segments. Based on conditional statistics we show that an intermediate length scale has a major contribution to the gradient of line segments and that a scale similarity between the moments of mean gradients and the moments of the local gradients exists. We propose a presumed pdf that allows us to compute gradient statistics based on the principle of decomposition and reconstruction of line segments. Furthermore, we adopt the scale-by-scale scalar energy budget equation derived in chapter 4 to show that the non-universality of higher order moments originates from a coupling of dissipative effects to the inertial subrange. Finally, in chapter 7 a brief summary of the main results is given.

1.1 Governing Equations

1.1.1 Velocity Field

We assume that the motion of the fluid is governed by the Navier-Stokes equations and shall restrict ourselves to incompressible and Newtonian fluids. If so, the Navier-Stokes[1] equations read

$$\begin{aligned} \frac{\partial u_j}{\partial t} + u_i \frac{\partial u_j}{\partial x_i} &= -\frac{\partial p}{\partial x_j} + \nu \frac{\partial^2 u_j}{\partial x_i^2} + f_j \,, \quad j = 1,2,3 \\ \frac{\partial u_i}{\partial x_i} &= 0 \,, \end{aligned} \tag{1.1}$$

where p is the pressure, obtained by dividing the dynamic pressure by the density ρ; ν is the kinematic viscosity, and $u_j(\boldsymbol{x}, t)$ the Eulerian velocity field, which depends on position $\boldsymbol{x}$ and time t. f_j denotes an external forcing which acts on large scales only. The Navier-Stokes equations contain all necessary information to fully characterize the motion of turbulent flows. For solving eq. 1.1 adequate initial and boundary conditions must be specified. For simplicity we assume periodic boundary conditions, where all dependent variables fulfill the condition

$$u_i(x_1 + n_1 L, x_2 + n_2 L, x_3 + n_3 L) = u_i(x_1, x_2, x_3) \,, \tag{1.2}$$

[1] The standard rule for summation over repeated indices applies.

for all $\boldsymbol{x}$ and all integers $\boldsymbol{n}$. The period L is taken as 2π. Throughout this work, we further restrict ourselves to statistically isotropic velocity fields. In that case, we do not need to distinguish between mean and fluctuating quantities, and therefore u_j and p denote the velocity and the pressure fluctuations, respectively. The Navier-Stokes equations reveal two important mathematical properties: The non-linearity of the advective term and the non-locality of the pressure term. By taking the divergency of eq. 1.1 and assuming that the forcing term is rotational, we obtain the so called Poisson equation for the pressure

$$\frac{\partial^2 p}{\partial x_i^2} = -\frac{\partial u_i}{\partial x_j}\frac{\partial u_j}{\partial x_i}\,, \tag{1.3}$$

where we have exploited solenoidality of u_j. For periodic domains, the Poisson equation can be inverted by applying a Fourier transform to eq. 1.3. It follows that

$$\widehat{p}_\kappa = \frac{1}{\kappa^2}\mathcal{F}\left(\frac{\partial u_i}{\partial x_j}\frac{\partial u_j}{\partial x_i}\right)\,. \tag{1.4}$$

The forward Fourier transform is denoted by $\mathcal{F}$ and κ is the modulus of the wavevector $\boldsymbol{\kappa}$. The solution of the Poisson equation is defined up to an additive constant, since $\hat{p}_0$ is arbitrary. Equation 1.4 illustrates the non-locality of the pressure field by the application of the Fourier transform.

1.1.2 Scalar Field

Additionally, we consider the motion of a conserved passive scalar $\Phi(\boldsymbol{x}, t)$, governed by the advection-diffusion equation

$$\frac{\partial \Phi}{\partial t} + u_i\frac{\partial \Phi}{\partial x_i} = D\frac{\partial^2 \Phi}{\partial x_i^2}\,, \tag{1.5}$$

where D is the molecular diffusivity. Equation 1.5 is linear in terms of the scalar $\Phi(\boldsymbol{x}, t)$, but $\Phi(\boldsymbol{x}, t)$ is coupled through the convective term in a non-linear way to the velocity field $u_i(\boldsymbol{x}, t)$. The scalar is passive which means that the motion of the scalar has no impact on the velocity field. Furthermore, the scalar is conserved, because eq. 1.5 contains no source or sink term. Examples of scalar turbulence are the temperature field or the motion of a non-reactive contaminant when the concentration is so low that it has no dynamical effect on the flow field.

In order to keep the scalar in a statistically steady state a uniform mean gradient is imposed on the scalar field. To this end the scalar field is decomposed into mean and fluctuating components, i.e.

$$\Phi(\boldsymbol{x}, t) = \Gamma x_2 + \phi(x, t)\,. \tag{1.6}$$

Here, Γ is the magnitude of the uniform mean scalar gradient and $\phi(\boldsymbol{x}, t)$ denotes the fluctuating scalar field. Due to the linearity of eq. 1.5, Γ can be taken as unity without loss of generality. By means of eq. 1.6, we can rewrite eq. 1.5 in terms of the scalar fluctuation

$$\frac{\partial \phi}{\partial t} + u_i \frac{\partial \phi}{\partial x_i} = D \frac{\partial^2 \phi}{\partial x_i^2} - \Gamma u_2 \,. \tag{1.7}$$

1.1.3 Characteristic Numbers

The governing equations can be rewritten in normalized form by introducing a characteristic velocity scale U, a characteristic length scale L and a scalar reference value Φ_{ref}. With $\tilde{x}_i = x_i/L$, $\tilde{u}_i = u_i/U$, $\tilde{t} = tL/U$, $\tilde{p} = p/U^2$ and $\tilde{f}_i = f_i L/U^2$, we obtain for the Navier-Stokes equations

$$\frac{\partial \tilde{u}_j}{\partial \tilde{t}} + \tilde{u}_i \frac{\partial \tilde{u}_j}{\partial \tilde{x}_i} = -\frac{\partial \tilde{p}}{\partial \tilde{x}_j} + \frac{1}{\mathrm{Re}} \frac{\partial^2 \tilde{u}_j}{\partial \tilde{x}_i^2} + \tilde{f}_j \,. \tag{1.8}$$

Only one non-dimensional number, namely the Reynolds number $\mathrm{Re} = UL/\nu$, appears. The scalar transport equation reads in normalized form

$$\frac{\partial \tilde{\Phi}}{\partial \tilde{t}} + \tilde{u}_i \frac{\partial \tilde{\Phi}}{\partial \tilde{x}_i} = \frac{1}{\mathrm{Re}} \frac{1}{\mathrm{Sc}} \frac{\partial^2 \tilde{\Phi}}{\partial \tilde{x}_i^2} \,, \tag{1.9}$$

where the Schmidt number, defined as $\mathrm{Sc} = \nu/D$ appears as additional non-dimensional quantity. The product of Reynolds and Schmidt number is defined as the Peclet number Pe. The Peclet number characterizes the interplay between advection and diffusion effects and can be expressed as

$$\mathrm{Pe} = \mathrm{Re}\,\mathrm{Sc} = \frac{\mathcal{O}(u_i \frac{\partial \phi}{\partial x_i})}{\mathcal{O}(D \frac{\partial^2 \phi}{\partial x_i^2})} \propto \frac{UL}{D} \,. \tag{1.10}$$

1.2 A Statistical Description of Turbulence

Turbulent flows are governed by deterministic equations, cf. eqs. 1.1 and 1.5. But under the condition of high Reynolds numbers, turbulent flows evolve in a complex spatially and temporally stochastic way. The Reynolds number, as the most important non-dimensional number to characterize flows, can be interpreted as the ratio of inertial forces to viscous forces acting on a fluid element. When the Reynolds number is small the viscous forces damp perturbations and the flow remains in a deterministic laminar state. When the Reynolds number exceeds a critical value the flow becomes unstable and a transition from laminar flow to a turbulent flow with strong fluctuations takes place. However, turbulent flows are not fully random and the presence of coherent structures indicate a certain level of organization or

symmetries in a statistically sense. In this section we will introduce the mathematical tools for the statistically description of turbulent flows.

1.2.1 Random Variables

In turbulent flows the variables $u_i(\boldsymbol{x},t)$, $p(\boldsymbol{x},t)$ and $\phi(\boldsymbol{x},t)$ are random variables. A random variable ϕ can be completely characterized by its probability density function $f_\phi(\psi)$, where ψ is the sample-space variable corresponding to ϕ. The mean value of the random variable can be obtained by

$$\langle\phi(\boldsymbol{x},t)\rangle = \int \psi f_\phi(\psi;\boldsymbol{x},t)\mathrm{d}\psi\,, \tag{1.11}$$

and the nth order moment of the random variable is defined by

$$\langle\phi^n(\boldsymbol{x},t)\rangle = \int \psi^n f_\phi(\psi;\boldsymbol{x},t)\mathrm{d}\psi\,. \tag{1.12}$$

The random variable is called centered if the mean of the first moment $\langle\phi\rangle$ equals zero. The centered second moment $\left\langle\phi^2\right\rangle$ is called variance, and the square-root of the variance is called standard deviation and is denoted by σ_ϕ. The dimensionless quantities $S = \left\langle\phi^3\right\rangle / \left\langle\phi^2\right\rangle^{3/2}$ and $F = \left\langle\phi^4\right\rangle / \left\langle\phi^2\right\rangle^2$ are called skewness and flatness, respectively.

The mean value of $\phi(\boldsymbol{x},t)$ can also be obtained directly from a series of numerical or experimental data. In the case of an instationary process the averaging procedure has to be repeated over N realizations

$$\langle\phi(\boldsymbol{x},t)\rangle = \frac{1}{N}\sum_i^N \phi_i(\boldsymbol{x},t) \tag{1.13}$$

and is called ensemble average. For statistically stationary flows the temporal average can be obtained by

$$\langle\phi(\boldsymbol{x})\rangle = \frac{1}{\Delta t}\int_t^{t+\Delta t} \phi(\boldsymbol{x},t')\mathrm{d}t'\,. \tag{1.14}$$

The ergodic theorem states that for a stationary process the temporal and the ensemble average yield the same result. An ergodic variable becomes both uncorrelated and statistically independent with itself for large time differences.

1.2.2 Statistical Symmetries

The Navier-Stokes equations reveal several symmetries. Although generally a single realization of a turbulent field exhibits no obvious symmetries, the averaged quantities reveal statistical symmetries. Turbulent flows are typically described by statistical

methods, like central moments, pdf equations, or two-point correlations. Statistical symmetries can be exploited to simplify these equations and reduce the number of independent variables.

Statistical stationarity[2] holds when the n-point pdf f_n of a random variable $\boldsymbol{u}(\boldsymbol{x}, t)$ is independent of time, i.e.

$$\begin{aligned} &f_n(\boldsymbol{u}_1, \boldsymbol{x}_1, t_1; \cdots; \boldsymbol{u}_n, \boldsymbol{x}_n, t_n) = \\ &f_n(\boldsymbol{u}_1, \boldsymbol{x}_1, t_1 + \tau; \cdots; \boldsymbol{u}_n, \boldsymbol{x}_n, t_n + \tau)\,. \end{aligned} \tag{1.15}$$

with an arbitrary time shift τ. Homogeneity correspond to stationarity in space: A n-point pdf of a centered random variable is independent regarding a shift $\boldsymbol{r}$ in space, i.e.

$$\begin{aligned} &f_n(\boldsymbol{u}_1, \boldsymbol{x}_1, t_1; \cdots; \boldsymbol{u}_n, \boldsymbol{x}_n, t_n) = \\ &f_n(\boldsymbol{u}_1, \boldsymbol{x}_1 + \boldsymbol{r}, t_1; \cdots; \boldsymbol{u}_n, \boldsymbol{x}_n + \boldsymbol{r}, t_n)\,. \end{aligned} \tag{1.16}$$

As consequence, all central moments are invariant regarding space-translation of their arguments. We restrict ourselves here to centered random variables and allow gradients of mean quantities, but require that gradients of mean quantities are constant. Statistical invariance regarding rotation and reflection is called isotropy

$$\begin{aligned} &f_n(\boldsymbol{u}_1, \cdots, \boldsymbol{u}_n; \boldsymbol{r}_1, \cdots, \boldsymbol{r}_{n-1}) = \\ &f_n(\mathbf{D}\boldsymbol{u}_1, \cdots, \mathbf{D}\boldsymbol{u}_n; \mathbf{D}\boldsymbol{r}_1, \cdots, \mathbf{D}\boldsymbol{r}_{n-1})\,, \end{aligned} \tag{1.17}$$

where $\mathbf{D}$ is an arbitrary transformation $\mathbf{D} \in \mathrm{O}(3)$, which is the full rotation group. Due to homogeneity and isotropy the mean of a vectorial quantity disappears, i.e. $\langle \boldsymbol{u} \rangle = 0$.

[2]For brevity in the following we will omit the word “statistically”

2 Direct Numerical Simulation of Turbulent Flows

Even for the simplest turbulent flows, an analytical solution of the Navier-Stokes equations is not known. Therefore, a solution of the Navier-Stokes equations can only be obtained by numerical methods. Direct numerical simulation (DNS) solves the Navier-Stokes equations for all scales down to the Kolmogorov length and provides a complete description of the flow, where the three-dimensional flow fields are known as a function of space and time. Because of growing computational capabilities DNS of turbulent flows has become an indispensable tool. cf. Siggia (1981) and She et al. (1990).

In the course of this chapter we present the techniques used to numerically solve the Navier-Stokes equations as well as the evolution equation of a passive scalar. All results presented in this thesis rely on DNS and much effort has been spent to develop an accurate, highly optimized code for the simulation of turbulent flows.

2.1 Pseudo-Spectral Methods

Pseudo-spectral methods are both efficient and accurate, but require a periodic domain, cf. Rogallo (1981) and Canuto et al. (1988). Here, the domain is a cube of size $L = 2\pi$ which is discretized on a grid with N^3 grid points. In real space, the grid is defined as

$$\boldsymbol{x} = (i, j, k)\frac{2\pi}{N}\,, \tag{2.1}$$

where $1 \leq i, j, k \leq N$. The wavenumber components $\boldsymbol{\kappa}$ in Fourier space read

$$\boldsymbol{\kappa} = (i, j, k)\frac{2\pi}{L}\,, \tag{2.2}$$

where $-\frac{N}{2} + 1 \leq i, j, k \leq \frac{N}{2}$. A scalar field ϕ given on the physical grid can now be transformed to Fourier space by

$$\hat{\phi}(\boldsymbol{k}, t) = \frac{1}{N^3}\sum_{\boldsymbol{x}} \phi(\boldsymbol{x}, t)\exp(-i\boldsymbol{\kappa}\cdot\boldsymbol{x}) \tag{2.3}$$

and the Fourier coefficients $\hat{\phi}(\boldsymbol{k}, t)$ can be transformed back to real space by

$$\phi(\boldsymbol{x}, t) = \sum_{\boldsymbol{k}} \hat{\phi}(\boldsymbol{x}, t)\exp(i\boldsymbol{\kappa}\cdot\boldsymbol{x})\,. \tag{2.4}$$

For any real field $\phi(\boldsymbol{x}, t)$ the condition $\hat{\phi}^*(\boldsymbol{\kappa}, t) = \hat{\phi}(-\boldsymbol{\kappa}, t)$ holds, where the star denotes the complex conjugate of $\hat{\phi}(\boldsymbol{\kappa}, t)$. The advantage of this condition is that only one-half of the Fourier coefficients of any real field need to be calculated and stored.

When we evaluate a transport equation in Fourier space, the first derivative of the dependent variable $\phi(\boldsymbol{x})$ can be transformed according to

$$\mathcal{F}\left[\frac{\partial}{\partial x_i}\phi(\boldsymbol{x})\right] = i\kappa_i\hat{\phi}(\boldsymbol{\kappa})\,, \tag{2.5}$$

and the Fourier transform of the second derivative reads

$$\mathcal{F}\left[\frac{\partial^2}{\partial x_i^2}\phi(\boldsymbol{x})\right] = -\kappa_i^2\hat{\phi}(\boldsymbol{\kappa})\,, \tag{2.6}$$

respectively. By using Fourier transform we can thus replace derivative operators by multiplication by the wavenumber. All derivatives appearing in linear terms of the transport equation can be treated in this way. However, the Fourier transformation of a non-linear term in real space

$$\mathcal{F}\left[\phi(\boldsymbol{x})^2\right] = \hat{\phi}(\boldsymbol{\kappa}) * \hat{\phi}(\boldsymbol{\kappa}) \tag{2.7}$$

turns into a convolution in Fourier space. This operation is computationally very expensive and requires $\mathcal{O}(N^{2\cdot 3})$ operations. Therefore, instead of directly evaluating the convolution operation, the multiplication of the non-linear term is computed in real space. This approach requires only $\mathcal{O}(N^3 \log N^3)$ operations and is called pseudo-spectral method since only differentiation is performed in Fourier space.

2.1.1 Velocity Field

We solve the three-dimensional Navier-Stokes equations for incompressible fluids in rotational form

$$\frac{\partial \boldsymbol{u}}{\partial t} + \boldsymbol{\omega} \times \boldsymbol{u} = -\nabla\left(p + \frac{1}{2}\boldsymbol{u}^2\right) + \nu\nabla^2\boldsymbol{u} + \boldsymbol{f} \tag{2.8}$$

with the continuity equation

$$\nabla \cdot \boldsymbol{u} = 0\,, \tag{2.9}$$

where $\boldsymbol{\omega} = \nabla \times \boldsymbol{u}$ is the vorticity, p is the ratio of pressure and density, and ν is the kinematic viscosity. $\boldsymbol{f}$ is a forcing term which acts on large scales only. Equation 2.8 is solved by a pseudo-spectral method in Fourier space. Applying eq. 2.3 to eq. 2.8 yields

$$\frac{\partial \hat{\boldsymbol{u}}}{\partial t} + \mathcal{F}\left(\boldsymbol{\omega} \times \boldsymbol{u}\right) = -i\boldsymbol{\kappa}\hat{P} - \nu\kappa^2\hat{\boldsymbol{u}} + \mathcal{F}(\boldsymbol{f})\,, \tag{2.10}$$

where $P = p + \frac{1}{2}u^2$ and $u^2 = u_i u_i$. Quantities in Fourier space are denoted by a hat. An equation for the pressure $\hat{P}$ can be obtained when the divergency of eq. 2.10 is taken and the incompressibility condition is used

$$\hat{P} = -\frac{1}{\kappa^2} i\boldsymbol{\kappa} \cdot \mathcal{F}\left(\boldsymbol{\omega} \times \boldsymbol{u}\right) . \tag{2.11}$$

Instead of solving for $\hat{P}$ directly by eq. 2.11, the projection tensor

$$P_{jk} = \delta_{jk} - \frac{\kappa_j \kappa_k}{\kappa^2} , \tag{2.12}$$

is applied to the velocity field $\hat{\boldsymbol{u}}(\boldsymbol{\kappa}, t)$ in order to ensure incompressibility.

2.1.2 Scalar Field

Additionally to the turbulent flow field an equation for a fluctuating scalar field $\phi(\boldsymbol{x}, t)$ is solved, cf. eq. 1.5. The fluctuating scalar field $\phi(\boldsymbol{x}, t)$ is periodically in all three directions. This enables us to employ Fourier methods. Fourier transform of eq. 1.5 yields

$$\frac{\partial \hat{\phi}}{\partial t} + \mathcal{F}\left(u_i \frac{\partial \phi}{\partial x_i}\right) = -\kappa^2 D\hat{\phi} - \Gamma\hat{\phi} . \tag{2.13}$$

Writing the temporal derivative in discretized form yields

$$\frac{\hat{\phi}^{n+1} - \hat{\phi}^n}{\Delta t} = -\frac{3}{2}\hat{f}^n + \frac{1}{2}\hat{f}^{n-1} - \frac{1}{2}\kappa^2 D\left(\hat{\phi}^{n+1} + \hat{\phi}^n\right) - \Gamma\hat{u}_2^n , \tag{2.14}$$

where the non-linear term is abbreviated as $\hat{f} = \mathcal{F}\left(u_i \frac{\partial \phi}{\partial x_i}\right)$. This equation can be solved explicitly for $\hat{\phi}^{n+1}$, but requires $\hat{f}$ at the previous time step $n-1$.

2.1.3 Dealiasing

Aliasing errors result from evaluation of the non-linear terms and always appear when two functions are multiplied on a discrete grid. To illustrate the origin of aliasing errors we consider the Fourier transform of two discrete functions a and b:

$$a_j = \sum_{n=-N/2}^{N/2-1} \hat{a}_n \exp\left(i\frac{2\pi}{N} jn\right) \tag{2.15}$$

$$b_j = \sum_{m=-N/2}^{N/2-1} \hat{b}_m \exp\left(i\frac{2\pi}{N} jm\right) \tag{2.16}$$

Multiplication of a and b and denoting their product as c yields

$$\hat{c}_\kappa = \sum_{n+m=\kappa} \hat{a}_n \hat{b}_m + \sum_{n+m=\kappa\pm N} \hat{a}_n \hat{b}_m \,, \tag{2.17}$$

where the second term represents the aliasing errors. Equation 2.17 reveals that mainly large wavenumbers are affected by aliasing.

It is important to remove aliasing errors at least to some extent from the solution, since aliasing errors can be a source for instability or amplified decay. Aliasing errors can be fully removed by isotropic truncation by the 2/3-rule:

$$\hat{\phi}(\kappa,t) = \begin{cases} \hat{\phi}(\kappa,t) & \text{if } \kappa^2 < \left(\frac{2}{3}\frac{N}{2}\right)^2 \\ 0 & \text{else} \end{cases} \tag{2.18}$$

where $N/2$ is the largest resolved wavenumber. However, this approach has a considerable shortcoming, in particular when considering small scale turbulence in real space. The cut-off filter is local in spectral space but non-local in real space. Thus, the cut-off filter induces Gibbs oscillations in real space. This effect is problematic when searching for minima and maxima points in real space, since the Gibbs oscillations are considered erroneously as extremal points. In order to overcome this problem we use a dealiasing filter which provides a compromise between a sharp cut-off in spectral space and reduced Gibbs oscillations in real space, i.e.

$$\hat{\phi}(\kappa,t) = \hat{\phi}(\kappa,t) \exp\left(-\alpha \left(2\kappa/N\right)^\beta\right) \tag{2.19}$$

where $\alpha = \beta = 36$ has been chosen, cf. Hou and Li (2007). With this set of parameters we allow for aliasing errors, but compared to the 2/3-rule more active wavenumbers are retained. For well resolved simulations, i.e. $\kappa_{\max}\eta > 2$ as in the present work, this does not affect the accuracy. Equation 2.19 is calculated once at the start of the simulation and stored for reuse in subsequent time steps. This approach avoids recurrently evaluation of the exponential term.

A different way to remove aliasing errors is to evaluate the right hand side of the governing equations on shifted grids such that the aliasing errors cancel out. This approach can fully remove aliasing errors but with the cost of additional computational expensive evaluations of the right hand side of the governing equations.

2.1.4 Temporal advancement

For temporal advancement of both the velocity and the scalar field, the non-linear term is advanced by a second-order Adams-Bashforth method and the linear terms are advanced by a second-order Crank-Nicholson method. The time step of advection and diffusion equations is determined by the Courant-Friedrichs-Lewy criterion and

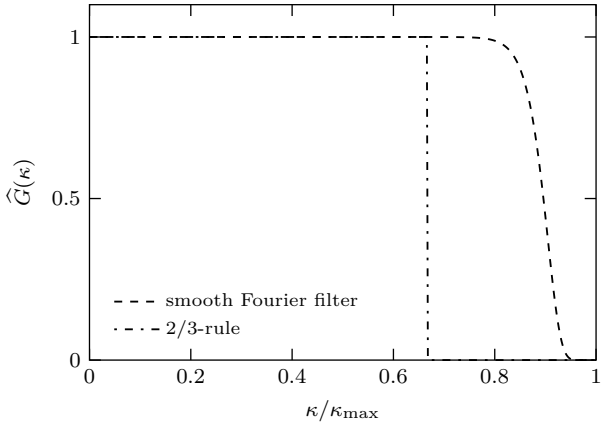

Figure 2.1: Dealiasing filter kernel; comparing 2/3-rule and smooth Fourier filter.

states that a tracer particle should move only a fraction of the grid size Δx in one time step Δt. For the advective term the condition

$$\Delta t_{\text{adv}} = c_\lambda \frac{\Delta x}{u_{\max}} \tag{2.20}$$

holds, where $u_{\max} = \|\boldsymbol{u}\|_\infty$ is the maximum norm of $\boldsymbol{u}$. The restriction of the diffusive term comes from its mean square displacement in three dimensions $\Delta x^2 = 6\nu\Delta t$ and gives the condition

$$\Delta t_{\text{diff}} = c_\lambda \frac{\Delta x^2}{6\nu} \,. \tag{2.21}$$

However, this condition is not needed, since the employed Crank-Nicholson method is unconditionally stable. The parameter c_λ is called Courant number. The value $c_\lambda \approx 0.20$ was chosen for all simulations.

2.2 Code Design and Parallelization

A spatial decomposition of the cubic computational domain is mandatory for massive-parallel computation on distributed-memory platforms. For the used Fourier transform the data along a global grid line need to be accessible for each corresponding computational process. For cartesian topologies two different decomposition strategies can be used. The one-dimensional slab decomposition distributes the memory in slices in y-direction. Any operation in the xOz plane can be computed in local memory, but each process holds only parts of the whole data in memory. Since the Fourier transform is a non-local operation the data has to be exchanged between

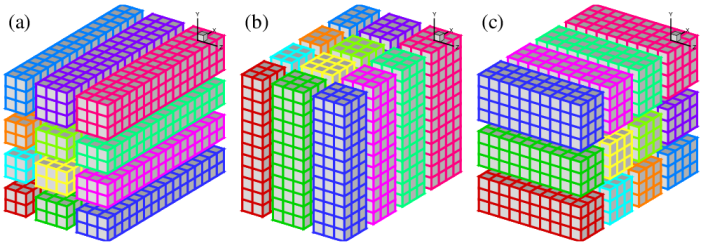

Figure 2.2: Two-dimensional pencil decomposition of the computational domain. Pictures taken from Li and Laizet (2010).

the processes. For operations in y or z direction the data is thus transposed using the `MPI_ALLTOALL` subroutine. The slab decomposition reveals significant limitation for massive-parallel computations. The number of computational processes can not exceed the number of grid points in one direction, which is typically between 512 and 4096, while simulation runs are conducted on more than 16384 processes. A block or pencil decomposition overcomes this limitation by performing the decomposition in two dimensions as shown in fig. 2.2. However, Fourier transforms in different directions always require a rotation of the data by the `MPI_ALLTOALL` subroutine, which is a global, time-consuming operation. The procedure to conduct a three-dimensional Fourier transform from real to Fourier space is as follows:

- Fourier transform in x-direction
- Rotate the pencil in y-direction and conduct the Fourier transform in y-direction
- Rotate the pencil in z-direction and conduct the Fourier transform in z-direction

Implementing the communication for block decomposition can be a very demanding task. Here, we use the excellent decomposition library `2decomp`, cf. Li and Laizet (2010), which also implements the fast Fourier transforms. On the Intel architecture a threaded version of `FFTW 3.2`, cf. Frigo and Johnson (2005), is utilized and on the BG/Q architecture a threaded version of IBM's high performance library `ESSL` is utilized.

The pencil decomposition allows for many different combinations to distribute rows and columns between the nodes. To achieve the best performance the timing for one three-dimensional forward and one three-dimensional backward FFT is measured for various possible row/column combinations. Figure 2.3 shows the result of the measurement using the example of a computational grid with 4096^3 collocation points and 32 768 computational cores, where each node provides 16 computational cores. Figure 2.3 reveals that the computation is faster when the number of rows matches exactly the number of cores per node, namely for the combination 16×2048. The

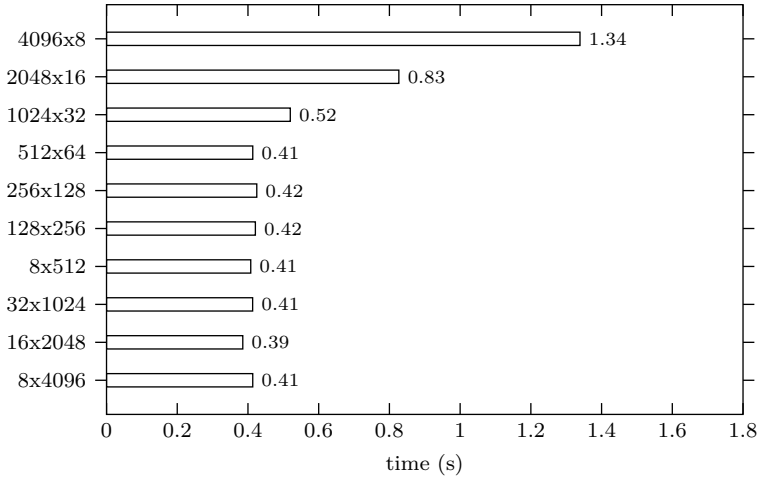

Figure 2.3: Measured time for one three-dimensional forward and one three-dimensional backward FFT for different row/column combinations with 32 768 processes for a computational grid with 4096^3 collocations points.

wall-clock time for one computational time step, involving temporal advancement of both velocity and scalar field, equals for this setup 6.0 seconds.

A new massive-parallel DNS code has been developed in Fortran 95 based on the `2decomp` library. The communication between processes utilizes the message passing interface (MPI). On SMP architectures an additional hybrid parallelization based on OpenMP can be utilized to improve the communication. The DNS code exhibits an excellent scaling up to 524 288 threads, cf. fig. 2.4. Input and output of three-dimensional fields is done with either binary MPI-IO or parallel HDF5. On the IBM BlueGene/Q architecture binary MPI-IO is advantageous due to the better alignment of the data in memory. With 32768 processes and a problem size of 4096^3 points 5 GB/s can be written. The written data files contain all necessary information to continue the simulation even with a differing number of processes.

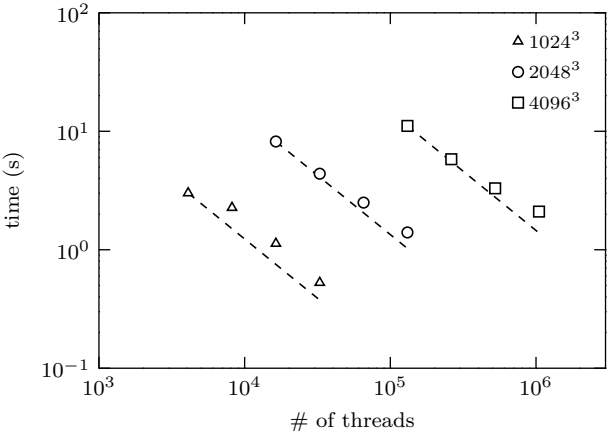

Figure 2.4: Wall-clock time required for one time step. The dashed lines indicate ideal scaling.

3 Statistical Properties of Turbulence Obtained by DNS

3.1 Introduction

In the course of this chapter we will investigate the fine-scale properties of turbulent flows and of turbulent mixing of a passive scalar by means of direct numerical simulation.

Recent advances in high performance computing on massive parallel systems, cf. Moin and Mahesh (1998) and Donzis et al. (2008b), enable us to conduct simulations of turbulent flows at sufficient high Reynolds numbers with at the same time high resolution of the fine-scales. The present simulations comprise a wide range of resolved scales which is necessary for calculating scaling properties with adequate precision. We examine results from simulations with Taylor microscale based Reynolds numbers in the range between $\mathrm{Re}_\lambda = 88$ and $\mathrm{Re}_\lambda = 529$. Thereby, we are close to related laboratory experiments, which reach Reynolds numbers with up to $\mathrm{Re}_\lambda \approx 800$, cf. Mydlarski and Warhaft (1998).

3.2 Simulation Parameters

Different direct numerical simulations with Reynolds number varying between $\mathrm{Re}_\lambda = 88$ and $\mathrm{Re}_\lambda = 529$ have been conducted on the supercomputer JUQUEEN at Forschungscentre Juelich. The simulations have been carried out with a hybrid MPI/OpenMP parallelized simulation code that efficiently utilizes the BlueGene/Q architecture. The biggest run has been conducted utilizing 131 072 threads. All simulation runs as well as the postprocessing have required overall a computational time of 45 million core hours.

The three-dimensional incompressible Navier-Stokes equations as well as a transport equation for the fluctuations of a passive scalar are solved by a dealiased pseudo-spectral approach, cf. Rogallo (1981) and Canuto et al. (1988). Temporal integration is carried out by an explicit, second order Adams-Bashforth method, cf. Butcher (2003). The integration domain is a triply periodic cube with length 2π. An external stochastic forcing, cf. Eswaran and Pope (1988), is applied to the velocity field to maintain a statistically steady state. The forcing is assumed to be statistically homogeneous, isotropic and is applied at low wavenumbers within a spectral shell of prescribed radius κ_F only. Various forcing schemes have been adopted in the literature. The small-scale statistics, however, are not affected by the specific schema, see Wilczek (2011), Sreenivasan (1998) and Yeung and Zhou (1997).

A uniform mean scalar gradient is applied to the scalar field which keeps the scalar fluctuations as well in a statistically stationary state. The Schmidt number, defined as $\mathrm{Sc} = \nu/D$, equals unity for all cases.

In the following we will present fundamental properties of the DNS, cf. Tennekes and Lumley (1972), Batchelor (1953) and Pope (2000). The numerical parameters are listed in tab. 3.1. The number of collocation points is 512^3 for case R0 and increases up to 4096^3 for case R5. For case R0, the initial conditions for the velocity and scalar field obey a prescribed spectrum $\propto \kappa^4 \exp\left(-2(\kappa/\kappa_0)^2\right)$ but random phases. The cases R1-R5 were initialized by interpolation of the final state of the smaller case to the new mesh. The Reynolds number is adjusted solely by reducing the viscosity. The forcing parameters are kept constant for all cases. Statistics are evaluated over a time period t_{avg} after reaching the statistically steady state. Stationarity enables us to calculate ensemble averages by using data taken at various points in time. The number of analyzed ensembles ranges from $M = 189$ for case R0 to $M = 5$ for case R5.

As a consequence of the stochastic forcing, statistics fluctuate around a mean value (averaged within the box). Figure 3.1 shows the temporal evolution of various one-point quantities for case R2. The fluctuation intensity is up to 30% of the long time mean value which is slightly larger than reported by Overholt and Pope (1998), probably as the original work was conducted at a lower Reynolds number, namely $\mathrm{Re}_\lambda \approx 27$. Due to these strong temporal fluctuations ensemble averages have to be calculated over several integral times in order to obtain properly converged statistics. Furthermore, fig. 3.2 displays the spatial structure of the scalar ϕ and the scalar derivative ϕ_x along a straight line in x-direction for all cases. The intermittency at small scales is manifested by the scalar gradient. Figure 3.2 illustrates the increase of intermittency with the Reynolds number

3.2.1 Characteristic Quantities

Due to the non-linearity of the Navier-Stokes equations, turbulent flows reveal in the limit of large Reynolds numbers a wide range of different length and time scales. The largest length scale of a turbulent flow is the integral length scale l_t. It describes the size of the largest vortices and is defined by

$$l_t = \frac{3\pi}{4} \frac{\int \kappa^{-1} E(\kappa) \mathrm{d}\kappa}{\int E(\kappa) \mathrm{d}\kappa} \,. \tag{3.1}$$

The integral length scale l_ϕ of the passive scalar is defined by

$$l_\phi = \frac{\pi}{2} \frac{\int \kappa^{-1} E_\phi(\kappa) \mathrm{d}\kappa}{\int E_\phi(\kappa) \mathrm{d}\kappa} \,, \tag{3.2}$$

Table 3.1: Summary of different DNS cases. Reynolds number variation between $\mathrm{Re}_\lambda = 88$ and $\mathrm{Re}_\lambda = 529$.

	R0	R1	R2	R3	R4	R5
N	512	1024	1024	2048	2048	4096
Re_λ	88	119	184	215	331	529
Sc	1	1	1	1	1	1
ν	0.01	0.0055	0.0025	0.0019	0.0010	0.00048
$\kappa_{\max}\eta$	3.93	4.99	2.93	4.41	2.53	2.95
$\langle k \rangle$	11.15	11.38	11.42	12.70	14.35	23.95
$\langle \varepsilon \rangle$	10.78	11.04	10.30	11.87	12.55	28.51
$\langle \phi^2 \rangle$	1.95	1.86	1.94	2.47	2.25	2.41
$\langle \chi \rangle$	3.92	3.92	4.01	5.00	4.76	6.78
$-2\Gamma\langle u\phi \rangle$	3.93	3.98	4.03	4.95	4.79	5.76
λ	0.322	0.238	0.166	0.143	0.107	0.064
λ_ϕ	0.173	0.125	0.085	0.075	0.053	0.032
η	0.0175	0.0111	0.0062	0.0049	0.0030	0.0014
τ	1.03	1.03	1.11	1.07	1.14	0.84
τ_ϕ	0.50	0.47	0.48	0.49	0.47	0.36
τ_η	0.031	0.022	0.016	0.013	0.009	0.004
l_t	1.02	0.94	0.97	1.01	0.97	1.02
l_ϕ	0.68	0.63	0.64	0.67	0.65	0.68
$\langle \epsilon \rangle l_t / u'^3$	0.54	0.50	0.47	0.46	0.44	0.44
$\langle \chi \rangle l_t / (u' \langle \phi^2 \rangle)$	0.75	0.72	0.72	0.66	0.71	0.70
$S(\phi)$	-0.02	0.08	0.03	0.09	-0.10	-0.05
$F(\phi)$	3.01	3.03	3.02	2.89	3.02	2.95
$\langle \phi_y^2 \rangle / \langle \phi_x^2 \rangle$	1.06	1.06	1.05	1.04	1.03	1.02
$S(\partial_\parallel \phi)$	1.65	1.73	1.60	1.55	1.56	1.36
$S(\partial_L u)$	-0.52	-0.54	-0.55	-0.57	-0.59	-0.64
$F(\partial_\perp \phi)$	12.67	16.11	19.03	21.43	27.12	34.30
$F(\partial_\parallel \phi)$	15.14	19.55	22.28	24.14	29.91	37.49
t_{avg}/τ	100	30	30	10	10	2
M	189	62	61	10	10	5
Δt	1.4e-4	8.0e-5	8.0e-5	2.85e-5	2.75e-5	1.01e-5

where the three-dimensional spectra of the turbulent energy and the scalar variance are denoted by $E(\kappa)$ and $E_\phi(\kappa)$, respectively. The magnitude of the wavenumber is denoted by κ. The integral length scale of the velocity field ($l_t \approx 1$) is larger than the integral length scale of the scalar field ($l_\phi \approx 0.67$). Both integral length scales are small compared to the size of the computational domain to ensure that the flow quantities are not affected by the periodic boundary conditions, cf. Davidson (2004). On the other hand, the smallest length scale present in a turbulent velocity field is the Kolmogorov length η defined as

$$\eta = \left(\frac{\nu^3}{\langle \varepsilon \rangle} \right)^{1/4} , \tag{3.3}$$

where $\langle \varepsilon \rangle$ denotes the mean energy dissipation

$$\langle \varepsilon \rangle = 2\nu \langle s_{ij} s_{ij} \rangle \tag{3.4}$$

and s_{ij} the fluctuating strain rate tensor

$$s_{ij} = \frac{1}{2} \left(\frac{\partial u_i}{\partial x_j} + \frac{\partial u_j}{\partial x_i} \right) . \tag{3.5}$$

Scales smaller than the Kolmogorov length disappear because of the damping of viscosity. The smallest length scale of the scalar field is the Batchelor length η_B defined as

$$\eta_B = \eta \mathrm{Sc}^{-1/2} , \tag{3.6}$$

which equals the Kolmogorov length for unity Schmidt number. The third length scale, the Taylor microscale λ, is an intermediate length scale with $\eta < \lambda < l_t$. It is defined as

$$\lambda = \sqrt{10\nu \frac{\langle k \rangle}{\langle \varepsilon \rangle}} , \tag{3.7}$$

where $\langle k \rangle$ denotes the mean turbulent kinetic energy with

$$\langle k \rangle = \frac{1}{2} \langle u_i u_i \rangle . \tag{3.8}$$

The Taylor microscale λ is used to define the Taylor based Reynolds number as

$$\mathrm{Re}_\lambda = \frac{u_{\mathrm{rms}} \lambda}{\nu} , \tag{3.9}$$

where $u_{\mathrm{rms}} = \langle u_i u_i \rangle / 3$ denotes the root-mean-square of velocity fluctuations. The Taylor based Reynolds number Re_λ is used throughout this thesis to characterize turbulent flows. The corresponding microscale of the passive scalar is defined by

$$\lambda_\phi = \sqrt{6D \frac{\langle \phi^2 \rangle}{\langle \chi \rangle}} , \tag{3.10}$$

where $\langle \phi^2 \rangle$ denotes the mean scalar variance and $\langle \chi \rangle$ denotes the mean scalar dissipation

$$\langle \chi \rangle = 2D \langle \left(\frac{\partial \phi}{\partial x_i} \right)^2 \rangle \,. \tag{3.11}$$

The ratio λ/λ_ϕ is virtually Reynolds number independent and equals 1.95. The mean production of scalar variance is given by $-2\Gamma\langle u\phi \rangle$, where Γ denotes the mean scalar gradient taken as unity without loss of generality. For statistically stationary homogeneous turbulence $-2\Gamma\langle u\phi \rangle$ equals the mean scalar dissipation $\langle \chi \rangle$.

An integral time scale τ can be defined as

$$\tau = \frac{\langle k \rangle}{\langle \varepsilon \rangle} \,, \tag{3.12}$$

which is the slowest time scale in a turbulent flow. For all cases the integral time τ is of the order unity. The integral time scale of the scalar field can be defined similarly as

$$\tau_\phi = \frac{\langle \phi^2 \rangle}{\langle \chi \rangle} \,. \tag{3.13}$$

The ratio τ/τ_ϕ is virtually independent of Reynolds number and is in the range between 2.0 and 2.3. The fastest time scale is the Kolmogorov time τ_η, defined as

$$\tau_\eta = \left(\frac{\nu}{\langle \varepsilon \rangle} \right)^{1/2} \,. \tag{3.14}$$

The numerical time step Δt is approximately two orders of magnitude smaller than the Kolmogorov time t_η.

The Taylor based Reynolds number can be written as the ratio of the slowest time scale to the fastest time scale, namely

$$\frac{\tau}{\tau_\eta} \propto \mathrm{Re}_\lambda \,. \tag{3.15}$$

Furthermore, the ratio between the largest scale l_t and the smallest scale η can be shown to scale with the Taylor based Reynolds number as

$$\frac{l_t}{\eta} \propto \mathrm{Re}_\lambda^{3/2} \,. \tag{3.16}$$

Equation 3.15 and eq. 3.16 indicate that with increasing Reynolds number the separation between slow (large) and fast (small) scales becomes larger.

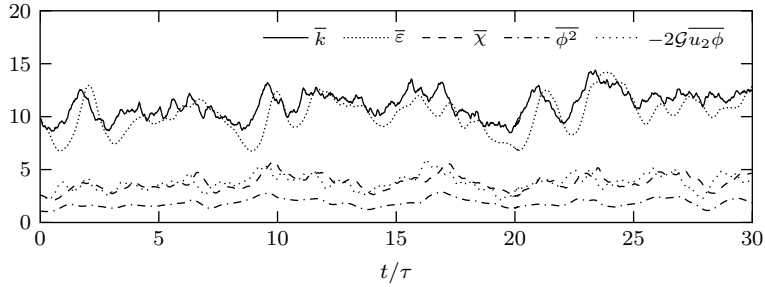

Figure 3.1: Temporal evolution of various spatially (within the box) averaged quantities for case R2 after reaching the statistically steady state.

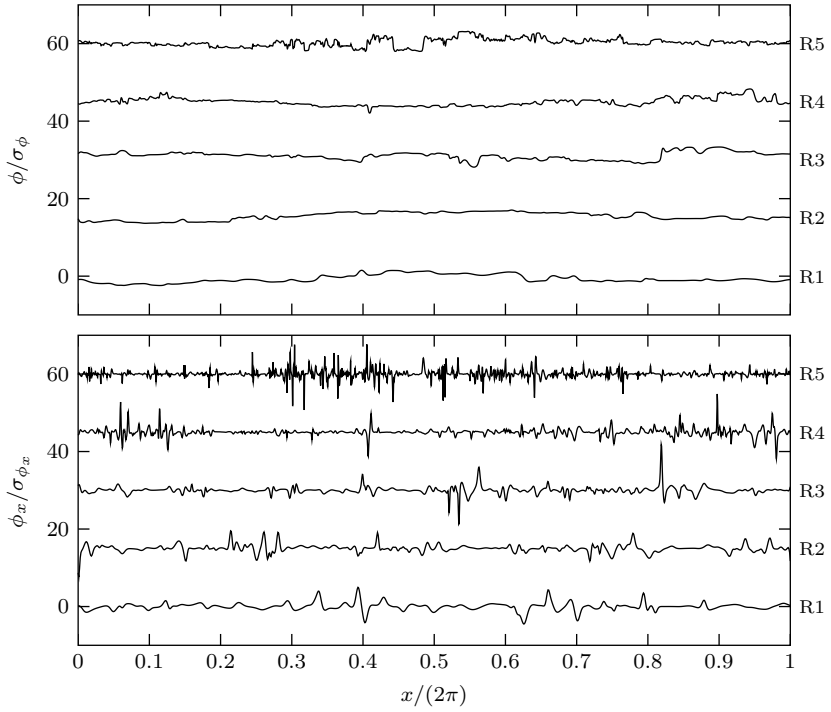

Figure 3.2: Spatial structure of the scalar ϕ (top) and the scalar derivative ϕ_x along a straight line in x-direction. For clarity all curves are normalized by their standard deviation and the curves for case R2, R3, R4 and R5 are shifted upward by 15, 30, 45 and 60, respectively.

3.2.2 Resolution Condition

Since direct numerical simulation employs no models it is required that even the smallest scales down to the Kolmogorov scale η or Batchelor scale η_B are adequately resolved by the numerical grid. The number of required grid points N can be estimated by dimensional arguments. According to eq. 3.16 the ratio of the smallest length scale η to the largest length scale ℓ_t is proportional to $\mathrm{Re}_l^{-3/4}$, where

$$\mathrm{Re}_l = u' l_t / \nu \tag{3.17}$$

denotes the turbulent Reynolds number. For well resolved direct numerical simulations the smallest length scale η should equal the grid spacing Δx leading to an estimate for the number of grid points N in each direction as

$$N \propto \frac{\ell_t}{\eta} \propto \mathrm{Re}_\ell^{3/4} \propto \mathrm{Re}_\lambda^{3/2} \,. \tag{3.18}$$

Thus, the total number of grid points is

$$N^3 \propto \mathrm{Re}_\lambda^{9/2} \,. \tag{3.19}$$

This estimate reveals that DNS is computationally very expensive, particularly for high Reynolds numbers.

The grid size is very important for the accuracy of the DNS. For spectral methods the resolution requirement can be reformulated in terms of the maximum wavenumber appearing in the truncated Fourier series $\kappa_{\max}$ as $\kappa_{\max}\eta > 1$. However, the local Kolmogorov length $\eta(\boldsymbol{x})$ strongly fluctuates around its mean value because of the intermittent nature of the instantaneous dissipation ε such that in regions of large local dissipation the turbulent flow field is under-resolved. Therefore, Yakhot and Sreenivasan (2005) proposed the more restrictive resolution condition

$$\kappa_{\max}\eta \geq 2 \,. \tag{3.20}$$

This is supported by Ishihara et al. (2007), who found that eq. 3.20 should be satisfied to properly resolve the tails of the velocity gradient pdf. Donzis and Yeung (2010) and Donzis et al. (2008a) analyzed in detail the resolution needed to obtain higher order moments of velocity and scalar gradients. Their results indicate that $\kappa_{\max}\eta \geq 2.5$ is required to accurately compute the fourth order moments of the scalar or energy dissipation.

In order to study geometrical properties and to identify local minima and maxima points, cf. chapter 5 the resolution condition can be restated. We require that a turbulent field can be locally expanded as a Taylor series up to order two. This is equivalent to the condition that the turbulent field is locally two times continuously differentiable. If this condition is violated the pdf of the length of dissipation elements or turbulent line segments is under-resolved at small scales for $\ell \to 0$. By parameter studies we found that $\kappa_{\max}\eta \geq 2.4$ is necessary. All cases satisfy this condition.

3.2.3 Structure of Turbulent Fields Obtained by Direct Numerical Simulation

It is instructive to visualize the turbulent fields obtained by direct numerical simulations. Figure 3.3 illustrates the structure of the scalar field ϕ for case R5 by means of a two-dimensional slice through the computational domain. The scalar field reveals large coherent regions of roughly constant scalar value. The size of these regions is of the order of the scalar integral length scale l_ϕ. These regions are separated by sharp highly convoluted boundaries. At these boundaries the scalar dissipation χ attains large values. Figure 3.4 shows the logarithm of the scalar dissipation and fig. 3.5 shows a magnification of the bottom left corner marked in fig. 3.5. The scalar dissipation is characterized by a very fine filamented structures. The scalar dissipation χ is a highly intermittent quantity and regions of high χ are confined in localized regions of space. Both figures display the scalar integral length scale l_ϕ, the Kolmogorov length scale η, and the scalar micro-scale λ_ϕ in order to underline the wide separation between l_ϕ and η at high Reynolds numbers.

Figures 3.6 and 3.7 illustrate the iso-surface of the normalized enstropy $\omega^2/\langle\omega^2\rangle$ for case R1 and case R5. The value of the iso-surface equals 8 for both cases. The iso-surface exhibits a very complex preferentially tube-like structure. With increasing Reynolds number these structures become substantially finer and fig. 3.7 shows a large number of eddies of different size. These eddies form clusters that are characterized by very fine details.

3.3 Phenomenology of Small-Scale Turbulent Mixing

In this section we examine small-scale turbulent mixing by means of statistics and scaling laws and ask for the mechanisms which generate and dissipate turbulent fluctuations. The small-scale structure of turbulent flows reveals universal properties at sufficiently high Reynolds number. Between the large and small scales exists a net energy transport. According to Kolmogorov (1941b) turbulent energy is injected into the fluid motion at large scale and is transported towards smaller scales at the mean rate $\langle\varepsilon\rangle$ by the mechanisms of stretching and folding. The turbulent energy is finally dissipated at the smallest scales because of viscosity. This process is called energy cascade.

By the many steps through the cascade it is expected that the impact of the large scales is diminished, cf. Kolmogorov (1941b) and Frisch (1995). This leads to Kolmogorov's first hypothesis which states that at sufficient high Reynolds number, the small scales become universal and the statistics of the small-scale motions are uniquely determined solely by ν and $\langle\varepsilon\rangle$. Under the condition of very large Reynolds numbers, at small scales and away from boundaries, the symmetries of the Navier-Stokes equations, which are broken by turbulence, are restored in a statistical sense, cf. Frisch (1995).

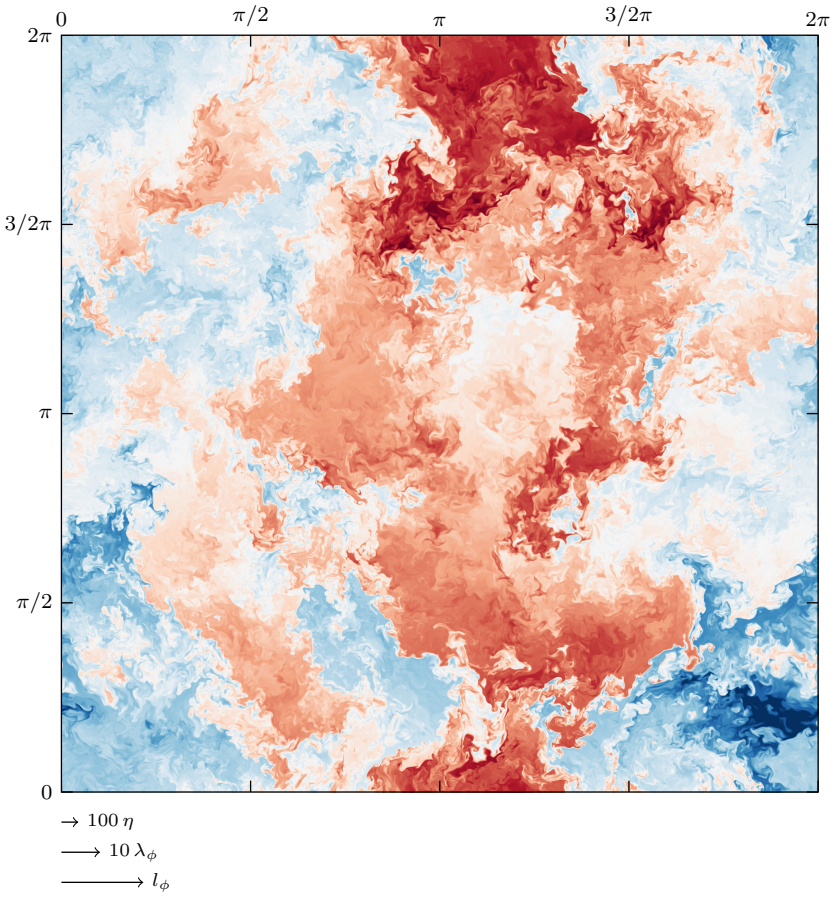

Figure 3.3: Two-dimensional slice through the field of the fluctuating passive scalar ϕ for case R5 in the xOy-plane. The depicted grid size has 4096×4096 points.

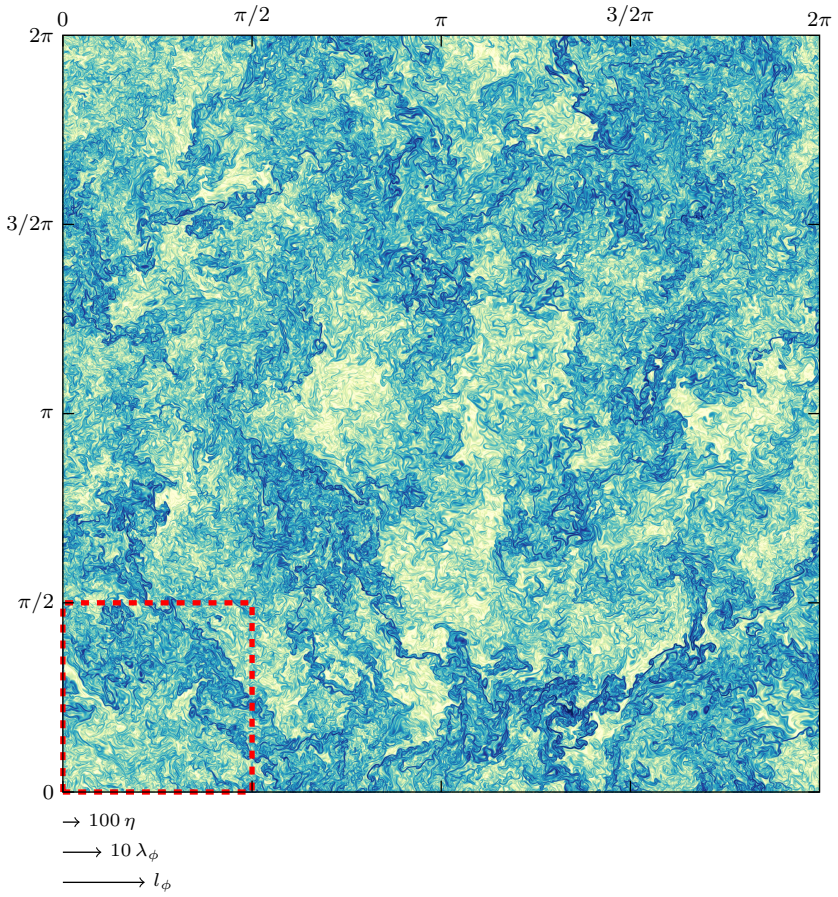

Figure 3.4: Two-dimensional slice of the logarithm of the scalar dissipation $\ln \chi$ for case R5 in the xOy-plane. The depicted grid size has 4096×4096 points.

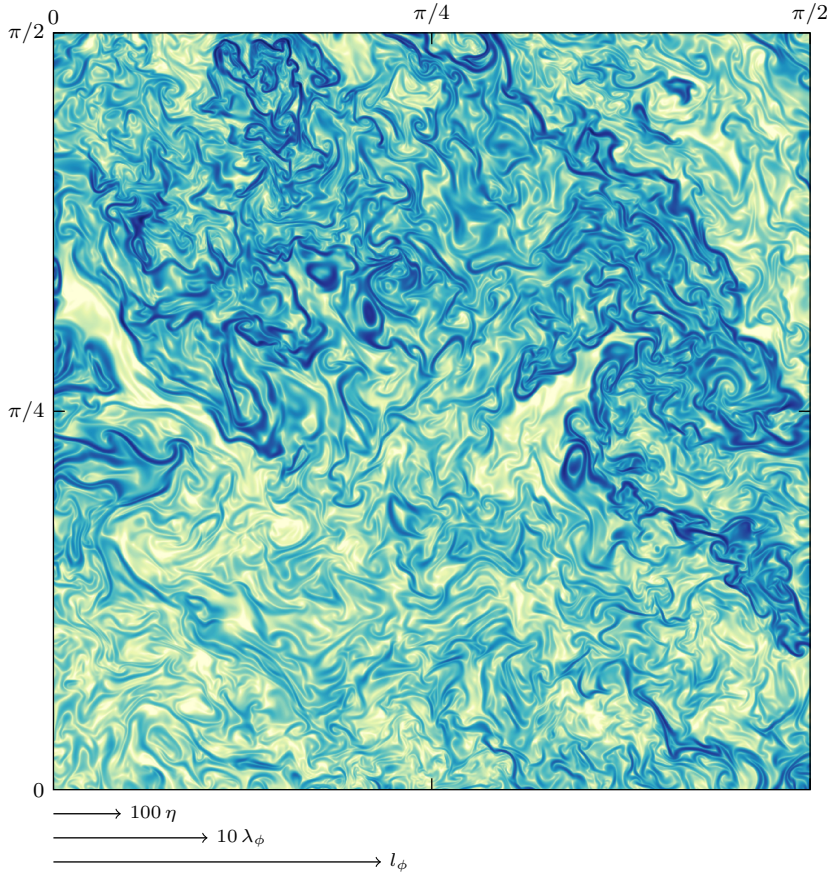

Figure 3.5: Two-dimensional slice of the logarithm of the scalar dissipation $\ln \chi$ for case R5. A magnification of the bottom left corner of size $\pi/2 \times \pi/2$ marked in fig. 3.4 is shown for clarity.

Figure 3.6: Three-dimensional iso-surface (top-view) of the normalized enstrophy $\omega^2/\langle\omega^2\rangle$, where the value of the iso-surface equals 8, for case R1. A magnification of the bottom left corner of size $\pi/2 \times \pi/2 \times \pi/2$ or $256 \times 256 \times 256$ grid points, respectively, is shown.

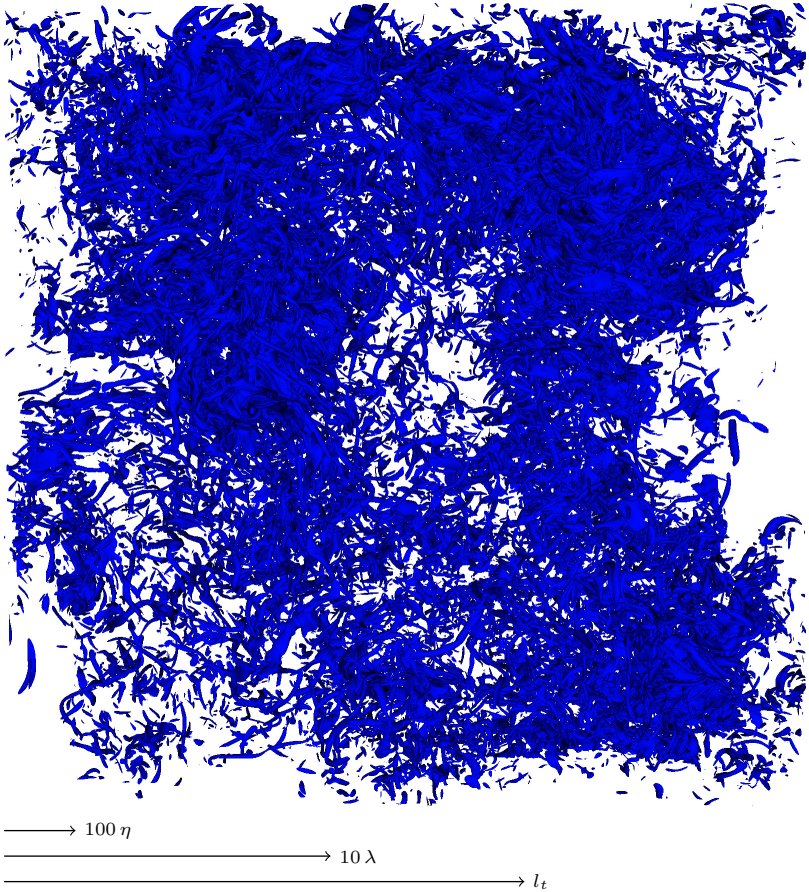

Figure 3.7: Three-dimensional iso-surface (top-view) of the normalized enstrophy $\omega^2/\langle\omega^2\rangle$, where the value of the iso-surface equals 8, for case R5. A magnification of the bottom left corner of size $\pi/2 \times \pi/2 \times \pi/2$ or $1024 \times 1024 \times 1024$ grid points, respectively, is shown.

The range between the large scales and the small scales, i.e. $l_t \gg r \gg \eta$, is referred to as inertial subrange. Kolmogorov's second similarity hypothesis states that at sufficient high Reynolds numbers, the distribution functions within the inertial subrange are uniquely determined by $\langle\varepsilon\rangle$ and are independent of ν. Below we will refer to Kolmogorov's similarity hypotheses as K41. In sec. 6.3.3 we will discuss that Kolmogorov's similarity hypotheses are incomplete as they do not account for the strong fluctuations of the energy dissipation ε.

Kolmogorov's hypotheses can be extended to the statistics of isotropic passive fields, cf. Obukhov (1949b) and Corrsin (1951), which are hereafter referred to by the abbreviation "KOC". Under the condition of sufficient large Reynolds numbers the statistics of the scalar fluctuations are determined in the dissipative range solely by the scalar diffusivity D as well as by the mean energy and scalar dissipation $\langle\varepsilon\rangle$ and $\langle\chi\rangle$. KOC scaling implies that within the inertial-convective subrange the statistics of the scalar fluctuations become independent of D. The statistical properties of the scalar field are coupled to the velocity field. Most findings obtained from the velocity field can be transferred to the scalar field. Note that in the present work, a uniform mean gradient is imposed on the scalar field. This induces an anisotropy which is significant even at the smallest scales. Sreenivasan (1991) and Schumacher et al. (2005) discussed the applicability of the local isotropy assumption to scalar fields.

3.3.1 Velocity and Scalar Spectra

The turbulent cascade is usually investigated in wavenumber space. Different scales of the turbulent flows can be distinguished by means of the spectra of the scalar variance and the spectra of the turbulent energy. The mean kinetic energy $\langle k\rangle$ is related to the spectrum of the turbulent energy $E(\kappa)$ by

$$\langle k\rangle = \int_0^\infty E(\kappa)\mathrm{d}\kappa \tag{3.21}$$

and the mean dissipation $\langle\varepsilon\rangle$ is related to $E(\kappa)$ by

$$\langle\varepsilon\rangle = 2\nu\int_0^\infty \kappa^2 E(\kappa)\mathrm{d}\kappa\,. \tag{3.22}$$

The dissipation is proportional to the square of velocity gradients and the factor κ^2 in eq. 3.22 reveals that large wavenumbers have the main contribution to the dissipation.

According to Kolmogorov's second hypothesis the major parameter within the inertial subrange is the mean dissipation $\langle\varepsilon\rangle$. Hence, the energy spectrum can be written on dimensional grounds as

$$\frac{E(\kappa)}{\langle\varepsilon\rangle^{2/3}\kappa^{-5/3}} = C\,, \tag{3.23}$$

where C is the Kolmogorov constant which is assumed to be universal.

The spectrum of the scalar variance $E_\phi(\kappa)$ depends within the inertial-convective subrange on the mean energy dissipation $\langle\varepsilon\rangle$ and additionally on the mean scalar dissipation $\langle\chi\rangle$, yielding on dimensional grounds

$$\frac{E_\phi(\kappa)}{\langle\varepsilon\rangle^{-1/3}\langle\chi\rangle\kappa^{-5/3}} = C_\phi\,, \tag{3.24}$$

where C_ϕ is the Obukhov-Corrsin constant, cf. Obukhov (1949a) and Corrsin (1951). For $\mathrm{Sc} \gg 1$, beyond the viscous cut-off length an additional scaling regime exists, namely the viscous-convective range which is established for $\eta^{-1} \ll \kappa \ll \mathrm{Sc}^{-1/2}\eta^{-1}$. Here, the scalar spectra takes the form $E_\phi(\kappa) = C_B\langle\chi\rangle(\nu/\langle\varepsilon\rangle)^{1/2}\kappa^{-1}$, where C_B is the Batchelor constant, cf. Batchelor (1959). The scalar variance is related to E_ϕ by

$$\langle\phi^2\rangle = \int_0^\infty E_\phi(\kappa)\mathrm{d}\kappa\,. \tag{3.25}$$

Figure 3.8 shows the three-dimensional spectra of the kinetic energy and the scalar variance for case R1 to case R5. The figure at the left hand side is compensated according to eqs. 3.23 and 3.24. Due to the compensated illustration the spectra reveal a horizontal slope within the inertial subrange. The Kolmogorov constant and the Obukhov-Corrsin constant obtained from fig. 3.8 are $C = 1.63$ and $C_\phi = 0.68$, respectively. They agree well with values from DNS and experiments. Gotoh et al. (2011) found $C = 1.61$ and $C_\phi = 0.67$ by a comparable DNS setup and for a similar range of Reynolds numbers. Yeung et al. (2002) obtained from DNS the value $C_\phi = 0.67$. Sreenivasan (1996) compared various experiments and found values within the range $C_\phi = 0.75$ and $C_\phi = 0.92$.

The width of this horizontal slope indicates the inertial and the inertial-convective subrange, respectively. It ranges from less than one half decade for $\mathrm{Re}_\lambda = 119$ up to more than one decade for $\mathrm{Re}_\lambda = 529$. Both spectra reveal a significant spectral bump before the dissipation range at $\kappa\eta \approx 0.2$. For E_ϕ, the peak of the bump is more distinct compared to the curve for E and shifted slightly to the right. Watanabe and Gotoh (2004) explained this effect by the stronger non-locality of the scalar variance transfer compared to the velocity case. Spectral bumps have been previously observed, cf. Champagne et al. (1977). The reason for the spectral bump is unclear. Mydlarski and Warhaft (1996) suggested that a true 5/3 scaling would not occur until $\mathrm{Re}_\lambda \approx 10^4$ and that the spectral bump stems from over-compensation of the spectrum by 5/3 instead of a smaller value. Yeung et al. (2002) attributed the spectral bump of the scalar field to diffusive effects and suggested that it might

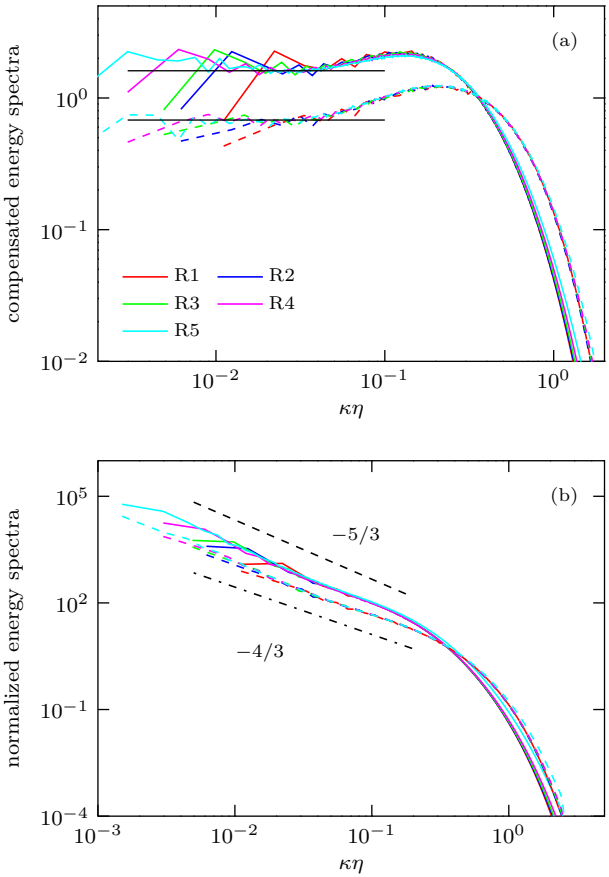

Figure 3.8: Compensated (a) and normalized (b) spectra of the kinetic energy (solid) and the scalar variance (dashed) for all cases.

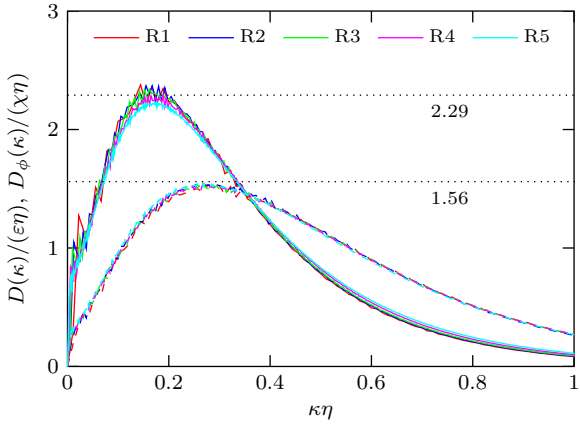

Figure 3.9: Normalized dissipation spectra of the turbulent energy $2\nu\kappa^2 E(\kappa)/(\langle\varepsilon\rangle\eta)$ (solid) and the scalar variance $2D\kappa^2 E_\phi(\kappa)/(\langle\chi\rangle\eta)$ (dashed) for all cases.

be regarded as a precursor of the Batchelor scaling, i.e. κ^{-1}, that applies for high Schmidt numbers.

In addition, figure 3.8 shows on the right hand side the normalized energy spectra for case R1 to case R5. Within the inertial-subrange the velocity field has a scaling exponent close to 5/3 and the scalar spectrum has a scaling exponent close to 4/3. The lower scaling exponent of the latter was explained by Celani et al. (2005) by the uniform mean gradient which is imposed to the scalar field and destroys isotropy. Additionally, the lower scaling exponent may explain the significant spectral bump of the scalar case. The dissipative range of E and E_ϕ reaches beyond $\kappa\eta = 1$ which implies a well resolved numerical simulation.

Figure 3.9 shows the normalized dissipation spectra of the turbulent energy,

$$2\nu\kappa^2 E(\kappa)/(\langle\varepsilon\rangle\eta)\,,$$

and the normalized dissipation spectra of the scalar variance,

$$2D\kappa^2 E_\phi(\kappa)/(\langle\chi\rangle\eta)\,,$$

for all cases. The peak of the former occurs at $\kappa\eta \approx 0.16$ with a value of 2.29. The peak of the latter occurs at $\kappa\eta \approx 0.25$ with a value of 1.56. This finding is in perfect agreement with the DNS of Watanabe and Gotoh (2004). The curves collapse for all cases, indicating that the small scales are properly resolved as well.

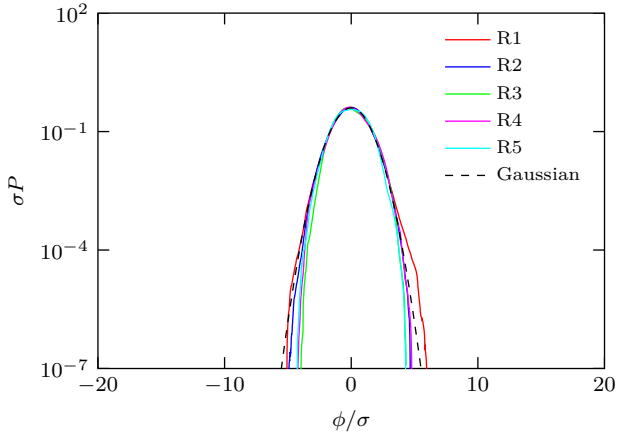

Figure 3.10: Normalized pdf of the passive scalar for all cases. Each pdf is normalized by the respective standard deviation. The dashed black line represents a Gaussian distribution with unity variance.

3.3.2 Probability Density Functions

It is customary to describe turbulence by probability density functions as they capture the whole statistical process. Figure 3.10 displays the normalized pdf of the passive scalar fluctuations ϕ for all cases. Each curve is normalized by the respective standard deviation σ. Independently of Reynolds number the normalized pdf of ϕ is very close to Gaussian, i.e. the flatness fluctuates around a value of 3 and the skewness fluctuates around zero, cf. tab. 3.1. However, obtaining reliable pdfs of the scalar fluctuations require very long data series for ensemble averaging, as the pdf tends only slowly to its asymptotic form. This is different for small-scale quantities where a few ensembles yields already well converged statistics. Figure 3.11 displays the normalized pdfs of the longitudinal $\partial u/\partial x$ and transversal $\partial u/\partial y$ velocity gradients for case R4. The former pdf is negatively skewed with moderately stretched tails. The latter pdf is symmetric and has longer stretched tails. Additionally, the normalized pdf of the scalar gradient $\partial\phi/\partial x$ for case R4 is shown. The pdf is symmetric and exhibits compared to the velocity field long stretched exponential tails. This is a characteristic feature of scalar fields revealing the stronger intermittency.

Figure 3.12 shows for all cases the normalized pdf of the energy dissipation ε (top) and the normalized pdf of the scalar dissipation χ (bottom). Both pdfs exhibit stronger tails with increasing Reynolds numbers, which is equivalent to an increasing rate of intermittency. The pdfs of χ have longer tails than the respective pdfs of ε. The tails of the pdfs can be modeled by stretched exponentials. For the pdf of χ the

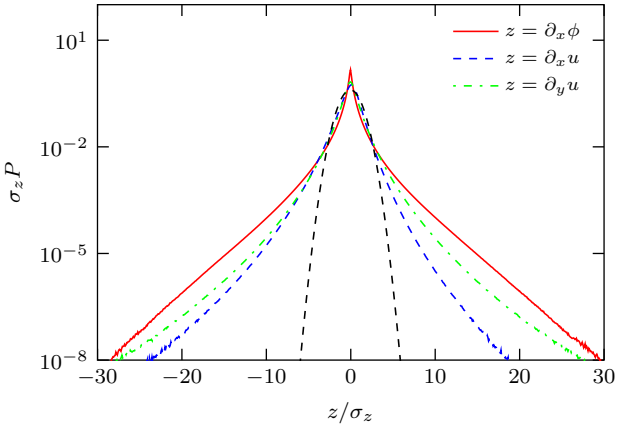

Figure 3.11: Normalized pdf of the longitudinal and transversal velocity gradients and of the scalar gradient in direction perpendicular to the mean gradient for case R4. The dashed black line represents a Gaussian distribution with unity variance.

analytic result $P(\chi) \propto \exp(-\chi^{1/3})$ occurs in the limit of very large Peclet numbers, where the scalar is advected in a smooth incompressible flow that is changing very rapidly in time, cf. Chertkov et al. (1998) and Schumacher and Sreenivasan (2005). Our results indicate that the limiting result is approached in the strong turbulence regime for case R5.

Figure 3.13 shows the normalized pdf of the logarithm of the energy dissipation and scalar dissipation, respectively, for all cases. Both pdfs display in the left and right tails deviations from log-normality because of the intermittent nature of dissipation. For the scalar dissipation these deviations are more significant. The left tails, which are determined by small events, are more pronounced than the log-normal curve while the right tails, which are determined by large events, remains sparser, cf. Ferchichi and Tavoularis (2002), Vedula et al. (2001) and Emran and Schumacher (2008). With increasing Reynolds number the curves tend very slowly toward log-normality. Departures from log-normality are not surprising, as for isotropic turbulence, the dissipation is a sum of independent log-normal variables which is not log-normal, cf. Papoulis and Pillai (2002).

3.3.3 Energy and Scalar Dissipation Anomaly

For homogeneous isotropic turbulence under the condition of very large Reynolds numbers the mean energy dissipation becomes independent of viscous effects, and the mean scalar dissipation becomes independent of diffusive effects, cf. Taylor

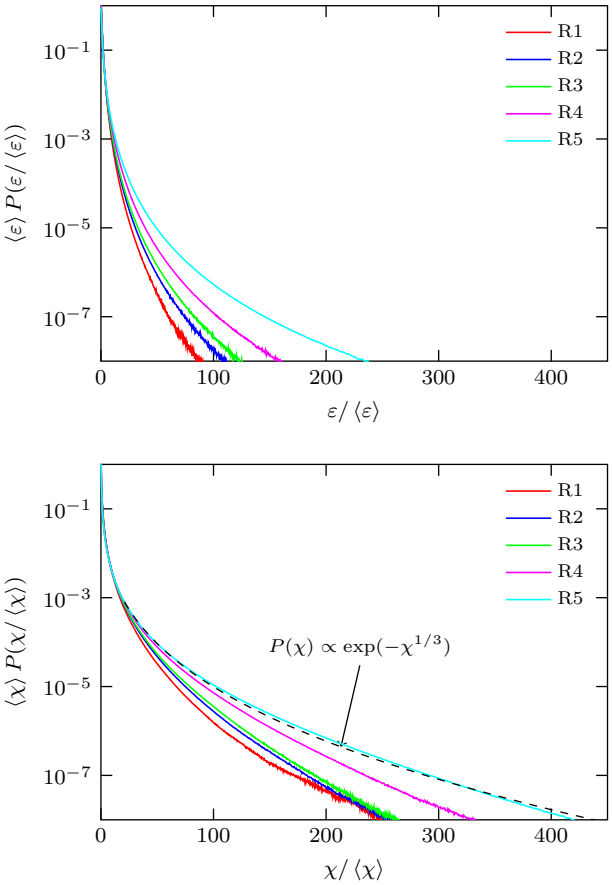

Figure 3.12: Normalized pdf of the energy dissipation (top) and normalized pdf of the scalar dissipation (bottom) for all cases. The black dashed line denotes $P(\chi) \propto \exp(-\chi^{1/3})$.

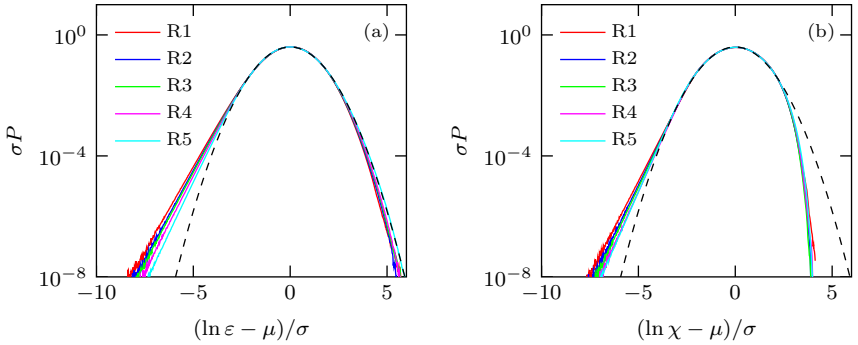

Figure 3.13: Normalized and centered pdf of the logarithm of the energy dissipation (a) and the scalar dissipation (b). The black dashed line denotes a normal distribution.

(1938) and Kolmogorov (1941b). This feature of turbulent flows is denoted as dissipation anomaly and has the consequence that for sufficiently high Reynolds numbers the normalized energy dissipation $\langle\varepsilon\rangle l_t/u'^3$ and the normalized scalar dissipation $\langle\chi\rangle l_t/\langle\phi^2\rangle/u'$ become independent of Reynolds number, cf. Kaneda et al. (2003), Sreenivasan (1998) and Donzis et al. (2005). Here, l_t, $\langle\phi^2\rangle$ and u' are viscosity-independent (large-scale) length, scalar, and velocity scales, respectively.

The normalized energy and scalar dissipation are shown in fig. 3.14 versus Reynolds number for all cases, where $\langle\varepsilon\rangle l_t/u'^3$ and $\langle\chi\rangle l_t/\langle\phi^2\rangle/u'$ tend to an asymptotic value. This asymptotic value is attained for the normalized scalar dissipation at smaller Reynolds number than for the normalized energy dissipation. DNS data by Donzis et al. (2005) and Gotoh et al. (2011) reveal an excellent agreement with the present data. Doering and Foias (2002) proposed a functional form for the normalized energy dissipation, namely

$$\frac{\langle\varepsilon\rangle l_t}{u'^3} = A\left(1+\sqrt{1+(B/\mathrm{Re}_\lambda)^2}\right), \tag{3.26}$$

which can be directly adopted to the normalized scalar dissipation

$$\frac{\langle\chi\rangle l_t}{\langle\phi^2\rangle u'} = A'\left(1+\sqrt{1+(B'/\mathrm{Re}_\lambda)^2}\right). \tag{3.27}$$

Fitting the present data to eq. 3.26 and eq. 3.27 leads to $A = 0.2$, $B = 96$, $A' = 0.3$ and $B' = 52$. The behavior shown in fig. 3.14 is universal for all turbulent flows away from solid walls, cf. Sreenivasan (1995).

The implication of fig. 3.14 is that a minimum Reynolds number ($\mathrm{Re}_\lambda \approx 200$) is necessary in order to obtain a constant scaling behavior. Mydlarski and Warhaft (1996, 1998) discriminate between weak turbulence for $\mathrm{Re}_\lambda < 100$ and strong turbulence for $\mathrm{Re}_\lambda > 200$ with a transition region in-between and they found that a

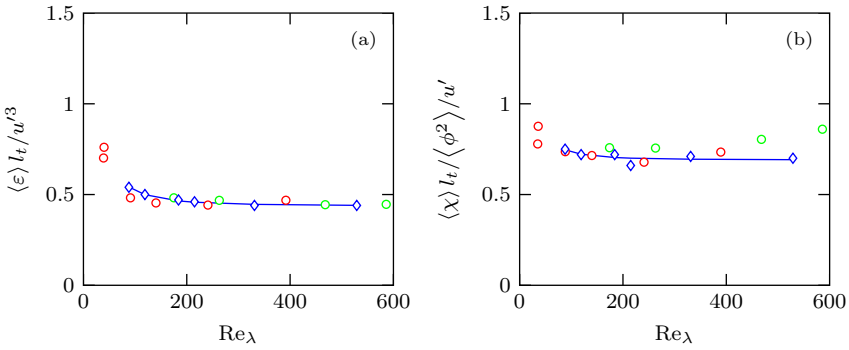

Figure 3.14: Normalized energy dissipation (a) and normalized scalar dissipation (b). Present data (blue diamonds) and best fit of the present data according to eq. 3.26 and eq. 3.27 (solid blue line). For comparison: Donzis et al. (2005) (red circles) and Gotoh et al. (2011) (green circles). The latter data are scaled to match our definition of χ.

well-developed inertial-subrange is established for $\mathrm{Re}_\lambda > 200$. For weak turbulence, statistics are affected by viscosity and the quantities l_t, $\langle\phi^2\rangle$ and u' are not sufficient to properly normalize the energy and the scalar dissipation. Nevertheless, in the weak turbulence regime, turbulence is fully developed in the sense that production equals dissipation.

3.3.4 Basic Equations

We consider a passive scalar governed by eq. 4.1 evolving in homogeneous isotropic turbulence. The transport equation for ϕ^2 reads

$$\frac{\partial\phi^2}{\partial t} + u_i\frac{\partial\phi^2}{\partial x_i} = D\frac{\partial\phi^2}{\partial x_i^2} - 2D\left(\frac{\partial\phi}{\partial x_i}\right)^2 - 2\Gamma u_2\phi\,. \tag{3.28}$$

The sink term is the instantaneous scalar dissipation defined as

$$\chi = 2D\left(\frac{\partial\phi}{\partial x_i}\right)^2, \tag{3.29}$$

and the source term is the instantaneous production of scalar variance defined as

$$\mathcal{P}_\phi = -2\Gamma u_2\phi\,. \tag{3.30}$$

Taking an ensemble average of eq. 3.28 and considering homogeneity results in

$$\frac{\partial\langle\phi^2\rangle}{\partial t} = -2D\Big\langle\left(\frac{\partial\phi}{\partial x_i}\right)^2\Big\rangle - 2\Gamma\big\langle u_2\phi\big\rangle\,, \tag{3.31}$$

reflecting the balance of the mean production of scalar variance and the mean scalar dissipation, where $-2\Gamma\langle u_2\phi\rangle$ is always positive. It is remarkable that a reduction of scalar variance is only effected by the scalar dissipation. Convection alone cannot reduce the scalar variance, but is important for the dispersion of the scalar field into fine filaments, as we will see below. In addition, homogeneity implies that the mean scalar gradient is constant. In the statistically stationary case scalar dissipation equals scalar production.

An equation for the scalar gradient can be derived by taking the gradient of eq. 1.5. We obtain

$$\frac{\partial g_j}{\partial t} + u_i \frac{\partial g_j}{\partial x_i} = -A_{ij} g_i + D \frac{\partial^2 g_j}{\partial x_i^2} - \Gamma \frac{\partial u_2}{\partial x_j}\,, \tag{3.32}$$

where g_j is an abbreviation for $\partial\phi/\partial x_j$, and A_{ij} is the fluctuating velocity gradient tensor defined as $\partial u_i/\partial x_j$. The fluctuating velocity gradient tensor A_{ij} can be decomposed as $A_{ij} = s_{ij} + w_{ij}$ into the deviatoric, symmetric rate of the strain tensor

$$s_{ij} = \frac{1}{2}\left(\frac{\partial u_i}{\partial x_j} + \frac{\partial u_j}{\partial x_i}\right)\,, \tag{3.33}$$

and into the anti-symmetric rate of rotation tensor

$$w_{ij} = \frac{1}{2}\left(\frac{\partial u_i}{\partial x_j} - \frac{\partial u_j}{\partial x_i}\right)\,. \tag{3.34}$$

In order to derive an equation for the scalar gradient variance $\langle g^2\rangle = \langle g_j g_j\rangle$ we multiply eq. 3.32 by $2g_j$ an obtain

$$\frac{\partial g^2}{\partial t} + u_i \frac{\partial g^2}{\partial x_i} = -2 g_j s_{ij} g_i - 2D\left(\frac{\partial g_j}{\partial x_i}\right)^2 + D\frac{\partial^2 g^2}{\partial x_i^2} - 2\Gamma g_j \frac{\partial u_2}{\partial x_j}\,, \tag{3.35}$$

where we used the identity $g_i w_{ij} g_j = 0$ to replace A_{ij} by s_{ij}. After applying an ensemble average and taking homogeneity into account eq. 3.35 reads

$$\frac{\partial\langle g^2\rangle}{\partial t} = \underbrace{-2\langle g_j s_{ij} g_i\rangle}_{\mathcal{P}_g} \underbrace{- 2D\langle\left(\frac{\partial g_j}{\partial x_i}\right)^2\rangle}_{\chi_g} - 2\Gamma\Big\langle g_j \frac{\partial u_2}{\partial x_j}\Big\rangle\,. \tag{3.36}$$

Multiplying eq. 3.36 by $2D$ yields a transport equation for the mean scalar dissipation $\langle\chi\rangle$. Since the scalar field is passive the velocity field has a one-way impact on the scalar gradient. The turbulent motion enhances mixing of the passive scalar by vortex-stretching and subsequent molecular diffusion. The first term on the right hand side of eq. 3.36 represents the vortex-stretching term that accounts for the interaction of the scalar field with the rate of strain tensor s_{ij}. Compressive and extensive strain disperse the scalar field and generates small-scale fluctuations and fine filaments. On average the vortex-stretching term is positive and represents

the production of scalar gradient variance $\langle g^2 \rangle$. It is denoted in the following by $\mathcal{P}_g$. The vortex-stretching term can be recast by expressing it in the strain basis. The fluctuating strain rate tensor s_{ij} is real and symmetric, and thus has generally three real eigenvalues λ_i with $\lambda_3 \leq \lambda_2 \leq \lambda_1$. Due to incompressibility the condition $\lambda_3 + \lambda_2 + \lambda_1 = 0$ holds. The corresponding eigenvectors are denoted by $\boldsymbol{e}_i$. Figure 3.15 shows the pdf of the cosine of the angle between the scalar gradient g_i and the eigenvectors $\boldsymbol{e}_i$ of the strain rate tensor. It reveals an alignment between g_i and the eigenvector $\boldsymbol{e}_3$, which corresponds to the most compressive eigenvalue λ_3. This is a purely kinematic result which is virtually unaffected by Reynolds number variations. The vortex-stretching term can be expressed as

$$g_i s_{ij} g_j = \|\boldsymbol{g}\|^2 \left[\lambda_1 \cos^2(\boldsymbol{g}, \boldsymbol{e}_1) + \lambda_2 \cos^2(\boldsymbol{g}, \boldsymbol{e}_2) + \lambda_3 \cos^2(\boldsymbol{g}, \boldsymbol{e}_3) \right] , \tag{3.37}$$

cf. Tsinober (2001), and thus, gradient production depends on both strain intensity and orientation of the scalar gradient with respect to the strain principal axes as well as on the magnitude of the scalar gradient. Gradient production is enhanced by alignment of the scalar gradient with the most compressive strain rate direction $\boldsymbol{e}_3$, cf. Kerr (1985) and Ashurst et al. (1987). However, the mechanisms of scalar gradient production are more complicated than implied by eq. 3.37, cf. Gulitski et al. (2007). The interaction between strain, scalar gradient, and vorticity affect scalar gradient production in a coupled non-linear way. Figure 3.16 shows the normalized gradient production conditioned on vorticity, strain and the gradient magnitude. Gradient production is hence more intense in regions of large strain but almost independent of vorticity. This observation is virtually independent of Reynolds number. In addition, gradient production depends strongly on the gradient magnitude itself, i.e. intense gradient production can be observed in regions of large gradient magnitude. Note that for small values of $g^2/\langle g^2 \rangle$ the normalized conditional scalar gradient production collapses for all Reynolds numbers, but for larger gradient magnitudes it depends strongly on Reynolds number.

The counterpart of gradient production is the scalar gradient dissipation χ_g, represented by the second term on the right hand side of eq. 3.36. It cuts in when the thickness of the filaments, which are generated by the vortex-stretching mechanism, are of the order of the Kolmogorov length.

The last term of eq. 3.36 represents gradient production by the mean gradient at an integral scale and is small compared to the gradient production by the vortex-stretching term $\mathcal{P}_g$. As a result, for statistical stationary homogeneous turbulence, the gradient dissipation χ_g equals the gradient production $\mathcal{P}_g$. This is further illustrated in tab. 3.2 for all cases. While both $\mathcal{P}_g$ and χ_g increase with Reynolds number, the normalized scalar gradient production

$$\frac{\mathcal{P}_g \, 2^{3/2} D \nu^{1/2}}{\langle \chi \rangle \langle \varepsilon \rangle^{1/2}} = \frac{-\langle g_i g_j s_{ij} \rangle}{\langle g^2 \rangle \langle s_{ij} s_{ij} \rangle^{1/2}} , \tag{3.38}$$

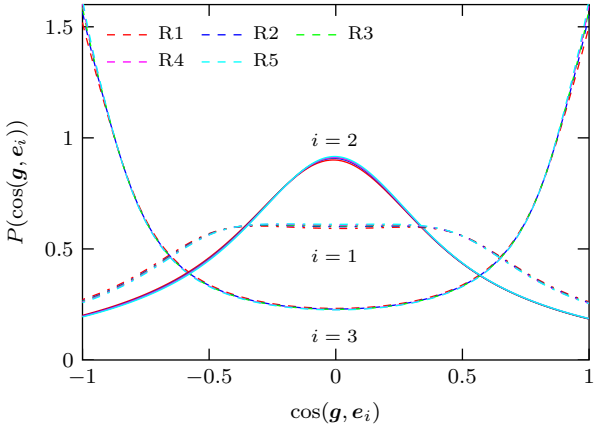

Figure 3.15: Pdf of the cosine between the scalar gradient $\boldsymbol{g}$ and the eigenvectors $\boldsymbol{e}_i$ of the fluctuating strain rate tensor.

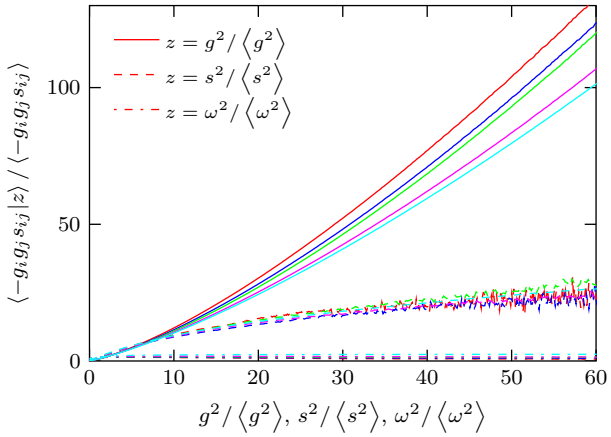

Figure 3.16: Normalized scalar gradient production conditioned of the normalized strain rate, vorticity and scalar gradient itself.

Table 3.2: Mean gradient dissipation χ_g and mean gradient production $\mathcal{P}_g$ for different Reynolds number.

	R0	R1	R2	R3	R4	R5
Re_λ	88	119	184	215	331	529
$\mathcal{P}_g$	4.30e3	1.09e4	3.51e4	7.23e4	1.85e5	1.22e6
χ_g	4.40e3	1.09e4	3.53e4	7.24e4	1.85e5	1.21e6
$\frac{\mathcal{P}_g 2^{3/2} D\nu^{1/2}}{\langle\chi\rangle\langle\varepsilon\rangle^{1/2}}$	0.47	0.48	0.48	0.49	0.49	0.50

is almost independent of Reynolds number, cf. tab. 3.2. The slight increase from 0.47 for case R0 to 0.50 for case R5 may be attributed to the imposed anisotropy. In the limit of large Reynolds numbers eq. 3.38 tends to the value 0.5. This result confirms the alignment between the scalar gradient and the strain-rate tensor.

3.3.5 Structure Function Analysis

The main difficulties regarding the statistical description of turbulent flows originate from the non-linearity of the governing equations, i.e. the Navier-Stokes equations, and the correlation between different scales, cf. Frisch (1995). It is customary to examine turbulent flows by means of two-point statistics as they capture not only the local but also the non-local phenomena which are inherent to turbulent flows. Based on the governing equations one can derive transport equations for all moments of the velocity increments $\Delta u = u(\boldsymbol{x}) + u(\boldsymbol{x}+\boldsymbol{r})$ or the scalar increments $\Delta\phi = \phi(\boldsymbol{x}) + \phi(\boldsymbol{x}+\boldsymbol{r})$, where $\boldsymbol{r}$ is the separation vector between the two points, cf. Hill (2001). Of course, as every statistical approach in turbulence theory, these transport equations are not closed because of the non-linearity of the convective term. Instead, they constitute an infinite hierarchy of moments where each level couples to the next higher one.

The transport equations for the two-point correlations of the longitudinal velocity and the passive scalar fluctuations in isotropic homogeneous turbulence have been first derived by Karman and Howarth (1938) and Corrsin (1951). Kolmogorov (1941a) and Yaglom (1949) rewrote these equations for the second order moments of the longitudinal velocity increment D_{LL} and the scalar increment $D_{\phi\phi}$ (adopting the notation by Monin and Yaglom (1975)):

$$-D_{LLL}(r) + 6\nu\frac{\partial D_{LL}}{\partial r} = \frac{4}{5}\langle\varepsilon\rangle r\,, \tag{3.39}$$

$$-D_{L\phi\phi}(r) + 2D\frac{\partial D_{\phi\phi}}{\partial r} = \frac{2}{3}\langle\chi\rangle r\,. \tag{3.40}$$

Here, $D_{LLL} = \langle(\Delta u)^3\rangle$ and $D_{L\phi\phi} = \langle(\Delta u)(\Delta\phi)^2\rangle$ are the third order longitudinal structure function and the third order mixed longitudinal velocity scalar structure function, respectively. Equations 3.39 and 3.40 are valid in statistically stationary, homogeneous and isotropic turbulence. Note that eqs. 3.39 and 3.40 are incomplete because they lacks either an unsteady term or a forcing term that maintains a statistically stationary state.

As a result of Kolmogorov's second similarity hypothesis, within the inertial subrange, the third order structure function decouples from the second order structure function, yielding

$$-D_{LLL}(r) = \frac{4}{5}\langle\varepsilon\rangle r\,, \tag{3.41}$$

which is exact in the asymptotic limit of infinite Reynolds numbers. This equation is called four-fifths-law and is today regarded as the only non-trivial exact result in turbulence theory. Figure 3.17 illustrates the four-fifths-law for all cases. The third order structure function D_{LLL} is compensated by $-4/5\langle\varepsilon\rangle r$, so that within the inertial subrange a plateau at unity is attained. With increasing Reynolds number the plateau becomes wider and approaches the theoretical limit of unity.

Yagloms's equation can be written for scales in the inertial subrange as

$$-D_{L\phi\phi}(r) = \frac{2}{3}\langle\chi\rangle r\,. \tag{3.42}$$

Figure 3.18 displays the third order mixed velocity-scalar structure function $D_{L\phi\phi}(r)$ compensated by $-\frac{2}{3}\langle\chi\rangle r$ for all cases. Due to the imposed mean scalar gradient in x_2-direction, two-point statistics depend on the direction in which the separation vector $\boldsymbol{r}$ is taken and statistical quantities exhibit an axial symmetry around the x_2-axis and reflectional invariance to the plane perpendicular to the mean gradient. In the following we will focus on the case that $\boldsymbol{r}$ is perpendicular to the direction of the mean scalar gradient. Similarly to the velocity case the compensated third order mixed velocity-scalar structure function exhibits a plateau within the inertial range. The width of the scaling regime increases with Reynolds number, and generally, the scaling regime is enlarged toward small scales compared to the velocity field at equal Reynolds number. However, the theoretical limit of unity is not attained in the inertial range. This can be attributed primarily to the anisotropy of the scalar field and less to finite Reynolds number effects. In sec. 4.2 we will derive a generalized Yaglom equation that accounts for the mean scalar gradient and the anisotropy. Additionally, figs. 3.17 and 3.18 show that in the dissipative regime the compensated third order velocity structure functions and the compensated third order mixed structure functions follow closely a r^2 scaling, which can be derived from a Taylor-series expansion of the compensated increments.

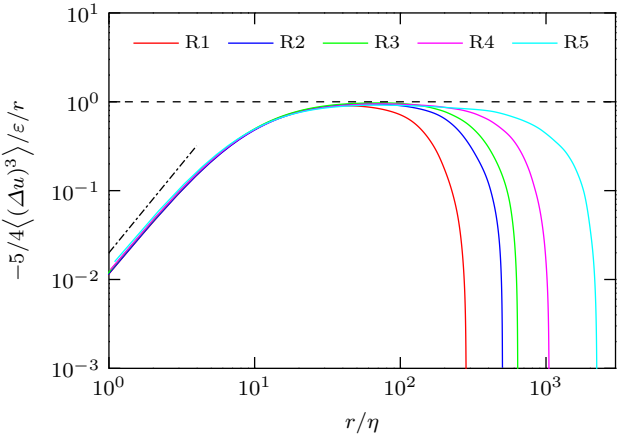

Figure 3.17: Normalized and compensated third order longitudinal velocity structure function. The dashed-dotted line denotes a r^2 scaling.

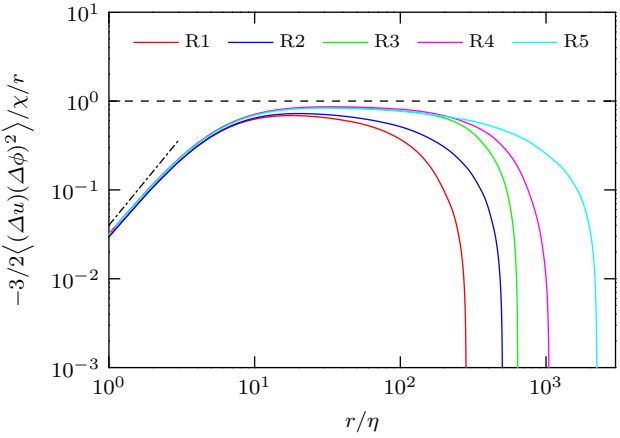

Figure 3.18: Normalized and compensated third order mixed velocity scalar structure function. The dashed-dotted line denotes a r^2 scaling.

4 Dynamics of Turbulent Mixing

4.1 Introduction

The objective of the present chapter is twofold. First, we derive from first principles an equation for the even moments of the scalar increment $S_{2n}(r) = \langle(\Delta\phi)^{2n}\rangle$ that generalizes Yaglom's equation to statistically homogeneous but not isotropic scalar fields. Thus, we allow for a constant mean scalar gradient that injects scalar energy and imposes an anisotropy to the scalar field. The anisotropy persists even at the smallest scales, and as a result, structure functions depend on the orientation of the separation vector $\boldsymbol{r}$. The small-scale anisotropy of scalar fields is still an open question. Schumacher et al. (2005) and Ferchichi and Tavoularis (2002) showed by means of Direct Numerical Simulation (DNS) and from experiments that even at very high Schmidt numbers or Reynolds numbers the small-scale statistics approach isotropy only slowly. Casciola et al. (2003) derived an exact evolution equation for the velocity increment in shear turbulence by spherical integration, which corresponds to averaging over all directions. This equation was interpreted as a scale-by-scale energy budget over a sphere of radius r. In the present work, we will adopt this approach for the moments of the scalar increment. Additionally, we will examine how the scalar scale-by-scale energy budget is altered by variations of the Schmidt number.

By examining the generalized Yaglom equation we gain insight into the production and dissipation mechanisms of scalar turbulence, as well as the transport phenomena which are responsible for the transport of scalar energy from large scales down to small scales. Energy transport is crucial for Large-Eddy Simulation (LES), which directly solves the large flow-dependent scales, while the smaller scales are subject to closure. As closure involves only the more universal small scales, the models are expected to be universal as well. Meneveau (1994) and Jiménez and Moser (2000) stated that the correct representation of the energy flux between resolved and unresolved scales is a necessary condition that LES models have to satisfy in order to preserve the statistical properties of the large scales. Based on this observation, Meneveau (1994) derived a physically sound subgrid model from the filtered Kolmogorov equation for homogeneous isotropic turbulence that consistently satisfies the energy flux toward subgrid scales. This model was recently extended by Cui et al. (2007) and Cui et al. (2004) to non-homogeneous wall-bounded and rotating flows. Additionally, an extension to scalar turbulence was given. Using a similar idea, Lévêque et al. (2007) derived a shear-improved Smagorinsky model that incorporates the scale-by-scale energy budget equation.

The second objective addressed by the present chapter is to examine the scale-by-scale energy budget for scalar fields in the context of LES, which is significant for the afore-mentioned models. To this end, we extend the generalized Yaglom equation to the filtered scalar increment. This equation directly incorporates the energy flux associated with the resolved and unresolved scales, cf. Gualtieri et al. (2007). Based on this equation we first show by means of an *a-priori* analysis how the energy budget is altered by filtering, and we interpret the physical transport mechanisms in filtered scalar turbulence. The subgrid terms can be closed by a gradient flux approach that relies on a subgrid viscosity. By means of the scale-by-scale energy budget equation, we will show that a gradient flux approach satisfies the budget very well, which justifies this approach in the sense of an *a-priori* test. Next, we conduct an LES of scalar turbulence where the subgrid terms are closed by a gradient flux approach to discuss the filtered energy budget equation in the context of an *a-posteriori* test. This enables us to examine the quality of the LES. The present analysis is complemented by studying the impact of Schmidt number variations in the context of LES.

The content of this chapter is published in Gauding et al. (2014).

4.2 The Generalized Yaglom Equation

4.2.1 Governing Equations

We consider a passive scalar field advected by statistically homogeneous isotropic turbulence. A uniform mean gradient Γ in x_2-direction is imposed on the scalar field. This induces a preferential excitation of the scalar fluctuations by the velocity component in the direction of the mean scalar gradient leading to an anisotropy of scalar statistics. Statistical quantities of the scalar reveal an axial symmetry around the x_2-axis and reflectional invariance to the plane perpendicular to the mean gradient, cf. Gotoh et al. (2011). The scalar fluctuations ϕ are statistically homogeneous and obey the following equation

$$\frac{\partial \phi}{\partial t} + u_i \frac{\partial \phi}{\partial x_i} = D \frac{\partial^2 \phi}{\partial x_i^2} - \Gamma u_2 \,, \tag{4.1}$$

where t is the time, x_i the spatial coordinate, and u_i and D denote the velocity and the molecular diffusivity, respectively.

4.2.2 Derivation of the Generalized Scale-by-scale Energy Budget Equation

The aim of the present section is to generalize eq. 3.40 for arbitrary even moments and for non-isotropic but still homogeneous scalar fields. The following derivation

is based on the procedure presented in Hill (2002), Danaila et al. (1999), Danaila et al. (2012) and Gauding et al. (2011). Let us write the transport equation of the scalar fluctuation ϕ at two independent points $\boldsymbol{x}$ and $\boldsymbol{x}'$, which are separated by the separation vector $\boldsymbol{r} = \boldsymbol{x}' - \boldsymbol{x}$

$$\partial_t \phi + u_i \partial_i \phi = D\partial_i^2 \phi - \Gamma u_2 \tag{4.2}$$

$$\partial_t \phi' + u_i' \partial_i' \phi' = D\partial_i'^2 \phi' - \Gamma u_2' \,. \tag{4.3}$$

Here, the abbreviations $\partial_t = \partial/\partial t$ and $\partial_i = \partial/\partial x_i$ are used for temporal and spatial derivatives, respectively. The notation ∂_i and ∂_i' will be used for derivatives with respect to $\boldsymbol{x}$ and $\boldsymbol{x}'$. Derivatives with respect to the separation distance will be written explicitly, i.e. $\partial/\partial r_i$. The two spatial points $\boldsymbol{x}$ and $\boldsymbol{x}'$ are independent and have no relative motion. Also for the flow quantities, the prime refers to the point $\boldsymbol{x}'$, i.e. $\phi' = \phi(\boldsymbol{x}', t)$ and $u_i' = u_i(\boldsymbol{x}', t)$.

As ϕ is independent of $\boldsymbol{x}'$, and ϕ' is independent of $\boldsymbol{x}$, an equation for the scalar increment $\Delta\phi = \phi' - \phi$ can be derived by subtracting eq. 4.2 from eq. 4.3 and using the identities $\partial_i \phi = -\partial_i \Delta\phi$ and $\partial_i' \phi' = \partial_i' \Delta\phi$. Multiplication of the resulting equation with $2n(\Delta\phi)^{2n-1}$, where n is a positive integer, and subsequent ensemble-averaging yields an equation for the even moments of the scalar increment, namely

$$\begin{aligned}
&\frac{\partial\left\langle(\Delta\phi)^{2n}\right\rangle}{\partial t} + \frac{\partial\left\langle(u_i)(\Delta\phi)^{2n}\right\rangle}{\partial x_i} + \frac{\partial\left\langle(u_i')(\Delta\phi)^{2n}\right\rangle}{\partial x_i'} + 2n\Gamma\left\langle(\Delta u_2)(\Delta\phi)^{2n-1}\right\rangle \\
=&D\left[\frac{\partial^2\left\langle(\Delta\phi)^{2n}\right\rangle}{\partial x_i^2} + \frac{\partial^2\left\langle(\Delta\phi)^{2n}\right\rangle}{\partial {x_i'}^2}\right. \\
&\left. - 2n(2n-1)\left(\left\langle(\Delta\phi)^{2n-2}\left(\frac{\partial\Delta\phi}{\partial x_i}\right)^2\right\rangle + \left\langle(\Delta\phi)^{2n-2}\left(\frac{\partial\Delta\phi}{\partial x_i'}\right)^2\right\rangle\right)\right].
\end{aligned} \tag{4.4}$$

Due to homogeneity, the even moments of the scalar increment $\left\langle(\Delta\phi)^{2n}\right\rangle$ are independent of the position $\boldsymbol{x}$, but depend only on the separation distance r. In the next step, in addition to the separation vector, also referred to as correlation variable,

$$\boldsymbol{r} = \boldsymbol{x}' - \boldsymbol{x} \,, \tag{4.5}$$

we introduce a new coordinate as suggested by Hill (1997)

$$\boldsymbol{X} = \frac{1}{2}\left(\boldsymbol{x} + \boldsymbol{x}'\right) \,, \tag{4.6}$$

where $\boldsymbol{X}$ is the midpoint between the two points $\boldsymbol{x}$ and $\boldsymbol{x}'$. We can now express the spatial derivatives as

$$\partial_i' = \frac{\partial}{\partial r_i} + \frac{1}{2}\frac{\partial}{\partial X_i} \tag{4.7}$$

$$\partial_i = -\frac{\partial}{\partial r_i} + \frac{1}{2}\frac{\partial}{\partial X_i} \,. \tag{4.8}$$

By applying the transformation rules, eqs. 4.7 and 4.8, to eq. 4.4, and considering that due to homogeneity $\partial\langle\cdot\rangle/\partial X_i = 0$, we obtain a general equation for the even moments

$$\begin{aligned}
&\frac{\partial}{\partial t}\Big\langle(\Delta\phi)^{2n}\Big\rangle(\boldsymbol{r}) + \frac{\partial}{\partial r_i}\Big\langle(\Delta u_i)(\Delta\phi)^{2n}\Big\rangle(\boldsymbol{r}) + 2n\Gamma\Big\langle(\Delta u_2)(\Delta\phi)^{2n-1}\Big\rangle(\boldsymbol{r}) \\
&\quad = 2D\frac{\partial^2}{\partial r_i^2}\Big\langle(\Delta\phi)^{2n}\Big\rangle(\boldsymbol{r}) \\
&\quad - 2nD(2n-1)\Big\langle(\Delta\phi)^{2n-2}\left(\frac{\partial(\Delta\phi)}{\partial x_i}\right)^2 + \left(\frac{\partial(\Delta\phi)}{\partial x_i'}\right)^2\Big\rangle(\boldsymbol{r})\,,
\end{aligned} \tag{4.9}$$

where each term reveals an explicit dependence on $\boldsymbol{r}$. The derivation of eq. 4.9 follows exactly from the governing equations for incompressible and homogeneous, but not necessarily isotropic flows. For the 4th moment $\big\langle(\Delta\phi)^4\big\rangle$, which is significant for the flatness of the scalar increment, eq. 4.9 simplifies to

$$\begin{aligned}
&\frac{\partial}{\partial t}\Big\langle(\Delta\phi)^4\Big\rangle(\boldsymbol{r}) + \frac{\partial}{\partial r_i}\Big\langle(\Delta u_i)(\Delta\phi)^4\Big\rangle(\boldsymbol{r}) + 4\Gamma\Big\langle(\Delta u_2)(\Delta\phi)^3\Big\rangle(\boldsymbol{r}) \\
&\quad = 2D\frac{\partial^2}{\partial r_i^2}\Big\langle(\Delta\phi)^4\Big\rangle(\boldsymbol{r}) - 24D\Big\langle(\Delta\phi)^2\left(\frac{\partial\phi}{\partial x_i}\right)^2\Big\rangle(\boldsymbol{r})\,.
\end{aligned} \tag{4.10}$$

From now on we limit ourselves to the second moment $\langle(\Delta\phi)^2\rangle$. In this case eq. 4.9 simplifies further to

$$\begin{aligned}
&\frac{\partial}{\partial t}\Big\langle(\Delta\phi)^2\Big\rangle(\boldsymbol{r}) + \frac{\partial}{\partial r_i}\Big\langle(\Delta u_i)(\Delta\phi)^2\Big\rangle(\boldsymbol{r}) + 2\Gamma\Big\langle(\Delta u_2)(\Delta\phi)\Big\rangle(\boldsymbol{r}) \\
&\qquad = 2D\frac{\partial^2}{\partial r_i^2}\Big\langle(\Delta\phi)^2\Big\rangle(\boldsymbol{r}) - 4D\Big\langle\frac{\partial\phi}{\partial x_i}\frac{\partial\phi}{\partial x_i}\Big\rangle\,.
\end{aligned} \tag{4.11}$$

Let us now discuss the different terms of eq. 4.11. The first term on the left hand side vanishes when we consider stationary flows. The second term denotes the interscale transport term in correlation space and represents the transport of scalar energy between large and small scales. The third term denotes a production term due to the mean scalar gradient at large scales. Production depends on the mean scalar gradient Γ and the scalar flux $\langle(\Delta u_2)(\Delta\phi)\rangle$ at scale r, which is negative over all scales, corresponding to a positive production term. The first term on the right hand side of eq. 4.11 represents diffusive transport in correlation space. The second term on the right hand side is twice the scalar dissipation

$$\big\langle\chi\big\rangle = 2D\langle\left(\frac{\partial\phi}{\partial x_i}\right)^2\rangle \tag{4.12}$$

and thus a one-point quantity. It is notable that this term is a one-point quantity only for the second moment and turns into a two-point quantity when higher order moments are considered, as can be seen from eq. 4.9.

The imposed mean scalar gradient is the source for anisotropy in eq. 4.11. When a uniform mean scalar gradient is imposed on the scalar field, the fluctuations are injected at all scales down to the Kolmogorov length scale η yielding an anisotropy that is present even at the smallest scales. The production term is further studied by analyzing the scaling of the scalar flux $\langle(\Delta u_2)(\Delta\phi)\rangle$ in correlation space. Lumley (1964) predicted by dimensional arguments that the spectrum of the scalar flux $E_{u_2\phi}(\kappa)$ in isotropic turbulence with imposed uniform mean scalar gradients reads

$$E_{u_2\phi}(\kappa) = \hat{c}_{u_2\phi}\Gamma\langle\varepsilon\rangle^{1/3}\kappa^{-7/3}\,, \tag{4.13}$$

where κ is the wave number and $\hat{c}_{u_2\phi}$ is a nondimensional constant. The scalar flux spectrum quantifies how the scalar flux is distributed over the scales. Lumley's dimensional analysis can be applied as well to correlation space yielding

$$\langle(\Delta u_2)(\Delta\phi)\rangle = c_{u_2\phi}\Gamma\langle\varepsilon\rangle^{1/3}r^{4/3}\,. \tag{4.14}$$

Figure 4.1a shows the production term $-2\Gamma\big\langle(\Delta u_2)(\Delta\phi)\big\rangle$ as a function of the separation distance r, normalized with the Kolmogorov length scale η, whereby the separation vector $\boldsymbol{r}$ points in the direction of the three coordinate axes. Additionally, fig. 4.1a depicts the 4/3-scaling according to eq. 4.14. The scaling obtained from the present DNS at moderate Reynolds number is closer to r than to $r^{4/3}$. This is however in agreement with observations from literature, cf. Watanabe and Gotoh (2007b). Bos et al. (2005) showed that Lumley's scaling is attained only at very high Reynolds numbers.

Additionally, the production term strongly depends on the direction of $\boldsymbol{r}$. It reveals an identical behavior for $\boldsymbol{r}$ pointing in x_1- or x_3-direction, but attains a lower value when $\boldsymbol{r}$ points in x_2-direction, which is the direction of the mean scalar gradient. Only in the theoretical limit $r \to \infty$ the directional dependence tends to disappear, since the limit

$$\lim_{r\to\infty} 2\Gamma\big\langle(\Delta u_2)(\Delta\phi)\big\rangle(\boldsymbol{r}) = 4\Gamma\big\langle u_2\phi\big\rangle \tag{4.15}$$

is independent of $\boldsymbol{r}$ and approaches the one-point limit. However, this does not mean that large scales become isotropic, because isotropy would require that mean vectorial quantities like $\langle u_i\phi\rangle$ would disappear.

The transport term $-\big\langle(\Delta\phi)(\Delta u_i)^2\big\rangle n_i$ exhibits as well a strong anisotropy, cf. fig. 4.1c. Here, the value in x_2-direction is larger than in the two other directions. The second order scalar structure function $\big\langle(\Delta\phi)^2\big\rangle$ is virtually independent of direction, cf. fig. 4.1b. However, in the limit $r \to 0$, $\langle(\Delta\phi)^2\rangle$ is directly linked to the variance of the scalar gradient. The small-scale anisotropy is reflected by the fact that the ratio $\langle\partial_\parallel\phi^2\rangle/\langle\partial_\perp\phi^2\rangle \approx 1.06$ is unequal unity. Hereby, $\partial_\parallel$ denotes the derivative along a line which is parallel to the direction of the mean scalar gradient, while $\partial_\perp$ denotes the derivative along a line perpendicular to the mean scalar gradient.

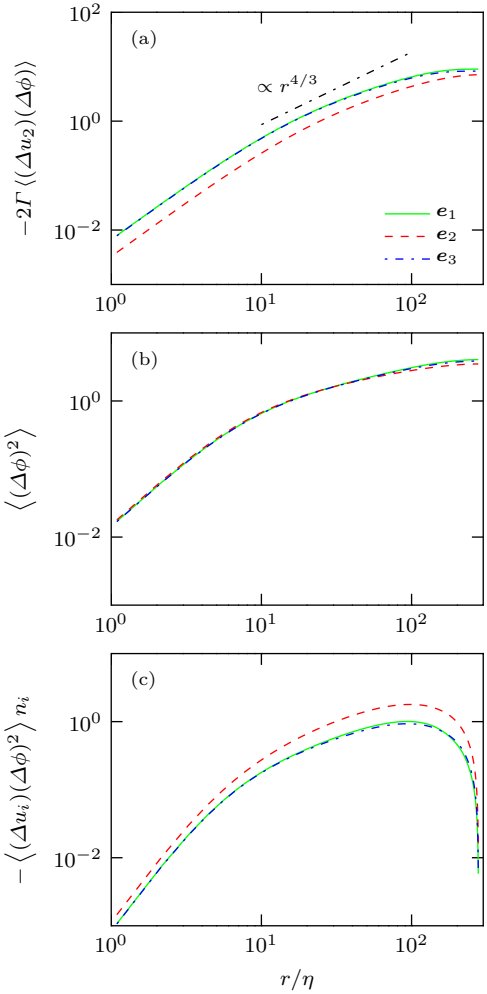

Figure 4.1: Production (a), diffusive transport (b) and turbulent transport (c) terms present in eq. 4.11 for case A2. The separation vector $\boldsymbol{r}$ points along the three coordinate axes, with $\boldsymbol{e}_1$, $\boldsymbol{e}_2$ and $\boldsymbol{e}_3$ being the respective unit vectors. The separation distance r is normalized with the Kolmogorov length scale η. While the second order structure function (b) is independent of the direction, a clear directional dependence is observed for the production (a) and turbulent transport (c) terms. The values in x_2-direction (red lines), parallel to the mean scalar gradient, deviate from the values in the x_1- and x_3-direction, which are identical.

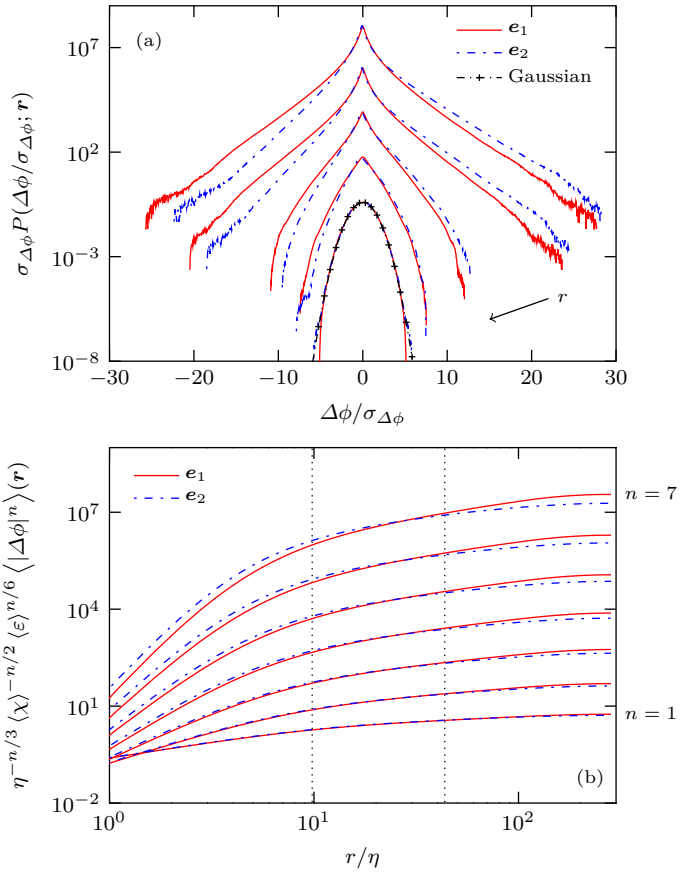

Figure 4.2: Normalized probability density function of the scalar increment $\Delta\phi(\boldsymbol{r})$ for the separation vector $\boldsymbol{r}$ pointing parallel (blue, dashed) and perpendicular (red, solid) to the mean scalar gradient (a) for case A2. The curves are for $r_n/\eta = 4^{n-1}(\Delta x/\eta)$, where the arrow denotes the direction of increasing r. Additionally, the curves are shifted vertically by two decades for clarity. The black dashed line represents a Gaussian distribution. The lower figure (b) shows the normalized moments of the scalar increment for the separation vector $\boldsymbol{r}$ pointing parallel (blue, dashed) and perpendicular (red, solid) to the mean scalar gradient. The order of the moment increases from bottom to top. The vertical dotted lines denote the lower and upper bound of the inertial range, respectively.

The anisotropy of the scalar increment $\Delta\phi$ can be further analyzed by means of its probability density function (pdf). Figure 4.2a shows the normalized pdf $P(\Delta\phi;\boldsymbol{r})$ for different separation lengths and for $\boldsymbol{r}$ pointing parallel and perpendicular to the mean scalar gradient to capture the effect of the anisotropy. Because of internal intermittency the statistics of $\Delta\phi$ depend on the separation length r. At large separation lengths the pdf is close to Gaussian. But for smaller scales the pdf departs strongy from Gaussianity with progressively longer stretched exponential tails. Additionally, the pdfs are symmetric for $\boldsymbol{r}$ pointing perpendicular to the mean gradient while revealing a positive skewness for $\boldsymbol{r}$ pointing parallel to the mean gradient. This skewness becomes more pronounced at smaller scales where the scalar increment can be interpreted as the scalar derivative. The moments of the scalar increment are related to the pdf by

$$\langle|\Delta\phi|^n\rangle(\boldsymbol{r}) = \int_{-\infty}^{\infty} |\Delta\phi|^n P(\Delta\phi;\boldsymbol{r})\mathrm{d}(\Delta\phi)\,, \tag{4.16}$$

where we take the absolute value of $\Delta\phi$. The moments $\langle|\Delta\phi|^n\rangle(\boldsymbol{r})$ are shown normalized by the Kolmogorov variables in fig. 4.2b for n up to the seventh order. The lower order moments are virtually independent of direction because they depend mainly on the core region of the pdf. The core region of the pdf originates from small events. Here, the curves can be collapsed independently of direction solely by the standard deviation $\sigma_{\Delta\phi}$. For the higher order moments the directional dependence is more significant because here the tails of the pdf make a vast contribution.

Equation 4.11 can be recast in a similar form as the Yaglom equation by spatially averaging over a sphere of radius r. Taking a spherical average in r-space was first introduced by Nie and Tanveer (1999) and further studied by Hill (2002) for structure functions of the velocity increment. Casciola et al. (2003) used the spherical average to derive scaling laws based on an averaged dissipation rate in the spirit of the refined theory of Oboukhov (1962) and Kolmogorov (1962). By taking a spherical average with radius r of eq. 4.11 we obtain

$$\begin{aligned}\underbrace{-\frac{1}{4\pi r^2}\int_{\partial V}\left\langle(\Delta u_i)(\Delta\phi)^2\right\rangle n_i\mathrm{d}\Omega}_{T(r)}\;\underbrace{-\frac{1}{4\pi r^2}\int_V 2\Gamma\left\langle(\Delta u_2)(\Delta\phi)\right\rangle\mathrm{d}V}_{P(r)}\\ \underbrace{+2D\frac{\mathrm{d}}{\mathrm{d}r}\left[\frac{1}{4\pi r^2}\int_{\partial V}\left\langle(\Delta\phi)^2\right\rangle\mathrm{d}\Omega\right]}_{K(r)} = \frac{2}{3}\langle\chi\rangle r\,,\end{aligned} \tag{4.17}$$

where the divergence theorem was used to replace the volume integration by surface integration, namely

$$\int_V \frac{\partial}{\partial r_i}\left\langle(\Delta u_i)(\Delta\phi)^2\right\rangle\mathrm{d}V = \int_{\partial V}\left\langle(\Delta u_i)(\Delta\phi)^2\right\rangle n_i\mathrm{d}\Omega\,. \tag{4.18}$$

Equation 4.17 represents the budget between production $P(r)$, turbulent transport $T(r)$, diffusive transport $K(r)$ and dissipation $\langle\chi\rangle$ of scalar energy at scale r. Additionally, n_i denotes the components of a unit vector normal to the sphere, and V represents the volume of a sphere with radius r. The boundary of the volume is denoted by ∂V and the solid angle is denoted by $\mathrm{d}\Omega$. Averaging over spheres removes the directional dependence of the structure functions so that the final result depends only on the separation distance r. For the numerical evaluation of the terms, the spherical average is approximated by a three-directional average along the Cartesian coordinate axes. Gotoh et al. (2011) confirmed that a three-directional average is appropriate to approximate the spherical average.

Equation 4.17 is not closed because of the coupling to the velocity field. The objective here is not to close eq. 4.17, but rather to illustrate various physical effects. Therefore, we analyze eq. 4.17 by means of Direct Numerical Simulation (DNS), where all terms are directly accessible.

4.2.3 Direct Numerical Simulation

The three-dimensional incompressible Navier-Stokes equations as well as a transport equation for the fluctuations of a passive scalar are efficiently solved by a fully dealiased pseudo-spectral method, cf. Rogallo (1981) and Canuto et al. (1988). The integration domain is a triply periodic cube with length 2π. An external stochastic forcing, cf. Eswaran and Pope (1988), is applied to the velocity field to maintain a statistically steady state. The forcing is assumed to be statistically homogeneous and isotropic, and it is applied at low wavenumbers within a spectral shell of prescribed radius only. Various forcing schemes have been adopted in the literature, cf. Sreenivasan (1998) and Yeung and Zhou (1997). The small-scale statistics, however, are not affected by the specific scheme. A uniform mean scalar gradient is applied to the scalar field which keeps the scalar fluctuations as well in a statistically stationary state.

The Schmidt number, defined as $\mathrm{Sc} = \nu/D$, is varied between 0.11 and 5.56, while keeping the Reynolds number constant. The smallest length scales are well resolved as the conditions $\kappa_{\max}\eta > 1.5$ for $\mathrm{Sc} \leq 1$ as well as $\kappa_{\max}\eta_B > 1.5$ for $\mathrm{Sc} > 1$ are satisfied, cf. Watanabe and Gotoh (2007a). Here, $\kappa_{\max}$ denotes the maximum wavenumber, and $\eta_B = \mathrm{Sc}^{-1/2}\eta$ denotes the Batchelor length scale. For $\mathrm{Sc} > 1$ the scalar field attains smaller length scales than the velocity field, i.e. $\eta_B < \eta$. Further properties of the DNS, which were conducted on the supercomputer JUQUEEN at the Research Center Jülich, Germany, are given in tab. 4.1.

When calculating statistics in correlation space, the convergence of the statistics is better for small values of r than for large r. In order to achieve properly converged statistics at large scales, long integration times are required. Due to limited computational time, a compromise between scale separation and statistical convergence

Table 4.1: Parameters of the DNS cases. For all cases, the Reynolds number is identical, while the Schmidt number is varied between 0.11 and 5.56. For the large Schmidt number case, the grid is refined in order to well resolve all scales down to the Batchelor length scale. The velocity field is statistically identical to case R1.

Case	A1	A2	A3	A4
N	1024	512	512	512
Sc	5.56	1.0	0.25	0.11
Re_λ	119	119	119	119
Pe_λ	662	119	30	13.1
ν	0.0055	0.0055	0.0055	0.0055
λ	0.238	0.238	0.238	0.238
λ_ϕ	0.060	0.127	0.234	0.335
η	0.0112	0.0112	0.0112	0.0112
l_t	0.97	0.97	0.97	0.97
η_B	0.0047	0.0112	0.0225	0.0338
$\kappa_{\max}\eta$	3.82	1.91	1.91	1.91
$\kappa_{\max}\eta_B$	1.60	1.91	3.84	5.76
τ	1.04	1.07	1.07	1.07
$T_{\max} = t_{\max}/\tau$	82	495	495	495

has to be found. Therefore, the energy-budget equation is first evaluated for case A2 where data sets over 495 integral eddy turnover times are available. The Taylor microscale based Reynolds number equals $\mathrm{Re}_\lambda = 119$. Later, the effect of Schmidt number variations is examined by means of all cases given in tab. 4.1.

4.2.4 Evaluation of the Generalized Scale-by-scale Energy Budget Equation

It is customary to compensate eq. 4.17 by $\langle\chi\rangle\, r$,

$$\frac{T(r)}{\langle\chi\rangle r} + \frac{P(r)}{\langle\chi\rangle r} + \frac{K(r)}{\langle\chi\rangle r} = \frac{2}{3}\,, \tag{4.19}$$

so that the left hand side sums up to 2/3 for all scales. The terms of eq. 4.19 obtained from the DNS of case A2 are shown in fig. 4.3 as a function of r/η. The budget is well satisfied at all scales, as the compensated production, turbulent transport and diffusive transport terms sum up to 2/3 for all values of r.

Diffusive transport effects are dominant at small and intermediate scales and balance the scalar dissipation $\langle\chi\rangle$ in the limit $r \to 0$. Production of scalar energy is dominant at large scales and decreases toward smaller scales, but influences all scales down to the Kolmogorov scale. At the present Reynolds number, this underlines the

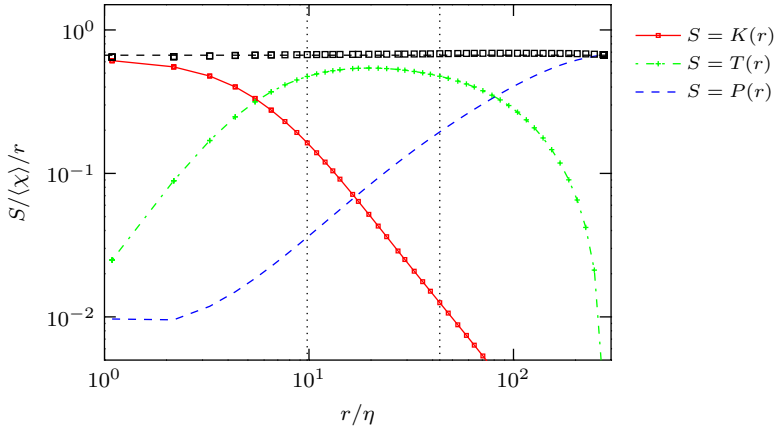

Figure 4.3: Scale-by-scale energy budget obtained from DNS for case A2. All terms are compensated by $\langle\chi\rangle r$. The squares represent the sum of diffusive transport $K(r)/\langle\chi\rangle/r$, turbulent transport $T(r)/\langle\chi\rangle/r$ and production $P(r)/\langle\chi\rangle/r$. For all scales, the terms sum up to 2/3, denoted by the black dashed line. The vertical dotted lines denote the lower and upper bound of the inertial range, respectively.

fact that production has a major contribution to eq. 4.17 and cannot be neglected. However, in the limit of large Reynolds numbers, the contribution of the production term at the small scales will become asymptotically small as it will obey Lumley's $r^{4/3}$ scaling, cf. eq. 4.14. Additionally, due to the moderate Reynolds number, the flow exhibits no clear separation of large and small scales, and either diffusion or production effects exist over the whole range of scales. The plateau of the transport term $T(r)$ represents the inertial range. The extent of the inertial range may be defined as the range within which the compensated transport term is above 90% of its maximum value, analogously to the approach introduced by Jayesh et al. (1994). This results in the inertial range to be in the interval $9.8 \leq r/\eta \leq 43.6$.

In the limit of large Reynolds numbers, the production term $P(r)$ and the diffusive transport term $K(r)$ become negligible in the inertial-convective range for $\eta \ll r \ll l_t$, and we obtain from eq. 4.17

$$\frac{1}{4\pi r^2}\int_{\partial V}\left\langle(\Delta u_i)(\Delta\phi)^2\right\rangle n_i \mathrm{d}\Omega \;\approx -\frac{2}{3}\langle\chi\rangle r\,. \tag{4.20}$$

The term on the left hand side may be interpreted as a spherically averaged longitudinal third order structure function. It equals $-2/3\langle\chi\rangle r$ similar to Yaglom's equation. In eq. 4.20 local isotropy is assumed implicitly by taking the large Reynolds number limit. This equation can also be interpreted as balance for the net transport of scalar energy $\left\langle(\Delta\phi)^2\right\rangle$ across a scale r.

The limiting behavior of eq. 4.17 can be further investigated. The production of $\left\langle(\Delta\phi)^2\right\rangle$ is mainly dominant at large scales, while in the large-scale limit $r \to \infty$ the contribution of $T(r)$ and $K(r)$ disappears. We can hence determine the large-scale limit of the compensated production term as

$$\lim_{r\to\infty} \frac{P(r)}{\langle\chi\rangle r} = \lim_{r\to\infty} \frac{1}{\langle\chi\rangle r} \left[-\frac{1}{4\pi r^2} \int_V 2\Gamma \left\langle (\Delta u_2)(\Delta\phi) \right\rangle \mathrm{d}V \right] . \tag{4.21}$$

For $r \to \infty$ the mixed velocity-scalar moment becomes independent of the separation distance r and approaches the one-point limit

$$\lim_{r\to\infty} \langle (\Delta u_2)(\Delta\phi) \rangle = 2\langle u_2\phi \rangle . \tag{4.22}$$

Hence, we can express the compensated production term as

$$\lim_{r\to\infty} \frac{P(r)}{\langle\chi\rangle r} = \frac{-2\Gamma\langle u_2\phi\rangle}{\langle\chi\rangle} , \tag{4.23}$$

which becomes unity for stationary turbulence as mean production $-2\Gamma\langle u_2\phi\rangle$ equals mean dissipation $\langle\chi\rangle$.

In summary, besides the above physical interpretation, the scalar scale-by-scale energy budget equation is useful to validate DNS data. One-point statistics, which are frequently evaluated, provide only an information about integral quantities. The scalar scale-by-scale energy budget equation is exactly derived from the governing equations, and the fulfillment of the budget validates DNS at each scale r from small scales up to large scales. Additionally, the scale-by-scale energy budget equation includes the one-point statistics in the large scale limit for $r \to \infty$.

4.3 Dependence of the Scale-by-scale Energy Budget on the Schmidt Number

In this section, we examine how the scalar scale-by-scale energy budget is affected by variations of the Schmidt number $\mathrm{Sc} = \nu/D$. To this end, simulations have been conducted with Sc varying by more than one order of magnitude between 0.11 and 5.56, while keeping the velocity field statistically constant. The smallest scale of the scalar field is the Batchelor length scale η_B which is related to the Kolmogorov length scale η by $\eta_B = \mathrm{Sc}^{-1/2}\eta$. Therefore, for $\mathrm{Sc} > 1$, $\eta_B < \eta$, the scalar field reveals smaller length scales than the velocity field. The normalized spectra of the scalar variance are shown in fig. 4.4. According to Obukhov (1949a) and Corrsin (1951) the scalar spectrum can be written for scales within the inertial-convective subrange as

$$E_\phi(\kappa) = C_{\mathrm{OC}}\varepsilon^{-1/3}\chi\kappa^{-5/3} , \tag{4.24}$$

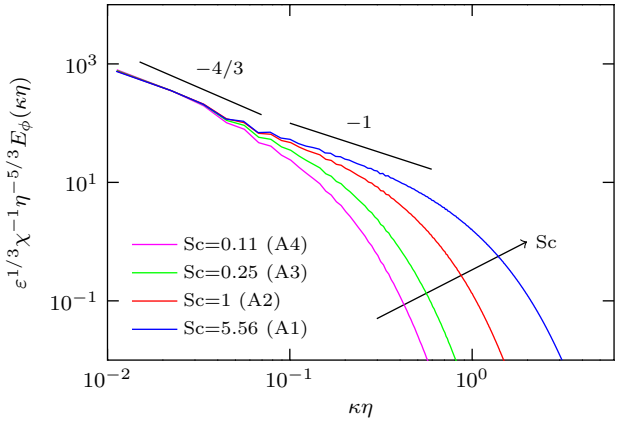

Figure 4.4: Normalized three-dimensional scalar energy spectra scaled by Kolmogorov variables for Schmidt numbers ranging from 0.11 to 5.56 (cases A1 to A4 in tab. 4.1). The spectra collapse in the inertial-convective range, revealing a $\kappa^{-4/3}$ scaling. For the largest Schmidt number, a viscous-convective range with a scaling of κ^{-1} emerges.

where C_{OC} is the Obukhov-Corrsin constant. However, fig. 4.4 shows that the scaling exponent within the inertial-convective subrange is close to $-4/3$. The depature of the scaling exponent from the prediction by eq. 4.24 originates from the imposed mean scalar gradient that breaks isotropy, cf. Watanabe and Gotoh (2007b), Yeung et al. (2002) and Yeung et al. (2005). For weakly diffusive scalars with $\mathrm{Sc} > 1$, in the so-called viscous-convective range $\eta^{-1} \ll \kappa \ll \eta_B^{-1}$, the scaling exponent is close to -1. Here, the scalar spectrum takes the form

$$E_\phi(\kappa) = C_B \chi (\nu/\varepsilon)^{1/2} \kappa^{-1}\,, \tag{4.25}$$

where C_B is the Batchelor constant, cf. Batchelor (1959). In order to clearly observe this feature, a sufficient scale separation between η and η_B is necessary. For $\mathrm{Sc} = 5.56$, fig. 4.4 suggests that a κ^{-1} scaling regime begins to emerge.

The corresponding compensated scalar scale-by-scale energy budget is shown in fig. 4.5 for the investigated range of Schmidt numbers. The compensated diffusive transport terms $K(r)$ and the compensated turbulent transport terms $T(r)$ are shown in fig. 4.5a. The separation distance r is normalized by η_B, which makes the diffusive transport terms collapse at the small scales. Additionally, fig. 4.5b shows the compensated production terms $P(r)$ and the compensated turbulent transport terms $T(r)$, where the separation distance r is now normalized by the integral length scale l_t, defined as

$$l_t = \frac{3\pi}{4} \frac{\int \kappa^{-1} E(\kappa) \mathrm{d}\kappa}{\int E(\kappa) \mathrm{d}\kappa} \,. \tag{4.26}$$

The normalization by l_t makes the curves of the compensated production term, as large scale quantities, collapse. The compensated turbulent transport term $T(r)$ strongly depends on the Schmidt number and exhibits a plateau region, as shown in fig. 4.5a and 4.5b. The width of the plateau increases with the Schmidt number, and the transport term approaches the 2/3-line, which is in agreement with Yaglom's limiting result, for the largest Peclet number of 662. Figure 4.5b shows additionally that with increasing Schmidt number the width of the plateau increases toward the small scales and an emerging overlap with the dissipative scales of the velocity field can be observed for the $\mathrm{Sc} = 5.56$ case. In order to illustrate the distribution of different scales, fig. 4.5b displays the Kolmogorov length scale η, the Taylor microscale λ, the interal length scale l_t, as well as the microscale of the scalar fields λ_ϕ. The latter is defined as

$$\lambda_\phi = \sqrt{6D \frac{\langle \phi^2 \rangle}{\langle \chi \rangle}} \,. \tag{4.27}$$

4.4 Scale-by-scale Energy Budget Equation for Coarse-grained Fields and LES

The scale-by-scale energy budget equation can be used in the context of Large-Eddy Simulation to study how the dynamics of the scalar field are altered by filtering the governing equations. The filtered transport equation of the passive scalar fluctuation ϕ for the case considered here reads

$$\frac{\partial \overline{\phi}}{\partial t} + \overline{u}_i \frac{\partial \overline{\phi}}{\partial x_i} = D \frac{\partial^2 \overline{\phi}}{\partial x_i^2} - \overline{u}_2 \mathcal{G} - \frac{\partial \tau_i}{\partial x_i} \,, \tag{4.28}$$

where filtering is denoted by an overbar and the scalar subgrid flux is defined by $\tau_i = \overline{u_i \phi} - \overline{u}_i \overline{\phi}$. The scalar subgrid flux τ_i is unclosed and has to be modeled to close eq. 4.28. The details of the LES which have been conducted in this work as well as the models applied to close the subgrid terms, are given below. First, the generalized energy budget equations will be extended to the context of LES.

4.4.1 Derivation of the Equation

By following the same steps as in the derivation of eq. 4.17, an equation for the second moment of the filtered scalar increment $\left\langle (\Delta \overline{\phi})^2 \right\rangle = \langle (\overline{\phi}(\boldsymbol{x} + \boldsymbol{r}) - \overline{\phi}(\boldsymbol{x}))^2 \rangle$ can be derived

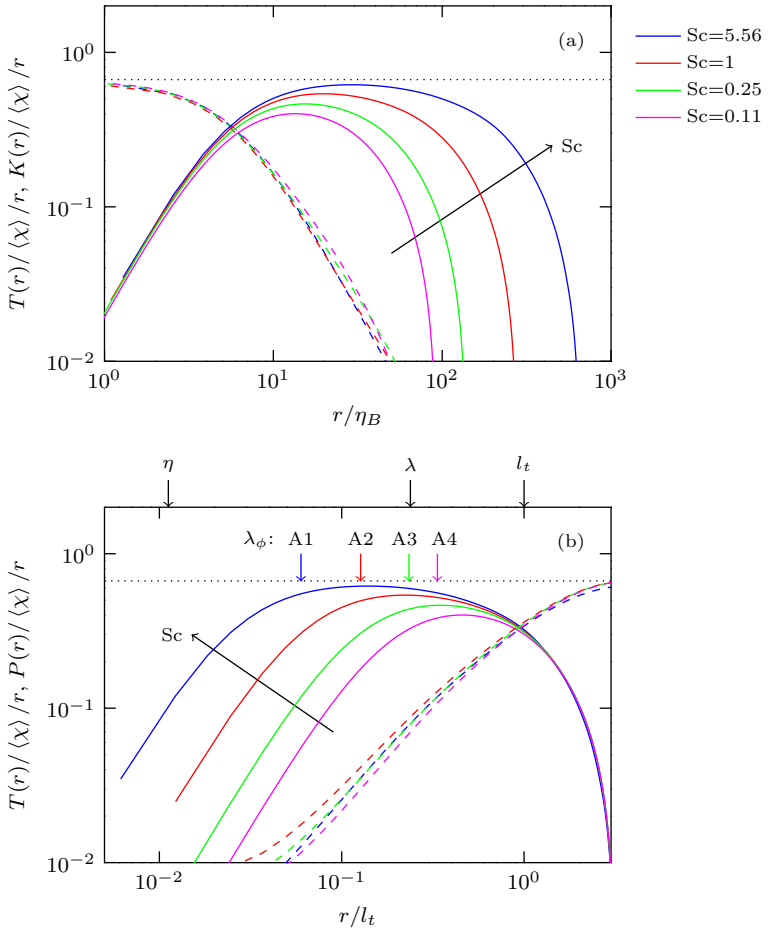

Figure 4.5: Dependence of the terms of eq. 4.17 compensated with $\langle\chi\rangle r$ on the Schmidt number. The compensated diffusive transport terms (a, dashed lines) collapse when the separation distance is normalized with the Batchelor length scale η_B. The compensated production terms (b, dashed lines) collapse when the separation distance is normalized with the integral length scale l_t. The compensated transport terms (a and b, solid lines) show a strong dependence on the Schmidt number. The transport terms either collapse on the small-scales (a) or on the large-scales (b). The colored arrows denote the microscale of the scalar field defined as $\lambda_\phi = \left(6D\langle\phi^2\rangle/\langle\chi\rangle\right)^{1/2}$.

$$\begin{aligned}&\frac{\partial}{\partial t}\big\langle(\Delta\overline{\phi})^2\big\rangle(\boldsymbol{r})+\frac{\partial}{\partial r_i}\big\langle(\Delta\overline{u}_i)(\Delta\overline{\phi})^2\big\rangle(\boldsymbol{r})+2G\big\langle(\Delta\overline{u}_2)(\Delta\overline{\phi})\big\rangle(\boldsymbol{r})\\ =&2D\frac{\partial^2}{\partial r_i^2}\big\langle(\Delta\overline{\phi})^2\big\rangle(\boldsymbol{r})-\underbrace{4D\big\langle\frac{\partial\overline{\phi}}{\partial x_i}\frac{\partial\overline{\phi}}{\partial x_i}\big\rangle}_{2\langle\overline{\chi}\rangle}-\left[\big\langle 2(\Delta\overline{\phi})\frac{\partial\tau_i'}{\partial x_i'}-2(\Delta\overline{\phi})\frac{\partial\tau_i}{\partial x_i}\big\rangle(\boldsymbol{r})\right],\end{aligned}\tag{4.29}$$

which corresponds to eq. 4.11, but has the additional term on the right hand side in the square brackets which accounts for the scalar subgrid flux. This term can be split into a subgrid transport term and a subgrid dissipation according to

$$\big\langle 2(\Delta\overline{\phi})\frac{\partial\tau_i'}{\partial x_i'}-2(\Delta\overline{\phi})\frac{\partial\tau_i}{\partial x_i}\big\rangle=\underbrace{2\frac{\partial}{\partial r_i}\big\langle(\Delta\overline{\phi})(\tau_i'+\tau_i)\big\rangle}_{=f(\boldsymbol{r}),\text{ subgrid transport}}-\underbrace{4\big\langle\tau_i\frac{\partial\overline{\phi}}{\partial x_i}\big\rangle}_{\neq f(\boldsymbol{r})}.$$

The first term on the right hand side represents the scalar subgrid transport which depends on the separation vector $\boldsymbol{r}$, and the second term represents the scalar subgrid dissipation which is defined as

$$\big\langle\chi_{\text{sgs}}\big\rangle=2\big\langle\tau_i\frac{\partial\overline{\phi}}{\partial x_i}\big\rangle.\tag{4.30}$$

The scalar subgrid dissipation is associated with the subgrid scales and is not resolved at the given filter width. On the other hand, the resolved scalar dissipation in eq. 4.29, which is associated with the large scales, is defined as

$$\big\langle\overline{\chi}\big\rangle=2D\big\langle\frac{\partial\overline{\phi}}{\partial x_i}\frac{\partial\overline{\phi}}{\partial x_i}\big\rangle.\tag{4.31}$$

This term represents that part of the scalar dissipation which is directly resolved on the specified grid. The sum of eqs. 4.30 and 4.31 is the total scalar dissipation $\big\langle\chi_{tot}\big\rangle=\big\langle\chi_{\text{sgs}}+\overline{\chi}\big\rangle$.

The subgrid transport term describes the average transport of scalar energy at scale r toward small scales. Two limits of the subgrid transport term can be investigated for very large and very small separation distances. For very large values of r, the subgrid transport term vanishes

$$\lim_{r\to\infty}2\frac{\partial}{\partial r_i}\big\langle(\Delta\overline{\phi})(\tau_i'+\tau_i)\big\rangle=\lim_{r\to\infty}2\frac{\partial}{\partial r_i}\big\langle\overline{\phi}'\tau_i'+\overline{\phi}'\tau_i-\overline{\phi}\tau_i'-\overline{\phi}\tau_i\big\rangle=0,$$

where the last equality follows from homogeneity and the decorrelation of two-point quantities for large r. This implies that large scales are not affected by filtering. In the small scale limit, $r\to 0$, the subgrid transport term can be written as

$$\lim_{r\to 0} 2D\frac{\partial}{\partial r_i}\Big\langle(\Delta\overline{\phi})(\tau_i'+\tau_i)\Big\rangle = \lim_{r\to 0} 2D\Big\langle\frac{\partial}{\partial r_i}\left[\frac{\partial\overline{\phi}}{\partial x_j}r_j(\tau_i'+\tau_i)\right]\Big\rangle$$
$$= 4D\Big\langle\frac{\partial\overline{\phi}}{\partial x_j}\tau_j\Big\rangle = 2\Big\langle\chi_{\mathrm{sgs}}\Big\rangle\,,$$

and hence balances the subgrid dissipation $\big\langle\chi_{\mathrm{sgs}}\big\rangle$. The same analysis can be conducted for the diffusive transport term. In the large scale limit, $r\to\infty$, the diffusive transport terms vanishes as the filtered increment $\langle(\Delta\overline{\phi})^2\rangle$ becomes independent of r. In the limit $r\to 0$ we obtain

$$\lim_{r\to 0} 2D\frac{\partial^2}{\partial r_i^2}\Big\langle(\Delta\overline{\phi})^2\Big\rangle = 4D\Big\langle\left(\frac{\partial\overline{\phi}}{\partial x_i}\right)^2\Big\rangle = 2\Big\langle\overline{\chi}\Big\rangle$$

which reveals that the diffusive transport term equals the resolved dissipation $\big\langle\overline{\chi}\big\rangle$ at small scales. Summarizing, in the small scale limit, $r\to 0$, the subgrid transport term and the diffusive transport term approach the one-point limit which equals the subgrid dissipation and the resolved dissipation, respectively.

By spherical integration of eq. 4.29 we obtain the generalized scale-by-scale energy budget equation for LES

$$\underbrace{-\frac{1}{4\pi r^2}\int_{\partial V}\Big\langle(\Delta\overline{u}_i)(\Delta\overline{\phi})^2\Big\rangle n_i\mathrm{d}\Omega}_{\overline{T}(r)}\ \underbrace{-\frac{1}{4\pi r^2}\int_V 2\Gamma\Big\langle(\Delta\overline{u}_2)(\Delta\overline{\phi})\Big\rangle\mathrm{d}V}_{\overline{P}(r)}$$
$$\underbrace{+2D\frac{\mathrm{d}}{\mathrm{d}r}\left[\frac{1}{4\pi r^2}\int_{\partial V}\Big\langle(\Delta\overline{\phi})^2\Big\rangle\mathrm{d}\Omega\right]}_{\overline{K}(r)}$$
$$\underbrace{-\frac{1}{4\pi r^2}\int_{\partial V}2\Big\langle(\Delta\overline{\phi})(\tau_i(\boldsymbol{x})+\tau_i(\boldsymbol{x}+\boldsymbol{r}))\Big\rangle n_i\mathrm{d}\Omega}_{\overline{T}_{\mathrm{sgs}}(r)} \tag{4.32}$$
$$= \frac{2}{3}(\underbrace{\Big\langle\overline{\chi}\Big\rangle+\Big\langle\chi_{\mathrm{sgs}}\Big\rangle}_{\big\langle\chi_{\mathrm{tot}}\big\rangle})r\,.$$

This equation for the second moment of the filtered scalar increment $\big\langle(\Delta\overline{\phi})^2\big\rangle$ corresponds to eq. 4.17. Compared to eq. 4.17, filtering introduces on the left hand side the subgrid transport term

$$\overline{T}_{\mathrm{sgs}} = -\frac{1}{4\pi r^2}\int_{\partial V}2\Big\langle(\Delta\overline{\phi})(\tau_i(\boldsymbol{x})+\tau_i(\boldsymbol{x}+\boldsymbol{r}))\Big\rangle n_i\mathrm{d}\Omega\,, \tag{4.33}$$

which compensates the change of the turbulent transport term $\overline{T}(r)$ and the diffusive transport term $\overline{K}(r)$ due to filtering at scales smaller than the filter width. This effect will be further discussed below.

The filtered energy budget equation, eq. 4.32, will be evaluated both in an *a-priori* and an *a-posteriori* analysis. For the *a-priori* analysis, the DNS data need to be filtered explicitly. For consistency, the same filter function and filter width are used as in the *a-posteriori* analysis, in which the actual LES results are compared with filtered DNS data. As this filter width is closely related to the grid spacing of the LES, the setup of the LES is discussed first, followed by the *a-priori* and *a-posteriori* analyses.

4.4.2 Large-Eddy Simulation

Large-Eddy Simulations of cases A2 and A3, cf. tab. 4.1, have been conducted and are compared to the corresponding DNS in the following sections. First, the parameters of the LES and the employed models are specified, and fundamental statistics are presented. Subsequently, the scalar energy budget is discussed in the context of LES according to the theory derived above.

The filtered governing equations are not closed and require modeling. The momentum equation is closed in spectral space by adopting the EDQNM model, cf. Métais and Lesieur (1992) and Lesieur and Metais (1996), which is well tested and commonly used for homogeneous isotropic turbulence. The scalar subgrid flux τ_i in the transport equation for the filtered scalar fluctuations $\overline{\phi}$, eq. 4.28, is modeled by the gradient flux approximation which states that

$$\tau_i = -\frac{\nu_{\mathrm{sgs}}}{\mathrm{Sc}_{\mathrm{sgs}}} \frac{\partial \overline{\phi}}{\partial x_i} \,, \tag{4.34}$$

where ν_{sgs} is the subgrid viscosity and $\mathrm{Sc}_{\mathrm{sgs}}$ is the subgrid Schmidt number taken as unity. The subgrid viscosity ν_{sgs} is calculated by the Smagorinsky model, cf. Smagorinsky (1963), where the Smagorinsky constant is chosen as 0.17 similar to values suggested in the literature, cf. Meneveau and Katz (2000) and Sagaut (2006).

As stated above, and similar to Yaglom's equation, eqs. 4.29 and 4.32 are not closed because of the triple correlation that arises due to the statistical approach. In addition, filtering introduces the subgrid transport term

$$2\Big\langle (\Delta\overline{\phi})(\tau_i' + \tau_i) \Big\rangle \,, \tag{4.35}$$

which also requires closure in terms of the resolved quantities, namely $\Big\langle (\Delta\overline{\phi})^2 \Big\rangle$. Closure of the subgrid transport term can be achieved by inserting eq. 4.34 into eq. 4.35, which yields

$$2\Big\langle (\Delta\overline{\phi})(\tau_i' + \tau_i) \Big\rangle = -2\Big\langle (\Delta\overline{\phi}) \frac{1}{\mathrm{Sc}_{\mathrm{sgs}}} \left(\nu_{\mathrm{sgs}}' \frac{\partial \overline{\phi}'}{\partial x_i'} + \nu_{\mathrm{sgs}} \frac{\partial \overline{\phi}}{\partial x_i} \right) \Big\rangle \,. \tag{4.36}$$

We now assume that the subgrid viscosity ν_{sgs} is not correlated with $\partial\overline{\phi}/\partial x_i$ or $\Delta\overline{\phi}$, and we can hence rewrite eq. 4.36 as

$$\begin{aligned} 2\big\langle(\Delta\overline{\phi})(\tau_i' + \tau_i)\big\rangle &= -2\big\langle\frac{\nu_{\mathrm{sgs}}}{\mathrm{Sc}_{\mathrm{sgs}}}\big\rangle\big\langle(\Delta\overline{\phi})\left(\frac{\partial\overline{\phi}'}{\partial x_i'} + \frac{\partial\overline{\phi}}{\partial x_i}\right)\big\rangle \\ &= -2\left[\big\langle\frac{\nu_{\mathrm{sgs}}}{\mathrm{Sc}_{\mathrm{sgs}}}\big\rangle\frac{\partial\big\langle(\Delta\overline{\phi})^2\big\rangle}{\partial r_i}\right], \end{aligned} \tag{4.37}$$

where the chain rule and the transformation into the correlation coordinate r_i (eqs. 4.7 and 4.8) are used in the last step. This result can be inserted into eq. 4.32 and yields

$$\begin{aligned} &-\frac{1}{4\pi r^2}\int_{\partial V}\big\langle(\Delta\overline{u}_i)(\Delta\overline{\phi})^2\big\rangle n_i\mathrm{d}\Omega - \frac{1}{4\pi r^2}\int_V 2\Gamma\big\langle(\Delta\overline{u}_2)(\Delta\overline{\phi})\big\rangle\mathrm{d}V \\ &+2\frac{\mathrm{d}}{\mathrm{d}r}\left[\frac{D+\nu_{\mathrm{sgs}}/\mathrm{Sc}_{\mathrm{sgs}}}{4\pi r^2}\int_{\partial V}\big\langle(\Delta\overline{\phi})^2\big\rangle\mathrm{d}\Omega\right] = \frac{2}{3}\big\langle\chi_{\mathrm{r}} + \chi_{\mathrm{sgs}}\big\rangle r\,. \end{aligned} \tag{4.38}$$

Comparing this equation for $\langle(\Delta\overline{\phi})^2\rangle$ with the generalized Yaglom equation for $\langle(\Delta\phi)^2\rangle$, eq. 4.17, reveals an identical structure. Filtering introduces only an additional contribution to the diffusive transport term and to the dissipation term, which can be both expressed in terms of the subgrid diffusivity $\nu_{\mathrm{sgs}}/\mathrm{Sc}_{\mathrm{sgs}}$ only. The suggested model for the subgrid transport term will be validated in an *a-priori* test in the next section.

Large-Eddy Simulations are conducted in a cubic domain of size 2π based on the pseudo-spectral method described above, complemented by the corresponding LES models. The most important parameter that characterizes the LES is the filter width Δ_f in real space or the cutoff wave number κ_c in spectral space, which are implicitly defined by the grid spacing and the used dealiasing filter. The LES results are compared to the corresponding DNS data in an *a-posteriori* test. Because by LES only a filtered flow representation is obtained, we cannot compare this directly to the DNS. Therefore, the DNS data have to be filtered in an appropriate way to provide a proper reference. Ideally, both filter kernels should be identical. However, for LES the grid spacing induces an implicit filter whose mathematical form is unknown, while the DNS data have to be filtered explicitly with a specified filter function. Explicit filtering takes place in spectral space by multiplication with a filter kernel $\widehat{G}(\boldsymbol{\kappa})$ and reads for an arbitrary variable ψ

$$\widehat{\overline{\psi}}(\boldsymbol{\kappa}) = \widehat{G}(\boldsymbol{\kappa})\widehat{\psi}(\boldsymbol{\kappa})\,, \tag{4.39}$$

where $\widehat{\psi}$ denotes the spectral representation of ψ, and $\boldsymbol{\kappa}$ is the wavenumber vector. A Gaussian filter kernel

$$\widehat{G}(\boldsymbol{\kappa}) = \exp\left(-\frac{\Delta_f^2\kappa^2}{4\,\gamma}\right) \tag{4.40}$$

Table 4.2: Global flow and scalar quantities of the DNS, filtered DNS and LES for the cases A2 (Sc = 1.0) and A3 (Sc = 0.25) defined in tab. 4.1. As the Reynolds number is kept constant, the turbulent kinetic energy $\langle k \rangle$ and its dissipation $\langle \varepsilon \rangle$ are statistically identical for both cases, while the scalar quantities vary with the Schmidt number.

	Case A2 (Sc = 1.0)			Case A3 (Sc = 0.25)		
	DNS	$\text{DNS}_{\text{filt.}}$	LES	DNS	$\text{DNS}_{\text{filt.}}$	LES
N	512	512	64	512	512	64
Re_λ	119	-	-	119	-	-
$\langle k \rangle$	11.12	10.11	10.72	11.12	10.11	10.72
$\langle \varepsilon \rangle$	10.31	-	-	10.31	-	-
$\langle \overline{\varepsilon} \rangle$	-	4.15	3.63	-	4.15	3.63
$\langle \chi \rangle$	3.86	-	-	3.77	-	-
$\langle \overline{\chi} \rangle$	-	0.91	0.97	-	1.95	2.11
$\langle \chi_{\text{sgs}} \rangle$	-	2.75	2.79	-	1.67	1.57
$\langle \overline{\chi} \rangle + \langle \chi_{\text{sgs}} \rangle$	3.77	3.66	3.76	3.77	3.62	3.68
$-2\Gamma \langle u_2 \phi \rangle$	3.98	3.81	3.76	3.89	3.75	3.68
$\langle \phi^2 \rangle$	1.89	1.62	1.71	1.56	1.45	1.54

is used with γ equal to 6, as suggested in the literature, cf. Fröhlich (2006). The Gaussian filter is local in real and spectral space but does not provide a sharp cut-off between scales, cf. Sagaut (2006). The DNS is conducted on a grid with 512 grid points in each direction, and the LES is conducted with 64 grid points in each direction. This yields a filter width $\Delta_f = 0.147$ and a cut-off wavenumber $\kappa_c = 21.33$ corresponding to $\Delta_f / \eta = 13.13$.

Table 4.2 gives an overview of mean quantities for DNS, filtered DNS and LES. The LES resolves more than 96 % of the turbulent kinetic energy $\langle k \rangle$ and more than 90 % of the scalar variance $\langle \phi^2 \rangle$, which is both clearly above the lower limit of 80 % stated for well resolved LES, cf. Pope (2000). The resolved scalar dissipation, $\langle \overline{\chi} \rangle$, agrees very well between filtered DNS and LES and it sums up together with the subgrid dissipation $\langle \chi_{\text{sgs}} \rangle$ to the total dissipation within a statistical error. As a large scale quantity, the production term $-2\Gamma \langle u_2 \phi \rangle$ is virtually unaffected by filtering.

The velocity energy spectrum and the scalar energy spectrum are shown in fig. 4.6 for DNS, filtered DNS and LES. The velocity energy spectrum reveals a $\kappa^{-5/3}$ scaling while the scalar energy spectrum reveals a $\kappa^{-4/3}$ scaling. The origin for the lower scaling exponent of the scalar energy spectrum is discussed in sec. 4.3. The spectra show a very good agreement between DNS, filtered DNS and LES for scales larger than the cutoff length indicating that the LES results represent the resolved scales correctly. As the energy contained in the smaller, unresolved scales is not contained in the filtered representation of the flow, the spectra of the LES and

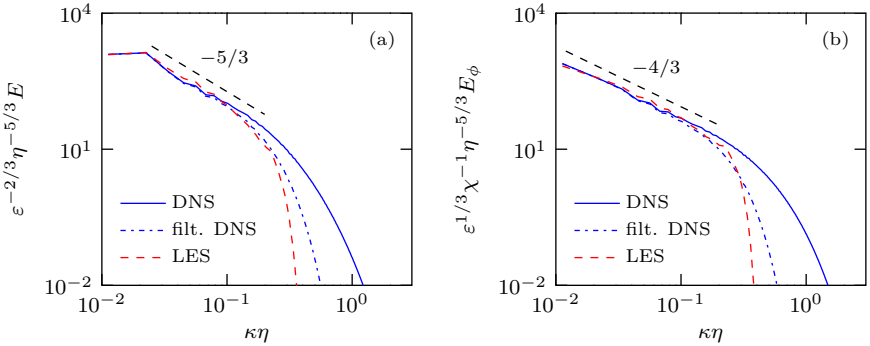

Figure 4.6: Normalized three-dimensional velocity (a) and scalar (b) energy spectra computed from the DNS, filtered DNS and LES data of case A2 (Sc = 1.0). The velocity spectrum reveals the well known $\kappa^{-5/3}$ scaling, while the scalar spectrum reveals a $\kappa^{-4/3}$ scaling induced by the mean scalar gradient. The LES correctly reproduces the large scales, and it is in good agreement with the filtered DNS.

filtered DNS decrease rapidly close to the cutoff wavenumber. The small deviation of the LES from the filtered DNS at small scales is due to the deviation of the implicit filter function induced by the LES grid from the Gaussian filter kernel which has been used to filter the DNS.

4.4.3 A-priori Analysis of the LES Budget

The equation for the filtered scalar increment $\langle \Delta\overline{\phi} \rangle$, eq. 4.32, is first evaluated by means of an *a-priori* analysis. Figure 4.7 shows, for the filtered DNS of case A2, the production term $\overline{P}(r)$, turbulent transport term $\overline{T}(r)$, diffusive transport term $\overline{K}(r)$, and subgrid transport term $\overline{T}_{\text{sgs}}(r)$. The terms are compensated by $\langle \chi_{tot} \rangle r$ such that they sum up to 2/3. As the sum of the four compensated terms reaches this theoretical value within an error of less than 2.5%, the budget is very well satisfied for all scales. A more detailed discussion how the different terms are altered in the filtered solution compared to the DNS follows in the next section in the context of an *a-posteriori* analysis.

The second objective of this *a-priori* analysis is the validation of the model for the subgrid transport term, which was proposed in the previous section. This can be done by comparing the exact subgrid term $\overline{T}_{\text{sgs}}$ obtained by filtered DNS, eq. 4.35, with the modeled subgrid term by eq. 4.37. The latter will be denoted as $\overline{T}_{\text{sgs}}^{\text{mod}}$. Both terms are shown in fig. 4.8 in compensated form. For this *a-priori* test, the subgrid viscosity is obtained from the filtered velocity field by

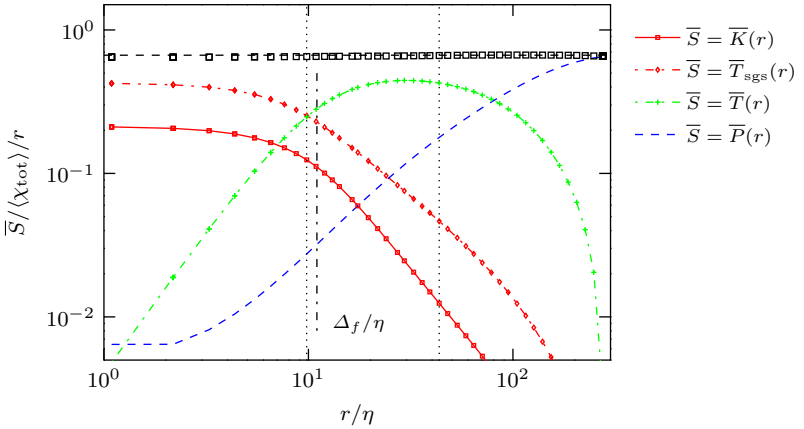

Figure 4.7: Filtered scale-by-scale energy budget from DNS (*a-priori*) of case A2 (Sc = 1.0), normalized by η and compensated by $\langle\chi\rangle r$. The squares represent the sum of diffusive transport $\overline{K}(r)$, subgrid transport $\overline{T}_{\rm sgs}(r)$, turbulent transport $\overline{T}(r)$ and production $\overline{P}(r)$. All terms sum up to 2/3 (black dashed line) revealing that the budget is well satisfied for all r. The vertical dotted lines denote the lower and upper bounds of the inertial range, respectively. The vertical dashed-dotted line denotes the filter width $\Delta_f/\eta = 13.13$.

$$\nu_{\rm sgs} = -\frac{1}{2}\frac{\langle\tau_{ij}\overline{s}_{ij}\rangle}{\langle\overline{s}_{ij}\overline{s}_{ij}\rangle}\,, \tag{4.41}$$

where $\tau_{ij} = \overline{u_i u_j} - \overline{u}_i\overline{u}_j$, and $\overline{s}_{ij}$ is the filtered strain rate tensor. A good agreement can be observed, particularly for small r where the subgrid transport term is large. This result justifies the closure of the subgrid transport term by a gradient flux assumption and, additionally, the decorrelation assumption from eq. 4.36 to eq. 4.37.

4.4.4 A-posteriori Anlysis of the LES Budget and its Single Terms

Now, eq. 4.32 is evaluated in an *a-posteriori* analysis using the LES calculations described above. For case A2 (Sc = 1.0), the four terms of the filtered budget as well as their sum are shown in fig. 4.9 in the same compensated form as in the previous section. The smallest separation length r is equal to the grid spacing, resulting in the LES curves starting at higher values due to the coarser grid, which has only 64 grid points in each direction compared to 512 grid points in the DNS. Hence, fig. 4.9 corresponds to the part of fig. 4.7 which is right of the vertical line indicating the filter width of the LES. Also in the *a-posteriori* case, the budget is very well satisfied as the terms sum up to the theoretical value of 2/3 for all scales.

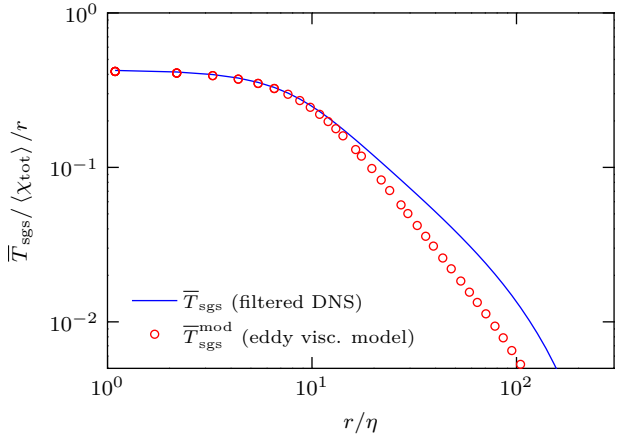

Figure 4.8: Comparison of the compensated subgrid transport term for case A2 obtained from filtered DNS (eq. 4.35, blue line) and obtained by modeling the subgrid flux by an eddy viscosity approach (eq. 4.37, red circles).

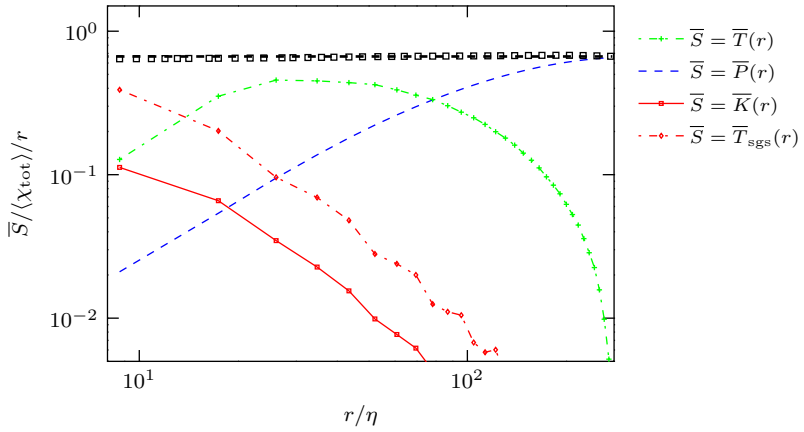

Figure 4.9: Filtered scale-by-scale energy budget from LES (*a-posteriori*) of case A2 (Sc = 1.0). The compensation of the terms as well as the meaning of the curves are the same as in fig. 4.7. The budget begins at larger values of the separation distance r due to the coarser grid used in the LES. Also in the *a-posteriori* case, the terms sum up to the theoretical value of 2/3 for all scales.

Let us now discuss each term separately. Figure 4.10 illustrates the terms of the budget for DNS, filtered DNS and LES in compensated form and shows how the terms are altered due to the filtering. The results from LES and filtered DNS agree very well for all four terms and for all length scales, indicating that the energy flux between large and small scales is correctly captured by the employed LES models.

The production term $\overline{P}(r)$, shown in fig. 4.10c, is monotonically increasing in r/η and dominates the energy budget for large scales. As a large scale quantity it is almost unaffected by filtering and well reproduced by the LES. Figure 4.10a depicts the turbulent transport term $\overline{T}(r)$, which quantifies the energy flux across a specific scale r, i.e. the energy which is fed on average from scales larger than r to scales smaller than r. The width of the plateau, which can be observed in the DNS curve, represents the inertial range. Filtering drastically changes the transport at small and intermediate scales and reduces the width of the plateau. Thus, the energy flux cannot be sustained by the transport term alone. It has to be supported by the subgrid transport term $\overline{T}_{\mathrm{sgs}}(r)$, which is shown in fig. 4.10b. The subgrid transport term is only present in filtered DNS and LES and represents the scalar energy transfer from resolved to unresolved scales. This is the principal task of the LES model. A good agreement between filtered DNS and LES reveals that the subgrid transport is well satisfied in the present LES. The diffusive transport term $\overline{K}(r)$ is mainly present at small scales, where it dominates the energy budget, cf. fig. 4.10d. Filtering the DNS data substantially reduces the diffusive transport term at small scales, as the filtered flow representation does not account for the effect of the now unresolved scales. It is supported by the subgrid transport term $\overline{T}_{\mathrm{sgs}}(r)$ in order to satisfy the budget for $r \to 0$.

4.4.5 Schmidt Number Analysis

While an evaluation of the equation for the LES scalar energy budget as well as a term-by-term analysis have been performed for the unity Schmidt number case A2 in the previous two sections, a Schmidt number variation has also been carried out for the LES, and the results of case A3 ($\mathrm{Sc} = 0.25$) are discussed in this section. Figure 4.11 shows the four terms of the budget for DNS, filtered DNS and LES in the same compensated form that was employed in fig. 4.10. For all terms, the results obtained from LES and filtered DNS agree very well for all scales, implying that also the overall budget (not shown here) is very well satisfied. As the effect of the Schmidt number on the production, turbulent transport and diffusive transport terms has already been discussed above for the DNS, the focus is here on how the effect of the filtering and the contribution of the subgrid transport term are altered with varying Schmidt number.

As has been pointed out previously, the production term $\overline{P}(r)$, shown in fig. 4.11c, is virtually unaffected by the Schmidt number as well as by the filtering. In fig.

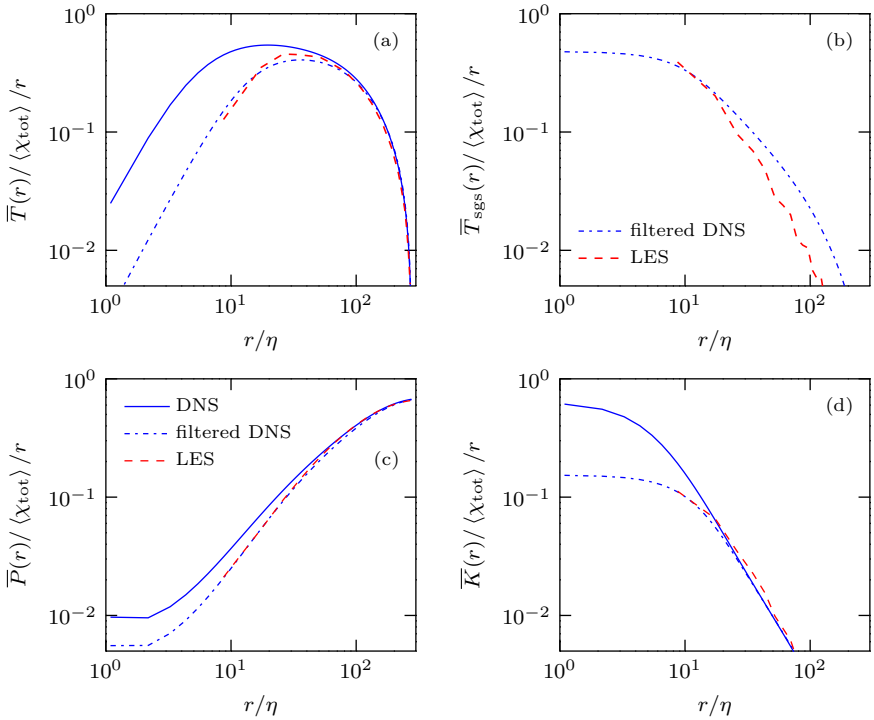

Figure 4.10: Term-by-term comparison of the compensated terms involved in the filtered energy budget equation, eq. 4.32, for case A2 (Sc = 1.0). The turbulent transport (a), production (c) and diffusion (d) terms are obtained from the DNS, filtered DNS and LES, while the subgrid transport term (b) is only available in the filtered DNS and LES. All terms obtained from the LES are in very good agreement with the filtered DNS data. Compared to the DNS, the turbulent transport and diffusion terms are reduced in the LES at small scales, which is compensated by the existence of the subgrid transport term.

4.5a, the turbulent transport term $T(r)$ was shown as a function of the separation distance normalized by the Batchelor length scale η_B, resulting in the curves for the various Schmidt numbers to collapse at the small scales. It was observed that the extent of the inertial range decreases with decreasing Schmidt number. The same effect can be seen when comparing fig. 4.11a with fig. 4.10a, which show the turbulent transport term $\overline{T}(r)$ for $\mathrm{Sc} = 1.0$ and $\mathrm{Sc} = 0.25$, respectively. Here, the separation distance is normalized with the Kolmogorov length scale η, which makes the curves collapse at the large scales. Compared to the unity Schmidt number case, the relative contribution of the turbulent transport term at scales smaller than the filter width is reduced for smaller Schmidt numbers, because the size of the smallest scalar length scale increases due to the higher diffusivity. The same argument can be used to explain the smaller deviation of the filtered diffusion term $\overline{K}(r)$ from the diffusion term obtained from DNS for the $\mathrm{Sc} = 0.25$ case, cf. fig. 4.11d, compared to the unity Schmidt number case, cf. fig. 4.10d. However, the extent of the range where the diffusion term dominates the budget increases with decreasing Schmidt number due to the higher diffusivity.

As a result, the subgrid transport term $\overline{T}_{\mathrm{sgs}}(r)$, which is depicted in fig. 4.11b, and thereby the importance of the subgrid model, are reduced for the smaller Schmidt number case. For the unity Schmidt number case, the smallest scalar scales are so small compared to the filter width that almost the whole contribution of the turbulent transport and diffusive transport terms at the smallest scales is lost due to the filtering. Hence, the subgrid transport term, which has to compensate this, dominates the filtered budget at the smallest scales. This is no longer the case for the $\mathrm{Sc} = 0.25$ case, in which the diffusive transport term and the subgrid transport term are of the same order at the smallest scales, cf. figs. 4.11b and 4.11d.

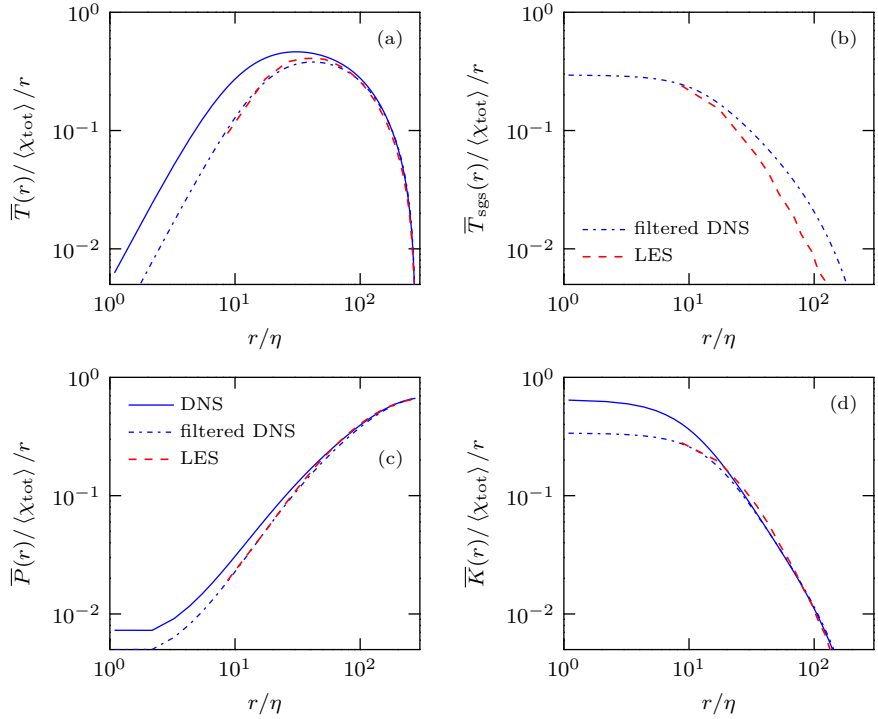

Figure 4.11: Term-by-term comparison of the compensated terms involved in the filtered energy budget equation, eq. 4.32, for case A3 (Sc = 0.25). The order of the terms and the meaning of the lines is the same as in fig. 4.10.

5 Decomposition of Turbulent Fields by the Method of "Turbulent Line Segments"

5.1 Introduction

In the course of this chapter we will examine turbulent scalar fields based on a physically motivated decomposition, where the signal along a straight line is decomposed into relatively simple sub-units, the so-called turbulent line segments. By this novel decomposition the complexity of the signal can be reduced and it is possible to relate the two-point statistics of these sub-units to the two-point statistics of the whole signal. Wang (2008) pointed out that a suitable method to decompose the turbulent field should be self-contained and fulfill two properties, namely completeness and uniqueness. The former means that each material point should be included once and only once in a decomposed sub-unit and the latter means that the decomposition should be non-arbitrary.

We propose to decompose the turbulent signal of a passive scalar ϕ along a straight line into piece-wise monotonously increasing or decreasing line segments. The segments start at a local minimum point and end at a local maximum point or vice versa and can be understood as a one-dimensional version of a dissipation element (DE), cf. Wang and Peters (2006, 2008), where the ending points are local extrema along the straight line. The introduced decomposition of the scalar field is self-contained and generates statistics at an intermediate scale.

Turbulent line segments (TLS) are parameterized by the length ℓ and the scalar difference $\Delta\phi$ between the end and start point, cf. fig. 5.1. Depending on the sign of $\Delta\phi$, there exist positive (increasing) or negative (decreasing) segments. A joint probability density function of ℓ and $\Delta\phi$ provides most information necessary to statistically reconstruct the scalar field. The two parameters ℓ and $\Delta\phi$ are statistically not independent. Additionally, fig. 5.1 depicts the mean gradient $g = \Delta\phi/\ell$ of turbulent line segments. The mean gradient g is not an additional independent variable because statistics of g can be derived from joint statistics of $\Delta\phi$ and ℓ. By definition g is constant within each segment. The value of g is compared to the local scalar gradient in fig. 5.1 for each segment. The mean gradient g is related to the local scalar gradient in x-direction by

$$\frac{1}{\ell}\int_0^\ell \frac{\partial\phi}{\partial x}\mathrm{d}x = \frac{\Delta\phi}{\ell} = g\,. \tag{5.1}$$

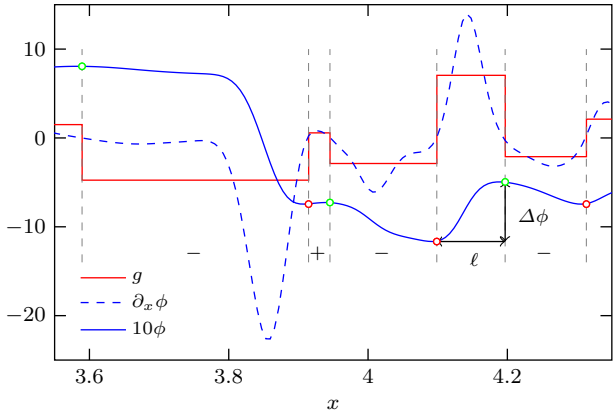

Figure 5.1: Illustration of the concept of turbulent line segments and of the definition of $\Delta\phi$ and ℓ. For clarity the value of the scalar ϕ is multiplied by 10. Additionally the local gradient $\partial_x\phi$ and the mean gradient $g = \Delta\phi/\ell$ are shown. Maximum points are marked by a green circle and minimum points are marked by a red circle.

This shows that g can be considered as an average of the local scalar gradient over an individual segment. Based on dimensional arguments the mean scalar dissipation $\langle\chi\rangle \propto \langle(\partial\phi/\partial x)^2\rangle$ within each segment is expected to be correlated with $\langle g^2\rangle$.

One of the main advantages of the present approach compared to the theory of dissipation elements is that turbulent line segments can be directly related to conventional two-point statistics. On the other hand it shares with dissipation elements the property that the distance between two extremal points ℓ result from the signal itself and provides information about the length distribution of the turbulent field. Differently from traditional two-point statistics the correlation length ℓ becomes a stochastic variable.

This chapter is organized in the following way. We begin with a brief introduction of the numerical method used to compute turbulent line segments from data obtained by direct numerical simulation, cf. tab. 3.1. Next, we parameterize the curve of turbulent line segments by a harmonic series and show that small segments follow closely a sinusoidal profile. In a next step an equation for the normalized length distribution of turbulent line segments is introduced. The normalized distribution function of the mean length is independent of Reynolds number. In order to compute the dimensional length distribution for arbitrary Reynolds numbers the scaling of the normalization parameter, namely the mean length as the only parameter used to collapse the pdfs, has to be known. Based on DNS a scaling with the Kolmogorov length is found, i.e. $\ell_m \propto \eta$, which will be theoretically confirmed. Then, we present several statistical properties of turbulent line segments with a focus on the Reynolds

number dependence. This comprises a discussion of the effect of strain on turbulent line segments. The joint distribution functions and the respective marginal statistics of $\Delta\phi$ and ℓ as well as g and ℓ are discussed. Additionally, conditional moments are defined and the results are compared with those of the conventional scalar structure functions. Finally, the method of turbulent line segments is employed to provide a novel description of the physics behind cliff-ramp structures. We will show that the width of the steepest gradients scales with the Kolmogorov length η and is approximately 6η. Ramps in the scalar profile occur preferentially for descending segments which are oriented parallel to the mean scalar gradient. Additionally, we will show how cliff-ramp structures are related to small-scale anisotropy.

5.2 Numerical Method

Turbulent line segments are efficiently computed by a fully MPI parallelized algorithm. Finding the extreme points of $\phi(x)$ turns into the problem of finding the roots of the first derivative $\phi_x(x)$. To this end, the first and second derivatives of $\phi(x)$ are calculated and exactly interpolated by a spectral method to a finer mesh. On this new mesh the zero-crossings of the first derivative act as the starting point for a Newton iteration that yields the exact position of the extreme points. The extreme points are only counted when the separation between two successive extreme points is larger than the original grid width.

Because turbulent line segments reveal a length distribution, two different methods to compute statistical quantities can be defined. On the one hand, we can take averages over individual segments and treat each segment as one realization. This yields to segment-weighted averages that describe geometrical features of turbulent line segments like the mean length or the mean scalar difference. Unless otherwise stated we will use segment-weighted statistics throughout this thesis. On the other hand, it is useful to compute statistics, where each individual segment is weighted by its length. By this weighting technique it is possible to reconstruct volume-weighted ensemble averages of the whole field. In the following we will denote this as volume-weighted statistics as each grid point contributes equally to the statistics.

The following analysis will focus on line segments along straight lines perpendicular to the mean scalar gradient $\boldsymbol{\Gamma}$ in x-direction. Thus the computed statistics are not directly affected by anisotropy. The effect of anisotropy and cliff-ramp structures on turbulent line segments will be examined in detail in sec. 5.7.5.

An illustration of turbulent line segments in the computational domain is given in fig. 5.2 where the length ℓ and the mean gradient g are shown as field variables. Relatively large contiguous regions of long segments can be observed which adjoin to regions with smaller segments. Despite the fact that the segments are calculated in x-direction they have relatively large coherent regions in perpendicular directions. This is particularly noticeable for the mean gradient g where thin ribbon-like regions

occur. These regions are sharply bounded and have been denoted as cliff-ramp structures in the literature, cf. Holzer and Siggia (1994) and Tong and Warhaft (1994). Similarly, cliff-ramp structures have a width that is much smaller compared to the extension in the two other directions, cf. Tsinober (2001).

5.3 Phenomenology of Turbulent Line Segments

Turbulent line segments characterize the dynamic process of small-scale quantities, like the scalar gradient and the scalar dissipation. Understanding the dissipation mechanisms is an important step to resolve turbulent mixing. Within a turbulent line segment, the value of the passive scalar is by definition monotone. This is different for the scalar gradient which is zero at the ending points but may have a very irregular structure within the turbulent line segments with the occurrence of rare large values and one or more local extrema. Figure 5.3 illustrates the curve of the passive scalar and its gradient for two different turbulent line segments. The value of the scalar ϕ is normalized according to

$$\phi^* = \frac{\phi - \phi_\mathrm{m}}{\Delta\phi}\,, \tag{5.2}$$

where $\phi_\mathrm{m} = 1/2(\phi_\mathrm{end} + \phi_\mathrm{start})$ is the mean value. The gradient $\partial_x\phi$ is normalized by the mean gradient g of the individual segment. The length coordinate is transformed to a new coordinate ξ, defined as

$$\xi = \pi\left(\frac{x}{\ell} - \frac{1}{2}\right)\,, \tag{5.3}$$

which normalizes each individual segment of the length ℓ to a coordinate between $-\pi/2$ and $\pi/2$. Figure 5.3a shows a segment where ϕ^* rises at a small distance resulting in a locally large gradient with a maximum value of almost five times the mean value at $\xi \approx -\pi/4$ while afterwards the gradient is close to zero. Figure 5.3b additionally shows that ϕ^* may change curvature several times within a segment resulting in several local extrema of $\partial_x\phi$ in the interval $-\pi/2 \leq \xi \leq \pi/2$.

By definition, within turbulent line segments, the value of ϕ^* monotonously increases or decreases and has zero-gradient boundary conditions at the end points. Additionally, due to the normalization according to eq. 5.2 fixed values at the boundaries occur with $\phi^*(\xi = 0) = 0$ and $\phi^*(\xi = 1) = 1$. A suitable functional description that satisfies these conditions is an expansion by a harmonic series, namely

$$\frac{\phi - \phi_\mathrm{m}}{\Delta\phi} = \frac{1}{2}\sin\xi + \sum_{i=2}^{\infty} a_i \sin\big(2(i-1)\xi\big)\,, \tag{5.4}$$

which is similar to an approach by Bourlioux et al. (2006). Here, due to the boundary conditions the constant term and the cosines are omitted. Figure 5.4

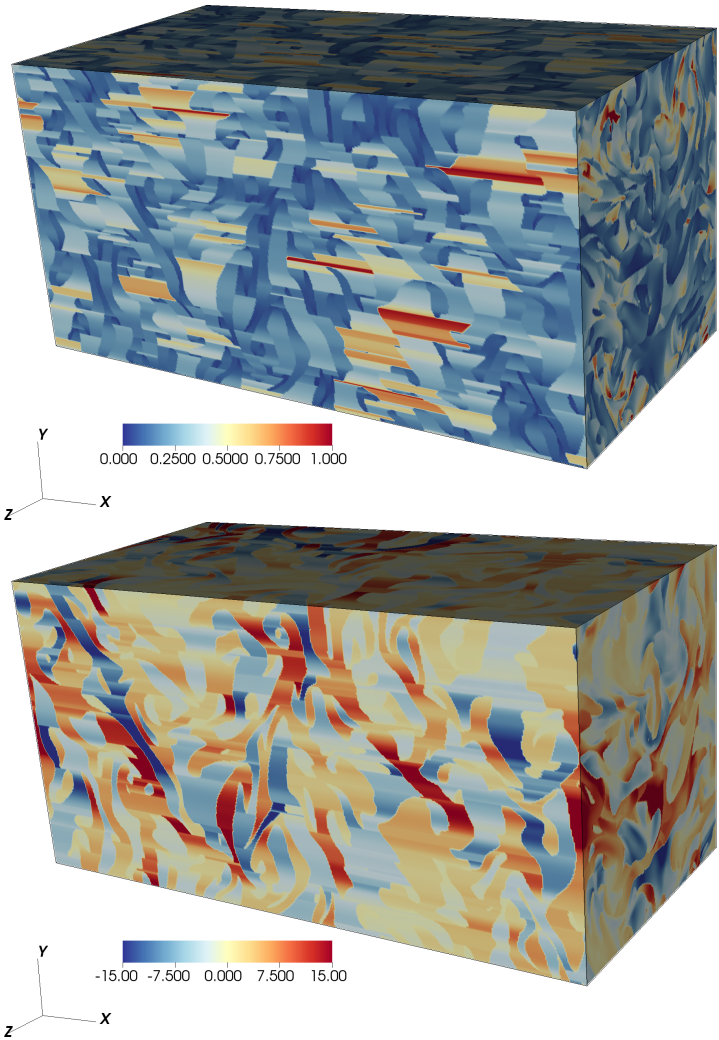

Figure 5.2: Illustration of the length ℓ (top) and the mean gradient $g = \Delta\phi/\ell$ (bottom) of turbulent line segments for case R0. For clearity only a subset with size $2\pi \times \pi \times \pi$ is shown.

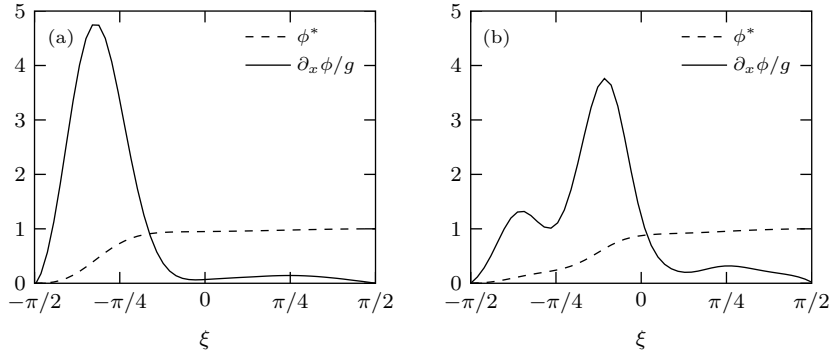

Figure 5.3: Illustration of the normalized scalar $\phi^*(\xi)$ and the local scalar gradient $\partial_x\phi$ normalized by the mean gradient g for two different turbulent line segments.

Table 5.1: Higher order coefficient a_2 for different length classes as well as for all length classes obtained from DNS for case R1.

ℓ/ℓ_m	1	1.5	2	3.5	all
a_2	-0.021	-0.041	-0.058	-0.068	-0.040

shows ϕ^* calculated from DNS for case R1 and the approximation by eq. 5.4, where the coefficients are obtained by curve-fitting to the DNS data. The series is truncated after the first and after the second order term, respectively. The first order solution reveals concerning the slope small deviations from the DNS data around the inflection point. But we can achieve a very good agreement with the DNS by considering the series up to the second order. The higher order correction by the coefficient a_2 is small, namely $a_2 = -0.040$. Note that by retaining the second order term the zero gradient boundary conditions cannot be exactly satisfied.

Let us now consider ϕ^* for different length classes. This is shown in fig. 5.5 for $\ell/\ell_m \leq 1.0$, $1.0 < \ell/\ell_m \leq 2.0$ and $\ell/\ell_m > 2.0$. When ℓ is small, the profile of the segment will be mostly determined by dissipative effects and can be well approximated by retaining only the first order of eq. 5.4, i.e. $\phi^* = 1/2 \sin\xi$. When the considered length class is larger the strong non-linearity of the convective term affects the scalar field and the deviation from the simple sinusoidal profile becomes significant. This is further illustrated in tab. 5.1, where the magnitude of the second order correction coefficient a_2 increases with the length class ℓ. We may thus conclude that the deviation from the first order solution comes from the large segments.

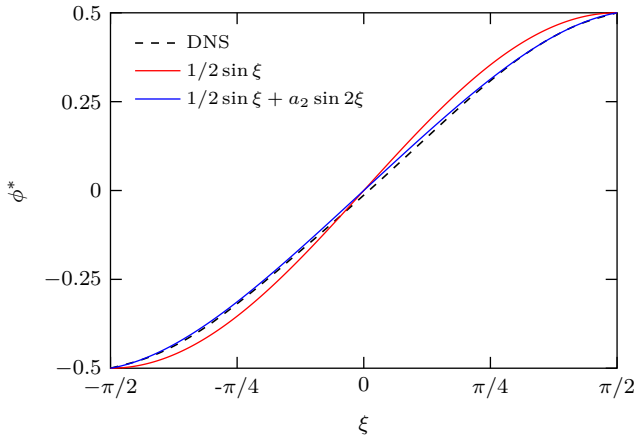

Figure 5.4: Averaged non-dimensional profile ϕ^* from DNS for case R1 and approximation by eq. 5.4 where the series is truncated after the first and second order.

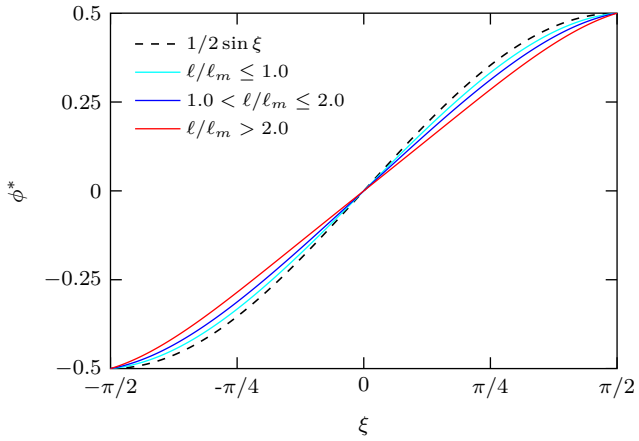

Figure 5.5: Averaged non-dimensional profile ϕ^* from DNS for case R1 for different length classes and comparison with the first order approximation.

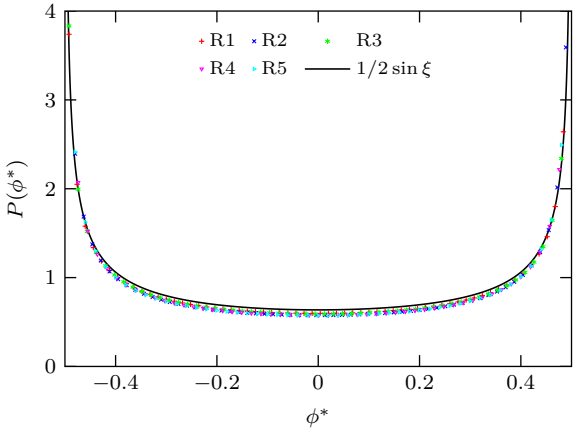

Figure 5.6: PDF of ϕ^* for all cases and comparison with the analytical result (black line), cf. eq. 5.6.

Next, we examine the marginal pdf of ϕ^*. With the ansatz $\phi^* = 1/2 \sin \xi$ and

$$P_{\mathrm{L}}(\phi^*; \phi_{\mathrm{m}}, \Delta\phi) = \frac{c}{|\partial\phi^*/\partial x|}\,, \tag{5.5}$$

we may derive an analytic expression for the pdf of ϕ^* by assuming an uniform distribution of ξ in the interval $[-\frac{\pi}{2}, \frac{\pi}{2}]$, cf. Papoulis and Pillai (2002). Equation 5.5 is valid for each combination of ϕ_m and $\Delta\phi$. Evaluation of eq. 5.5 directly yields

$$P_{\mathrm{L}}(\phi^*; \phi_{\mathrm{m}}, \Delta\phi) = \frac{2/\pi}{\sqrt{1 - 4{\phi^*}^2}}\,, \tag{5.6}$$

where the constant c is obtained from the normalization condition

$$\int P_{\mathrm{L}}(\phi^*; \phi_{\mathrm{m}}, \Delta\phi)\mathrm{d}\phi^* = 1\,. \tag{5.7}$$

Figure 5.6 shows $P_L(\phi^*)$ calculated from DNS for all cases and a comparison with the analytic result from eq. 5.6. A good agreement between DNS and eq. 5.6 is observed, where eq. 5.6 slightly overestimates the DNS data around $\phi^* \approx 0$. This comes from the first order approximation of the scalar profile which underestimates the slope of ϕ^* at the inflection point. Additionally, $P_L(\phi^*)$ is Reynolds number independent and all cases collapse to a single curve. This is due to the fact that by the normalization according to eq. 5.2 the scalar profiles ϕ^* within turbulent line segments become quasi-universal.

5.4 A PDF Equation for the Mean Length of Turbulent Line Segments

In temporally evolving flows the instantaneous profiles of turbulent line segments change on a small time scale comparable to the Kolmogorov time. Analyzing the temporal evolution of the length ℓ of turbulent line segments helps to understand the governing physical processes. The present analysis is based on Lagrangian particles which are convected by the turbulent flow. At each time step of the simulation we use the instantaneous position of the Lagrangian particle as starting point and measure, in the frozen turbulent scalar field, the distance until we reach an extreme point in both directions along the turbulent line segment under consideration. This procedure yields the length ℓ of the line segment that is connected with the respective Lagrangian particle. The advantage of using Lagrangian particles compared to fixed points is that the Lagrangian particle is convected by the flow field and thus the particles will stay within the same line segment for a longer time. This results in smoother statistics.

Figure 5.7 shows the normalized length of turbulent line segments ℓ/ℓ_m as a function of the normalized time t/τ_η obtained by DNS of case R1. The ratio ℓ/ℓ_m exhibits fast changes, where the length of the line segments changes abruptly in the form of jumps, and slow changes where the length changes continuously by diffusion, compression or stretching. This observation is in agreement with the results of Schaefer et al. (2009) who investigated the length evolution of dissipation elements. Fast changes can be attributed to two different physical effects: Firstly, by annihilation of minimum and maximum points due to diffusion, two adjacent segments join and form one large element. This is called reconnection and can be observed in fig. 5.7 at $t/t_\eta \approx 7$. Secondly, by perturbations due to diffusive or convective motion one large element can be cut into two smaller ones. This can be observed in fig. 5.7 at $t/t_\eta \approx 11$ and is called cutting. Slow changes arise from the relative motion of the extreme points which is called drift process. A slow change of the segment length can be observed in fig. 5.7 for $1 < t/\eta < 5$. On average small line segments are compressed by molecular diffusive effects and larger line segments are stretched by linear strain. For steady turbulence the generation of new line segments due to random motion and the annihilation of extreme points due to diffusion equals each other in a statistical sense.

An evolution equation for the pdf of the length of dissipation elements was first derived by Wang and Peters (2006, 2008). A similar equation was derived by Schaefer et al. (2012) for the pdf of the length of one-dimensional streamline segments based on a generalized Master equation. Both works can be directly applied to turbulent line segments. When we neglect the second order jump moment the normalized equation for the pdf of the length of turbulent line segments reads

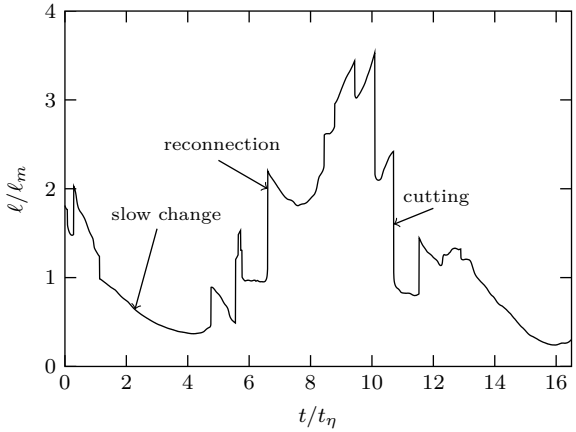

Figure 5.7: Fast and slow changes of the normalized length ℓ/ℓ_m of a turbulent line segment associated with a Lagrangian particle for case R1.

$$\begin{aligned}\frac{\partial \widetilde{P}(\tilde{\ell},\tilde{t})}{\partial \tilde{t}} + \frac{\partial}{\partial \tilde{\ell}}\left[\widetilde{P}(\tilde{\ell},\tilde{t})\left(\widetilde{v}_D(\tilde{\ell},\tilde{t}) + \tilde{a}(\tilde{\ell},\tilde{t})\tilde{\ell}\right)\right] \\ = \Lambda_c\left[2\int_0^\infty \widetilde{P}(\tilde{\ell}+\widetilde{z},\tilde{t})\mathrm{d}\widetilde{z} - \tilde{\ell}\widetilde{P}(\tilde{\ell},\tilde{t})\right] \\ + 2\widetilde{\mu}\left[\int_0^{\tilde{\ell}} \frac{\widetilde{y}}{\tilde{\ell}}\widetilde{P}(\tilde{\ell}-\widetilde{y},\tilde{t})\widetilde{P}(\widetilde{y},\tilde{t})\mathrm{d}\widetilde{y} - \widetilde{P}(\tilde{\ell},\tilde{t})\right].\end{aligned} \tag{5.8}$$

We use the molecular diffusivity D and the mean value of the length $\ell_m = \int \ell P(\ell)\mathrm{d}\ell$ as normalization parameters. Additionally, we define the normalized length $\tilde{\ell} = \ell/\ell_m$ and seek for solutions of the form $\widetilde{P} = P\ell_m$. The normalized pdf fulfills two constraints, namely

$$\int_0^\infty \widetilde{P}(\tilde{\ell})\mathrm{d}\tilde{\ell} = 1 \tag{5.9}$$

and

$$\int_0^\infty \tilde{\ell}\widetilde{P}(\tilde{\ell})\mathrm{d}\tilde{\ell} = 1\,. \tag{5.10}$$

For statistically steady turbulence ℓ_m and $\widetilde{P}(\tilde{\ell},t)$ are independent of time. The nondimensional time is defined as $\tilde{t} = t/(\ell_m^2/D)$. The macroscopic slow change of turbulent line segments is determined by two contributions: A strain dominated

term $\widetilde{a}$ which is important for large segments and a diffusively dominated term $\widetilde{v}_D$ which is important for small segments. The integrals on the right hand side represent the fast abrupt processes. The conditional mean strain rate a is defined as

$$a = \frac{1}{\ell}\left\langle \Delta u|\ell \right\rangle \tag{5.11}$$

where Δu is the velocity difference between maximum and minimum point along the straight line. This quantity will be further examined in sec. 5.6. We can now introduce the normalized conditional mean strain rate as $\widetilde{a} = a(\ell_m^2/D)$. The normalized drift velocity due to molecular diffusion is defined as

$$\widetilde{v}_D = \frac{v_D}{D/\ell_m} = -c_e \frac{4}{\tilde{\ell}}\,, \tag{5.12}$$

where c_e is a model parameter of order unity that takes complex three-dimensional effects into account. The fast processes are modeled by a Poisson-like cutting and reconnection process. The nondimensional numbers $\Lambda_c = \lambda\ell_m^3/D$ and $\widetilde{\mu} = \mu\ell_m^2/D$ denote the normalized cutting frequency per unit length and time, and the normalized reconnection frequency per unit time, respectively. For the steady state Λ_c is an eigenvalue of eq. 5.8 and can be obtained from the normalization condition $\int \tilde{\ell}\widetilde{P}\mathrm{d}\tilde{\ell} = 1$. The normalized drift velocity $\widetilde{v}_D$ is singular at the origin according to eq. 5.12. This leads to a linear rise of $\widetilde{P}(\tilde{\ell})$ at the origin and with eq. 5.12 the reconnection coefficient can be expressed by

$$\widetilde{\mu} = 4c_e \frac{\partial \widetilde{P}(\tilde{\ell})}{\partial \tilde{\ell}}\bigg|_{\tilde{\ell}\to 0}\,. \tag{5.13}$$

Equation 5.8 can be solved numerically using a finite difference scheme for the diffusion term when c_e and $\left\langle \Delta u|\ell \right\rangle$ are specified. Figure 5.8 shows the numerical solution of eq. 5.8 compared with DNS data for all cases. The normalized pdfs $\widetilde{P}(\tilde{\ell})$ collapse very well for all cases and become quasi-independent of Reynolds number, suggesting that the normalized pdfs are quasi-universal. In addition, the DNS data is in very good agreement with the result of the model equation. The normalized pdf $\widetilde{P}(\tilde{\ell})$ is non-Gaussian. At the origin the pdf rises linearly. The maximum of the pdfs occurs at $\tilde{\ell} \approx 0.55$ with a value of $\widetilde{P}_{\max} \approx 0.83$. The semi-logarithmic plot in the inset shows a clear exponential decaying tail which is an outcome of the assumed Poisson process. Additionally, the normalized pdfs are similar in shape to the ones obtained by means of dissipation elements based on the scalar field, cf. Wang and Peters (2006, 2008). However, for dissipation elements the maximum of the normalized pdfs occurs at a somewhat larger value ($\tilde{\ell} \approx 0.7 - 0.8$) with a smaller peak value ($\widetilde{P}_{\max} \approx 0.7 - 0.8$).

The normalized pdf $\widetilde{P}(\tilde{\ell})$ can be parameterized by the empirical model

$$\widetilde{P}(\tilde{\ell}) = \frac{a\tilde{\ell}}{1 + b\tilde{\ell}} \exp(-b\tilde{\ell})\,, \tag{5.14}$$

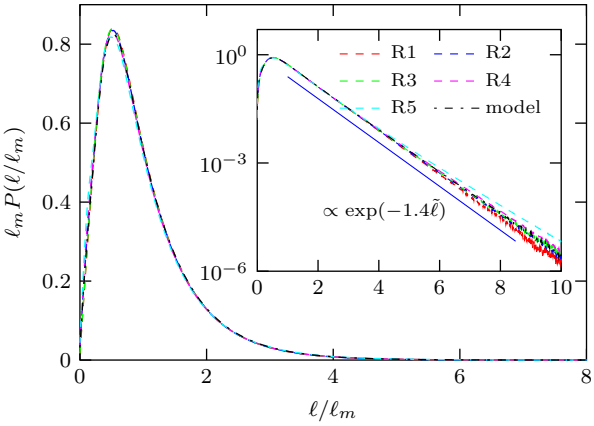

Figure 5.8: Normalized pdf of the length of turbulent line segments computed from DNS for all cases and comparison with the result from the model equation, cf. eq. 5.8. An excellent agreement between DNS and model is obtained. The normalized pdfs collapse for all cases to a single curve. The tail of the pdf satisfies the relation $\widetilde{P}(\tilde{\ell}) \propto \exp(-1.4\tilde{\ell})$.

where a best-fit of the DNS results leads to $a = 5.22$ and $b = 1.44$. This model agrees very well with the results from DNS, where the tails of the pdfs satisfy $\widetilde{P}(\tilde{\ell}) \propto \exp(-1.4\tilde{\ell})$. Note that due to the normalization of the pdf the parameters a and b are not independent. They are related by

$$a = \frac{b^2}{1 + \mathrm{e}\,\mathrm{Ei}(-1)}\,, \tag{5.15}$$

where Ei denotes the exponential integral function with $\mathrm{Ei}(-1) \approx -0.219$.

5.5 The Scaling of the Mean Length

In the previous paragraph we have shown that the marginal pdfs of the length ℓ become independent of Reynolds number when normalized by the mean length ℓ_m. A model has been deduced which is in good agreement with the results from DNS. To obtain the dimensional pdf from the normalized pdf $\widetilde{P}(\tilde{\ell})$ we need to know how the normalization quantity, i.e. the mean length ℓ_m, depends on the Reynolds number.

Due the anisotropy of the scalar field we will examine the mean length computed on the scalar field along straight lines in both x- and y-direction. The former direction is perpendicular and the latter direction is parallel to the mean scalar gradient. The corresponding mean lengths are denoted by $\ell_m^{\phi,x}$ and $\ell_m^{\phi,y}$, respectively, and are calculated for all cases, cf. tab. 5.2. With increasing Reynolds number both

Table 5.2: Scaling of the mean length ℓ_m of turbulent line segments as well as the ratio ℓ_m/η. Turbulent line segments calculated in the direction of the mean scalar gradient are denoted by $\ell_m^{\phi,y}$, and turbulent line segments calculated in perpendicular direction are denoted by $\ell_m^{\phi,x}$.

	R0	R1	R2	R3	R4	R5
Re_λ	88	119	184	215	331	529
$\ell_m^{\phi,x}$	0.1815	0.1160	0.0656	0.0521	0.0318	0.0152
$\ell_m^{\phi,y}$	0.1888	0.1198	0.0672	0.0531	0.0323	0.0153
$\ell_m^{\phi,x}/\eta$	10.402	10.473	10.517	10.628	10.638	10.798
$\ell_m^{\phi,y}/\eta$	10.822	10.815	10.768	10.820	10.803	10.874

ℓ_m decreases as the size of the smallest scales of the scalar field decrease as well. Additionally, $\ell_m^{\phi,y}$ is slightly larger than $\ell_m^{\phi,x}$, but with increasing Reynolds number the former approaches the latter. This may be explained by the assumption of local isotropy, which states that statistical quantities become independent of direction when the Reynolds number is sufficient high. Note that despite the fact that $\ell_m^{\phi,x}$ and $\ell_m^{\phi,y}$ differ, their normalized length pdfs collapse, cf. fig. 5.25, underlining the quasi-universality of the length pdf.

Based on the DNS data we propose that the mean length ℓ_m scales with the Kolmogorov length η, i.e.

$$\frac{\ell_m}{\eta} = \text{const}\,. \tag{5.16}$$

This ratio is shown in tab. 5.2. For turbulent line segments calculated in y-direction $\ell_m^{\phi,y}/\eta$ fluctuates around a constant mean value between 10.77 and 10.87 for all Reynolds numbers under consideration. This fluctuations can be attributed to statistical convergence issues suggesting that the proposed scaling by eq. 5.16 is satisfied. However, $\ell_m^{\phi,x}/\eta$, calculated in x-direction, increases systematically by 4% from 10.40 for case R0 to 10.79 for case R5 indicating that the normalization with the Kolmogorov length η yields an overcompensation. Based on the DNS data and fig. 5.9 we suggest that $\ell_m^{\phi,x}/\eta$ will approach $\ell_m^{\phi,y}/\eta$ exponentially when the Reynolds number is sufficiently high, i.e. $\mathrm{Re}_\lambda > 500$ and from then on will satisfy the scaling with η according to eq. 5.16. Below this Reynolds number dissipative effects persist resulting in the observed anisotropy. The effect of anisotropy on the statistics of turbulent line segments will be picked up again in sec. 5.7.5.

The DNS results indicate that the mean length ℓ_m of turbulent line segments is on average approximately 10.5η. According to the dissipation spectrum of the scalar variance the peak scalar dissipation occurs at a scale $r/\eta \approx 25$. This finding suggests that turbulent line segments comprise on average scales which are dominated by dissipative effects. However, the length distribution of turbulent line segments with

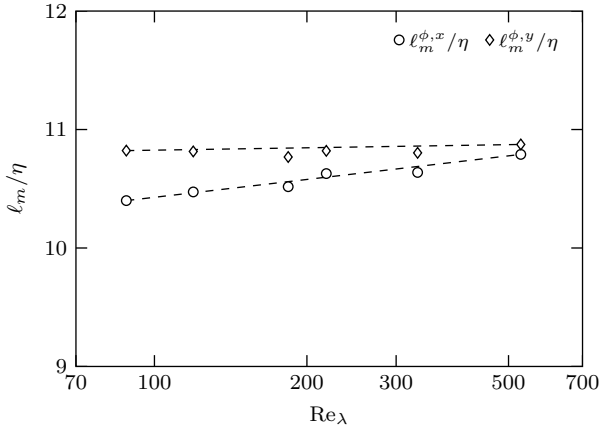

Figure 5.9: Scaling of the mean length of turbulent line segments with the Reynolds number for case R0 to case R5. The calculation of the segments is based on the field of the passive scalar ϕ, where the line along which the segments are calculated points in x-direction and in y-direction.

the presence of very long segments enables us to extend the analysis up to the inertial range by considering conditional statistics.

In the following the scaling of the mean length ℓ_m of the scalar field ϕ with the Reynolds number is further investigated by two different approaches: firstly by means of the pdf equation for ℓ, cf. eq. 5.8, and secondly by a statistical approach. Both approaches yield the same result and confirm the observed DNS result.

5.5.1 Derivation Based on the PDF-Equation for the Mean Length

As explained above the mean length of the segments is determined by compressive diffusive effects acting on small segments and extensive strain acting on large segments. From eqs. 5.8 and 5.13 we know that the reconnection frequency can be expressed as

$$\mu \propto D\frac{\partial P}{\partial \ell}\Big|_{\tilde{\ell}\to 0} = \frac{D}{\ell_m^2}\frac{\partial \widetilde{P}}{\partial \tilde{\ell}}\Big|_{\tilde{\ell}\to 0} \propto \frac{D}{\ell_m^2}\,, \tag{5.17}$$

where the second relation originates from the fact that the slope of the compensated pdf $\partial\widetilde{P}/\partial\tilde{\ell}$ at the origin is a Reynolds number independent constant. This is justified by fig. 5.8 by means of DNS data. We can thus express the mean length as a function of the reconnection frequency μ and the molecular diffusivity by

$$\ell_m \propto (D/\mu)^{1/2} \propto \eta \mathrm{Sc}^{-1/2}\,. \tag{5.18}$$

The last transformation follows from the assumption that $\mu \propto t_\eta^{-1}$, where the Kolmogorov time is defined as $t_\eta = (\nu/\varepsilon)^{1/2}$. This assumption can be justified by the observation that the reconnection process of segments occurs at a very small time scale, cf. fig. 5.7.

5.5.2 Derivation Based on Statistical Properties

The scaling of the mean length ℓ_m can be deduced as well from statistical properties of the scalar field ϕ along a straight line. Rice (1945) derived an equation that relates the expected number of zero-crossings N_0 of ϕ to its two-point correlation function $f_\phi = \langle \phi(x+r)\phi(x)\rangle / \langle \phi^2 \rangle$ according to

$$N_0 = \frac{1}{\pi}\left[-\frac{f_\phi''(0)}{f_\phi(0)}\right]^{1/2}, \tag{5.19}$$

where $f_\phi''(0)$ is the second derivative of the two-point correlation function at $r = 0$. Equation 5.19 is valid for any Gaussian field, where the pdf of ϕ and its first derivative ϕ_x can be collapsed by the standard deviation. Liepmann (1949) and Sreenivasan et al. (1983) experimentally studied eq. 5.19 for the turbulent velocity field. They found that despite the fact that turbulence is evidently not Gaussian, eq. 5.19 is well satisfied. Liepmann (1949) pointed out that essentially statistical independence between ϕ and its first derivative ϕ_x is required. This encourages us to adapt eq. 5.19 to estimate the mean length ℓ_m of turbulent line segments.

The mean length ℓ_m between two adjacent extreme points can be calculated by means of the number of zero-crossings N_E of the first derivative. This is due to the fact that the extreme points turn into the zero-crossings of the first derivative and, in addition, that the mean length ℓ_m is directly proportional to $1/N_E$. We thus adopt eq. 5.19, but instead of using the two-point correlation function of the scalar field f_ϕ, we use the two-point correlation function f_{ϕ_x} of the first derivative ϕ_x defined as

$$f_{\phi_x} = \langle \phi_x(x+r)\phi_x(x)\rangle / \langle \phi_x^2 \rangle \,. \tag{5.20}$$

Hence, Rice's theorem for the number of extrema N_E becomes

$$N_E = \frac{1}{\pi}\left[-\frac{f_{\phi_x}''(0)}{f_{\phi_x}(0)}\right]^{1/2}. \tag{5.21}$$

The two-point correlation functions f_ϕ and f_{ϕ_x} are depicted in fig. 5.10 as a function of r/η. The scalar derivative correlation function f_{ϕ_x} drops very fast and becomes by normalization with the Kolmogorov scale independent of Reynolds number. We can obtain f_{ϕ_x} from f_ϕ by

$$f_{\phi_x} = -\frac{\langle \phi^2 \rangle}{\langle \phi_x^2 \rangle}\frac{\mathrm{d}^2}{\mathrm{d}r^2} f_\phi \,. \tag{5.22}$$

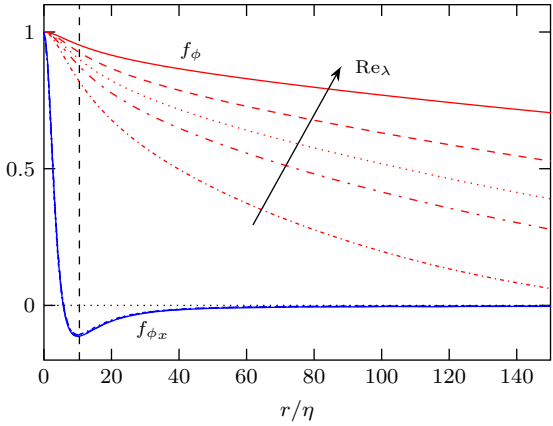

Figure 5.10: Two-point correlation function of the scalar $f_\phi(r) = \langle\phi(x+r)\phi(x)\rangle/\langle\phi^2\rangle$, red, and its gradient $f_{\phi_x}(r) = \langle\phi_x(x+r)\phi_x(x)\rangle/\langle\phi_x^2\rangle$, blue, for all cases. The arrow indicates increasing Reynolds number. $f_{\phi_x}(r/\eta)$ is independent of Reynolds number and all cases collapse to a single curve. The vertical dashed line denotes the normalized mean length $\ell_m/\eta = 10.5$ which virtually coincides with the minimum of $f_{\phi_x}(r/\eta)$.

Differently to f_ϕ, which is monotonously decreasing, f_{ϕ_x} has a distinct minimum at $r/\eta \approx 10.5$ which coincides with the normalized mean length ℓ_m/η. The present results suggest that for scalar fields it is generally valid that the location of the minimum of f_{ϕ_x} equals ℓ_m/η. However, a rigorous proof is missing.

The denominator of eq. 5.21 can be written as

$$f_{\phi_x}(0) = \langle\phi_x^2\rangle\,, \tag{5.23}$$

where $\langle\phi_x^2\rangle$ denotes the variance of the first scalar derivative. The second derivative of f_{ϕ_x}, needed for the nominator of eq. 5.21, can be expressed as

$$f''_{\phi_x}(0) = \langle\phi_{xx}^2\rangle\,, \tag{5.24}$$

where $\langle\phi_{xx}^2\rangle$ denotes the variance of the second scalar derivative. With eqs. 5.23 and 5.24 we obtain

$$\frac{1}{\ell_m} = N_E = \frac{1}{\pi}\left[\frac{\langle\phi_{xx}^2\rangle}{\langle\phi_x^2\rangle}\right]^{1/2}\,. \tag{5.25}$$

We want to emphasize again that eq. 5.25 is not exactly valid for turbulent flows since neither ϕ_x nor ϕ_{xx} are Gaussian and thus the assumption that yields eqs. 5.19 and 5.21 is not strictly valid.

Let us now adopt Kolmogorov's similarity hypothesis, cf. Kolmogorov (1941a,b), to relate the right hand side of eq. 5.25 to the Kolmogorov length η. The standard

Table 5.3: Scaling of several quantities occurring in Rice's theorem with the Taylor based Reynolds number for cases R0 to R5.

	R0	R1	R2	R3	R4	R5
Re_λ	88	119	184	215	331	529
ℓ_m	0.182	0.116	0.065	0.052	0.031	0.015
ℓ_m/η	10.40	10.47	10.52	10.63	10.64	10.79
c_{ϕ_x}	0.404	0.405	0.405	0.407	0.407	0.405
$c_{\phi_{xx}}$	0.182	0.183	0.183	0.186	0.185	0.185
$\pi c_{\phi_x}/c_{\phi_{xx}}$	6.98	6.94	6.97	6.88	6.90	6.90
c_{ϕ_y}	0.418	0.417	0.415	0.413	0.413	0.411
$c_{\phi_{yy}}$	0.192	0.192	0.190	0.190	0.190	0.190
$\pi c_{\phi_y}/c_{\phi_{yy}}$	6.84	6.82	6.86	6.83	6.84	6.81

deviation of ϕ_x and ϕ_{xx} are small scale quantities and thus scale both with the mean energy dissipation $\langle\varepsilon\rangle$, the mean scalar dissipation $\langle\chi\rangle$ and the Kolmogorov length η, yielding on dimensional grounds

$$\langle\phi_x^2\rangle^{1/2} = c_{\phi_x}\mathrm{Sc}^{1/2}\langle\chi\rangle^{1/2}\langle\varepsilon\rangle^{-1/6}\eta^{-2/3}\,, \tag{5.26}$$

and

$$\langle\phi_{xx}^2\rangle^{1/2} = c_{\phi_{xx}}\mathrm{Sc}^{1/2}\langle\chi\rangle^{1/2}\langle\varepsilon\rangle^{-1/6}\eta^{-5/3}\,. \tag{5.27}$$

The proportional constants are denoted by c_{ϕ_x} and $c_{\phi_{xx}}$, respectively, and are both independent of Reynolds number. Their values are given in tab. 5.3.

When we use eq. 5.26 and eq. 5.27 in eq. 5.25, we finally obtain the scaling relation

$$\frac{\ell_m}{\eta} = \pi\frac{c_{\phi_x}}{c_{\phi_{xx}}}\,. \tag{5.28}$$

The ratio $\pi c_{\phi_x}/c_{\phi_{xx}}$ is given in tab. 5.3 calculated by means of DNS for all cases. It is virtually independent of Reynolds number, namely $\pi c_{\phi_x}/c_{\phi_{xx}} \approx 6.9$. With eq. 5.28 the ratio ℓ_m/η should be thus also independent of Reynolds number and the value should be equal to 6.9. Comparison with DNS reveals that the ratio ℓ_m/η is indeed independent of Reynolds number, but the value is higher than predicted by eq. 5.28, namely $\ell_m/\eta \approx 10.5$. The reason for this deviation can be attributed to the non-Gaussianity of the scalar derivatives and the fact that the marginal pdfs of ϕ_x and ϕ_{xx} for different Reynolds numbers cannot be collapsed solely by the standard deviation.

Additionally, tab. 5.3 shows the constants c_{ϕ_y} and $c_{\phi_{yy}}$ for derivatives in y-direction. The ratio $\pi c_{\phi_y}/c_{\phi_{yy}} \approx 6.84$ is fully independent of Reynolds number and under-predicts the ratio $\ell_m^y/\eta \approx 10.8$ as well.

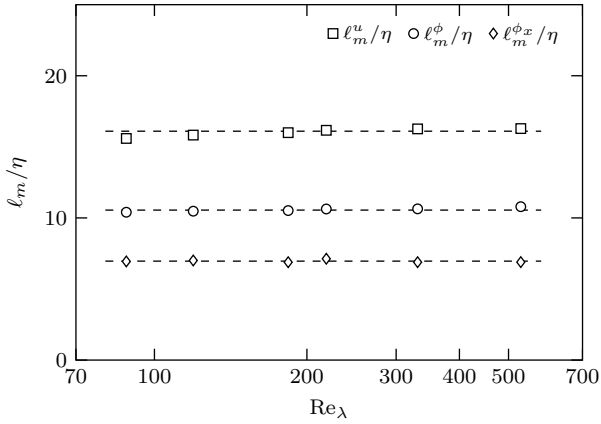

Figure 5.11: Scaling of the normalized mean length ℓ_m/η with the Reynolds number for all cases. The calculation of the segments is based on the field of the passive scalar ϕ, the u-component of the velocity field, and the gradient of the passive scalar in x-direction.

With the aforementioned scaling law for the mean length ℓ_m and the quasi-universal model for $\widetilde{P}(\tilde{\ell})$ we can reconstruct the length distribution of ℓ for any Reynolds number.

5.5.3 The Mean Length of Turbulent Line Segments Based on the Velocity and the Scalar Gradient

The method of turbulent line segments can basically be applied to all turbulent fields as long as the governing equations have a diffusive term which ensures the smoothness of the field. We will now consider turbulent line segments where the field that defines the extreme points is the field of the scalar gradient ϕ_x in x-direction and the u-component of the velocity field. We will use the notation $\ell_m^{\phi_x}$ and ℓ_m^u for the mean lengths, respectively. Figure 5.11 shows the ratios $\ell_m^{\phi_x}/\eta$ and ℓ_m^u/η. They are as well independent of Reynolds number for all cases under consideration. This result underlines that the mean length of turbulent line segments obtained from various turbulent fields scales with the Kolmogorov length. On average the segments of the velocity field ($\ell_m^u/\eta \approx 16$) are longer than the segments of the scalar field ($\ell_m/\eta \approx 10.5$), while the segments of the scalar gradient are even shorter ($\ell_m^{\phi_x}/\eta \approx 8$). This result is directly related to the fact that the scalar fields exhibits smaller scales than the velocity field which has already been observed for the dissipation spectra, cf. 3.9. On the other hand the field of the scalar gradient ϕ_x is a small scale quantity resulting in a relatively small mean length.

5.6 Compressive and Extensive Strain

In turbulent flows, the field of the passive scalar is subject to a straining motion where it is deformed by compression and stretching. The gradient of the scalar is reduced in the direction of the extensive strain and enhanced in the direction of the compressive strain. As a result the scalar field is dominated by a sheet-like structure, cf. Brethouwer et al. (2003). Turbulent line segments are affected as well by the velocity field due to compressive and extensive strain in terms of a velocity difference Δu. Here, Δu denotes the velocity difference between the extreme points of each segment, where the velocity is projected along the direction of the segment. If $\Delta u > 0$ an extensive strain acts on the segments, and when $\Delta u < 0$ a compressive strain acts on the segment.

The conditional mean strain rate $\langle a|\ell\rangle$ of the length class ℓ is defined by

$$\langle a|\ell\rangle = \frac{1}{\ell}\big\langle \Delta u|\ell\big\rangle\,. \tag{5.29}$$

For large values of ℓ the conditional mean strain rate approaches an asymptotic limit, called a_∞. The limit a_∞ is calculated by fitting eq. 5.29 to a model equation proposed by Wang and Peters (2008) in the context of dissipation element analysis,

$$\langle a|\tilde{\ell}\rangle = a_\infty\left(1 - \frac{0.4}{\tilde{\ell}+0.1}\right)\,. \tag{5.30}$$

The values of a_∞ are given in tab. 5.4 obtained by DNS. The value of a_∞ increases with Reynolds number from 2.55 for case R0 to 16.05 for case R5. However, the scaling of a_∞ with the Reynolds number has not been answered satisfactorily by now. On the one hand, a_∞ could be related to the mean strain rate $s = \sqrt{\langle s_{ij}s_{ij}\rangle}$. This is a small scale quantity and scales according to K41 with τ_η. On the other hand, a_∞ is calculated in the limit $\ell \to \infty$ suggesting a scaling with the integral time scale τ, or equivalently, with $\langle\phi^2\rangle/\langle\chi\rangle$. These scaling relations are compared in tab. 5.4 revealing that the scaling of a_∞ with the Kolmogorov time τ_η or the mean strain rate s, respectively, is correct, yielding an approximately Reynolds number independent value of $a_\infty\tau_\eta \approx 0.075$.

Figure 5.12 shows the normalized conditional velocity difference

$$\frac{\big\langle \Delta u|\tilde{\ell}\big\rangle}{a_\infty \ell_m} \tag{5.31}$$

versus ℓ/ℓ_m. We suggest to non-dimensionalize $\langle\Delta u|\ell\rangle$ by $a_\infty\ell_m$, because this choice of variables yields a perfect collapse of all curves independent of Reynolds number. In fig. 5.12 we observe a negative value of the normalized structure function for $\ell/\ell_m < 1$. The zero-crossing occurs independently of Reynolds number exactly at $\ell/\ell_m = 1$. This implies that on average segments smaller than the mean length ℓ_m

Table 5.4: Scaling of the strain rate a_∞ with the Reynolds number. The strain rate is normalized by the Kolmogorov time τ_η and the integral time τ.

	R0	R1	R2	R3	R4	R5
Re_λ	88	119	184	215	331	529
a_∞	2.55	3.76	5.01	5.87	7.57	16.06
τ_η	0.0305	0.0223	0.0156	0.0127	0.0089	0.0041
τ	1.03	1.03	1.11	1.07	1.14	0.84
$a_\infty \tau_\eta$	0.08	0.08	0.08	0.07	0.07	0.07
$a_\infty \tau$	2.64	3.88	5.55	6.28	8.66	13.49

are subject to a compressive strain. For segments larger than the mean length, i.e. $\ell/\ell_m > 1$, the value of the normalized velocity structure function is positive and thus these segments are on average subject to an extensive strain.

In addition, we observe for $0.5 < \ell/\ell_m < 8$ a linear increase with a slope slightly larger than unity. This linear increase was also observed by Wang (2009) and Gampert et al. (2011) in the context of dissipation elements. By assuming a decorrelation of the velocity structure function from the scalar structure function in the inertial range these authors concluded a scaling of $\langle \Delta u|\ell\rangle$ with ℓ/τ. Considering the present data, this conclusion is not valid for turbulent line segments. By means of the scaling $a_\infty \tau_\eta = \text{const.}$ we obtain for scales $\ell/\ell_m > 0.5$ instead the scaling law

$$\langle \Delta u|\ell\rangle \propto \frac{\ell}{\tau_\eta} \tag{5.32}$$

suggesting a scaling of the conditional velocity increment with the inverse Kolmogorov time.

5.7 Statistical Description of Turbulent Line Segments

5.7.1 The Distribution of $\Delta\phi$ and ℓ

The normalized joint probability density function (jpdf) of $\Delta\phi$ and ℓ is shown in fig. 5.13 for case R1 and case R5. The axes of the jpdf are normalized by the mean length ℓ_m and the standard deviation $\sigma_{\Delta\phi}$ of $\Delta\phi$, defined as $\sigma_{\Delta\phi} = \langle(\Delta\phi)^2\rangle^{1/2}$. Note that $\Delta\phi$ is a centered quantity. The jpdf shows two distinct wings which correspond to positive segments with $\Delta\phi > 0$ and negative segments with $\Delta\phi < 0$, respectively. Due to the symmetry of the jpdf with respect to the x-axis, positive and negative segments are statistically identical, and we can in particular conclude that the mean length of positive and negative segments is equal. Besides a distinct maximum near the origin at $\tilde{\ell} \approx 0.2$ and $\Delta\phi \approx 0$, we observe a decrease towards the origin since

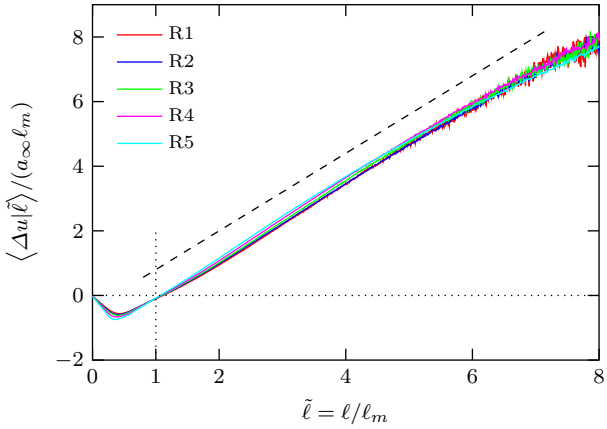

Figure 5.12: Normalized conditional velocity difference $\left\langle \Delta u|\tilde{\ell}\right\rangle/(a_\infty \ell_m)$ as a function of ℓ/ℓ_m for all cases.

small elements are annihilated because of molecular diffusion. Theoretically, there are two maxima at both wings because by definition no elements with $\Delta\phi = 0$ exists and therefore $P(\Delta\phi = 0, \ell) = 0$. However, these two maxima appear because of numerical effects as one single maxima. The region for larger ℓ is determined by extensive strain. Here, the positive and negative wings are clearly separated. This indicates that only very few long segments with very small scalar difference exists. Additionally the conditional mean scalar difference $\langle \Delta\phi|\ell/\ell_m\rangle$ is shown separately for positive and negative segments. These curves are symmetric with respect to the abscissa and their magnitude rises with ℓ/ℓ_m. This underlines that $\Delta\phi$ and ℓ are correlated and that large segments have on average a large scalar difference $\Delta\phi$. Even though the normalized length pdf is Reynolds number independent we will show below that the normalized joint pdf of $\Delta\phi$ and ℓ is not.

The conditional pdf $P(\Delta\phi|\ell)$ of the scalar difference can be obtained by the Bayes theorem according to

$$P(\Delta\phi|\ell) = \frac{P(\Delta\phi, \ell)}{P(\ell)} \tag{5.33}$$

where the marginal pdf $P(\ell)$ is defined as

$$P(\ell) = \int P(\Delta\phi, \ell)\mathrm{d}\Delta\phi\,. \tag{5.34}$$

The normalized conditional pdf is shown in fig. 5.14 for case R1 and R5 and at four different locations $\ell/\ell_m = 0.4$, $\ell/\ell_m = 1.0$, $\ell/\ell_m = 2.5$ and $\ell/\ell_m = 5.0$. Each curve

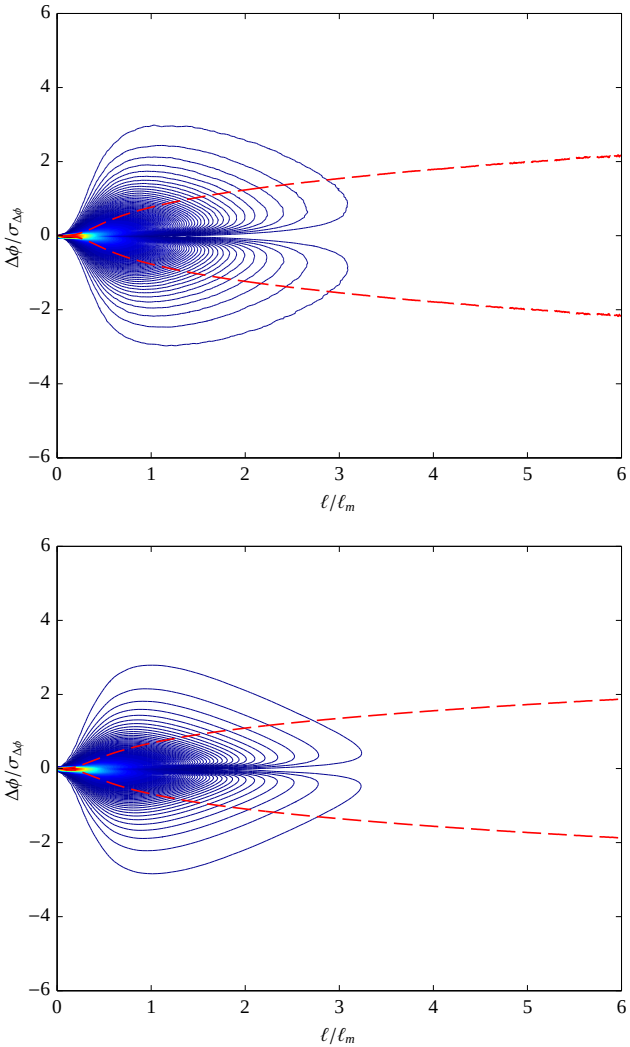

Figure 5.13: Normalized jpdf $\ell_m \sigma_{\Delta\phi} P(\ell/\ell_m, \Delta\phi/\sigma_{\Delta\phi})$ for case R1 (top) and case R5 (bottom). The red dashed line corresponds to the normalized conditional average $\left\langle \Delta\phi | \ell/\ell_m \right\rangle / \sigma_{\Delta\phi}$ evaluated separately for positive and negative segments.

is normalized to unity variance by the standard deviation $\sigma_{\Delta\phi}(\ell) = \langle(\Delta\phi)^2(\ell)\rangle^{1/2}$ of the corresponding length class ℓ. Figure 5.14 reveals that the pdfs are symmetric and centered with exponential tails and substantial deviations from Gaussianity. Similar to the scalar increment pdf $P(\Delta\phi|r)$, cf. fig. 6.1, the tails are longer and more stretched for small values of ℓ. This indicates that strong events are more probable at small scales. The tails become longer and more stretched with increasing Reynolds number (case R5). In addition, the conditional pdfs $P(\Delta\phi|\ell)$ reveal a vanishing probability for $\Delta\ell$ and $\Delta\phi$ approaching zero, because segments always have a finite length and scalar difference. Thus we observe two maxima at small positive and negative values of $\Delta\phi$ in particular for larger segments. For smaller segments this separation is numerically not resolved.

The marginal pdf of $\Delta\phi$ can be obtained by integration over the conditional pdf according to

$$P(\Delta\phi) = \int P(\Delta\phi|\ell)P(\ell)\mathrm{d}\ell \tag{5.35}$$

and thus all length classes are involved when determining $P(\Delta\phi)$. The normalized pdf $\sigma_{\Delta\phi}P(\Delta\phi/\sigma_{\Delta\phi})$ is shown in fig. 5.15a for all cases. It is also not Gaussian and has moderately stretched sub-exponential tails. The tails become somewhat more stretched with increasing Reynolds number.

Let us now consider the volume-weighted marginal pdf of $\Delta\phi$. It can be obtained from the conditional pdf by

$$P(\Delta\phi) = \frac{\int P(\Delta\phi|\ell)\ell P(\ell)\mathrm{d}\ell}{\int \ell P(\ell)\mathrm{d}\ell}\,, \tag{5.36}$$

where the weighting with ℓ takes into account that each segment occupies a volume that is proportional to its length. The volume-weighted normalized pdf of $\Delta\phi$ is depicted in fig. 5.15b for all cases. Compared to the segment-weighted normalized pdf it is considerably less peaked as short segments have on average a small scalar difference $\Delta\phi$.

5.7.2 Structure Functions and Conditional Moments

Turbulent flows are characterized by a complex spatial structure with various different length scales involved. Structure functions, where two points are separated by a distance r, provide useful information about the non-locality of turbulent flows, cf. Kolmogorov (1941a), Obukhov (1949b), Corrsin (1951), Yaglom (1949) and Monin and Yaglom (1975). The conventional nth order structure function is defined as

$$\langle(\Delta\phi)^n\rangle(\boldsymbol{r}) = \langle(\phi(\boldsymbol{x}+\boldsymbol{r}) - \phi(\boldsymbol{x}))^n\rangle\,. \tag{5.37}$$

For homogeneous anisotropic turbulence the structure function is independent of the position but depends on the direction of the separation vector $\boldsymbol{r}$. Here, we take

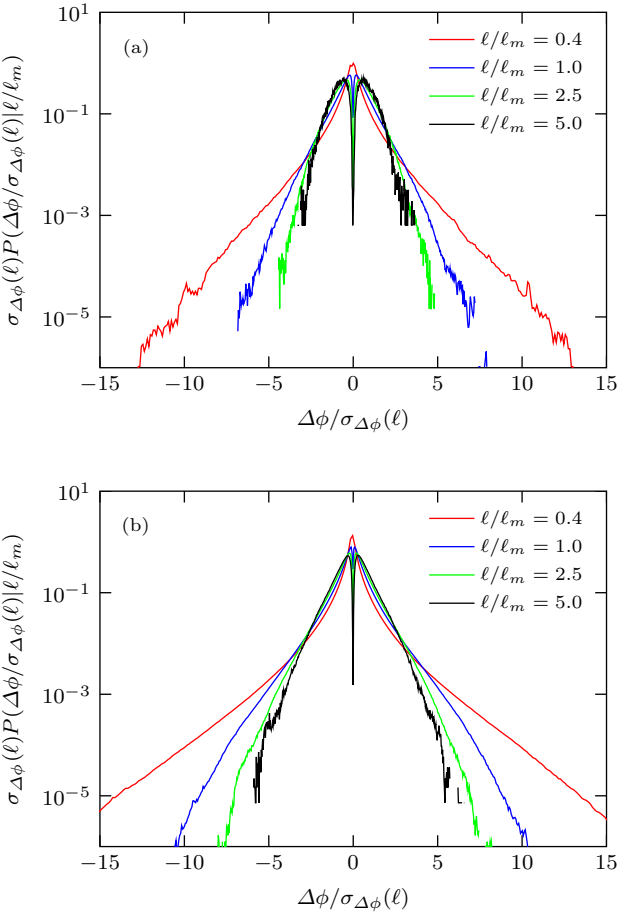

Figure 5.14: Normalized conditional pdf $\sigma_{\Delta\phi}(\ell)P(\Delta\phi/\sigma_{\Delta\phi}(\ell)|\ell/\ell_m)$ for case R1 (a) and case R5 (b). Each curve is normalized to unity variance.

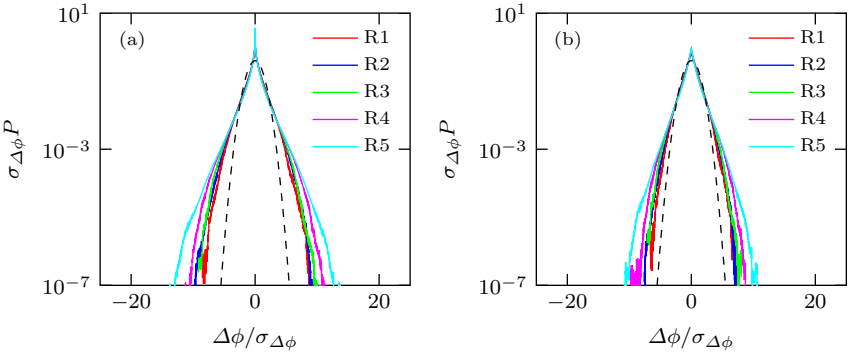

Figure 5.15: Normalized pdf of $\Delta\phi$ for all cases. The dashed line indicates a Gaussian with unity standard deviation. Segment-weighted (a) and volume-weighted (b).

the separation vector $\boldsymbol{r}$ along the x-axis so that it is aligned with the direction in which the turbulent line segments are calculated.

In the same spirit we can define the nth order conditional moment $\langle(\Delta\phi)^n|\ell\rangle$ of turbulent line segments. It is obtained from the conditional pdf $P(\Delta\phi|\ell)$ by integration over $\Delta\phi$, i.e.

$$\langle(\Delta\phi)^n|\ell\rangle = \int (\Delta\phi)^n P(\Delta\phi|\ell)\mathrm{d}(\Delta\phi)\,. \tag{5.38}$$

The conditional mean is calculated for segments belonging to the same length class instead for the fixed separation length r as for the conventional structure function. Differently from dissipation elements, $\Delta\phi$ can be positive or negative.

Figure 5.16 compares the second order conditional moment $\langle(\Delta\phi)^2|\ell/\eta\rangle$ of turbulent line segments with the conventional second order structure function $\langle(\Delta\phi)^2\rangle(r/\eta)$. Both functions are normalized by $\langle\phi^2\rangle$. For large values of r/η the second order conventional structure function tends to a value of two, which corresponds to its theoretical limit, i.e.

$$\lim_{r\to\infty}\frac{\langle(\Delta\phi)^2\rangle}{\langle\phi^2\rangle} = \lim_{r\to\infty}\frac{\langle\phi^2 - 2\phi\phi' + \phi'^2\rangle}{\langle\phi^2\rangle} = 2\,, \tag{5.39}$$

where for the last equality homogeneity and decorrelation of two-point quantities in the large scale limit have been used. Within the inertial subrange the structure functions scales as

$$\langle(\Delta\phi)^2\rangle \propto \left(\frac{r}{\eta}\right)^{0.6}\,. \tag{5.40}$$

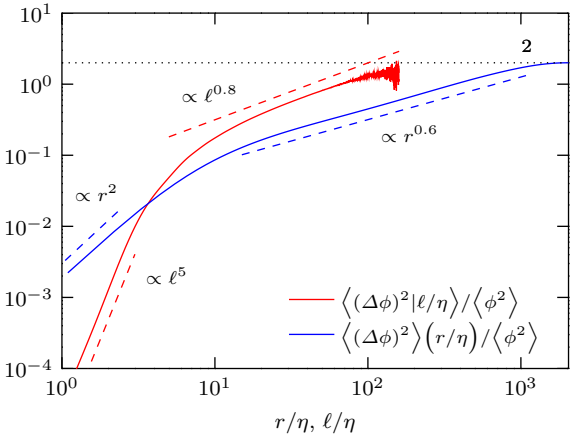

Figure 5.16: Comparison of second order structure function $\langle(\Delta\phi)^2\rangle(r/\eta)/\langle\phi^2\rangle$ and second conditional moment $\langle(\Delta\phi)^2|\ell/\eta\rangle/\langle\phi^2\rangle$ for case R5. Inertial subrange scaling can be observed within the range $20 \leq r/\eta \leq 1000$. The black dotted line indicates the large scale limit of two.

For small scales $r \to 0$, $\langle(\Delta\phi)^2\rangle$ can be expanded into a Taylor series, yielding

$$\lim_{r\to 0}\left\langle (\Delta\phi)^2 \right\rangle = \lim_{r\to 0} r^2 \left\langle \left(\frac{\partial\phi}{\partial x_1}\right)^2 \right\rangle \propto r^2 \,. \tag{5.41}$$

A scaling according to eq. 5.41 can be observed for $0 < r/\eta < 7$.

For turbulent line segments the separation length ℓ is limited by the length of the segments and well converged statistics can be computed up to $\ell/\eta \approx 150$. An inertial subrange scaling with

$$\langle(\Delta\phi)^2\,|\ell/\eta\rangle \propto \left(\frac{\ell}{\eta}\right)^{0.8} \tag{5.42}$$

is observed, where the scaling exponent is higher compared to the conventional structure function. In addition, it is noticed that the absolute value of $\langle(\Delta\phi)^2\,|\ell/\eta\rangle$ is higher compared to $\langle(\Delta\phi)^2\rangle$ for $\ell/\eta \geq 5$. This can be explained by the fact that turbulent line segments relate only extreme points while the conventional structure function contains all points.

The scaling of structure functions and turbulent line segments will be examined in detail in sec. 6.2.

5.7.3 The Distribution of g and ℓ

In particular for scalar mixing the scalar gradient plays an important role. Besides the local gradient, the mean gradient of turbulent line segments can be defined as

$$g = \frac{\Delta\phi}{\ell}\,, \tag{5.43}$$

which is related to the local gradient $\partial\phi/\partial x$ in x-direction by

$$\frac{1}{\ell}\int_0^\ell \frac{\partial\phi}{\partial x}\mathrm{d}x = \frac{\Delta\phi}{\ell} = g\,. \tag{5.44}$$

According to eq. 5.44 the mean gradient g is averaged over an intermediate length scale ℓ which equals on average the mean length ℓ_m. Despite the fact that g is defined as a segment-based average, it is a fluctuating quantity with zero mean.

The joint distribution function of $\Delta\phi$ and ℓ provides a complete statistical description of turbulent line segments. Quantities like the joint distribution function $P(g,\ell)$ can be directly derived from $P(\Delta\phi,\ell)$, i.e.

$$\begin{aligned} P_{g\ell}(g,\ell) &= \int_{-\infty}^{\infty} \delta\left(g - \frac{\Delta\phi}{\ell}\right) P_{\Delta\phi\ell}(\Delta\phi,\ell)\mathrm{d}(\Delta\phi) \\ &= \int_{-\infty}^{\infty} \ell\delta\left(g\ell - \Delta\phi\right) P_{\Delta\phi\ell}(\Delta\phi,\ell)\mathrm{d}(\Delta\phi) \\ &= \ell\, P_{\Delta\phi\ell}(g\ell,\ell)\,, \end{aligned} \tag{5.45}$$

where the second and third equality follow from the properties of the Dirac delta function, cf. Pope (2000). The normalized joint pdf $P(g,\ell)$ is shown in fig. 5.17 for case R1 and case R5, where the axes are normalized by mean length ℓ_m and $\sigma_g = \langle g^2\rangle^{1/2}$, respectively. Note that g is a centered quantity. The jpdf exhibits two wings for positive and negative gradients of g and is symmetric with respect to the x-axis, i.e. positive and negative mean gradients are statistically identical.

Additionally, the normalized conditional mean $\langle g/\sigma_g|\ell/\ell_m\rangle$ is depicted in fig. 5.17 separately for positive and negative segments. Beside a rise from the origin it exhibits only a small dependence on the length scale. This is different for higher moments as we will show below. In addition the jpdf has a distinct maximum near the origin. Large values of g can be found at scales $\ell/\ell_m \approx 0.6$, or respectively $\ell/\eta \approx 6$, but not for $\ell \to 0$. This corresponds in the jpdf $P(\Delta\phi,\ell)$ to the region in the upper left, where the scalar difference $\Delta\phi$ is large but the length ℓ is still small. In the scalar field this region shows up as large cliffs. These cliffs are typically formed in the scalar field by a compressive straining motion at intermediate scale. Cliffs are principally present in each direction of the scalar field. In the direction perpendicular to the mean scalar gradient they show up as rising or descending cliffs, which can be

treated as statistically equal. In the direction parallel to the mean scalar gradient so-called cliff-ramp structures are observed. This issue will be addressed in detail in sec. 5.7.5.

Tong and Warhaft (1994) suggested that the strain rate that acts on the cliffs is proportional to u'/l_t and therefore the thickness of the cliffs should scale with the Taylor length λ. On the other hand, Moisy et al. (2001) argued based on experimental measurements for various Reynolds numbers that the width of the steepest cliffs scales with the Kolmogorov scale η. Consistently, Batchelor (1959) estimated the thickness of scalar sheets as $\propto \eta$. Brethouwer et al. (2003) defined the width of the cliffs as the zero-crossing of the scalar gradient correlation function $f_{\phi_x}(r)$, cf. eq. 5.22, and estimated the width as $4\eta \mathrm{Sc}^{-1/2}$. These results agree well with the present finding obtained by turbulent line segments.

The second normalized conditional moment $\langle g^2/\sigma_g^2|\ell/\ell_m\rangle$ is shown in fig. 5.18 for all cases. Differently to the first normalized moment it exhibits a strong dependence on the length scale. Figure 5.18 confirms that the steepest mean gradients g are situated for all Reynolds numbers on average at $\ell/\ell_m = 0.6$. This result further supports the finding that the width of the steepest cliffs scales with the Kolmogorov length η, as $\ell_m \propto \eta$. All curves $\langle g^2|\ell/\ell_m\rangle/\sigma_g^2$ collapse when normalized by σ_g. The a maximum value $\langle g^2|\ell/\ell_m\rangle/\sigma_g^2 \approx 1.5$ occurs at $\ell/\ell_m \approx 0.6$.

Additionally, fig. 5.18 shows the inertial-convective range scaling of $\langle g^2|\ell\rangle$. The nth conditional moment of the mean gradient $\langle g^n|\ell\rangle$ can be generally expressed by means of the nth conditional moment of the scalar difference $\langle(\Delta\phi)^n|\ell\rangle$, namely

$$\langle g^n|\ell\rangle = \frac{\langle(\Delta\phi)^n|\ell\rangle}{\ell^n} \propto \ell^{\zeta_\phi(n)-n}\,. \tag{5.46}$$

Here, the second equality follows from the inertial range scaling behavior of $\langle(\Delta\phi)^n|\ell\rangle$ with the scaling exponent $\zeta_\phi(n)$. Note that eq. 5.46 is only non-zero for even moments. In sec. 6.2 we will show that the scaling exponent $\zeta_\phi(n)$ is always smaller than $n/3$. This yields for scales within the inertial subrange a negative scaling exponent for the second order conditional moment of g, i.e.

$$\langle g^2|\tilde{\ell}\rangle/\sigma_g^2 \propto \tilde{\ell}^{-1.05}\,. \tag{5.47}$$

The scaling exponent is independent of Reynolds number.

The normalized conditional pdf $\sigma_g(\ell)P(g/\sigma_g(\ell)|\ell/\ell_m)$ is depicted in fig. 5.19 for case R1 and case R5 at four different locations ℓ/ℓ_m equal 0.4, 1.0, 2.5, and 5.0. Here, $\sigma_g(\ell)$ denotes the standard deviation of g for the length class ℓ, defined as $\sigma_g(\ell) = \langle g(\ell)^2\rangle^{1/2}$, which is used to normalize the pdf for each length class to unity variance. The pdf is symmetric and exhibits approximately exponential tails which become more stretched with increasing Reynolds number. Therefore, the normalized pdf cannot be considered as universal. Similar to the conditional pdf of $\Delta\phi$, cf. fig. 5.14, the probability for $g = 0$ vanishes and we can observe two maxima at small

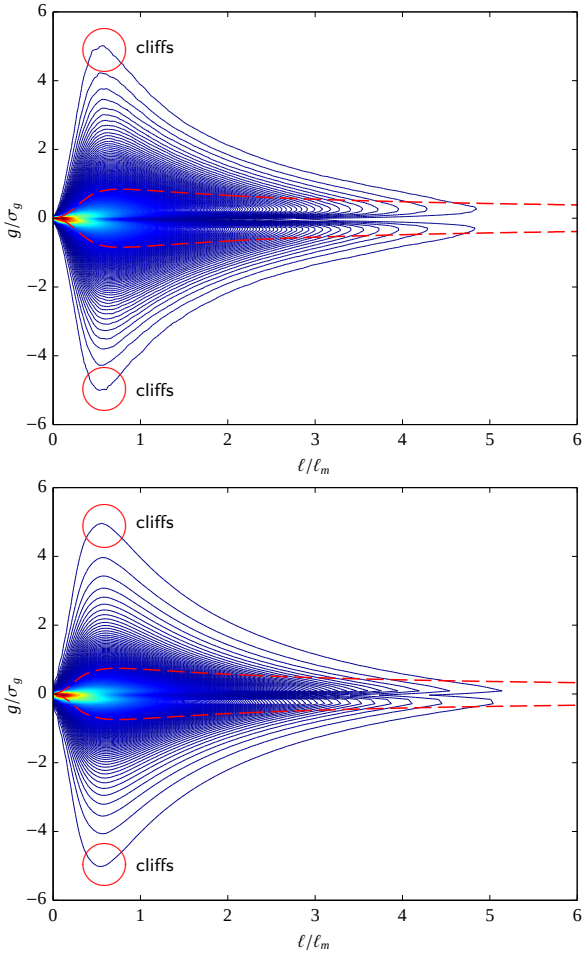

Figure 5.17: Normalized jpdf $\ell_m \sigma_g P(\ell/\ell_m, g/\sigma_g)$ for case R1 (top) and case R5 (bottom). The red dashed line corresponds to the normalized conditional mean $\left\langle g|\ell/\ell_m \right\rangle/\sigma_g$ evaluated separately for positive and negative segments.

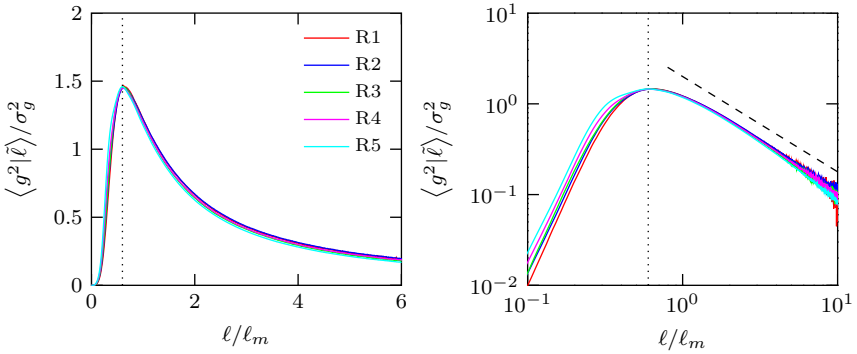

Figure 5.18: Normalized conditional mean $\langle g^2|\tilde{\ell}\rangle/\sigma_g^2$ for all cases. The vertical dotted line denotes the value $\ell/\ell_m = 0.6$ where the steepest gradients are situated on average. The dashed line represents the inertial-convective range scaling $\propto \ell^{-1.05}$.

positive and negative values of g. At high Reynolds number (case R5) these maxima are less distinct. Additionally, for both cases the tails become less stretched when the length class ℓ/ℓ_m increases, confirming that large extreme gradients occur especially at smaller length scales.

The occurrence of cliffs is closely related to scalar intermittency at small scales. The cliffs are relatively rare events and are located in the far tails of the marginal pdf $P(g)$, which is shown in fig. 5.20 normalized by σ_g. The marginal pdf $P(g)$ exhibits moderately stretched exponential tails and is far from Gaussian. With increasing Reynolds number the tails become wider and more stretched and the flatness of the pdf increases. For comparison the normalized pdf of the local gradient $P(\phi_x)$ is shown, which exhibits significantly wider substantially stretched exponential tails. But below we will show that the rate at which the flatness rises is the same for the pdf of g and ϕ_x. This results also suggest that the normalized marginal gradient pdfs do not converge to a single curve with increasing Reynolds number. Similar results have been reported by Yeung et al. (2005) and Ishihara et al. (2007).

5.7.4 Scaling of the Normalization Quantities with the Reynolds Number

Statistical quantities in the previous sections have been normalized by the standard deviation of the scalar difference $\sigma_{\Delta\phi}$ and the standard deviation of mean gradient σ_g of turbulent line segments. In order to obtain dimensional statistics, we need to know how the normalization quantities scale with the Reynolds number. The scaling of the mean length ℓ_m has been discussed previously.

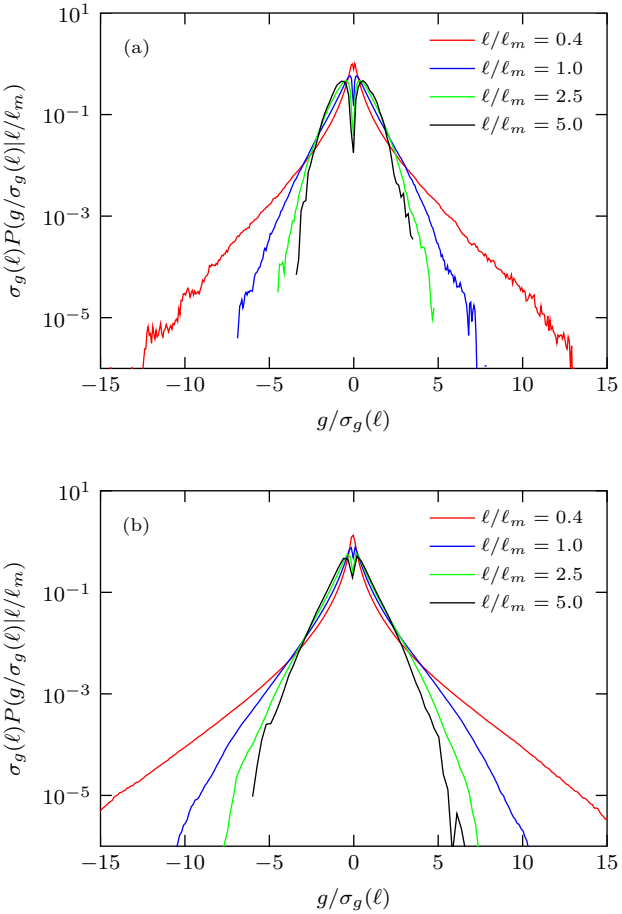

Figure 5.19: Normalized conditional pdf $\sigma_g(\ell)P(g/\sigma_g(\ell)|\ell/\ell_m)$ for case R1 (a) and case R5 (b). Each curve is normalized by $\sigma_g(\ell)$ to unity standard deviation, where $\sigma_g(\ell)$ denotes the standard deviation of g for the length class ℓ.

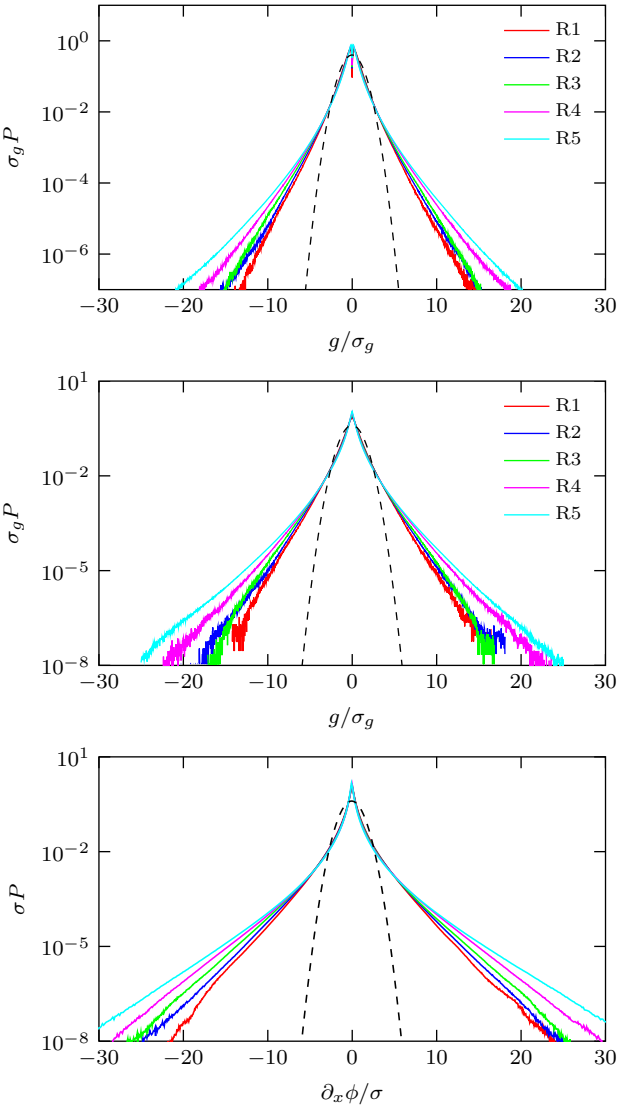

Figure 5.20: Normalized pdf $\sigma_g P(g/\sigma_g)$ of the mean gradient, volume-weighted and segment-weighted, as well as normalized pdf $\sigma_{\partial_x \phi} P(\partial_x \phi/\sigma_{\partial_x \phi})$ of the local gradient (from top to bottom) for all cases. The dashed black line represents the standard normal distribution.

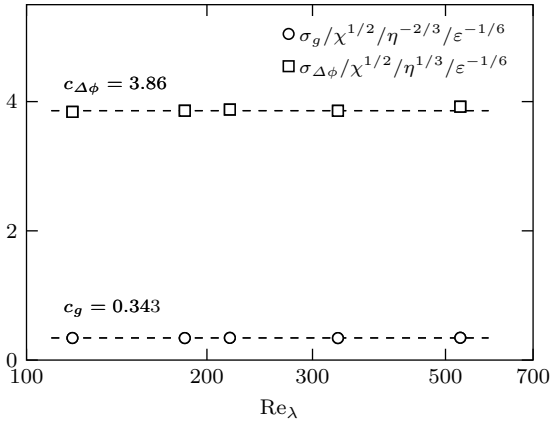

Figure 5.21: Scaling of $c_{\Delta\phi}$ and c_g with the Reynolds number for all cases, cf. eqs. 5.48 and 5.49.

As $\Delta\phi$ and g are small-scale quantities, their standard deviation should obey a scaling with the KOC variables, i.e.

$$\sigma_{\Delta\phi} = c_{\Delta\phi}\langle\chi\rangle^{1/2}\langle\varepsilon\rangle^{-1/6}\eta^{1/3}\,, \tag{5.48}$$

and

$$\sigma_g = c_g\langle\chi\rangle^{1/2}\langle\varepsilon\rangle^{-1/6}\eta^{-2/3}\,. \tag{5.49}$$

Here, $c_{\Delta\phi}$ and c_g are quasi-universal constants. Figure 5.21 shows $c_{\Delta\phi}$ and c_g as a function of Reynolds number, where $c_{\Delta\phi}$ equals 3.86 and c_g equals 0.343 independently of Reynolds number. This justifies the proposed KOC scaling according to eqs. 5.48 and 5.49.

5.7.5 Cliff-Ramp Structures

A characteristic feature of passive scalar mixing with imposed mean gradient is the persistence of non-zero skewness of the scalar derivative in the direction of the mean scalar gradient. This invalidates the local isotropy assumption of the Kolmogorov-Obukhov-Corrsin (KOC) theory for passive scalars. The non-zero skewness stems from sharp fronts at the border of coherent structures in the scalar field which manifest themselves as cliff and ramps, i.e. regions of steep gradients followed by a slow descent, cf. Sreenivasan et al. (1980) and Tavoularis (1985). This is illustrated by fig. 5.22, where the scalar ϕ and its gradient in y-direction $\partial_y\phi$ are shown along a straight line in y-direction through the box for case R1. A mean scalar gradient is a necessary condition for these ramps to exist. The velocity fluctuations in the

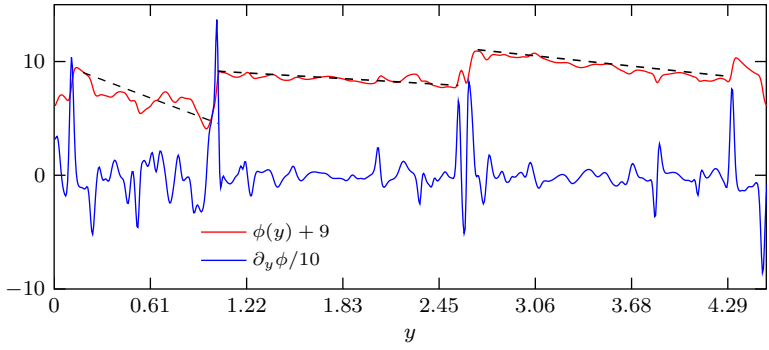

Figure 5.22: Cut along a straight line through the scalar field in y-direction for case R1 illustrating cliff-ramp structures. The occurrence of ramps is highlighted by black dashed lines. The scalar ϕ is shifted upwards by the value of 9 and the scalar gradient in y-direction $\partial_y \phi$ is divided by a factor of 10 for clarity.

direction of the mean scalar gradient cause an excitation of the scalar fluctuation field such that ramp-like features arise, but only in the direction of the mean scalar gradient. The scalar fluctuations are excited at all scales down to the Kolmogorov scale and thus the anisotropy persist even at the smallest scales. In the course of this section we will examine the anisotropy of the scalar field by the method of turbulent line segments. This approach provides additional novel insight into the physics behind cliff-ramp structures as it explains in which flow regimes such structures occur.

Figure 5.23 shows the normalized pdf of $\partial_y \phi$ and g where the segments are calculated in the direction of the mean scalar gradient for all cases. Compared to the corresponding pdfs in perpendicular direction, cf. fig. 5.20, both sides of the pdfs are altered, as the positive tails become more stretched and the negative tails become less stretched. Statistical quantities of the scalar reveal an axial symmetry around the direction of the mean gradient and reflectional invariance to the plane perpendicular to the mean gradient, cf. Gotoh et al. (2011).

By the decomposition along a straight line according to the local extrema it follows that within a positive segment the scalar difference $\Delta\phi$ is always positive while in a negative segment the scalar difference $\Delta\phi$ is always negative. This property renders the method of turbulent line segments perfectly suited to study cliff-ramp structures. In the present work, gradient statistics are positively skewed, yielding the following relation

$$\langle |\Delta\phi| \, | \ell, \Delta\phi > 0 \rangle \geq \langle |\Delta\phi| \, | \ell, \Delta\phi < 0 \rangle \, , \tag{5.50}$$

which states that on average for each length class ℓ the absolute value of the scalar difference is larger in the sub-ensemble of positive segments than in the sub-ensemble

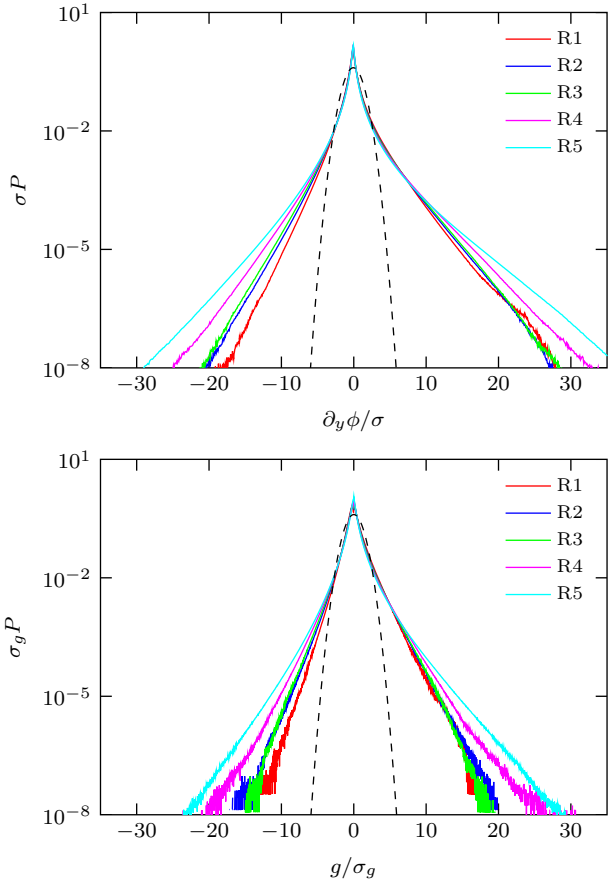

Figure 5.23: Normalized pdf of the sclar gradient $\partial_y \phi$ and normalized pdf of g, where the segments are calculated in y-direction. The dashed black line represents a Gaussian with unity variance.

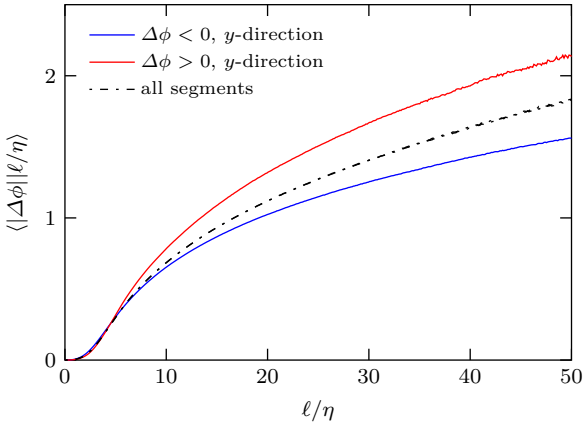

Figure 5.24: Conditional scalar difference $\langle|\Delta\phi||\ell/\eta, \Delta\phi\rangle$ for positive segments with $\Delta\phi > 0$, negative segments with $\Delta\phi < 0$ and all segments for case R1. The segments are computed in y-direction.

of negative segments. This is further illustrated in fig. 5.24, where the conditional mean of $|\Delta\phi|$ is shown for positive, negative and all segments. The conditional mean for all segments lies in between.

Let us now derive a relation between ℓ_m^- and ℓ_m^+, where the former denotes the mean length of negative segments and the latter the mean length of positive segments. To this end we multiply eq. 5.50 with $\ell/\ell_m P(\ell)$ and integrate the result over ℓ to obtain volume weighted statistics, yielding

$$\langle|\Delta\phi|\,|\Delta\phi > 0\rangle \geq \langle|\Delta\phi|\,|\Delta\phi < 0\rangle\,. \tag{5.51}$$

The above relation can be expressed by means of the pdfs of $\Delta\phi$, yielding

$$\frac{1}{N^+}\int_0^\infty |\Delta\phi| P(\Delta\phi)\mathrm{d}(\Delta\phi) \geq \frac{1}{N^-}\int_{-\infty}^0 |\Delta\phi| P(\Delta\phi)\mathrm{d}(\Delta\phi)\,, \tag{5.52}$$

where N^+ denotes the number of grid points associated with the ensemble of positive segments and N^- denotes the number of grid points associated with the ensemble of negative segments. From this result we derive

$$\frac{N^-}{N^+} \geq \frac{\int_{-\infty}^0 |\Delta\phi| P(\Delta\phi)\mathrm{d}(\Delta\phi)}{\int_0^\infty |\Delta\phi| P(\Delta\phi)\mathrm{d}(\Delta\phi)} = 1\,, \tag{5.53}$$

where the last equality follows from the fact that $\Delta\phi$ is a centered variable and thus the nominator and the denominator of eq. 5.53 equal each other. The number of

Table 5.5: Mean length ℓ_m of turbulent line segments for all cases for turbulent line segments computed in x- and y-direction. For turbulent line segments in y-direction the mean length of positive segments ℓ_m^+ and negative segments ℓ_m^- differ. For reference the gradient skewness $S(\phi_y)$ and the mean gradient skewness of turbulent line segments in y-direction $S(g_y)$ is given.

case	R0	R1	R2	R3	R4	R5
ℓ_m^x	0.182	0.116	0.065	0.052	0.031	0.015
ℓ_m^y	0.189	0.120	0.067	0.053	0.032	0.015
ℓ_m^-	0.223	0.139	0.076	0.059	0.036	0.016
ℓ_m^+	0.154	0.100	0.058	0.047	0.029	0.014
ℓ_m^-/ℓ_m^+	1.45	1.39	1.31	1.26	1.24	1.14
$S(\phi_y)$	1.65	1.73	1.60	1.55	1.56	1.36
$S(g_y)$	1.30	1.29	1.15	1.06	1.05	0.94

grid points of positive segments N^+ is directly proportional to the mean length of positive segments ℓ_m^+ and analogously $N^- \propto \ell_m^-$. This yields the final result

$$\frac{\ell_m^-}{\ell_m^+} \geq 1\,, \tag{5.54}$$

which only becomes an equality at infinite Reynolds number when the scalar gradient skewness tends to zero. The ratio ℓ_m^-/ℓ_m^+ is given in tab. 5.5 for all cases. It decreases with the Reynolds number from 1.45 for case R0 to 1.14 for case R5. Additionally, tab. 5.5 shows the values of the skewness of ϕ_y and g_y. Both decrease with Reynolds number. This finding suggests that the ratio ℓ_m^-/ℓ_m^+ can be understood as a surrogate of the definition of the scalar gradient skewness.

Figure 5.25 shows the normalized marginal pdf of the length separately for positive, negative, and all segments for case R1. The pdf is normalized by the Kolmogorov length, i.e. $\widetilde{P}(\tilde{\ell}) = \eta P(\ell/\eta)$, because the mean length ℓ_m depends on direction. All curves exhibit a linear rise at the origin for small segments. Small segments are dominated by a viscous drift which does not discriminate between positive and negative segments so that close to the origin all curves collapse and exhibit virtually the same slope. The maximum of all curves occurs at approximately $\ell/\eta \approx 5.5$. However, for negative segments the probability to have long segments is larger than for positive segments. This leads to the result that $\ell_m^- > \ell_m^+$. The pdf for all (positive and negative) segments is embedded in between the two, yielding

$$\ell_m^+ < \ell_m^y < \ell_m^-\,. \tag{5.55}$$

Additionally, the normalized pdf $\widetilde{P}(\tilde{\ell})$ for segments in x-direction is depicted. It collapses with $\widetilde{P}(\tilde{\ell})$ for segments in y-direction. This underlines that $\widetilde{P}(\tilde{\ell})$ can be

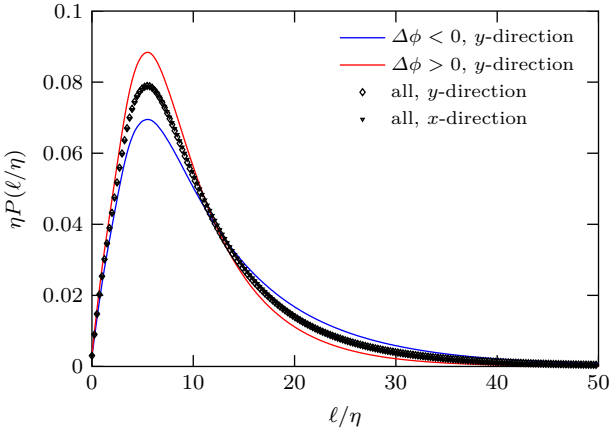

Figure 5.25: Normalized marginal pdf of the length of positive ($\Delta\phi > 0$), negative ($\Delta\phi < 0$), and all segments for case R1. The curves for negative and positive segments (in x-direction and in y-direction) are embedded in between and collapse independently of direction. The pdf is normalized by the Kolmogorov length η as the mean length ℓ_m depends on direction.

considered as quasi-universal, as it is not only independent of Reynolds number but also independent of direction, cf. sec. 5.5.

Furthermore, tab. 5.5 suggests that with increasing Reynolds number ℓ_m^+ and ℓ_m^- tend to ℓ_m^y. This result confirms the local isotropy assumption in the limit of large Reynolds numbers.

Next, we will address the question which phenomena lead to cliff-ramp structures and illustrate how the statistics of turbulent line segments are altered by cliff-ramp structures. Figure 5.26 shows the normalized joint pdf of $\Delta\phi$ and ℓ for case R1 and case R5. Differently to the joint pdf calculated for turbulent line segments perpendicular to the mean scalar gradient, cf. fig. 5.13, the wings of the jpdf exhibit an asymmetry with respect to $\Delta\phi$. The lower wing, which corresponds to the negative segments is longer than the upper wing which corresponds to the positive segments. This agrees with the finding that the mean length of negative segments ℓ_m^- is larger than the mean length of positive ones ℓ_m^+. With respect to the abscissa, the positive branch attains higher values and has a steeper slope at the origin than the negative one. Steep positive cliffs arise from the upper-left region where the length scale is still small but the scalar difference is already large. This region is less pronounced in the negative branch yielding on average smaller negative cliffs. This observation is further supported by fig. 5.27, where the normalized joint pdf of g and ℓ is shown for case R1 and case R5. The joint pdf inherits the asymmetry from the

joint pdf of $\Delta\phi$ and ℓ. Large negative and positive gradients occur approximately at a length scale $\ell/\ell_m \approx 0.55$, where large positive gradients are more probable than large negative gradients. In addition, the negative branch has a distinct tail for very long segments with rather small value of the gradient. Ramp-like structures stem from this region of the joint pdf and are only present in the negative wing, i.e. for negative gradients. The normalized joint pdfs $P(\Delta\phi, \ell)$ and $P(g, \ell)$ are not universal. However, with increasing Reynolds number the asymmetry between the upper and lower wing is reduced reflecting the fact that local isotropy will be approached in the limit of very large Reynolds numbers.

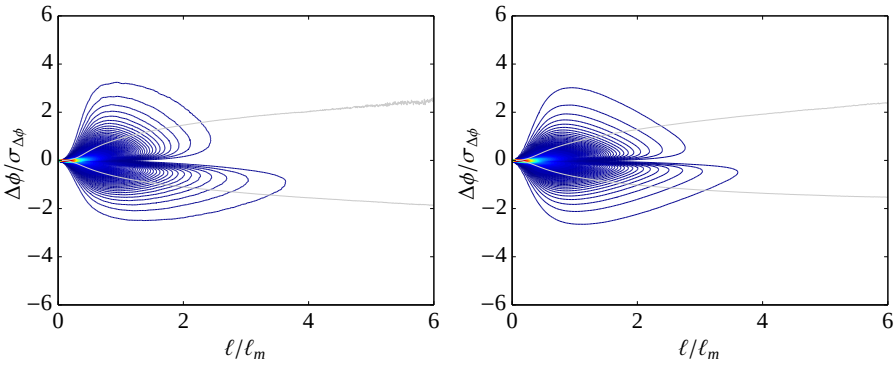

Figure 5.26: Normalized joint pdf of $\Delta\phi$ and ℓ for case R1 (left) and case R5 (right) computed for segments parallel to the direction of the scalar mean gradient.

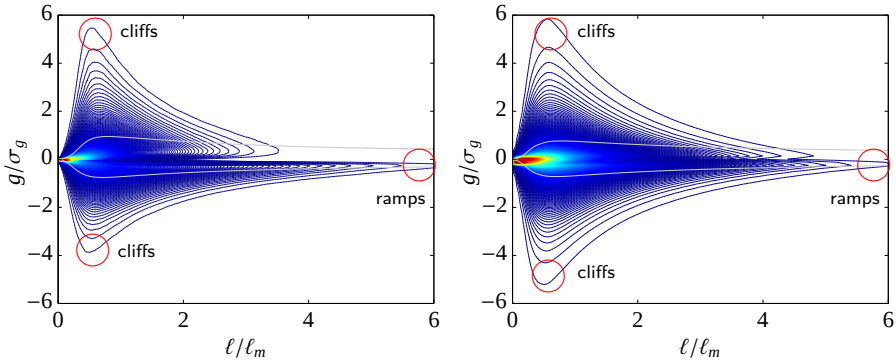

Figure 5.27: Normalized joint pdf of g and ℓ for case R1 (left) and case R5 (right) computed for segments parallel to the direction of the scalar mean gradient.

6 Regular and Anomalous Scaling of Two-Point Statistics and Gradients

6.1 Introduction

At sufficient high Reynolds numbers the statistics of fine-scale turbulence tend to become universal. Scaling laws for fine-scale turbulence, first formulated by Kolmogorov (1941a), Obukhov (1949b) and Corrsin (1951), are essentially closure hypotheses relating consecutive moments of the scalar or velocity increment to each other. For scalar turbulence there is only a single case, where no closure is needed. This is the exact equation for the third order mixed velocity-scalar structure function derived by Yaglom (1949), namely

$$\langle (\Delta u)(\Delta \phi)^2 \rangle = -2/3 \langle \chi \rangle r \,, \tag{6.1}$$

which is valid in the inertial subrange for stationary, homogeneous and isotropic turbulence at high Reynolds numbers. However, Yaglom's equation may lead to the erroneous assumption that a scaling which involves only $\langle \chi \rangle$ and r is universally valid, cf. Landau and Lifshitz (1963), Oboukhov (1962) and Kolmogorov (1962). Deviations from this laws, i.e. the deviation of the scaling exponents of structure functions from their respective values obtained from dimensional analysis, are denoted by anomalous scaling. Another kind of anomalous scaling is related to the case where the exponent of the $2n$th order moment does not equal n times the exponent of the second order moment. Anomalous scaling can be observed in the dissipative range and in the inertial subrange and originates from strong fluctuations of the dissipation and the occurrence of large rare events so that the degree of non-Gaussianity depends on scale, cf. Warhaft (2000) and Sreenivasan and Antonia (1997).

The problem of anomalous scaling can be understood as one of the unsolved problems in turbulence research, cf. Shraiman and Siggia (2000) and Falkovich and Sreenivasan (2006). One of the major aspects of the present chapter is to adopt Kolmogorov's phenomenology to the method of turbulent line segments. Additionally, we will examine anomalous scaling for structure functions and turbulent line segments in the inertial subrange and for the moments of the scalar gradient in the dissipative range. However, we will show that dissipative effects couple to the inertial subrange so that the whole range of scales has to be taken into account. Furthermore, we will propose a model for the scaling of the moments of the scalar gradient.

6.2 Structure Functions and Conditional Moments

For the nth-order moments of the absolute value of scalar increment $\langle|\Delta\phi|^n\rangle$ at high Reynolds and Peclet numbers, a power-law of the form

$$\langle|\Delta\phi|^n\rangle \propto r^{\zeta_\phi(n)} \tag{6.2}$$

can be observed within the inertial-convective range. Here, n is a positive integer and $\zeta_\phi(n)$ is called nth order scaling exponent. Eulerian increments are considered as the scalar differences are computed over spatial separations at the same instant of time. Additionally, we use the absolute value of $\Delta\phi$ in order to obtain non-vanishing exponents of the odd moments. The KOC-theory suggests that the scaling exponents are linear functions of n. This implies that the relation $\zeta_\phi(n) = n/3$ holds. However, for higher orders the scaling exponents deviate from the predicted values, cf. fig. 6.4. The deviation of ζ_ϕ from KOC-scaling increases with the order n. This deviation can be attributed to a phenomenon called internal intermittency, and was first observed by Batchelor and Townsend (1949). Internal intermittency has been attributed to local and temporal strong fluctuations of the energy dissipation ε and the scalar dissipation χ. It is evident in both inertial range and dissipative range, cf. Kolmogorov (1962) and Frisch (1995). Due to this effect the normalized conditional pdf $P(\Delta\phi|r)$, cf. fig. 6.1, is not self-similar for different scales and thus $\zeta_\phi(n)$ must deviate from the KOC prediction. Kraichnan (1974) argued that this deviation depends on the details of the nonlinear interaction between different scales and thus the scaling exponents cannot be derived from first-principles. Intermittency models for turbulent flows and scalar turbulence have been developed by many authors, cf. Kolmogorov (1962), Oboukhov (1962) and Kraichnan (1994).

In the same spirit we can define the scaling exponents for turbulent line segments $\zeta_\phi(n)$ as

$$\langle|\Delta\phi|^n|\ell\rangle \propto \ell^{\zeta_\phi(n)}\,. \tag{6.3}$$

Figure 6.2 shows for case R4 the nth order structure function $\langle|\Delta\phi|^n\rangle$ up to order 10 and the nth order conditional moment $\langle|\Delta\phi|^n|\ell\rangle$ up to order 8, both non-dimensionalized by Kolmogorov variables. The statistics for turbulent line segments are only shown up to the 8th order and for $r/\eta \leq 100$, because of statistical limitations. When the order n or the separation distance increase the required information resides in the far tails of the corresponding pdf, where convergence problems occur. Next, fig. 6.3 displays as well for case R4 the moments of the optimally compensated conventional structure functions

$$\left\langle(\Delta\phi)^n\right\rangle/(\eta^{n/3}\chi^{n/2}\varepsilon^{-n/6})/(r/\eta)^{\zeta_\phi(n)} \tag{6.4}$$

and the optimally compensated conditional moments

$$\left\langle(\Delta\phi)^n|\tilde{\ell}\right\rangle/(\eta^{n/3}\chi^{n/2}\varepsilon^{-n/6})/(\ell/\eta)^{\zeta_\phi(n)}\,. \tag{6.5}$$

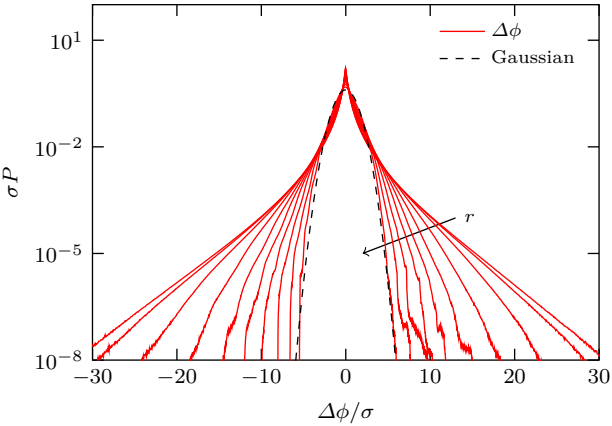

Figure 6.1: Normalized pdf of the scalar increment $\Delta\phi(r)$ for $r_n/\eta = 2^{n-1}\,(\Delta x/\eta)$, with $n = 1, \cdots, 10$, for case R5. The pdfs are normalized by their respective standard deviations. For $n = 10$ the scalar increment pdf collapses with the Gaussian distribution.

Note that the scaling exponents $\zeta_\phi(n)$ are different for conventional structure functions and turbulent line segments. In order to properly determine the scaling exponents, we need to determine the width of the inertial-convective range. This can be systematically conducted based on Yaglom's 2/3 law, cf. eq. 6.1. The width of the inertial-convective range is assumed as the range where the compensated mixed third-order structure function exceeds 90% of its maximum value, analogous to the approach by Jayesh et al. (1994). Figures 6.2 and 6.3 show the lower and upper bounds of the inertial-convective range by dashed lines, which correspond to the values $r/\eta = 14$ and $r/\eta = 151$, respectively. Turbulent line segments reveal an inertial-convective range scaling for separation lengths beginning somewhat below the lower bound. Whether a scaling up to the upper bound exists cannot be properly answered because of the aforementioned convergence limitations at larger scales. Additionally, fig. 6.2 depicts the structure functions and conditional moments computed in y-direction. For the former the scaling exponents are virtually independent of direction. The latter reveals a dependence on direction particularly for the higher order moments, where the scaling exponents in x-direction are larger than the ones in y-direction. The scaling exponents in the dissipative range are independent of direction. However, the absolute level differs for larger moments which reflects the scalar anisotropy.

Because of the relatively small extent of the inertial subrange, the scaling exponents are difficult to determine. Benzi et al. (1993) and Benzi et al. (1995) proposed a method, called "extended self-similarity (ESS)" to determine the scaling exponents

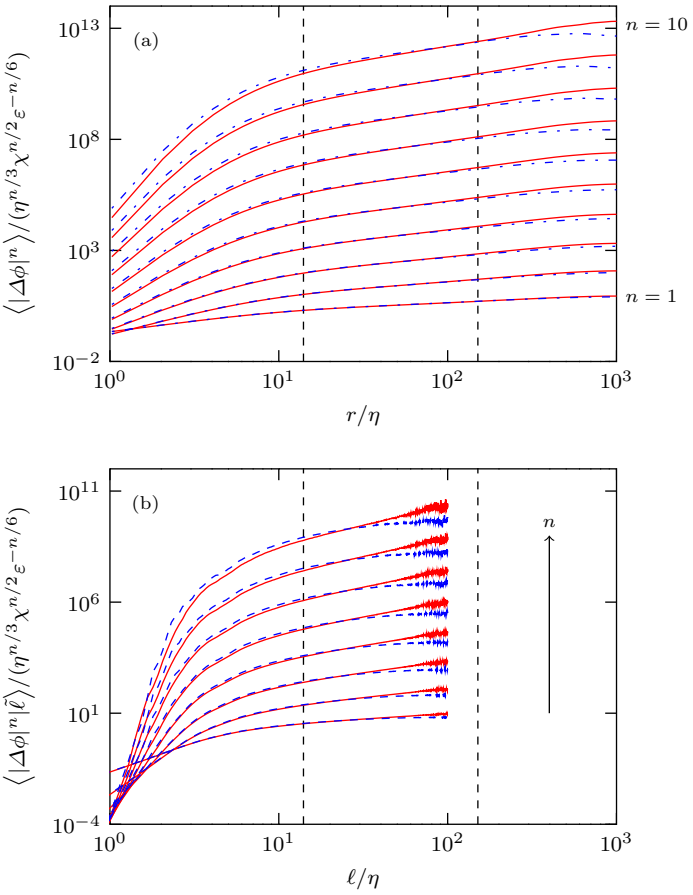

Figure 6.2: Moments of the normalized scalar increments for case R4. Structure functions (a) for $n = 1, \cdots, 10$, turbulent line segments (b) for $n = 1, \cdots, 8$ cut at $r/\eta = 100$. The moments of $\Delta\phi$ are non-dimensionalized by the Kolmogorov variables and the absolute value of $\Delta\phi$ is taken to obtain non-vanishing odd moments. The vertical dashed lines indicate the lower and upper bounds of the inertial-convective range. Additionally, for reference, the structure functions and conditional moments computed in y-direction are shown (blue dashed lines).

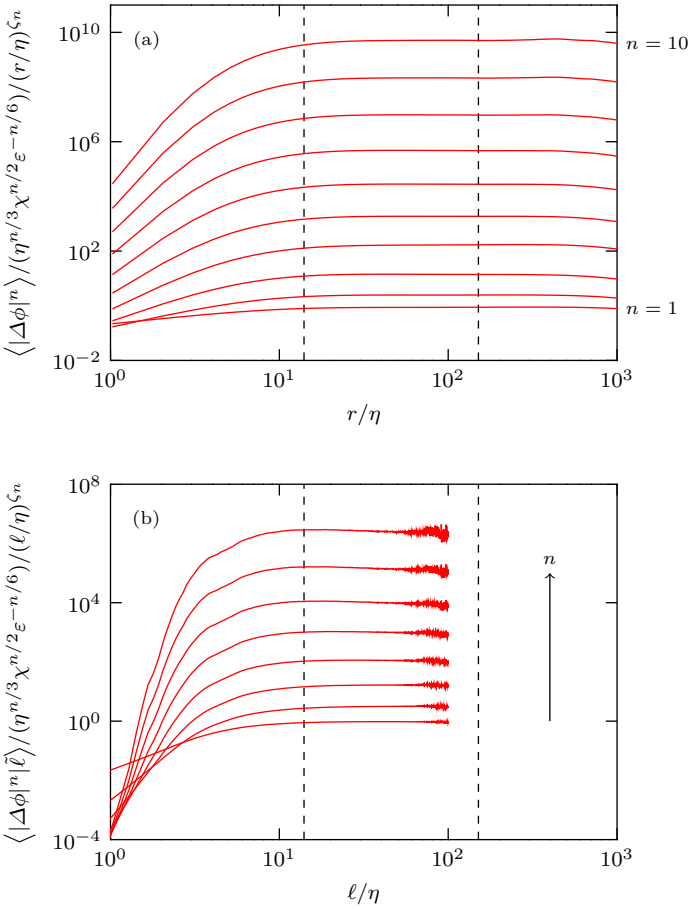

Figure 6.3: Moments of the optimally compensated increment for case R4. Structure functions (a) for $n = 1, \cdots, 10$, turbulent line segments (b) for $n = 1, \cdots, 8$ cut at $r/\eta = 100$. The moments of $\Delta\phi$ are non-dimensionalized by the Kolmogorov variables and the absolute value of $\Delta\phi$ is taken to obtain non-vanishing odd moments. The choice of the scaling exponent is such that a horizontal plateau is obtained in the inertial-convective range. The vertical dashed lines indicate the lower and upper bounds of the inertial-convective range.

of the velocity structure function by plotting the nth order structure function versus the third order structure function. As a result, a significantly increased scaling region can be identified. This is particularly useful for low Reynolds number flows. However, this approach reveals some limitations. Plotting the higher order structure function as a function of the third order structure yields only relative scaling exponents. Additionally, Stolovitzky and Sreenivasan (1993) found that ESS is limited to lower order moments and yields ambiguous results beginning from the eighth-order moments. Ruiz-Chavarria et al. (1996) extended the ESS method for the passive scalar field and plotted the nth order scalar structure function versus the second order scalar structure function. However, this yields as well only relative scaling exponents $\zeta_\phi(n)/\zeta_\phi(2)$, unless the precise second order scaling exponent is known. Due to this difficulties, and due to the fact that ESS is not well defined for turbulent line segments, we do not make use of the ESS method in the present work.

The results of the present DNS and the method to determine the scaling exponents are validated by means of fig. 6.4 where the scaling exponents of the absolute value of the velocity and scalar increments are illustrated. The scaling exponents $\zeta_\phi(n)$ of the scalar field deviate more than the respective scaling exponents $\zeta(n)$ of the velocity field from Kolmogorov's linear prediction underlining the stronger intermittency of the scalar field. The present results agree well with other DNS by Watanabe and Gotoh (2004) and experiments by Schmitt (2005). However, the scaling exponents cannot be considered as universal. Gylfason and Warhaft (2004) found a large variation of the scaling exponents for different experiments and Reynolds numbers, not only for the higher orders, but even starting at the fourth or sixth order. In addition, Lepore and Mydlarski (2009) found that the scaling exponents are very sensitive to boundary conditions. Figure 6.4 shows the variation of the scaling exponents between the cases under consideration by error bars. Considering the difficulties in determining the scaling exponents this variation is rather small. In addition, for turbulent line segments the scaling exponents are virtually Reynolds number independent.

The inertial-convective range scaling exponents for the conventional scalar structure function and for turbulent line segments are compared by means of fig. 6.5. Additionally, the KOC scaling is shown, which implies a linear relation, $\zeta_\phi(n) = n/3$, as no internal intermittency is taken into account. Compared to the scaling exponent of the scalar structure function, the scaling exponents of turbulent line segments are overall closer to the KOC prediction, but for $n \leq 3$ they exceed the KOC prediction. While the first order scalar structure function obeys virtually exactly KOC scaling, this is not the case for the first order moment of turbulent line segments, where $\zeta_\phi(1)$ equals 0.5 instead of 0.33. An additional feature of turbulent line segments is the fact that the deviation from the KOC prediction for higher orders is less significant. This finding suggests that the statistics of turbulent line segments are less affected by internal intermittency.

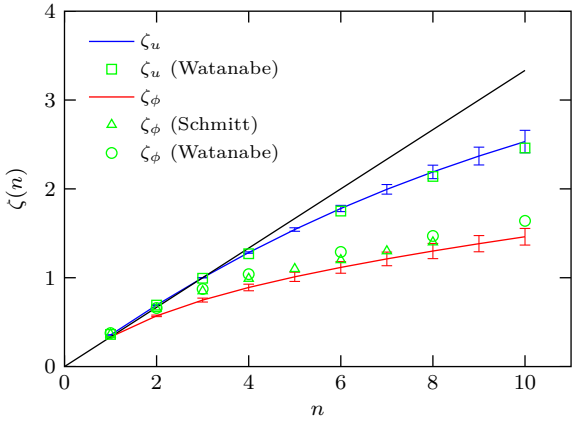

Figure 6.4: Scaling exponents $\zeta(n)$ and $\zeta_\phi(n)$ for the absolute value of velocity and scalar increment, respectively. Validation of the present results with other DNS by Watanabe and Gotoh (2004) and experiments by Schmitt (2005). The error bars indicate the variation between the different cases.

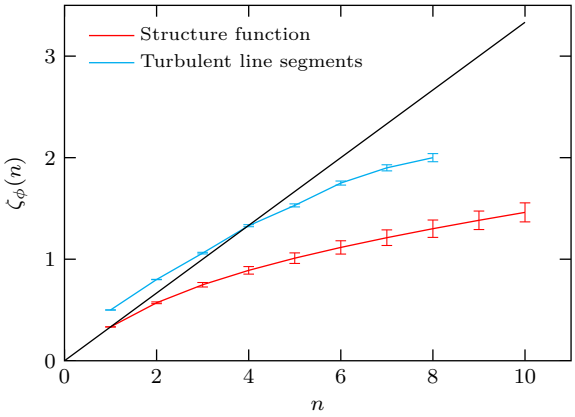

Figure 6.5: Scaling exponents $\zeta_\phi(n)$ for the absolute value of the scalar increment $\Delta\phi$ for the conventional structure function and turbulent line segments. The error bars indicate the variation between the different cases.

6.2.1 Reynolds Number Dependence and Scaling Laws

Let us now examine the Reynolds number dependence of the scalar structure function and the conditional means of $\Delta\phi$, respectively. The nth moment of $\Delta\phi$ can be expressed by, cf. Wang et al. (1999),

$$\langle(\Delta\phi)^n\rangle = F_n(\mathrm{Re}_r, \mathrm{Pe})\langle\chi\rangle^{n/2}\langle\varepsilon\rangle^{-n/6} r^{n/3}\,, \tag{6.6}$$

where at high Reynolds number F_n is a universal function that depends on the local Reynolds number, $\mathrm{Re}_r = \langle\varepsilon\rangle^{1/3} r^{4/3}/\nu$, and on the Peclet number Pe. Kolmogorov's second similarity hypotheses suggests that when $\mathrm{Re}_r \gg 1$, or $r \gg \eta$, the distribution of

$$\frac{\Delta\phi}{\langle\chi\rangle^{1/2}\langle\varepsilon\rangle^{-1/6} r^{1/3}} \tag{6.7}$$

becomes independent of ν and D. This yields for the normalized nth order moment in the inertial subrange

$$\frac{\langle(\Delta\phi)^n\rangle}{\langle\chi\rangle^{n/2}\langle\varepsilon\rangle^{-n/6} r^{n/3}} = c_n\,, \tag{6.8}$$

where c_n are universal constants that are especially independent of r. Below we will show that c_n is a constant only for $n = 2$ and that the higher order normalized moments become Reynolds number dependent because of the intermittent fluctuations of χ and ε. Equation 6.8 holds for turbulent line segments as well.

Figure 6.6 shows the second and fourth order moments of the structure functions (top) and the conditional moments for turbulent line segments (bottom) for all Reynolds numbers. Each curve is optimally compensated and normalized by the KOC variables to display a plateau in the inertial-convective subrange. The second order moments satisfy KOC scaling yielding to a collapse of all cases in both dissipative range and inertial-convective range. The value of c_2 is Reynolds number independent and equals 2.6 for structure functions and 3.2 for turbulent line segments. This is different for the fourth order, where a staggered arrangement can be observed. Therefore, c_4 depends on Reynolds number, or equivalently, the normalization by the KOC variables is incomplete. The scaling of c_4 as a function of Re_λ is illustrated in fig. 6.7, showing an inertial subrange scaling for structure functions according to

$$c_4 = 15\,\mathrm{Re}_\lambda^{0.4} \tag{6.9}$$

and for turbulent line segments according to

$$c_4 = 10\,\mathrm{Re}_\lambda^{0.4}\,. \tag{6.10}$$

The parameter c_4 for the former is larger than for the latter, but both increase at the same rate with the Reynolds number. The scaling obtained by eqs. 6.9 and 6.10 does not depend on r for scales lying in the inertial subrange.

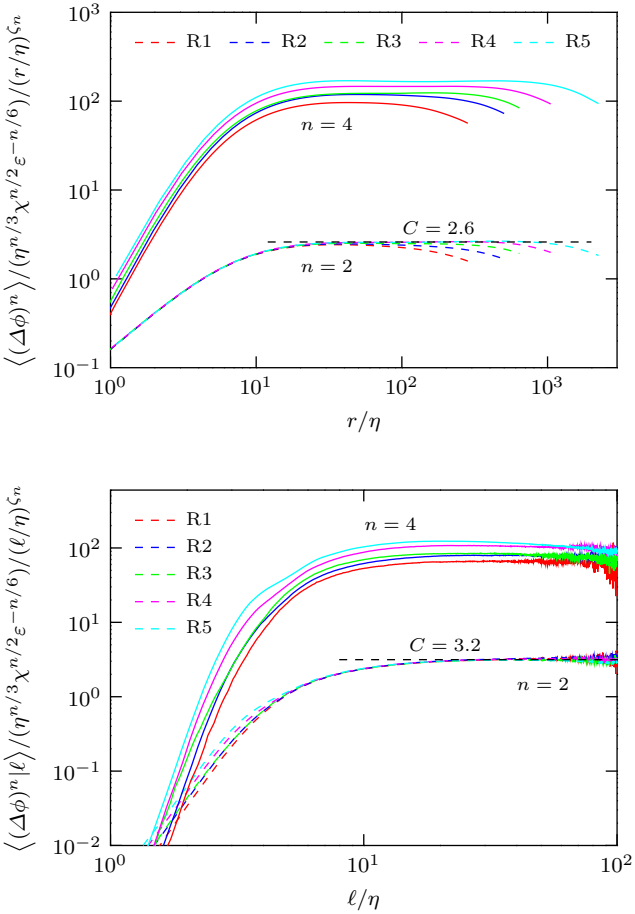

Figure 6.6: Normalized and compensated 2nd and 4th order scalar structure function (top) and conditional mean of turbulent line segments (bottom), each compensated by the optimal scaling exponent $\zeta_\phi(n)$.

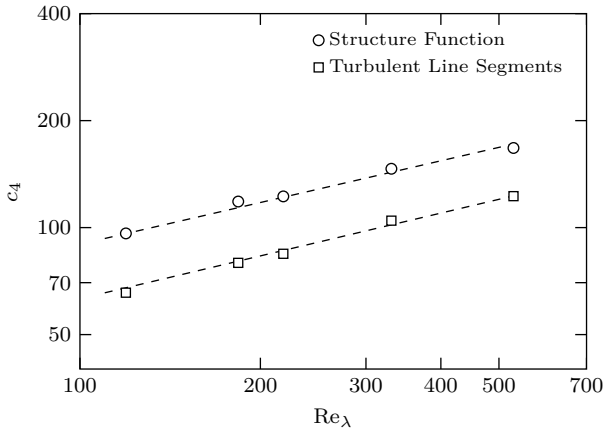

Figure 6.7: Scaling of the parameter c_4 as a function of the Reynolds number for structure functions and turbulent line segments.

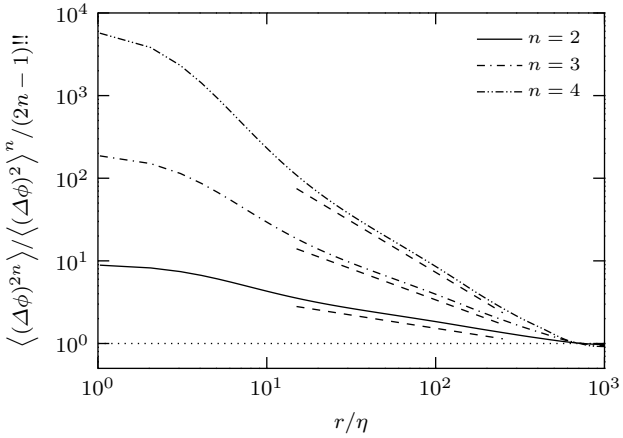

Figure 6.8: Higher order non-dimensional moments of the scalar increment as a function of r/η, normalized by their Gaussian values $(2n-1)!!$. The values indicate a super-Gaussian probability density function. For $r \to \infty$ each curve approaches unity and hence its Gaussian value.

The flatness $F_{\Delta\phi}(r)$ of the increment $\Delta\phi$ within the inertial-convective range can be written as

$$F_{\Delta\phi}(r) = \frac{\langle(\Delta\phi)^4\rangle}{\langle(\Delta\phi)^2\rangle^2} = \frac{c_4}{c_2^2} r^{\zeta_\phi(4)-2\zeta_\phi(2)}\,, \tag{6.11}$$

where the moments of $\Delta\phi$ are expressed by means of the actual scaling exponent $\zeta_\phi(n)$. The parameter c_2 and the scaling exponents $\zeta_\phi(n)$ are Reynolds number independent. However, this is not the case for c_4 and according to eq. 6.11 the Reynolds number dependence of c_4 in the inertial-convective range is directly transferred to the flatness $F_{\Delta\phi}(r)$. This consideration holds for structure functions and turbulent line segments. In addition the realizability constraint requires $\zeta_\phi(4) < 2\zeta_\phi(2)$ leading to an increase of $F_{\Delta\phi}(r)$ toward smaller scales. This implies that intermittency increases cumulatively on the way down the energy cascade. Figure 6.8 illustrates the fourth, sixth and eighth order non-dimensional moments of the scalar increment as a function of r/η. The values indicate a super-Gaussian probability density function for $\Delta\phi(r)$ and only in the limit $r \to \infty$ each curve approaches its Gaussian value.

6.2.2 A Scale-by-scale Budget Equation for Second and Fourth Order Moments of the Scalar Increment

Most works regarding anomalous scaling of structure function deal with the non-universality of velocity or scalar increment statistics at different scales within the inertial subrange. But not much attention has been paid to the scaling of the moments of the normalized increments as a function of Reynolds number. This point will be addressed in the course of the present section.

Let us recall the transport equations for the second and fourth order scalar increment, derived in sec. 4.2 from first principles. Solid angle integration of the transport equation for $\langle(\Delta\phi)^2\rangle$ yields, cf. eq. 4.17,

$$\underbrace{-\frac{1}{4\pi r^2}\int_{\partial V}\big\langle(\Delta u_i)(\Delta\phi)^2\big\rangle n_i \mathrm{d}\Omega}_{T_2(r)}\ \underbrace{-\frac{1}{4\pi r^2}\int_V 2G\big\langle(\Delta u_2)(\Delta\phi)\big\rangle \mathrm{d}V}_{P_2(r)} + \underbrace{2D\frac{\mathrm{d}}{\mathrm{d}r}\left[\frac{1}{4\pi r^2}\int_{\partial V}\big\langle(\Delta\phi)^2\big\rangle \mathrm{d}\Omega\right]}_{K_2(r)} = \frac{2}{3}\big\langle\chi\big\rangle r\,, \tag{6.12}$$

and solid angle integration of the transport equation for $\langle(\Delta\phi)^4\rangle$, cf. eq. 4.10, yields

$$\begin{aligned} &\underbrace{-\frac{1}{4\pi r^2}\int_{\partial V}\left\langle(\Delta u_i)(\Delta\phi)^4\right\rangle n_i \mathrm{d}\Omega}_{T_4(r)}\ \underbrace{-\frac{1}{4\pi r^2}\int_V 4G\left\langle(\Delta u_2)(\Delta\phi)^3\right\rangle \mathrm{d}V}_{P_4(r)} + \\ &\underbrace{2D\frac{\mathrm{d}}{\mathrm{d}r}\left[\frac{1}{4\pi r^2}\int_{\partial V}\left\langle(\Delta\phi)^4\right\rangle \mathrm{d}\Omega\right]}_{K_4(r)} = \underbrace{\frac{1}{4\pi r^2}\int_V 6\langle(\Delta\phi)^2\left(\chi+\chi'\right)\rangle \mathrm{d}V}_{I_4(r)} . \end{aligned} \tag{6.13}$$

Equations 6.12 and 6.13 can be understood as a scale-by-scale budget equation for $\langle(\Delta\phi)^2\rangle$ and $\langle(\Delta\phi)^4\rangle$, respectively. Normalizing the former by $2/3\langle\chi\rangle\eta$ yields

$$\widetilde{T}_2(r) + \widetilde{P}_2(r) + \widetilde{K}_2(r) = \frac{r}{\eta}\,, \tag{6.14}$$

and normalizing the latter by $\langle\chi\rangle^2\langle\varepsilon\rangle\eta^{5/2}$ yields

$$\widetilde{T}_4(r) + \widetilde{P}_4(r) + \widetilde{K}_4(r) = \widetilde{I}_4(r)\,, \tag{6.15}$$

where the non-dimensional terms are denoted by a tilde.

The respective terms of eqs. 6.14 are shown in fig. 6.9 for case R4 as a function of r/η. According to eq. 6.14, the left hand side should sum up to (r/η) yielding a linear function of r. This is well satisfied for all values of r. Additionally, fig. 6.9 shows that at small scales, the diffusive term $\widetilde{K}_2(r)$ is dominant and balances the right hand side. Within the inertial subrange the normalized transport term $\widetilde{T}_2(r)$ is dominant and equals (r/η). The width of the inertial subrange is determined by the criteria of Jayesh et al. (1994), yielding $14 < r/\eta < 151$. For case R4 with $\mathrm{Re}_\lambda = 331$ statistics within the inertial range are virtually unaffected by dissipative effects or large-scale phenomena. At large scales the normalized production term $\widetilde{P}(r)$ is dominant and approaches r/η.

Let us now consider the budget of the normalized fourth moment according to eq. 6.15. The corresponding terms are displayed in fig. 6.10 for case R4. The budget is as well satisfied for all scales. On the right hand side of eq. 6.15 a correlation between the second order increment $(\Delta\phi)^2$ and the scalar dissipation χ appears, which is a non-linear function of r. We observe a virtually linear slope for $r/\eta > 10$ but a slightly larger slope toward dissipative scales. The interpretation of each term is similar to those in the equation for the second order. However, the diffusion term and the production term drop less fast toward inertial range scales retaining dissipative or large-scale effects within the inertial subrange.

Figure 6.11 shows $\widetilde{I}_4$ as a function of r/η for all cases. A strong Reynolds number dependence can be observed with a staggered arrangement where a larger Reynolds number leads to a displacement upwards. Note, that this is different for the equation

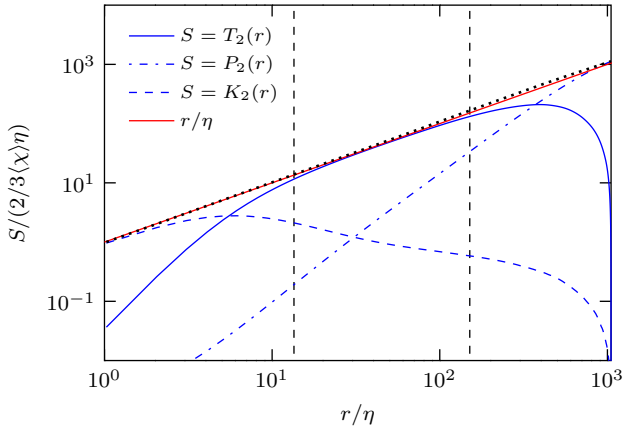

Figure 6.9: Normalized second order scalar scale-by-scale budget equation for case R4. The budget is well satisfied as the terms of the left hand side sum up to r/η. The sum of the left hand side $\widetilde{T}_2(r/\eta) + \widetilde{P}_2(r/\eta) + \widetilde{K}_2(r/\eta)$ is denoted by the black dotted line.

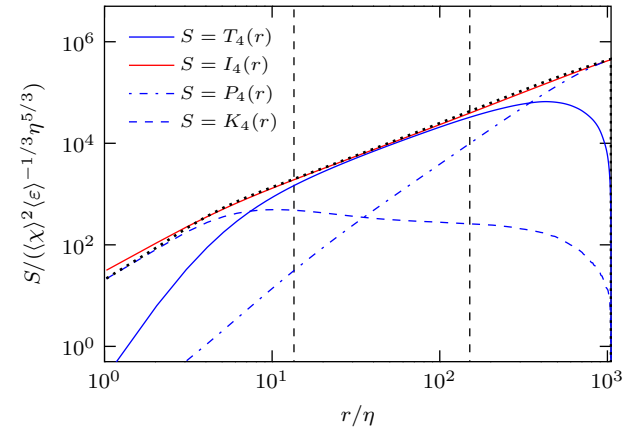

Figure 6.10: Normalized fourth order scalar scale-by-scale budget equation for case R4. The budget is well satisfied as the sum of the terms of the left hand side $\widetilde{T}_4(r/\eta) + \widetilde{P}_4(r/\eta) + \widetilde{K}_4(r/\eta)$ yielding the right hand side $\widetilde{I}_4(r)$. The sum of the left hand side is denoted by the black dotted line.

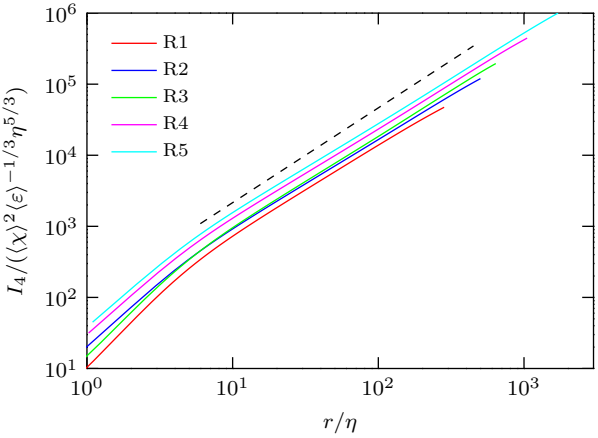

Figure 6.11: Normalized volume integrated right hand side $\widetilde{I}_4(r/\eta)$, cf. eq. 6.15, for all cases. The scaling in the inertial subrange is close to $\propto r^{4/3}$ (black dashed line).

of the second order increment, cf. eq. 6.14, where the right hand side equals always r/η for all cases. Figures 6.12 and 6.13 illustrate the normalized transport terms $\widetilde{T}_2(r)$ and $\widetilde{T}_4(r)$ for all cases. While $\widetilde{T}_2(r)$ collapses for all Reynolds numbers within the dissipative and inertial range $\widetilde{T}_4(r)$ inherits the Reynolds number dependence from $\widetilde{I}_4(r)$. We may thus suggest that the Reynolds number dependence of $\widetilde{T}_4(r)$ as well as that of $\widetilde{I}_4(r)$ stems from the normalized correlation between $(\Delta\phi)^2$ and χ. Due to this correlation we suppose that dissipative effects are persistent in the inertial subrange. Let us now consider the non-dimensional ratio

$$\frac{\langle(\Delta\phi)^2\chi\rangle}{\langle(\Delta\phi)^2\rangle\langle\chi\rangle} \tag{6.16}$$

which is depicted in fig. 6.14 as a function of r/η. Within the dissipative range and the inertial subrange this ratio is larger than unity and exhibits a strong Reynolds number dependence. This reasserts that the Reynolds number dependence originates form the correlation between $(\Delta\phi)^2$ and χ. Additionally, in the limit $r \to \infty$ the correlation $\langle(\Delta\phi)^2\chi\rangle$ approaches the one-point quantity $\langle\phi^2\chi\rangle$, where ϕ^2 and χ should be decorrelated as the former is a large-scale quantity and the latter is a small-scale quantity. According to fig. 6.14, eq. 6.16 tends to unity for $r \to \infty$ justifying the decorrelation of ϕ^2 and χ at large scales.

Next, we will examine the scaling exponents of the transport terms. As expected, the width of the inertial subrange increases with Reynolds number. Within the inertial subrange for $\eta \ll r \ll l_t$ eq. 6.14 simplifies to

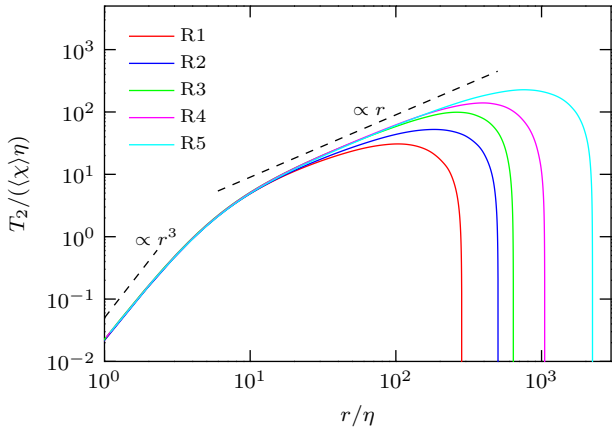

Figure 6.12: Normalized solid angle averaged second order mixed velocity-scalar structure function $\widetilde{T_2}(r/\eta)$ for all cases.

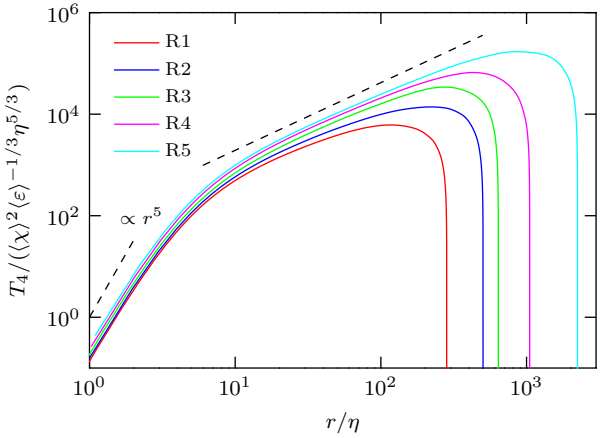

Figure 6.13: Normalized solid angle averaged fourth order mixed velocity-scalar structure function $\widetilde{T_4}(r/\eta)$ for all cases. The scaling in the inertial subrange is close to $\propto r^{4/3}$ (black dashed line).

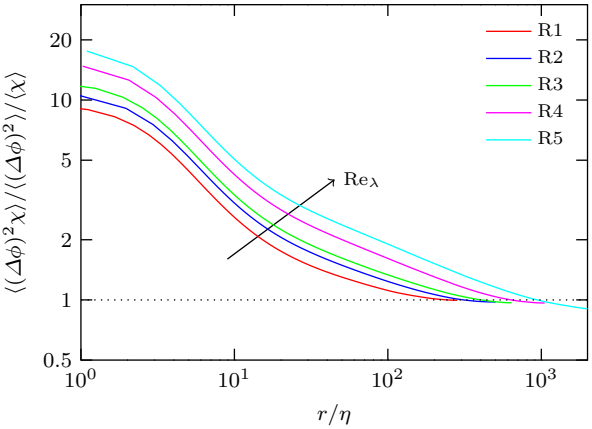

Figure 6.14: Normalized correlation $\langle(\Delta\phi)^2\chi\rangle$ as a function of r/η for all cases. The ensemble average of two-point quantities $\langle(\Delta\phi)^2\chi\rangle$ and $\langle(\Delta\phi)^2\rangle$ is computed by means of a solid angle average.

$$\widetilde{T}_2(r) = \frac{r}{\eta}\,, \tag{6.17}$$

which corresponds to Yaglom's equation without requiring isotropy. The scaling according to eq. 6.17 is well confirmed by fig. 6.12. Similarly, eq. 6.15 simplifies within the inertial subrange to

$$\widetilde{T}_4(r) = \widetilde{I}_4(r)\,, \tag{6.18}$$

and thus $\widetilde{T}_4$ inherits not only the Reynolds number dependence from $\widetilde{I}_4$ but also the inertial subrange scaling exponent. From eqs. 6.13 and 6.18 it is *a priori* not obvious that an inertial subrange scaling exists. However, fig. 6.13 shows that $\widetilde{T}_4(r)$ obeys a power law with a scaling close to $r^{4/3}$. The actual scaling exponent departs from the scaling exponent obtained from dimensional grounds, which would be 5/3, because of internal intermittency.

Until now we have only obtained a relation between the anomalous scaling of $\widetilde{I}_4$ and $\widetilde{T}_4$, but the link to the fourth order moment of the scalar increment $S_4(r) = \langle(\Delta\phi)^4\rangle$ is still missing. Internal intermittency and the resulting Reynolds number dependence of the flatness of $\Delta\phi$ manifests itself in the increase of c_4 with Reynolds number. We seek now for a normalization of S_4 that lead to a collapse of all curves independently of Reynolds number. Previously, the Reynolds number dependence has been attributed to the correlation between $(\Delta\phi)^2$ and χ and the persistence of dissipative effects in

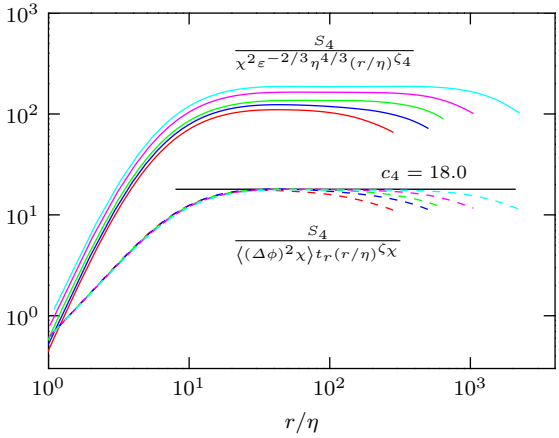

Figure 6.15: Optimally compensated fourth order structure function (solid lines) and comparison with the proposed normalization according to eq. 6.19 (dashed lines). By the latter normalization all cases collapse to a single curve independently of Reynolds number. Same legend as for fig. 6.14. The ensemble averages of all two-point quantities are computed by means of a solid angle average.

the inertial subrange. As Kolmogorov scaling is not able to capture Reynolds number effects, a normalization of S_4 is required that accounts for internal intermittency. Therefore, we propose following normalization of $S_4(r)$

$$\frac{S_4(r)}{\langle(\Delta\phi)^2\chi\rangle t_r(r/\eta)^{\zeta_\chi}}\,, \tag{6.19}$$

where t_r is a characteristic turnover time at scale r defined on dimensional arguments for scales in the inertial subrange by

$$t_r = \langle\varepsilon\rangle^{-1/3} r^{2/3}\,. \tag{6.20}$$

The scaling exponent ζ_χ is chosen such that a horizontal slope for scales in the inertial subrange occur. For the present data ζ_χ is small, i.e. $\zeta_\chi \approx -0.05$, and with this the scaling exponent of the denominator of eq. 6.19 equals $\zeta_\phi(4)$.

The fourth order structure function $S_4(r)$ normalized according to eq. 6.19 is depicted in fig. 6.15 for all cases. Additionally, $S_4(r)$ is depicted optimally compensated by the Kolmogorov variables. Figure 6.15 illustrates that only the former normalization leads to a collapse of all cases to a single curve, and hence, c_4 becomes independent of Reynolds number and equals 18.0.

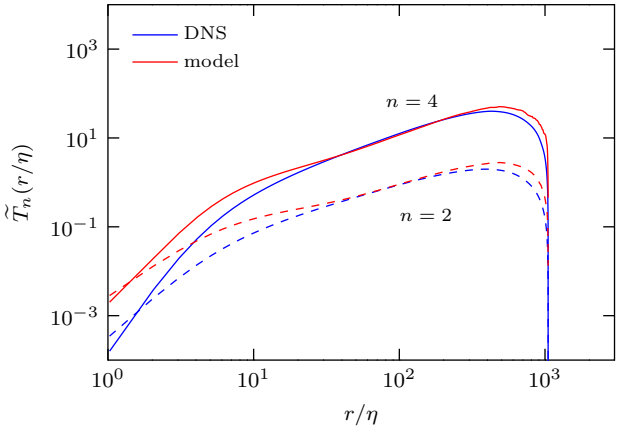

Figure 6.16: Comparison of the solid angle averaged second and fourth order mixed velocity-scalar structure function $\widetilde{T}_n(r/\eta)$ and the gradient-flux approximation according to eq. 6.21 and 6.22 for case R4. The constant c_D equals 0.6 for both curves.

6.2.3 Closure of the Turbulent Transport Term

The scale-by-scale budget equations, cf. eqs. 6.12 and 6.13, contain the transport terms $T_2(r)$ and $T_4(r)$ that are not closed due to the correlation between Δu_i and $(\Delta\phi)^n$. Closure can be achieved by means of a gradient-flux approximation in correlation space, which states for arbitrary even moments

$$\frac{1}{4\pi r^2}\int_{\partial V}\left\langle(\Delta u_i)(\Delta\phi)^{2n}\right\rangle n_i \mathrm{d}\Omega = -\nu_t(r)\frac{\mathrm{d}}{\mathrm{d}r}\left[\frac{1}{4\pi r^2}\int_{\partial V}\left\langle(\Delta\phi)^{2n}\right\rangle \mathrm{d}\Omega\right], \qquad (6.21)$$

where the solid angle average is incorporated to account for the scalar anisotropy. The turbulent viscosity $\nu_t(r)$ at scale r is defined based on dimensional arguments as

$$\nu_t(r) = c_D\langle\varepsilon\rangle^{1/3} r^{4/3}. \qquad (6.22)$$

Because this closure relies solely on $\langle\varepsilon\rangle$ and r it is expected to be valid in the inertial subrange.

The proposed model is validated by means of fig. 6.16 where for case R4 the turbulent transport terms $T_2(r)$ and $T_4(r)$ are displayed. For comparison the respective results obtained from the gradient-flux approximation are shown. The constant c_D equals 0.6 for both moments. However, c_D varies with Reynolds number. Figure 6.16 reveals a very good agreement between DNS and eq. 6.21, particularly for scales lying in the inertial subrange.

6.3 Statistics of Local and Mean Gradients

6.3.1 Flatness of Turbulent Line Segments

The flatness is a natural measure of the intermittency of a statistical quantity. In turbulent flows the small-scale quantities, like gradients of the scalar field, are more affected by intermittency than their respective large-scale quantity. However, intermittency of the scalar field is, for finite Reynolds numbers, not independent from anisotropy as events at the large scales couple directly to the small scales. This can be seen from the fact that the flatness of the scalar gradient in the direction parallel to the mean scalar gradient is larger than the flatness perpendicular to that direction. At high Reynolds number rare extreme events become more probable than predicted by a Gaussian distribution and thus the flatness increases with Reynolds number.

Within the theory of turbulent line segments we can define two fine-scale quantities. Firstly, the local gradient $\phi_x = \partial\phi/\partial x$ and, secondly, the mean gradient of an individual line segment $g = \Delta\phi/\ell$. The flatness of g and ϕ_x is defined by

$$F_g = \frac{\langle g^4 \rangle}{\langle g^2 \rangle^2} \quad \text{and} \quad F_{\phi_x} = \frac{\langle \phi_x^4 \rangle}{\langle \phi_x^2 \rangle^2} \,. \tag{6.23}$$

By expressing the moments of g trough of the conditional average $\langle g^n | \ell \rangle$ and the length distribution $P_\ell(\ell)$ the flatness F_g can be obtained by

$$F_g = \frac{\int \langle g^4 | \ell \rangle P_\ell(\ell) \mathrm{d}\ell}{\left[\int \langle g^2 | \ell \rangle P_\ell(\ell) \mathrm{d}\ell\right]^2} = \frac{\int \tilde{\ell}^{-4} \langle (\widetilde{\Delta\phi})^4 | \tilde{\ell} \rangle \widetilde{P}_\ell(\tilde{\ell}) \mathrm{d}\tilde{\ell}}{\left[\int \tilde{\ell}^{-2} \langle (\widetilde{\Delta\phi})^2 | \tilde{\ell} \rangle \widetilde{P}_\ell(\tilde{\ell}) \mathrm{d}\tilde{\ell}\right]^2} \,. \tag{6.24}$$

For the second equality the relation $g = \Delta\phi/\ell$ is used in order to express the moments of the conditional mean gradient by the moments of the conditional scalar difference. In addition, the length is normalized by its mean, i.e. $\tilde{\ell} = \ell/\ell_m$, yielding a normalized length distribution function $\widetilde{P}_\ell(\tilde{\ell}) = \ell_m P_\ell(\ell/\ell_m)$. The conditional moments of $\Delta\phi$ are non-dimensionalized by the KOC variables, yielding

$$\langle (\widetilde{\Delta\phi})^2 | \tilde{\ell} \rangle = \frac{\langle (\Delta\phi)^2 | \tilde{\ell} \rangle}{\langle \chi \rangle \langle \varepsilon \rangle^{1/3} \ell_m^{-2/3}} \tag{6.25}$$

and

$$\langle (\widetilde{\Delta\phi})^4 | \tilde{\ell} \rangle = \frac{\langle (\Delta\phi)^4 | \tilde{\ell} \rangle}{\langle \chi \rangle^2 \langle \varepsilon \rangle^{2/3} \ell_m^{-4/3}} \,. \tag{6.26}$$

where $\ell_m \propto \eta$, and $\mathrm{Sc} = 1$. Equation 6.24 implies that it is sufficient to know the second and fourth conditional moments of $\Delta\phi$ as well as the quasi-universal length distribution $\widetilde{P}_\ell(\tilde{\ell})$ to determine F_g. The moments of $\Delta\phi$ are weighted by the

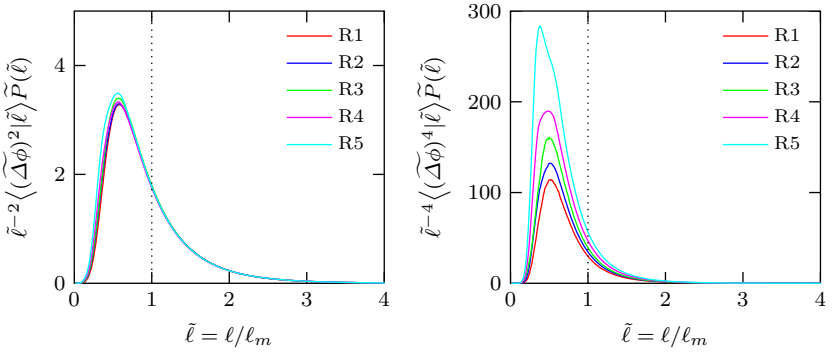

Figure 6.17: Normalized integrand of the nominator (left) and the denominator (right) of eq. 6.24 for all cases. Normalization of the conditional moments according to eqs. 6.25 and 6.26.

prefactors $1/\tilde{\ell}^2$ and $1/\tilde{\ell}^4$, respectively. By the integration of eq. 6.24 over ℓ basically all length scales are involved, but because of the prefactors smaller length scales have a major contribution to F_g. This is illustrated in fig. 6.17, where the integrand of the normalized nominator and denominator is shown. The former has a distinct maximum at approximately $\ell/\ell_m \approx 0.6$ and the latter at approximately $\ell/\ell_m \approx 0.45$. The integrand of the normalized denominator collapses for all Reynolds numbers. This is not the case for the integrand of the normalized nominator which depends strongly on Reynolds number and the value of the maximum rises with the Reynolds number. Since $\widetilde{P}_\ell(\tilde{\ell})$ is quasi-universal, the Reynolds number dependence of F_g comes solely from the Reynolds number dependence of the denominator of eq. 6.24 and thus from the fourth order conditional moment of $\Delta\phi$.

6.3.2 Reynolds Number Dependence and Scaling Laws

The KOC theory suggests to normalize the scalar gradient by $\langle\chi\rangle$ and D leading to a flatness of the scalar gradient (and all higher order non-dimensional moments) that is independent of Reynolds number. However, fig. 6.18 illustrates that the flatness of the scalar gradient and the mean gradient g of turbulent line segments increase both with the Reynolds number. The flatness of the scalar gradient F_{ϕ_x} (perpendicular to the direction of the mean gradient) obeys a power law according to

$$F_{\phi_x} = 1.42\,\mathrm{Re}_\lambda^{0.5}\,, \tag{6.27}$$

reflecting that internal intermittency becomes more pronounced at high Reynolds numbers. The scaling exponent of eq. 6.27 agrees well with the finding of Sreenivasan

and Antonia (1997) and Warhaft (2000), who investigated the scaling of the gradient flatness for Taylor based Reynolds numbers up to 10^4. Additionally, F_{ϕ_y} (parallel to the direction of the mean gradient) is larger than F_{ϕ_x}. This stems from the fact that the production of scalar fluctuations is excited by the velocity fluctuations in y-direction. The scaling exponent of F_{ϕ_y} is somewhat smaller than 0.5 indicating that the flatness of both directions may approach each other for very large Reynolds numbers, which will be expected under the assumption of local isotropy.

Next, we will examine the flatness in the context of turbulent line segments and consider the mean gradients $g_y = \Delta\phi(y)/\ell(y)$ (for segments parallel to the direction of the mean gradient) and $g_x = \Delta\phi(x)/\ell(x)$ (for segments perpendicular to the direction of the mean gradient). We find from fig. 6.18 that the flatness F_{g_x} increases at the same rate as F_{ϕ_x}, i.e.

$$F_{g_x} = 0.74\,\mathrm{Re}_\lambda^{0.5}\,, \tag{6.28}$$

but at a considerably lower level. This can be explained by the fact that g is already a mean quantity, i.e. g can be understood as the local gradient averaged over an intermediate length scale, which corresponds to the length of each individual segment. On average this length scale equals the mean length ℓ_m. Again, the flatness of g_y, is somewhat larger than the flatness of g_x, and an approach of both quantities for very high Reynolds numbers can be expected.

Let us now examine the sixth normalized moment, called hyper-flatness (HF), defined by

$$HF_{\phi_x} = \frac{\langle \phi_x^4 \rangle}{\langle \phi_x^2 \rangle^2}\,, \quad HF_g = \frac{\langle g^4 \rangle}{\langle g^2 \rangle^2}\,. \tag{6.29}$$

From fig. 6.19 we obtain the scaling laws

$$HF_{\phi_x} = 3.6\,\mathrm{Re}_\lambda^{1.15} \tag{6.30}$$

and

$$HF_{g_x} = 0.91\,\mathrm{Re}_\lambda^{1.15}\,. \tag{6.31}$$

Again, the hyper-flatness of g_x and the hyper-flatness of ϕ_x increase both with the same scaling exponent but at different levels. This feature will be used in sec. 6.4 to establish a scale-similarity between the moments of the local gradient ϕ_x and the mean gradient g. The hyper-flatness increases at a larger rate compared to the flatness which is as well reflected by stretched exponential tails of the distribution function. Although the flatness and hyper-flatness of g are both lower compared to the one of ϕ_x, they depart from their Gaussian values, which would be 3 for the flatness and 60 for the hyper-flatness, respectively.

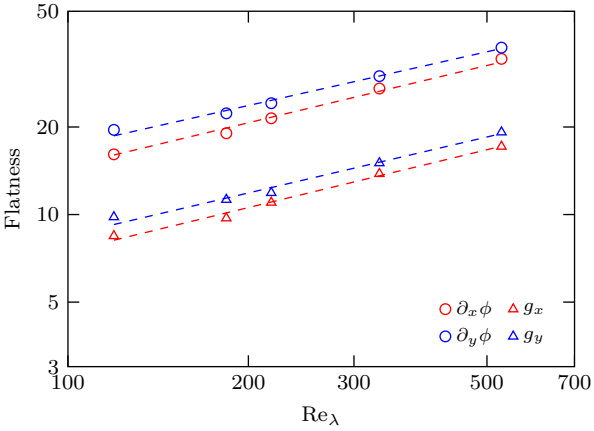

Figure 6.18: Scaling of the flatness of ϕ_x and ϕ_y and g (calculated for segments in x and y direction) as a function of Re_λ.

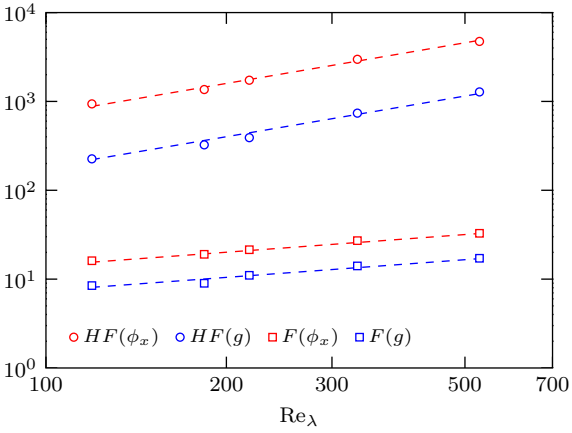

Figure 6.19: Scaling of the flatness and hyper-flatness of ϕ_x and g as a function of Re_λ.

6.3.3 Kolmogorov's Refined Similarity Hypothesis for Passive Scalars

In the previous section we applied the theory proposed by Kolmogorov (1941b), Obukhov (1949b) and Oboukhov (1962) (KOC), relating the small-scale velocity and scalar statistics to the average energy dissipation $\langle\varepsilon\rangle$ and the average scalar dissipation $\langle\chi\rangle$. The Kolmogorov (1941b) theory (K41) was developed based on the model of the local energy cascade and on dimensional arguments and cannot be considered as universally valid, cf. Monin and Yaglom (1975). It implies that the flatness of scalar derivatives $\partial\phi/\partial x_i$ should be constant and independent of Reynolds number, but fig. 6.18 shows that this is not true. Additionally, the flatness of the scalar increment $\Delta\phi$ within the inertial range should be constant, which is as well not satisfied, cf. fig. 6.8.

When normalizing the Navier-Stokes equations by the Kolmogorov variables the Reynolds number

$$\mathrm{Re}_\eta = \frac{u_\eta\,\eta}{\nu} \tag{6.32}$$

equals unity and disappears as free parameter. This feature is as well transferred to any equation derived from the Navier-Stokes equations. Therefore, Kolmogorov scaling is not able to capture the Reynolds number dependence of statistical quantities.

The K41 theory was extended to account for strong intermittency of the local energy dissipation by Oboukhov (1962) and Kolmogorov (1962), which have become known as refined similarity hypothesis (RSH). A local average at scale r of the energy dissipation $\varepsilon(\boldsymbol{x},t)$ is defined by

$$\varepsilon_r(\boldsymbol{x},t) = \frac{6}{\pi r^2}\int_{|\boldsymbol{r}'|\le r/2} \varepsilon(\boldsymbol{x}+\boldsymbol{r}',t)\mathrm{d}\boldsymbol{r}'\,. \tag{6.33}$$

Then the distribution functions of the velocity increments $\Delta u_i = u_i(\boldsymbol{x}+\boldsymbol{r},t)-u_i(\boldsymbol{x},t)$ at length scales $r \ll l_t$ are universal functions of solely ν, ε_r and r. For scales within the inertial subrange, i.e. $\eta \ll r \ll l_t$, the statistics of Δu become independent of viscosity ν. These hypotheses replace Kolmogorov's first and second hypotheses. In the context of the RSH, Kolmogorov added a third hypothesis which states that ε_r obeys a log-normal distribution. Oboukhov (1962) noted that the log-normal distribution is not strictly valid but is representative for non-linear processes with a systematically increasing intermittency with decreasing scale size.

The refined similarity hypothesis for passive scalars (RSHP), developed by Van Atta (1971) and Antonia and Van Atta (1978), takes strong fluctuations in the local rates of dissipation for both velocity and scalar into account. Based on the RSHP the second and fourth order moments of the scalar gradient become

$$\langle\left(\frac{\partial\phi}{\partial x}\right)^2\rangle \propto \frac{\langle\chi_r\rangle}{D} = \frac{\langle\chi\rangle}{D} \tag{6.34}$$

and

$$\langle \left(\frac{\partial \phi}{\partial x} \right)^4 \rangle \propto \frac{\langle \chi_r^2 \rangle}{D} , \tag{6.35}$$

where χ_r denotes a local average of the scalar dissipation

$$\chi_r(\boldsymbol{x}, t) = \frac{6}{\pi r^2} \int_{|\boldsymbol{r}'| \leq r/2} \chi(\boldsymbol{x} + \boldsymbol{r}', t) \mathrm{d}\boldsymbol{r}' . \tag{6.36}$$

Because of homogeneity the relation $\langle \chi \rangle = \langle \chi_r \rangle$ holds, and additionally, ensemble averages do not depend on neither $\boldsymbol{x}$ nor r. Equations 6.34 and 6.35 were first derived by Wyngaard and Tennekes (1970) for the moments of the velocity field. Then, the scalar gradient flatness can be written as

$$F_{\phi_x} = \frac{\langle \chi_r^2 \rangle}{\langle \chi_r \rangle}, \tag{6.37}$$

The refined similarity theory for passive scalars assumes that the joint probability distribution of χ_r and ε_r is log-normal for $r \ll l_t$. The standard deviations of $\ln \chi_r$ and $\ln \varepsilon_r$ are denoted by $\sigma_{\phi,r}$ and σ_r, respectively. The variances are given by

$$\sigma_{\phi,r}^2 = A_\phi + \mu_\phi \ln \frac{l_t}{r} , \quad \sigma_r^2 = A + \mu \ln \frac{l_t}{r} , \tag{6.38}$$

where μ_ϕ and μ are denoted intermittency parameters which are positive and generally considered as universal. The constants A_ϕ and A depend on the large scales. The assumption of log-normality was subject to controversial discussions. It violates the realizability condition, cf. Frisch (1995), which requires that the scaling exponents $\zeta_\phi(n)$ increase monotonously. Kraichnan (1974) questioned the log-normality assumption because of the non-linearity of the governing equations that can invalidate simple arguments for log-normality and additionally due to the fact that the sum of independent log-normal variables is not log-normal. Wang et al. (1999) suggested by means of DNS that the log-normality assumption is correct for the first moment but showed that departures from log-normality become significant for higher order moments.

By means of the log-normality assumptions the moments of χ_r can be determined as

$$\langle \chi_r \rangle \propto \exp\left(\sigma_\phi^2/2\right) , \quad \langle \chi_r^2 \rangle \propto \exp\left(2\sigma_\phi^2\right) . \tag{6.39}$$

With eqs. 6.38 and 6.39 the scalar gradient flatness becomes

$$F_{\phi_x} \propto \exp\left(\sigma_\phi^2\right) . \tag{6.40}$$

Exploiting log-normality and expressing the variance σ_ϕ by eq. 6.38 yields

$$F_{\phi_x} \propto \exp\left[\mu_\phi \ln\left(\frac{l_t}{r}\right)\right] \propto \left(\frac{l_t}{r}\right)^{\mu_\phi} . \tag{6.41}$$

The length scale r at which χ_r is calculated is not precisely defined. However, in order to determine the scaling of the scalar gradient flatness with the Reynolds number an appropriate length scale r is required. The method of turbulent line segments defines by the mean length ℓ_m a characteristic length scale of scalar gradients. As $\ell_m \propto \eta$ we set $r \propto \eta$ and obtain

$$F_{\phi_x} \propto \left(\frac{l_t}{\eta}\right)^{\mu_\phi} \propto \mathrm{Re}_\lambda^{3\mu_\phi/2} . \tag{6.42}$$

The mean gradient g of turbulent line segments is defined on a mean length scale ℓ_m, cf. eq. 5.44. When we interpret g as a surrogate for χ_r we can reformulate eq. 6.37 and obtain

$$F_{\phi_x} \propto F_g \propto \frac{\langle g^4 \rangle}{\langle g^2 \rangle^2} \propto \mathrm{Re}_\lambda^{3\mu_\phi/2} , \tag{6.43}$$

and hence F_{ϕ_x} and F_g have the same Reynolds number dependence. This consideration is justified by figs. 6.18 and 6.19 where F_g and F_{ϕ_x} exhibit the same scaling exponent, but with a different proportionality constant.

It is customary to estimate the intermittency coefficient μ_ϕ by means of the correlation of χ, namely

$$\langle \chi(\boldsymbol{x}+\boldsymbol{r},t)\chi(\boldsymbol{x},t)\rangle \propto r^{-\mu_\phi} . \tag{6.44}$$

A review by Sreenivasan and Antonia (1997) indicates that μ_ϕ can be estimated by a value between 0.35 and 0.4. For the present DNS we obtain $\mu_\phi \approx 0.31$ with negligible fluctuations between different Reynolds numbers. For the intermittency coefficient of the velocity field we obtain as well independently of Reynolds number $\mu = 0.24$. This difference reflects the different levels of intermittency between the scalar and the energy dissipation. Inserting $\mu_\phi \approx 0.31$ in eqs. 6.42 and 6.43 yields

$$F_{\phi_x} \propto F_g \propto \mathrm{Re}_\lambda^{0.465} , \tag{6.45}$$

which somewhat under-estimates the scaling obtained directly from DNS, cf. eqs. 6.27 and 6.28.

6.4 Reconstruction of Fine-Scale Statistics

The joint pdfs of the length and the scalar difference or the scalar gradient contain most information required to reconstruct statistical properties of the whole field. In this section we will examine the relation between statistics of turbulent line segments and conventional gradient statistics. Therefore, volume-weighted statistics are used throughout this section. After that we will propose a method to reconstruct the pdf of the mean scalar gradient.

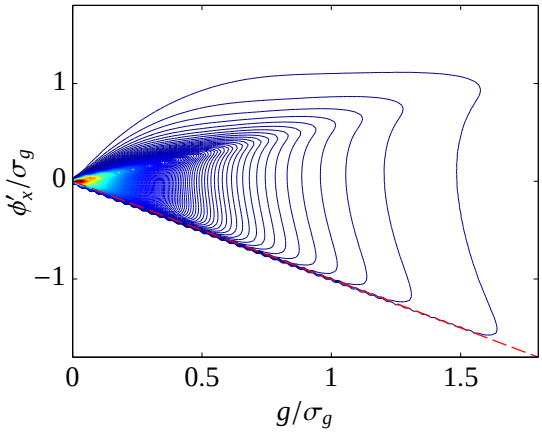

Figure 6.20: Normalized joint pdf of ϕ'_x and g. The joint pdf is point-symmetric and therefore only the right part for $g \geq 0$ is displayed. Both axes are normalized with σ_g. The red line denotes the lower limit $\phi'_x/\sigma_g = -g/\sigma_g$.

6.4.1 Relation between the moments of ϕ_x and g

In order to derive relations between the moments of ϕ_x and g we define a segment based local scalar gradient fluctuation ϕ'_x, defined by

$$\phi'_x(x) = \phi_x(x) - g\,, \tag{6.46}$$

which is a centered stochastic quantity. For positive segments, ϕ'_x is positive when the local gradient is larger than the mean gradient and negative when the local gradient is smaller than the mean gradient. Here, ϕ'_x varies between $-g$ and infinity. The lower bound occurs at the endpoints of the segments or at inflection points within the segments and stems from the fact that at these points ϕ_x vanishes.

Figure 6.20 shows the normalized joint pdf of g and ϕ'_x for positive segments with $g \geq 0$, where the lower bound is depicted by a red line. The joint pdf is point-symmetric and has a distinct maximum close to the origin. With increasing g large values of ϕ'_x are more probable than predicted by a normal distribution.

Equation 6.46 can be used to derive relations between the moments of ϕ_x and g. Because of

$$\langle |g| \rangle = \frac{1}{N} \sum_{i=1}^{N} \left[\frac{1}{\ell} \int_0^\ell \left| \frac{\partial \phi}{\partial x} \right| \mathrm{d}x \right]_i = \langle |\phi_x| \rangle\,, \tag{6.47}$$

the magnitude of the first moments of ϕ_x and g equal each other. Here, the term in the angular brackets is an average within each individual segment. The outer summation is an average over all segments that leads to the final ensemble average.

Additionally, we can derive a relation between the variance of ϕ'_x and g. The variance $\langle \phi_x^2 \rangle$ can be obtained by

$$\begin{aligned} \langle \phi_x^2 \rangle &= \int \langle \phi_x^2 | g \rangle P(g) \mathrm{d}g \\ &= \int \left(\langle \phi_x'^2 | g \rangle + 2 \langle \phi'_x g | g \rangle + \langle g^2 | g \rangle \right) P(g) \mathrm{d}g \\ &= \int (c_g + 1)\, g^2 P(g) \mathrm{d}g = (c_g + 1) \langle g^2 \rangle , \end{aligned} \tag{6.48}$$

where, by definition the conditional average of the fluctuating quantity ϕ'_x vanishes so that

$$\langle \phi'_x g | g \rangle = g \langle \phi'_x | g \rangle = 0 . \tag{6.49}$$

Additionally, we assume on dimensional grounds that

$$\langle \phi_x'^2 | g \rangle = c_g g^2 . \tag{6.50}$$

This relation is justified by means of DNS, cf. fig. 6.21. The constant c_g is independent of Reynolds number and equals approximately 0.5. The significance of this result is that we can state that the variance of the local gradient $\langle \phi_x^2 \rangle$ is related to the variance of the mean gradient $\langle g^2 \rangle$ of turbulent line segments by a simple linear relation

$$\langle \phi_x^2 \rangle = (1 + c_g) \langle g^2 \rangle = 1.5 \langle g^2 \rangle , \tag{6.51}$$

This result can be generalized for higher order moments. Let us now consider the non-dimensional ratio of the nth order moments of ϕ_x and g

$$c_n = \frac{\langle |\phi_x|^n \rangle}{\langle |g|^n \rangle} , \tag{6.52}$$

which is displayed in tab. 6.1 with n up to the sixth order. The value of c_n is independent of Reynolds number but increases with the order n. Thus, a scale similarity between the local gradient ϕ_x and the mean gradient g, at length scale ℓ_m, exists. As a consequence we can calculate higher order moments of ϕ_x by solely knowing the corresponding moments of g as well as the constant c_n. The increase of c_n with the Reynolds number can be explained by rewriting eq. 6.52 as

$$c_n = \frac{\int |\phi_x|^n P(\phi_x) \mathrm{d}\phi_x}{\int |g|^n P(g) \mathrm{d}g} . \tag{6.53}$$

Here, the tails of the pdf of the local gradient $P(\phi_x)$ are determined by more intense events compared to those of $P(g)$. As the tails make a vast contribution to the higher order moments the nominator of eq. 6.53 grows faster than the denominator with the order n.

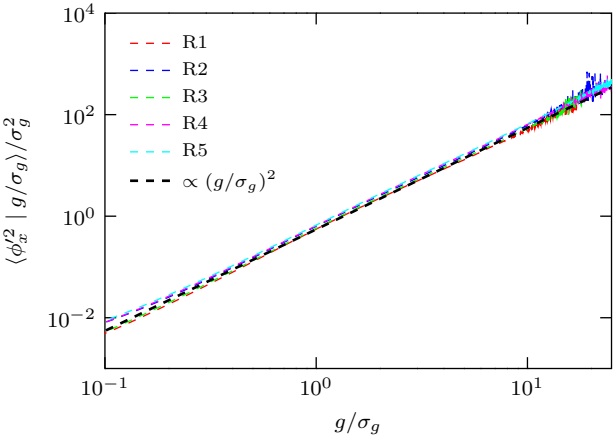

Figure 6.21: Normalized conditional mean $\langle \phi_x'^2 | g \rangle$ for all cases. The black dashed line represents $0.5\,(g/\sigma_g)^2$.

Equation 6.52 can be further supported by means of the scaling of the flatness and hyper-flatness of ϕ_x and g as a function of the Reynolds number, cf. section 6.3.2. The ratio of the even moments of ϕ_x and g can be written as

$$\frac{\langle \phi_x^{2n} \rangle}{\langle g^{2n} \rangle} = \frac{\langle (\phi_x/\sigma_{\phi_x})^{2n} \rangle}{\langle (g/\sigma_{\phi_g})^{2n} \rangle} \left(\frac{\langle \phi_x^2 \rangle}{\langle g^2 \rangle} \right)^n \propto \frac{\mathrm{Re}_\lambda^{m_{\phi_x}(2n)}}{\mathrm{Re}_\lambda^{m_g(2n)}} c_2^n \neq f(\mathrm{Re}_\lambda)\,, \tag{6.54}$$

where $\langle (\phi_x/\sigma_{\phi_x})^{2n} \rangle$ and $\langle (g/\sigma_{\phi_g})^{2n} \rangle$ are the even non-dimensional moments which obey the scaling relations

$$\langle (\phi_x/\sigma_{\phi_x})^{2n} \rangle \propto \mathrm{Re}_\lambda^{m_{\phi_x}(2n)} \tag{6.55}$$

and

$$\langle (g/\sigma_{\phi_g})^{2n} \rangle \propto \mathrm{Re}_\lambda^{m_g(2n)}\,, \tag{6.56}$$

with the scaling exponents $m_{\phi_x}(2n)$ and $m_g(2n)$. According to fig. 6.18 the scaling exponents up to $n = 3$ are equal for ϕ_x and g. Equation 6.54 emphasizes that the ratio $\langle \phi_x^{2n} \rangle / \langle g^{2n} \rangle$ is Reynolds number independent under the conditions that the non-dimensional moments of ϕ_x and g reveal the same scaling exponents and additionally that c_2 is Reynolds number independent.

6.4.2 Reconstruction of the Marginal Gradient PDF

The pdf of scalar gradients is highly non-Gaussian and reveals a rather complex shape, where depending on Reynolds number, it is not clear whether the tails are

Table 6.1: Ratio $c_n = \langle|\phi_x^n|\rangle / \langle|g^n|\rangle$ for all cases with n up to the sixth order showing that c_n is virtually independent of Reynolds number. Thus a scale-similarity between the moments of the local gradient ϕ_x and the mean gradient g exists.

	R1	R2	R3	R4	R5
Re_λ	119	184	215	331	529
c_1	1.00	1.00	1.00	1.00	1.00
c_2	1.51	1.52	1.53	1.52	1.52
c_3	2.72	2.76	2.82	2.84	2.82
c_4	5.23	5.35	5.58	5.56	5.46
c_5	10.22	10.44	11.26	11.03	10.49
c_6	19.88	20.07	22.82	21.23	19.50

exponential or stretched exponential. Thoroddsen and Van Atta (1992) suggested on the basis of experiments with Taylor based Reynolds numbers Re_λ up to 40 an exponential shape of the tails, i.e.

$$P(x/\sigma) \propto \exp(-\alpha x/\sigma)\,, \tag{6.57}$$

where x stands for the scalar gradient and σ for its variance. Holzer and Siggia (1994) suggested a stretched-exponential ansatz, i.e.

$$P(x/\sigma) \propto \exp(-\alpha (x/\sigma)^\beta)\,, \tag{6.58}$$

over a range of x/σ from a fraction of its root-mean-square value outward. According to Holzer and Siggia (1994) eq. 6.58 holds for $x/\sigma > 0.1$ and is therefore not suitable to reconstruct moments. Because of the relatively high Reynolds number in the present work, we observe preferentially stretched exponential tails. This is illustrated in fig. 6.22a where a good agreement between DNS and eq. 6.58 is obtained. The fitting parameters are shown in fig. 6.22b as a function of Re_λ. The parameter α increases with Reynolds number. The parameter β is smaller than unity and decreases with Reynolds number. This implies that the tails become more stretched with Reynolds number suggesting that a simple exponential ansatz, cf. eq. 6.57, is only suitable for low Reynolds number flows.

In order to model the pdf of g of turbulent line segments an ansatz according to eqs. 6.57 and 6.58 is not suitable. The pdf of g has vanishing probability at $g = 0$ and exhibits particularly for lower Reynolds numbers two distinct maxima close to the origin. This form cannot be realized by eq. 6.58. Therefore, we extend the ansatz of Holzer and Siggia (1994) and propose that the normalized gradient pdf satisfies following presumed pdf

$$\sigma_g P(g/\sigma_g) = \mathcal{N}\,|g/\sigma_g|^\gamma \exp(-\alpha\,|g/\sigma_g|^\beta)\,, \tag{6.59}$$

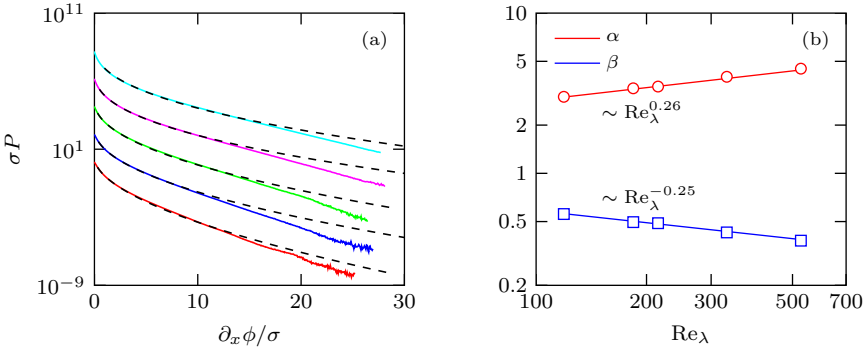

Figure 6.22: Normalized pdf $\sigma_{\phi_x} P(\phi_x/\sigma_{\phi_x})$ (a, same legend as for fig. 6.14). Since the pdfs are symmetric only the positiv branch is shown. The pdfs have been shifted vertically for clarity. The black dashed line represents a best fit to eq. 6.58. Fitting coefficients as a function of Re_λ (b).

where $\mathcal{N}$ achieves the normalization of the pdf, so that only three free parameters α, β and γ remain. The pre-exponential factor ensures that $P(g=0)=0$. Figure 6.23 shows the normalized pdf of g obtained from DNS for all cases. Additionally, the best-fit of eq. 6.59 is displayed separately for each case, where a good agreement between DNS and presumed pdf is obtained over the whole range. The corresponding coefficients are shown in fig. 6.24. The parameter α increases with Reynolds number meaning that the pdfs become steeper. The parameter β is smaller than unity, decreases with Reynolds number, and appears to approach a constant for higher Reynolds numbers. This is a feature of distinct stretched exponential tails. The pre-exponential parameter γ is approximately constant with $\gamma \approx 1.05$.

The pdf fully describes the statistical process so that we can compute all normalized moments of g by eq. 6.59, namely

$$\begin{aligned} \langle |g/\sigma_g|^n \rangle &= \int_{-\infty}^{\infty} |g/\sigma_g|^n \ \sigma_g P(g/\sigma_g) \mathrm{d}(g/\sigma_g) \\ &= \frac{\mathcal{N}}{\beta} \alpha^{-\frac{1+\gamma+n}{\beta}} \Gamma\left(\frac{1+\gamma+n}{\beta}\right), \end{aligned} \tag{6.60}$$

where we take the absolute value in order to obtain non-vanishing odd moments. On the other hand, the moments can be calculated by means of the normalized length distribution $\eta P_\ell(\ell/\eta)$ and the nth conditional average of $\langle |g|^n | \ell \rangle$ by

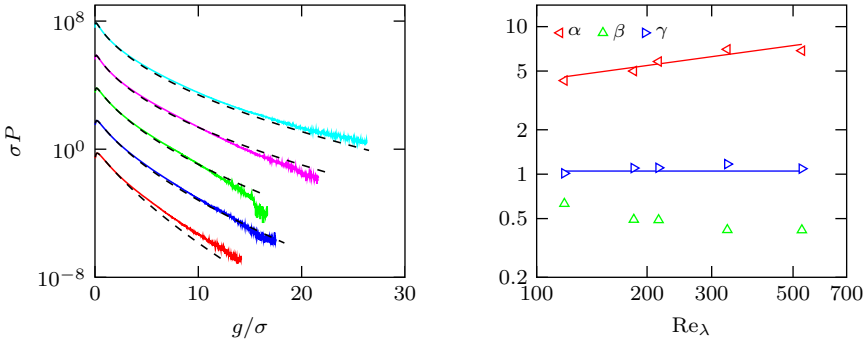

Figure 6.23: Normalized pdf of g (same legend as for fig. 6.14) and comparison with the presumed pdf according to eq. 6.59 obtained by a best-fit for all cases (black dashed lines). Since the pdfs are symmetric only the positive branch is shown. For clarity the curves are shifted vertically.

Figure 6.24: Parameters of the presumed pdf equation for all cases obtained by best-fit of DNS data.

$$\begin{aligned}\langle |g|^n \rangle &= \frac{1}{\ell_m/\eta} \int_0^\infty \langle |g|^n \, |\ell/\eta\rangle (\ell/\eta) \eta P_\ell(\ell/\eta) \mathrm{d}(\ell/\eta) \\ &= \frac{1}{\ell_m/\eta} \int_0^\infty \frac{1}{(\ell/\eta)^n} \langle |\Delta\phi|^n \, |\ell/\eta\rangle (\ell/\eta) \eta^{1-n} P_\ell(\ell/\eta) \mathrm{d}(\ell/\eta) \, .\end{aligned} \tag{6.61}$$

Note that we have normalized the length distribution function P_ℓ by η instead of ℓ_m. This is possible because $\ell_m \propto \eta$. The prefactor as well as the factor (ℓ/η) take into account that the nth moment of g is volume-weighted. For the last equality we make use of the identity

$$\langle g^n | \ell \rangle = \frac{\langle (\Delta\phi)^n | \ell \rangle}{\ell^n} \, . \tag{6.62}$$

Equation 6.61 can be recast in a non-dimensional form, namely

$$\frac{\langle |g|^n \rangle}{\langle \chi \rangle^{\frac{n}{2}} \langle \varepsilon \rangle^{-\frac{n}{6}} \eta^{\frac{2n}{3}}} = \frac{1}{\ell_m/\eta} \int_0^\infty \frac{\langle |\Delta\phi|^n | \ell/\eta \rangle}{\langle \chi \rangle^{\frac{n}{2}} \langle \varepsilon \rangle^{-\frac{n}{6}} \eta^{\frac{n}{3}}} \left(\frac{\ell}{\eta} \right)^{1-n} \eta P_\ell(\ell/\eta) \mathrm{d}(\ell/\eta) \tag{6.63}$$

which reveals that eq. 6.61 can be expressed by the quasi-universal solution of $\eta P(\ell/\eta)$ and the normalized conditional moments of $|\Delta\phi|$. The latter exhibit power law behavior in the viscous and the inertial range, i.e. in the viscous range

$$\frac{\langle |\Delta\phi|^n | \ell/\eta \rangle}{\langle \chi \rangle^{\frac{n}{2}} \langle \varepsilon \rangle^{-\frac{n}{6}} \eta^{\frac{n}{3}}} = c_n^D \, (\ell/\eta)^{\zeta_\phi^D(n)} \, , \tag{6.64}$$

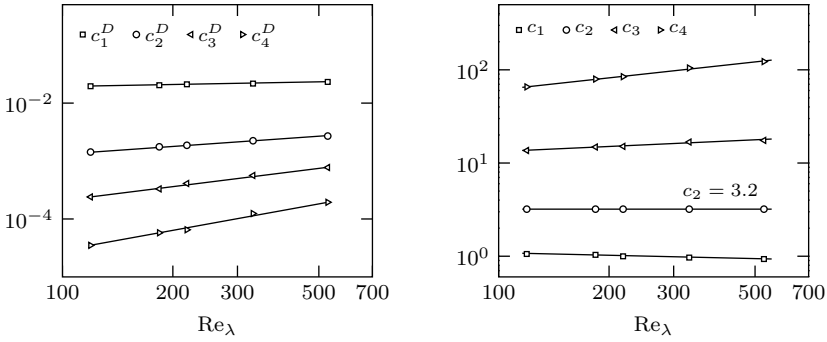

Figure 6.25: Parameter c_n^D and c_n for all cases obtained from DNS.

and in the inertial range

$$\frac{\langle |\Delta\phi|^n | \ell/\eta \rangle}{\langle \chi \rangle^{\frac{n}{2}} \langle \varepsilon \rangle^{-\frac{n}{6}} \eta^{\frac{n}{3}}} = c_n \, (\ell/\eta)^{\zeta_\phi(n)} \ , \tag{6.65}$$

where $\zeta_\phi(n)$ and $\zeta_\phi^N(n)$ are the nth order scaling exponents for the inertial and viscous range, respectively. Both are virtually independent of Reynolds number. From DNS we obtained $\zeta_\phi^D(1) = 2.7$, $\zeta_\phi^D(2) = 5.3$, and $\zeta_\phi^D(3) = 8.0$. The inertial range scaling has been discussed in sec. 6.2 and the values for $\zeta_\phi(n)$ are displayed in fig. 5.16. The parameters c_n and c_n^D are displayed in fig. 6.25. Except for c_2 they depend on Reynolds number, and obey a power law. This leads to the following approximation for the normalized conditional moments

$$\frac{\langle |\Delta\phi|^n | \ell/\eta \rangle}{\langle \chi \rangle^{\frac{n}{2}} \langle \varepsilon \rangle^{-\frac{n}{6}} \eta^{\frac{n}{3}}} = \left[\frac{1}{c_n (\ell/\eta)^{\zeta_\phi(n)}} + \frac{1}{c_n^D (\ell/\eta)^{\zeta_\phi^D(n)}} \right]^{-1} . \tag{6.66}$$

The validity of this approximation is shown in fig. 6.26 for case R2.

The moments of $|\Delta\phi|$ can be determined when the scaling exponents $\zeta_\phi(n)$ and $\zeta_\phi^D(n)$ as well as the Kolmogorov constants c_n and c_n^D are know. With this, we can calculate by means of eq. 6.63 the non-dimensional moments $\langle |g/\sigma_g|^n \rangle$. Three moments are sufficient to determine the free parameters of eq. 6.59. The fourth

parameter $\mathcal{N}$ follows from the normalization condition. This leads to the following system of equations

$$1 = \frac{\mathcal{N}}{\beta}\alpha^{-\frac{1+\gamma}{\beta}}\Gamma\left(\frac{1+\gamma}{\beta}\right) \tag{6.67}$$

$$1 = \frac{\mathcal{N}}{\beta}\alpha^{-\frac{3+\gamma}{\beta}}\Gamma\left(\frac{3+\gamma}{\beta}\right) \tag{6.68}$$

$$\langle g^4\rangle/\sigma_g^4 = \frac{\mathcal{N}}{\beta}\alpha^{-\frac{5+\gamma}{\beta}}\Gamma\left(\frac{5+\gamma}{\beta}\right) \tag{6.69}$$

$$\langle g^6\rangle/\sigma_g^6 = \frac{\mathcal{N}}{\beta}\alpha^{-\frac{7+\gamma}{\beta}}\Gamma\left(\frac{7+\gamma}{\beta}\right) \tag{6.70}$$

that depends solely on the flatness $\langle g^4\rangle/\sigma_g^4$ and hyper-flatness $\langle g^6\rangle/\sigma_g^6$. The reconstruction of the normalized pdf of g by means of eqs. 6.67-6.70 is shown in fig. 6.27 for case R2. A good agreement between modeling based on the presumed pdf and DNS is achieved.

With eq. 6.61 we can attribute the non-universality of the normalized pdf of g to the non-universality of the higher order conditional moments of $\Delta\phi$. Due to the integration with the probability density function of the length ℓ generally all length scales contribute to the moments of g. However, for higher order moments, smaller scales have a larger influence because in eq. 6.61 the conditional moments are weighted by the prefactor $1/(\ell/\eta)^n$.

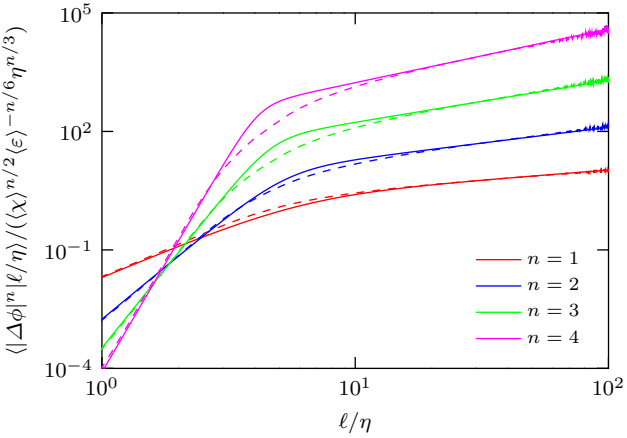

Figure 6.26: Normalized nth order conditional mean of $|\Delta\phi|$ (solid lines) and the approximation by eq. 6.66 (dashed lines) for case R2.

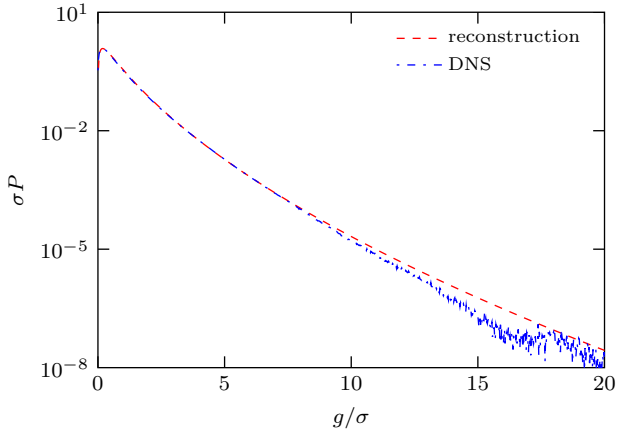

Figure 6.27: Reconstruction of the normalized pdf of g and comparison with DNS (case R2).

7 Summary and Conclusion

In this thesis the turbulent mixing of passive scalars has been examined in terms of statistics and scaling laws, where the focus is on the Reynolds number dependence. To this end, highly-resolved DNS with Taylor based Reynolds numbers varying between 88 and 529 has been conducted. First, the DNS has been validated and characteristic properties of the DNS have been presented. Here, the aim was as well to highlight the intermittent nature of turbulent flows. It turned out that the present DNS is appropriate to compute higher-order statistics of small-scale quantities.

The DNS data have been analyzed by means of standard statistics in the sense of the Kolmogorov-Obhukov-Corrsin theory as well as by an approach that decomposes the turbulent field along a straight line into so-called turbulent line segments. The decomposition is based on the local minima and maxima points of the scalar field so that within each individual segment the scalar value varies monotonously. These segments have been parameterized by their length ℓ and the scalar difference $\Delta\phi$ between the end points, and additionally, by the scalar mean gradient $g = \Delta\phi/\ell$. Based on this parameterization, the DNS has been analyzed by the respective joint and marginal pdfs. Different to other small-scale quantities, the pdf of the length of line segments exhibits a clear exponential tail. The length pdf quantifies the distribution of length scales in physical space and becomes Reynolds number independent when normalized by the mean length ℓ_m. From DNS it has been shown that the mean length ℓ_m scales with the Kolmogorov length η and this finding has been additionally supported by a theoretical derivation based on Rice's theorem. While the mean length obeys a quasi-universal distribution, this is not the case for the distribution functions of the scalar difference $\Delta\phi$ or the mean gradient g. Their tails are exponential or stretched-exponential and the non-Gaussianity becomes more pronounced toward small scales or for rising Reynolds numbers. Furthermore, conditional moments of $\Delta\phi$ have been computed and compared with conventional statistics in the spirit of the KOC theory. The second order moment of the scalar difference exhibits a scaling exponent of 0.8 rather than 2/3 as predicted from the KOC theory. This has been attributed to the fact that line segments relate only extreme points. The higher order conditional moments of line segments exhibit as well an inertial subrange scaling, which is *a-priori* not necessary. In particular the higher order scaling exponents of line segments are closer to the KOC prediction than those of conventional structure functions. By analyzing conditional statistics of g it has been further shown that an intermediate length scale has the main impact on the mean gradients of line segments. Additionally, a scale similarity between the

moments of the local gradients and the moments of the mean gradients has been found and used to reconstruct gradient statistics based on a presumed pdf approach. The scale-similarity is closely linked to the fact that the flatness of mean gradients of line segments increases with Reynolds number at the same rate as the flatness of local gradients.

The method of turbulent line segments provides novel insight into the physics behind cliff-ramp structures. It has been found that on average the width of the steepest gradients, that show up as cliffs in the scalar field, equals approximately 6 times the Kolmogorov length, independently of Reynolds number. Ramp-like structures occur in the scalar profile preferentially for descending segments which are oriented parallel to the mean scalar gradient. Finally, a relationship between the gradient skewness and the statistics of line segments has been established.

It is customary to examine turbulent flows by means of two-point statistics, because they capture the dynamics of the non-local structure that is inherent to turbulence. Therefore, the derivation of a generalized Yaglom equation was presented that is valid in homogeneous but anisotropic scalar turbulence. This equation was interpreted as a scalar scale-by-scale energy budget equation that incorporates the energy flux through a sphere of radius r. This budget was examined by means of DNS and in a filtered form for LES. Thereby, we found that for statistically homogeneous turbulence, modeling the subgrid transport by an eddy-viscosity approach is suitable to correctly predict the energy transport. The generalized Yaglom equation serves as a starting point for further analysis of the Reynolds number dependence of the flatness of scalar increments. To this end, the evolution equations for the fourth order scalar increment is analyzed. On the right hand side of this equation a correlation of the scalar dissipation and the second order scalar increment occurs. Due to this correlation we suppose that dissipative effects are persistent in the inertial subrange that lead to a strong dependence on Reynolds number. This Reynolds number dependence is inherited to the flatness of the scalar increments. Based on this finding we proposed to normalize the fourth order structure function by the correlation of the scalar dissipation and the second order scalar increment, and additionally for dimensional reasons, by a characteristic time scale. Thereby, the curves of the normalized fourth order structure function collapse independently of Reynolds number.

A Normalization of the Scalar Gradient PDF

By normalization of the marginal scalar gradient pdf $P(\phi_x)$ by the standard deviation σ_{ϕ_x} we find that the top of the pdf, i.e. the region for $-5 < \phi_x/\sigma_{\phi_x} < -5$, collapses well to a single curve, cf. fig. 5.20 (bottom). The top of the pdf stems from small events which obey nearly a Gaussian distribution. The tails of the normalized pdf, however, exhibit a strong dependence on Reynolds number. The tails stem from very rare large events that are more probable than predicted by a Gaussian distribution. In order to obtain a collapse of the tails we need to rescale the coordinates. To this end, we found that rescaling the abscissa by $\mathrm{Re}_\lambda^{1/2}$ and the ordinate by Re_λ^2 leads to a collapse of the tails for all Reynolds numbers to a single curve, cf. fig. A.1. As it is not possible to collapse the top and the tails of the pdf at the same time, the top depends now on the Reynolds number.

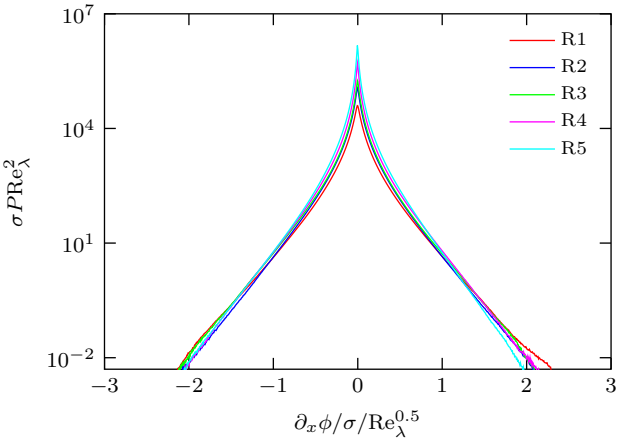

Figure A.1: Marginal pdf of the scalar gradient $\partial_x\phi$, normalized in such a way that the tails collapse to a single curve. For all cases.

B Skewness of the Longitudinal Velocity Gradients

Odd moments are very sensitive to deviations from Gaussianity. The skewness of the longitudinal velocity gradients is defined as

$$S(\partial_L u) = \frac{\langle \left(\frac{\partial u}{\partial x}\right)^3 \rangle}{\langle \left(\frac{\partial u}{\partial x}\right)^2 \rangle^{3/2}} \tag{B.1}$$

and manifests the dynamics of turbulence. In homogeneous isotropic turbulence $S(\partial_L u)$ can be also computed from the spectrum of the turbulent energy by

$$S(\partial_L u) = -\frac{3}{7}\sqrt{30}\nu \frac{\int_0^\infty \kappa^4 E(\kappa)\mathrm{d}\kappa}{\left(\int_0^\infty \kappa^2 E(\kappa)\mathrm{d}\kappa\right)^{3/2}}\,, \tag{B.2}$$

cf. Rotta (2010). Figure B.1 shows the values of $S(\partial_L u)$ as a function of Reynolds number for all cases. The negative skewness of the longitudinal velocity gradients increases with Reynolds number and obeys the scaling law

$$-S(\partial_L u) = 0.3\,\mathrm{Re}_\lambda^{0.12}\,. \tag{B.3}$$

Additionally, the DNS data from Ishihara et al. (2007) are also included in the figure and reveal a very good agreement with the present DNS.

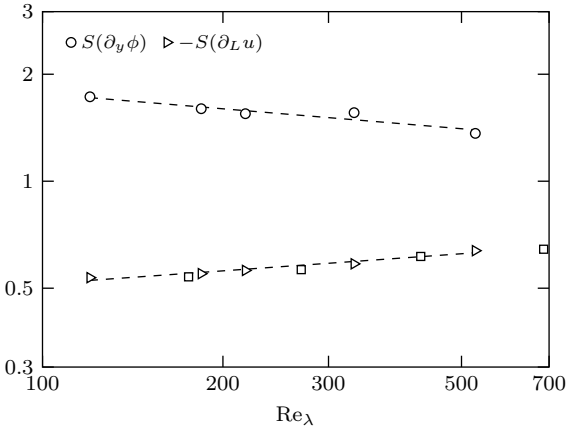

Figure B.1: Skewness of the longitudinal velocity gradients $S(\partial_L u)$ and comparison with DNS by Ishihara et al. (2007) (indicated by squares). For reference the skewness of the scalar derivative $S(\partial_y \phi)$ is also shown.

C Normalized Moments of the Energy Dissipation

For reference, fig. C.1 shows the scaling of the normalized moments of the energy dissipation $\langle \varepsilon^n \rangle / \langle \varepsilon \rangle^n$ with Reynolds number with n between 2 and 4. The higher order normalized moments are a measure for intermittency effects and increase with Reynolds number. They obey a scaling law of the form

$$\frac{\langle \varepsilon^n \rangle}{\langle \varepsilon \rangle^n} \propto \mathrm{Re}_\lambda^{p(n)} , \tag{C.1}$$

where the scaling exponent $p(n)$ is given in fig. C.1. For homogeneous isotropic turbulence the energy dissipation can be directly related to the longitudinal velocity gradients by

$$\langle \varepsilon \rangle = 15\nu \langle \left(\frac{\partial u_1}{\partial x_1} \right)^2 \rangle . \tag{C.2}$$

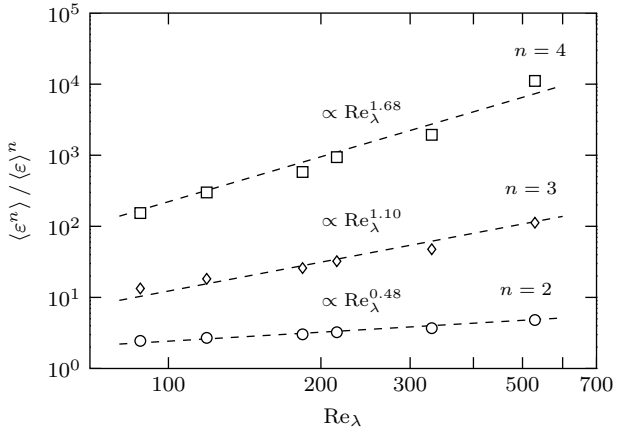

Figure C.1: Scaling of the normalized moments of the energy dissipation $\langle \varepsilon^n \rangle / \langle \varepsilon \rangle^n$ with Reynolds number for all cases.

D Reynolds Number Dependence of the Scalar Flux Spectrum

In chapter 4 the scalar flux $\left\langle (\Delta u_2)(\Delta\phi)\right\rangle$ is studied in correlation space. Lumley (1964) predicted by dimensional arguments that the spectrum of the scalar flux $E_{u_2\phi}(\kappa)$ in isotropic turbulence with imposed uniform mean scalar gradient Γ reads

$$E_{u_2\phi}(\kappa) = \hat{c}_{u_2\phi}\Gamma\langle\varepsilon\rangle^{1/3}\kappa^{-7/3}\,, \tag{D.1}$$

where $\hat{c}_{u_2\phi}$ is a nondimensional constant. The scalar flux spectrum quantifies how the scalar flux is distributed over the scales.

Figure D.1 shows the normalized scalar flux spectrum for all cases. For the present Reynolds numbers the scaling is closer to κ^{-2} than to $\kappa^{-7/3}$. This is in agreement with observations from literature, cf. Watanabe and Gotoh (2007b) and Mydlarski (2003). Bos et al. (2005) showed that Lumley's scaling is attained only at very high Reynolds numbers.

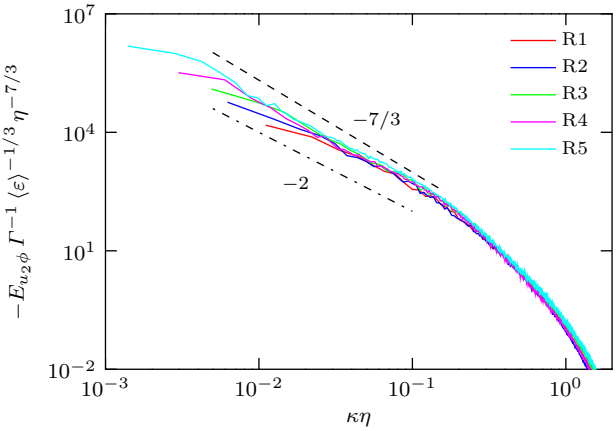

Figure D.1: Normalized scalar flux spectrum $E_{u_2\phi}$ for all cases. The dashed lines indicate κ^{-2} and $\kappa^{-7/3}$ scaling laws, respectively.

References

Antonia, R. and Van Atta, C. (1978). "Structure functions of temperature fluctuations in turbulent shear flows". In: *Journal of Fluid Mechanics* 84, pp. 561–580.

Ashurst, W. T., Kerstein, A., Kerr, R., and Gibson, C. (1987). "Alignment of vorticity and scalar gradient with strain rate in simulated Navier–Stokes turbulence". In: *Physics of Fluids* 30, p. 2343.

Batchelor, G. K. (1953). *The theory of homogeneous turbulence*. Cambridge University Press, Cambridge, UK.

Batchelor, G. (1959). "Small-scale variation of convected quantities like temperature in turbulent fluid". In: *Journal Fluid Mechanics* 5.1, pp. 113–133.

Batchelor, G. and Townsend, A. (1949). "The nature of turbulent motion at large wave-numbers". In: *Proceedings of the Royal Society of London. Series A. Mathematical and Physical Sciences* 199.1057, pp. 238–255.

Benzi, R., Ciliberto, S., Tripiccione, R., Baudet, C., Massaioli, F., and Succi, S. (1993). "Extended self-similarity in turbulent flows". In: *Physical review. A* 48.1, R29–R32.

Benzi, R., Ciliberto, S., Baudet, C., and Chavarria, G. R. (1995). "On the scaling of three-dimensional homogeneous and isotropic turbulence". In: *Physica D: Nonlinear Phenomena* 80.4, pp. 385–398.

Bos, W., Touil, H., and Bertoglio, J.-P. (2005). "Reynolds number dependency of the scalar flux spectrum in isotropic turbulence with a uniform scalar gradient". In: *Physics of Fluids* 17.12, p. 125108.

Bourlioux, A., Majda, A., and Volkov, O. (2006). "Conditional statistics for a passive scalar with a mean gradient and intermittency". In: *Physics of Fluids* 18, p. 104102.

Brethouwer, G., Hunt, J., and Nieuwstadt, F. (2003). "Micro-structure and Lagrangian statistics of the scalar field with a mean gradient in isotropic turbulence". In: *Journal of Fluid Mechanics* 474.1, pp. 193–225.

Butcher, J. C. (2003). "Numerical methods for ordinary differential equation". In: *Willey, New Zealand*.

Canuto, C., Hussaini, M. Y., Quarteroni, A., and Zang, T. A. (1988). *Spectral methods in fluid dynamics*. Springer, Berlin, Germany.

Casciola, C., Gualtieri, P., Benzi, R., and Piva, R. (2003). "Scale-by-scale budget and similarity laws for shear turbulence". In: *Journal of Fluid Mechanics* 476, pp. 105–114.

Celani, A., Cencini, M., Vergassola, M., Villermaux, E., Vincenzi, D., et al. (2005). "Shear effects on passive scalar spectra". In: *Journal of Fluid Mechanics* 523.1, pp. 99–108.

Champagne, F., Friehe, C., LaRue, J., and Wynagaard, J. (1977). "Flux measurements, flux estimation techniques, and fine-scale turbulence measurements in the unstable surface layer over land". In: *Journal of the Atmospheric Sciences* 34.3, pp. 515–530.

Chertkov, M., Falkovich, G., Kolokolov, I., and Lebedev, I. (1998). "Intermittent dissipation of a passive scalar in turbulence". In: *Physical review letters* 80.10, pp. 2121–2124.

Corrsin, S. (1951). "On the spectrum of isotropic temperature fluctuations in an isotropic turbulence". In: *Journal of Applied Physics* 22.4, pp. 469–473.

Cui, G. X., Xu, C.-X., Fang, L., Shao, L., and Zhang, Z. (2007). "A new subgrid eddy-viscosity model for large-eddy simulation of anisotropic turbulence". In: *Journal of Fluid Mechanics* 582.377-397, pp. 82–83.

Cui, G., Zhou, H., Zhang, Z., and Shao, L. (2004). "A new dynamic subgrid eddy viscosity model with application to turbulent channel flow". In: *Physics of Fluids* 16, pp. 2835–2842.

Danaila, L., Anselmet, F., Zhou, T., and Antonia, R. A. (1999). "A generalization of Yaglom's equation which accounts for the large-scale forcing in heated decaying turbulence". In: *Journal of Fluid Mechanics* 391, pp. 359–372.

Danaila, L., Krawczynski, J., Thiesset, F., and Renou, B. (2012). "Yaglom-like equation in axisymmetric anisotropic turbulence". In: *Physica D: Nonlinear Phenomena* 241.3, pp. 216–223.

Davidson, P. A. (2004). *Turbulence: An Introduction for Scientists and Engineers: An Introduction for Scientists and Engineers.* Oxford University Press.

Doering, C. R. and Foias, C. (2002). "Energy dissipation in body-forced turbulence". In: *Journal of Fluid Mechanics* 467, pp. 289–306.

Donzis, D., Sreenivasan, K., and Yeung, P. (2005). "Scalar dissipation rate and dissipative anomaly in isotropic turbulence". In: *Journal of Fluid Mechanics* 532, pp. 199–216.

Donzis, D. and Yeung, P. (2010). "Resolution effects and scaling in numerical simulations of passive scalar mixing in turbulence". In: *Physica D: Nonlinear Phenomena* 239.14, pp. 1278–1287.

Donzis, D., Yeung, P., and Sreenivasan, K. (2008a). "Dissipation and enstrophy in isotropic turbulence: resolution effects and scaling in direct numerical simulations". In: *Physics of Fluids* 20.4, p. 045108.

Donzis, D. A., Yeung, P., and Pekurovsky, D. (2008b). "Turbulence simulations on $\mathcal{O}(10^4)$ processors". In: *Proc. TeraGrid*.

Emran, M. and Schumacher, J. (2008). "Fine-scale statistics of temperature and its derivatives in convective turbulence". In: *Journal of Fluid Mechanics* 611, pp. 13–34.

Eswaran, V. and Pope, S. (1988). "An examination of forcing in direct numerical simulations of turbulence". In: *Computers & Fluids* 16.3, pp. 257–278.

Falkovich, G. and Sreenivasan, K. R. (2006). "Lessons from hydrodynamic turbulence". In: *Physics Today* 59, p. 43.

Ferchichi, M. and Tavoularis, S. (2002). "Scalar probability density function and fine structure in uniformly sheared turbulence". In: *Journal of Fluid Mechanics* 461, pp. 155–182.

Frigo, M. and Johnson, S. (2005). "The Design and Implementation of FFTW3". In: *Proceedings of the IEEE* 93.2, pp. 216–231. ISSN: 0018-9219.

Frisch, U. (1995). *Turbulence - The legacy of A.N. Kolmogorov*. Cambridge University Press, Cambridge, UK.

Fröhlich, J. (2006). *Large Eddy Simulation turbulenter Strömungen*. Wiesbaden, Germany: Teubner.

Gampert, M., Goebbert, J. H., Schaefer, P., Gauding, M., Peters, N., Aldudak, F., and Oberlack, M. (2011). "Extensive strain along gradient trajectories in the turbulent kinetic energy field". In: *New Journal of Physics* 13.4, p. 043012.

Gauding, M., Goebbert, J. H., and Peters, N. (2011). "Scale-by-scale Statistics of Passive Scalar Mixing with Uniform Mean Gradient in Turbulent Flows". In: *Proceedings of the 6th AIAA Theoretical Fluid Mechanics Conference*.

Gauding, M., Wick, A., Peters, N., and Pitsch, H. (2014). "Generalized Scale-by-Scale Energy Budget Equations for Large-Eddy Simulations of Scalar Turbulence at Various Schmidt Numbers". In: *Journal of Turbulence*. accepted.

Gotoh, T., Watanabe, T., and Suzuki, Y. (2011). "Universality and anisotropy in passive scalar fluctuations in turbulence with uniform mean gradient". In: *Journal of Turbulence* 12.48, pp. 1–27.

Gualtieri, P., Casciola, C. M., Benzi, R., and Piva, R. (2007). "Preservation of statistical properties in large-eddy simulation of shear turbulence". In: *Journal of Fluid Mechanics* 592, pp. 471–494.

Gulitski, G., Kholmyansky, M., Kinzelbach, W., Luthi, B., Tsinober, A., and Yorish, S. (2007). "Velocity and temperature derivatives in high-Reynolds-number turbulent flows in the atmospheric surface layer. Part 3. Temperature and joint statistics of temperature and velocity derivatives". In: *Journal of Fluid Mechanics* 589, pp. 103–124.

Gylfason, A. and Warhaft, Z. (2004). "On higher order passive scalar structure functions in grid turbulence". In: *Physics of Fluids* 16, p. 4012.

Hill, R. J. (1997). "Applicability of Kolmogorov's and Monin's equations of turbulence". In: *Journal of Fluid Mechanics* 353, pp. 67–81.

Hill, R. J. (2001). "Equations relating structure functions of all orders". In: *Journal of Fluid Mechanics* 434.1, pp. 379–388.

Hill, R. J. (2002). "Exact second-order structure-function relationships". In: *Journal of Fluid Mechanics* 468, pp. 317–326.

Holzer, M. and Siggia, E. D. (1994). "Turbulent mixing of a passive scalar". In: *Physics of Fluids* 6.5, pp. 1820–1837.

Hou, T. Y. and Li, R. (2007). "Computing nearly singular solutions using pseudo-spectral methods". In: *Journal of Computational Physics* 226.1, pp. 379–397.

Ishihara, T., Kaneda, Y., Yokokawa, M., Itakura, K., and Uno, A. (2007). "Small-scale statistics in high-resolution direct numerical simulation of turbulence: Reynolds number dependence of one-point velocity gradient statistics". In: *Journal of Fluid Mechanics* 592.1, pp. 335–366.

Jayesh, Tong, C., and Warhaft, Z. (1994). "On temperature spectra in grid turbulence". In: *Physics of Fluids* 6, pp. 306–312.

Jiménez, J. and Moser, R. D. (2000). "Large-eddy simulations: Where are we and what can we expect?" In: *AIAA Journal* 38.4, pp. 605–612.

Kaneda, Y., Ishihara, T., Yokokawa, M., Itakura, K., and Uno, A. (2003). "Energy dissipation rate and energy spectrum in high resolution direct numerical simulations of turbulence in a periodic box". In: *Physics of Fluids* 15, p. L21.

Karman, T. and Howarth, L. (1938). "On the statistical theory of isotropic turbulence". In: *Proceedings of the Royal Society of London. Series A, Mathematical and Physical Sciences* 164.917, pp. 192–215.

Kerr, R. M. (1985). "Higher-order derivative correlations and the alignment of small-scale structures in isotropic numerical turbulence". In: *Journal of Fluid Mechanics* 153, pp. 31–58.

Kolmogorov, A. N. (1941a). "Dissipation of energy in locally isotropic turbulence". In: *Dokl. Akad. Nauk SSSR.* Vol. 32. 1, pp. 16–18.

Kolmogorov, A. N. (1941b). "The local structure of turbulence in incompressible viscous fluid for very large Reynolds numbers". In: *Dokl. Akad. Nauk SSSR.* Vol. 30. 4, pp. 299–303.

Kolmogorov, A. N. (1962). "A refinement of previous hypotheses concerning the local structure of turbulence in a viscous incompressible fluid at high Reynolds number". In: *Journal of Fluid Mechanics* 13.1, pp. 82–85.

Kraichnan, R. H. (1974). "On Kolmogorov's inertial-range theories". In: *J. Fluid Mech* 62.2, pp. 305–330.

Kraichnan, R. H. (1994). "Anomalous scaling of a randomly advected passive scalar". In: *Physical review letters* 72.7, p. 1016.

Landau, L. and Lifshitz, E. (1963). *Fluid Mechanics.*

Lepore, J. and Mydlarski, L. (2009). "Effect of the scalar injection mechanism on passive scalar structure functions in a turbulent flow". In: *Physical review letters* 103.3, p. 034501.

Lesieur, M. and Metais, O. (1996). "New trends in large-eddy simulations of turbulence". In: *Annual Review of Fluid Mechanics* 28.1, pp. 45–82.

Lévêque, E., Toschi, F., Shao, L., and Bertoglio, J.-P. (2007). "Shear-improved Smagorinsky model for large-eddy simulation of wall-bounded turbulent flows". In: *Journal of Fluid Mechanics* 570.1, pp. 491–502.

Li, N. and Laizet, S. (2010). "2DECOMP & FFT-A Highly Scalable 2D Decomposition Library and FFT Interface". In: *Cray User Group 2010 conference*, pp. 1–13.

Liepmann, H. (1949). "Die Anwendung eines Satzes über die Nullstellen stochastischer Funktionen auf Turbulenzmessungen". In: *Helv. Phys. Acta* 22, p. 119.

Lumley, J. (1964). "The spectrum of nearly inertial turbulence in a stably stratified fluid". In: *Journal of the Atmospheric Sciences* 21.1, pp. 99–102.

Meneveau, C. (1994). "Statistics of turbulence subgrid-scale stresses: Necessary conditions and experimental tests". In: *Physics of Fluids* 6, pp. 815–833.

Meneveau, C. and Katz, J. (2000). "Scale-invariance and turbulence models for large-eddy simulation". In: *Annual Review of Fluid Mechanics* 32.1, pp. 1–32.

Métais, O. and Lesieur, M. (1992). "Spectral large-eddy simulation of isotropic and stably stratified turbulence". In: *Journal of Fluid Mechanics* 239.1, pp. 157–194.

Moin, P. and Mahesh, K. (1998). "Direct numerical simulation: a tool in turbulence research". In: *Annual Review of Fluid Mechanics* 30.1, pp. 539–578.

Moisy, F., Willaime, H., Andersen, J., and Tabeling, P. (2001). "Passive scalar intermittency in low temperature helium flows". In: *Physical Review Letters* 86.21, pp. 4827–4830.

Monin, A. and Yaglom, A. (1975). *Statistical fluid mechanics: mechanics of turbulence, vol. 2.* MIT Press, Cambridge, MA.

Mydlarski, L. (2003). "Mixed velocity–passive scalar statistics in high-Reynolds-number turbulence". In: *Journal of Fluid Mechanics* 475, pp. 173–203.

Mydlarski, L. and Warhaft, Z. (1996). "On the onset of high-Reynolds-number grid-generated wind tunnel turbulence". In: *Journal of Fluid Mechanics* 320, pp. 331–368.

Mydlarski, L. and Warhaft, Z. (1998). "Passive scalar statistics in high-Péclet-number grid turbulence". In: *Journal of Fluid Mechanics* 358, pp. 135–175.

Nelkin, M. (1992). "In what sense is turbulence an unsolved problem?" In: *Science* 255.5044, pp. 566–570.

Nie, Q. and Tanveer, S. (1999). "A note on third–order structure functions in turbulence". In: *Proceedings of the Royal Society of London. Series A: Mathematical, Physical and Engineering Sciences* 455.1985, pp. 1615–1635.

Oboukhov, A. (1962). "Some specific features of atmospheric turbulence". In: *Journal of Fluid Mechanics* 13.1, pp. 77–81.

Obukhov, A. (1949a). "Temperature field structure in a turbulent flow". In: *Izv. Acad. Nauk SSSR Ser. Geog. Geofiz* 13, pp. 58–69.

Obukhov, A. (1949b). "The local structure of atmospheric turbulence". In: *Dokl. Akad. Nauk. SSSR.* Vol. 67. 4, pp. 643–646.

Overholt, M. R. and Pope, S. B. (1998). "A deterministic forcing scheme for direct numerical simulations of turbulence". In: *Computers & Fluids* 27.1, pp. 11–28.

Papoulis, A. and Pillai, S. U. (2002). *Probability, random variables, and stochastic processes.* McGraw-Hill Education.

Pope, S. B. (2000). *Turbulent flows.* Cambridge University Press, Cambridge, UK.

Rice, S. O. (1945). "Mathematical analysis of random noise-conclusion". In: *Bell Systems Tech. J.* 24, pp. 46–156.

Rogallo, R. (1981). "NASA Technical Memorandum 81315". In: *NASA Ames Research Center.*

Rotta, J. C. (2010). *Turbulente Strömungen.* Vol. 8. Universitätsverlag Göttingen.

Ruiz-Chavarria, G., Baudet, C., and Ciliberto, S. (1996). "Scaling laws and dissipation scale of a passive scalar in fully developed turbulence". In: *Physica D: Nonlinear Phenomena* 99.2, pp. 369–380.

Sagaut, P. (2006). *Large eddy simulation for incompressible flows: an introduction.* Springer, Berlin, Germany.

Schaefer, P., Gampert, M., and Peters, N. (2012). "The length distribution of streamline segments in homogeneous isotropic decaying turbulence". In: *Physics of Fluids* 24, p. 045104.

Schaefer, P., Gampert, M., Wang, L., and Peters, N. (2009). "Fast and slow changes of the length of gradient trajectories in homogeneous shear turbulence". In: *Advances in Turbulence XII.* Springer, pp. 565–569.

Schmitt, F. G. (2005). "Relating Lagrangian passive scalar scaling exponents to Eulerian scaling exponents in turbulence". In: *The European Physical Journal B-Condensed Matter and Complex Systems* 48.1, pp. 129–137.

Schumacher, J., Sreenivasan, K. R., and Yeung, P. (2005). "Very fine structures in scalar mixing". In: *Journal of Fluid Mechanics* 531, pp. 113–122.

Schumacher, J. and Sreenivasan, K. R. (2005). "Statistics and geometry of passive scalars in turbulence". In: *Physics of Fluids* 17.12, pp. 125107–125107.

She, Z.-S., Jackson, E., and Orszag, S. A. (1990). "Intermittent vortex structures in homogeneous isotropic turbulence". In: *Nature* 344.6263, pp. 226–228.

Shraiman, B. I. and Siggia, E. D. (2000). "Scalar turbulence". In: *Nature* 405.6787, pp. 639–646.

Siggia, E. D. (1981). "Numerical study of small-scale intermittency in three-dimensional turbulence". In: *Journal of Fluid Mechanics* 107, pp. 375–406.

Smagorinsky, J. (1963). "General circulation experiments with the primitive equations: i. the basic experiment". In: *Monthly weather review* 91.3, pp. 99–164.

Sreenivasan, K. R. (1996). "The passive scalar spectrum and the Obukhov–Corrsin constant". In: *Physics of Fluids* 8, p. 189.

Sreenivasan, K. R. (1998). “An update on the energy dissipation rate in isotropic turbulence”. In: *Physics of Fluids* 10, pp. 528–529.
Sreenivasan, K. R. and Antonia, R. (1997). “The phenomenology of small-scale turbulence”. In: *Annual review of fluid mechanics* 29.1, pp. 435–472.
Sreenivasan, K. (1991). “On local isotropy of passive scalars in turbulent shear flows”. In: *Proceedings of the Royal Society of London. Series A: Mathematical and Physical Sciences* 434.1890, pp. 165–182.
Sreenivasan, K. (1995). “The energy dissipation in turbulent shear flows”. In: *Fluid Dyn. Aerospace Eng. Banglore*, pp. 159–190.
Sreenivasan, K., Prabhu, A., and Narasimha, R. (1983). “Zero-crossings in turbulent signals”. In: *J. Fluid Mech* 137, pp. 251–272.
Sreenivasan, K., Tavoularis, S., Henry, R., and Corrsin, S. (1980). “Temperature fluctuations and scales in grid-generated turbulence”. In: *Journal of Fluid Mechanics* 100.3, pp. 597–621.
Stolovitzky, G. and Sreenivasan, K. (1993). “Scaling of structure functions”. In: *Physical Review E* 48.1, R33.
Tavoularis, S. (1985). “Temperature fluctuations and heat flux in grid-generated isotropic turbulence with streamwise and transverse mean-temperature gradients”. In: *J. Fluid Mech* 153, pp. 441–460.
Taylor, G. I. (1938). “The spectrum of turbulence”. In: *Proceedings of the Royal Society of London. Series A-Mathematical and Physical Sciences* 164.919, pp. 476–490.
Tennekes, H. and Lumley, J. L. (1972). *A first course in turbulence*. The MIT press.
Thoroddsen, S. and Van Atta, C. (1992). “Exponential tails and skewness of density-gradient probability density functions in stably stratified turbulence”. In: *Journal of Fluid Mechanics* 244.1, pp. 547–566.
Tong, C. and Warhaft, Z. (1994). “On passive scalar derivative statistics in grid turbulence”. In: *Physics of Fluids* 6, p. 2165.
Tsinober, A. (2001). *An informal introduction to turbulence*. Vol. 63. Springer.
Van Atta, C. (1971). “Influence of fluctuations in local dissipation rates on turbulent scalar characteristics in the inertial subrange”. In: *Physics of Fluids* 14, p. 1803.
Vedula, P., Yeung, P., and Fox, R. (2001). “Dynamics of scalar dissipation in isotropic turbulence: a numerical and modelling study”. In: *Journal of Fluid Mechanics* 433, pp. 29–60.
Wang, L.-P., Chen, S., and Brasseur, J. G. (1999). “Examination of hypotheses in the Kolmogorov refined turbulence theory through high-resolution simulations. Part 2. Passive scalar field”. In: *Journal of Fluid Mechanics* 400, pp. 163–197.
Wang, L. (2008). “Geometrical Description of Homogeneous Shear Turbulence Using Dissipation Element Analysis”. PhD thesis. RWTH-Aachen University.
Wang, L. (2009). “Scaling of the two-point velocity difference along scalar gradient trajectories in fluid turbulence”. In: *Physical Review E* 79.4, p. 046325.

Wang, L. and Peters, N. (2006). "The length-scale distribution function of the distance between extremal points in passive scalar turbulence". In: *Journal of Fluid Mechanics* 554, pp. 457–476.

Wang, L. and Peters, N. (2008). "Length-scale distribution functions and conditional means for various fields in turbulence". In: *Journal of Fluid Mechanics* 608, pp. 113–138.

Warhaft, Z. (2000). "Passive scalars in turbulent flows". In: *Annual Review of Fluid Mechanics* 32.1, pp. 203–240.

Watanabe, T. and Gotoh, T. (2004). "Statistics of a passive scalar in homogeneous turbulence". In: *New Journal of Physics* 6.1, p. 40.

Watanabe, T. and Gotoh, T. (2007a). "Inertial-range intermittency and accuracy of direct numerical simulation for turbulence and passive scalar turbulence". In: *Journal of Fluid Mechanics* 590, pp. 117–146.

Watanabe, T. and Gotoh, T. (2007b). "Scalar flux spectrum in isotropic steady turbulence with a uniform mean gradient". In: *Physics of Fluids* 19.12.

Wilczek, M. (2011). "Statistical and Numerical Investigations of Fluid Turbulence". PhD thesis. Münster University.

Wyngaard, J. and Tennekes, H. (1970). "Measurements of the small-scale structure of turbulence at moderate Reynolds numbers". In: *Physics of Fluids* 13, p. 1962.

Yaglom, A. (1949). "On the local structure of a temperature field in a turbulent flow". In: *Dokl. Akad. Nauk SSSR.* Vol. 69. 6, pp. 743–746.

Yakhot, V. and Sreenivasan, K. R. (2005). "Anomalous scaling of structure functions and dynamic constraints on turbulence simulations". In: *Journal of statistical physics* 121.5-6, pp. 823–841.

Yeung, P., Donzis, D., and Sreenivasan, K. (2005). "High-Reynolds-number simulation of turbulent mixing". In: *Physics of Fluids* 17, p. 081703.

Yeung, P., Xu, S., and Sreenivasan, K. (2002). "Schmidt number effects on turbulent transport with uniform mean scalar gradient". In: *Physics of Fluids* 14, p. 4178.

Yeung, P. and Zhou, Y. (1997). "Universality of the Kolmogorov constant in numerical simulations of turbulence". In: *Physical Review E* 56.2, pp. 1746–1752.